The biogeochemistry and residual mean circulation of the Southern Ocean

by

Takamitsu Ito

Submitted to the Department of Earth Atmospheric and Planetary Sciences
in partial fulfillment of the requirements for the degree of

Doctor of Philosophy

at the

MASSACHUSETTS INSTITUTE OF TECHNOLOGY

Feburary 2005

Author .....
Department of Earth Atmospheric and Planetary Sciences
October 7, 2004

Certified by .....
John C. Marshall
Professor
Thesis Supervisor

Accepted by .....
Maria Zuber
Department Head, Department of Earth, Atmospheric and Planetary Sciences

The biogeochemistry and residual mean circulation of the Southern Ocean

by

Takamitsu Ito

Submitted to the Department of Earth Atmospheric and Planetary Sciences
on October 7, 2004, in partial fulfillment of the
requirements for the degree of
Doctor of Philosophy

Abstract

I develop conceptual models of the biogeochemistry and physical circulation of the Southern Ocean in order to study the air-sea fluxes of trace gases and biological productivity and their potential changes over glacial-interglacial timescales. Mesoscale eddy transfers play a dominant role in the dynamical and tracer balances in the Antarctic Circumpolar Current, and the transport of tracers is driven by the residual mean circulation which is the net effect of the Eulerian mean circulation and the eddy-induced circulation.

Using an idealized, zonally averaged model of the ACC, I illustrate the sensitivity of the uptake of transient tracers including CFC11, bomb-$\Delta^{14}C$ and anthropogenic CO_2 to surface wind stress and buoyancy fluxes over the Southern Ocean. The model qualitatively reproduces observed distribution of CFC11 and bomb-$\Delta^{14}C$, and a suite of sensitivity experiments illustrate the physical processes controlling the rates of the oceanic uptake of these tracers. The sensitivities of the uptake of CFC11 and bomb-$\Delta^{14}C$ are largely different because of the differences in their air-sea equilibration timescales. The uptake of CFC11 is mainly determined by the rates of physical transport in the ocean, and that of bomb-$\Delta^{14}C$ is mainly controlled by the air-sea gas transfer velocity. Anthropogenic CO_2 falls in between these two cases, and the rate of anthropogenic CO_2 uptake is affected by both processes.

Biological productivity in the Southern Ocean is characterized with the circumpolar belt of elevated biological productivity, "Antarctic Circumpolar Productivity Belt". Annually and zonally averaged export of biogenic silica is estimated by fitting the zonally averaged tracer transport model to the climatology of silicic acid using the method of least squares. The pattern of export production inferred from the inverse calculation is qualitatively consistent with recent observations. The pattern of inferred export production has a maximum on the southern flank of the ACC. The advective transport by the residual mean circulation is the key process in the vertical supply of silicic acid to the euphotic layer where photosynthesis occurs. In order to illustrate what sets the position of the productivity belt, I examined simulated biological production in a physical-biogeochemical model which includes an

explicit ecosystem model coupled to the phosphate, silica and iron cycle. Simulated patterns of surface nutrients and biological productivity suggest that the circumpolar belt of elevated biological productivity should coincide with the regime transition between the iron-limited Antarctic zone and the macro-nutrients limited Subantarctic zone. At the transition, organisms have relatively good access to both micro and macro-nutrients.

Kohfeld (in Bopp et al.; 2003) suggested that there is a distinct, dipole pattern in the paleo-proxy of biological export in the Southern Ocean at the LGM. I hypothesize that observed paleo-productivity proxies reflect the changes in the position of the Antarctic Circumpolar Productivity Belt over glacial-interglacial timescales. Increased dust deposition during ice ages is unlikely to explain the equatorward shift in the position of the productivity belt due to the expansion of the oligotrophic region and the poleward shift of the transition between the iron-limited regime and the macro-nutrient limited regime. I develop a simple dynamical model to evaluate the sensitivity of the meridional overturning circulation to the surface wind stress and the stratification. The theory suggest that stronger surface wind stress could intensify the surface residual flow and perturb the position of the productivity belt in the same sign as indicated by the paleo-productivity proxies.

Finally, I examined the relationship between the surface macro-nutrients in the polar Southern Ocean and the atmospheric pCO_2. Simple box models developed in 1980s suggests that depleting surface macro-nutrients in high latitudes can explain the glacial pCO_2 drawdown inferred from polar ice cores. A suite of sensitivity experiments are carried out with an ocean-atmosphere carbon cycle model with a wide range of the rate of nutrient uptake in the surface ocean. These experiments suggest that the ocean carbon cycle is unlikely to approach the theoretical limit where "preformed" nutrient is completely depleted due to the dynamics of deep water formation. The rapid vertical mixing timescales of convection preclude the ventilation of strongly nutrient depleted waters. Thus it is difficult to completely deplete the "preformed" nutrients in the Southern Ocean even in a climate with elevated dust deposition in the region, suggesting some other mechanisms for the cause of lowered glacial pCO_2.

Thesis Supervisor: John C. Marshall
Title: Professor

Acknowledgments

I would like to acknowledge John Marshall and Mick Follows for their guidance and support throughout my study at MIT. I also thank the thesis committee members, Ed Boyle, Kerry Emmanuel and Julian Sachs for their insightful comments for the thesis project, and I thank the climate modeling community at MIT for the development of MITgcm. I thank Bob Key for motivating the CFC11-bomb $\Delta^{14}C$ relationship in the Southern Ocean (chapter 2), and Stephanie Dutkiewicz and Payal Parekh for the development of the global ocean physical-biogeochemical model, and Samar Khatiwala and Francois Primeau for motivating the matrix formulation of the tracer transport (chapter 3).

Physical oceanography group at MIT provided a stimulating and exciting environment to study the circulation of the oceans and climate. I would like to thank Stephanie Dutkiewicz, Fanny Monteiro and Payal Parekh for discussions on ocean biogeochemistry, and Timour Radko for conversations on the residual mean circulation in the ACC. I thank the support stuff at MIT who have been helpful for various tasks including computer networking, printing, educational and financial administration.

At last but first in my heart, I thank my family for their love, patience and support. I eternally thank my wife Mitsuko for her support during difficult times and sharing wonderful moments in our life. My kids Kotaro and Keiko have been the greatest source of joy. I also thank my extended families in Japan for their support and prayers.

This work is supported by the Office of Polar Programs at NSF, NSF grant OCE-0136609 and OCE-0350672.

Contents

List of Figures

List of Tables

Chapter 1

Introduction

The Southern Ocean extends from the coast of Antarctica north to the southern part of the Atlantic Ocean, Indian Ocean and Pacific Ocean. The natural boundary between the northern basins and the Southern Ocean is the intense, eastward-flowing Antarctic Circumpolar Current (hereafter, ACC) and its associated quasi-zonal fronts where sharp changes in temperature, salinity and other properties are observed (Fig.1-1 and 1-2). The absence of topographic barriers in the latitude band of Drake Passage has important influences on the dynamics of the ACC and the transport of chemical and biological tracers there. A general review of the dynamics of the ACC can be found, for example, in (Rintoul et al., 2001). Here I briefly give an overview of some recent developments in understanding the dynamics and biogeochemistry of the Southern Ocean, which motivates several questions on the role of the Southern Ocean in the uptake of anthropogenic CO_2 into the oceans and past changes of the global nutrient and carbon cycle.

Fig. 1-3 shows the horizontal pathway of the ACC calculated from the temporally averaged geostrophic streamlines of the ACC based on the dynamic sea surface height, h, observed by the TOPEX-POSEIDON satellite altimeter[1]. The currents rapidly circulate from west to east along the circumpolar streamlines. The mean pathway of the ACC is determined by the interplay between bottom topography and

[1]Geostrophic streamlines, Ψ_g, are determined by $\Psi_g = \frac{gh}{f}$ where g is the gravitational constant and f is the Coriolis parameter. In Fig.1-3 Ψ_g varies by $5 \cdot 10^4$ m^2 s^{-1} across the Drake passage.

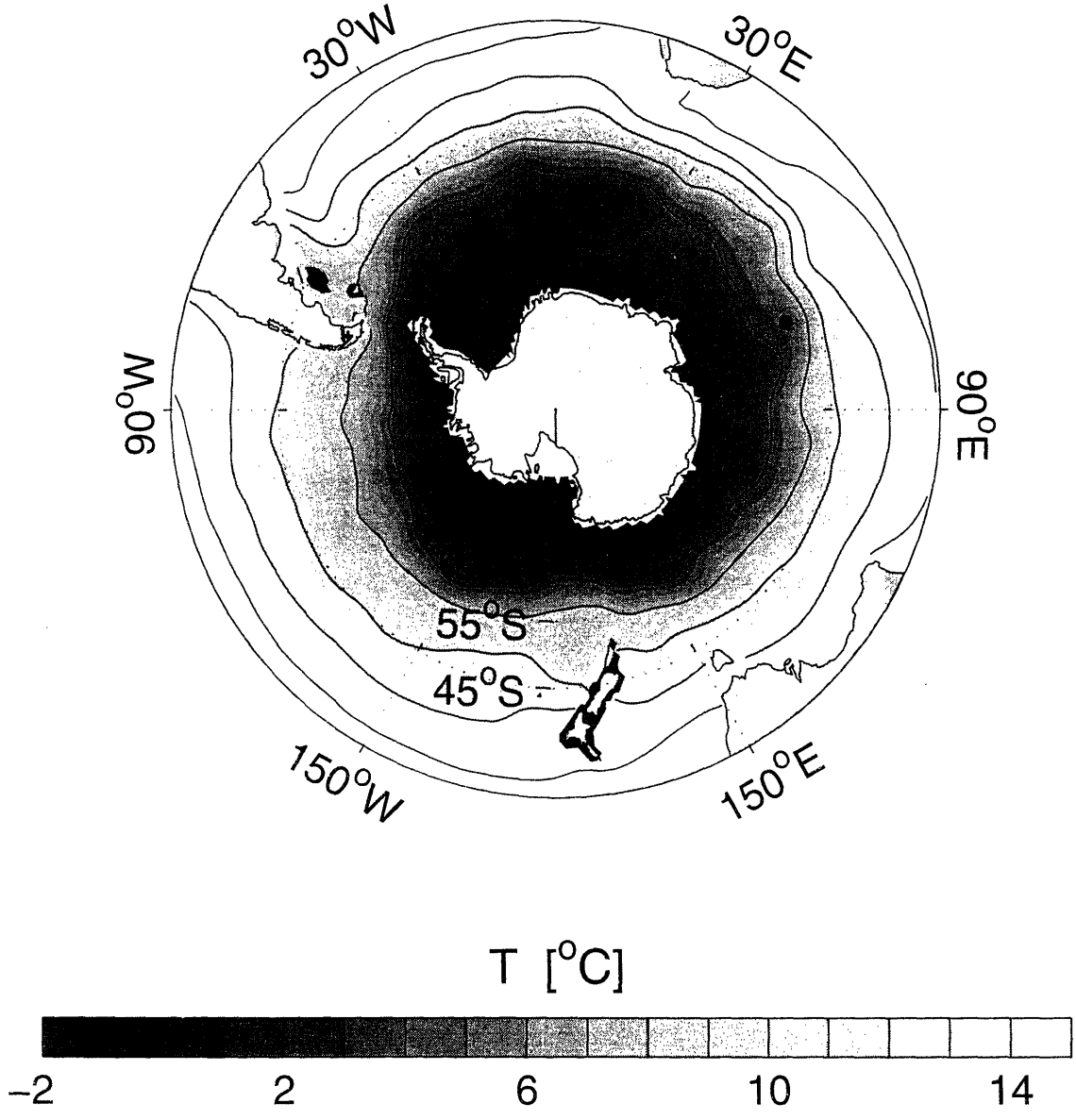

Figure 1-1: Annual mean surface temperature distribution in the Southern Ocean based on the World Ocean Atlas 2001 (Conkright et al., 2002). Contour interval is 4° C.

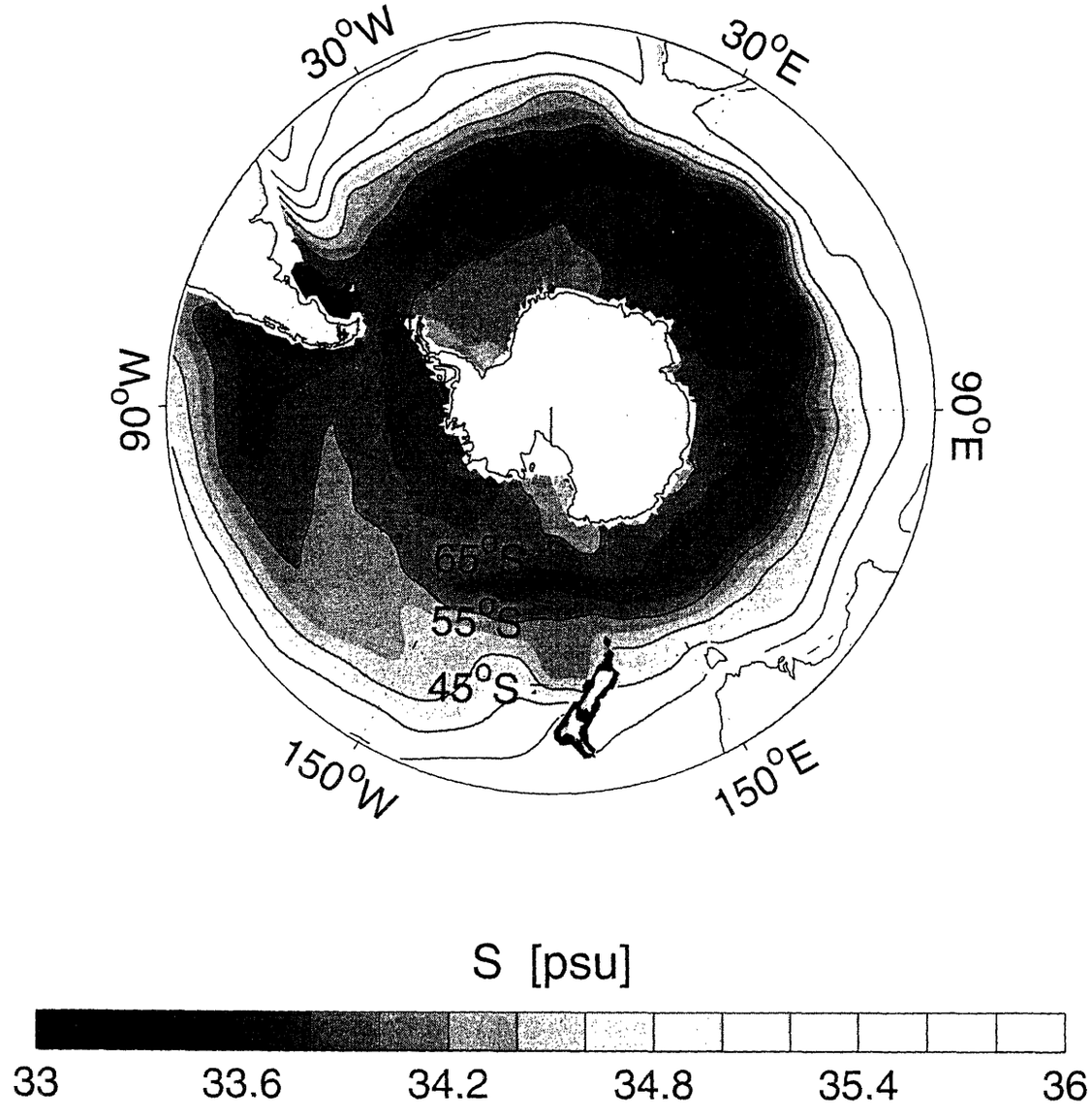

Figure 1-2: Annual mean surface salinity distribution in the Southern Ocean based on the World Ocean Atlas 2001 (Conkright et al., 2002). Contour interval is 0.4 psu.

the conservation of potential vorticity (Gille, 1995; Marshall, 1995). This horizontal circulation connects the Atlantic, Indian and Pacific basins. While this quasi-horizontal, circumpolar current is the dominant feature of the ACC, the circulations in the latitude-depth plane are crucial to the transport of chemical and biological tracers. Fig.1-4 and 1-5 show meridional sections of neutral density and oxygen in the Atlantic and Pacific sector. Early researchers have interpreted the qualitative pattern of the meridional overturning circulation following the distribution of tracers such as temperature, salinity and oxygen (Sverdrup et al., 1942) (Fig.1-6). To the south of the ACC deep waters upwell into the surface layers, and near the Antarctic convergence (Polar Front), surface waters subduct into the ocean interior and form Antarctic Intermediate Water (AAIW).

1.1 Residual mean circulation

Recent theoretical and modeling studies have led to a better understanding in the mechanisms controlling the structure and rates of the meridional overturning circulation in the Southern Ocean. In the latitude band of the ACC, the net meridional geostrophic flow must vanish since the zonal pressure gradient integrates out to zero around the latitudinal circle. Thus the meridional transport of heat, salt and chemical tracers must be carried by eddies below the base of the surface Ekman layer. In the surface Ekman layer, the interplay of the Ekman transport and the eddy-induced transport determines the transport of tracers and air-sea fluxes of buoyancy, CO_2, CFCs and other trace gases (Marshall, 1997; Speer et al., 2000; Marshall and Radko, 2003; Ito et al., 2004). Thus the mesoscale eddy fluxes are fundamentally important for the biogeochemistry of the Southern Ocean. However, biogeochemical studies in this area typically use highly idealized, diffusive parameterization of mesoscale eddy fluxes. The goal of this thesis is to bring together recent views of ocean dynamics and biogeochemistry to examine and explore the role of the Southern Ocean in the global carbon cycle in the past and present.

Fig. 1-7 illustrates the simplest description of the meridional overturning circu-

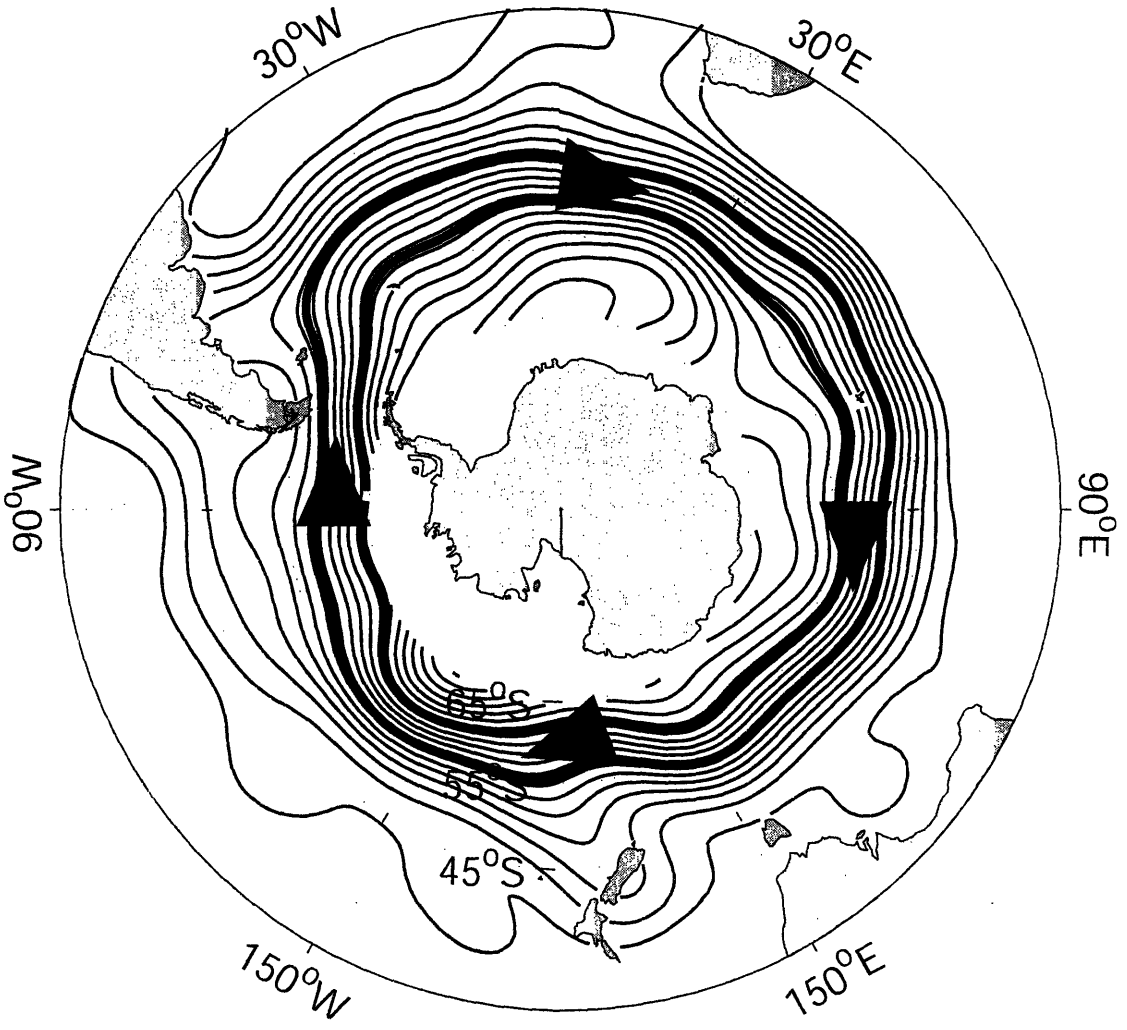

Figure 1-3: Geostrophic Streamlines of the ACC based on 4 year time-averaged TOPEX-POSEIDON dynamic sea surface topography. Contour interval is $1 \cdot 10^4$ $m^2\ s^{-1}$. Data is provided by Center of Space Research, University of Texas, Austin.

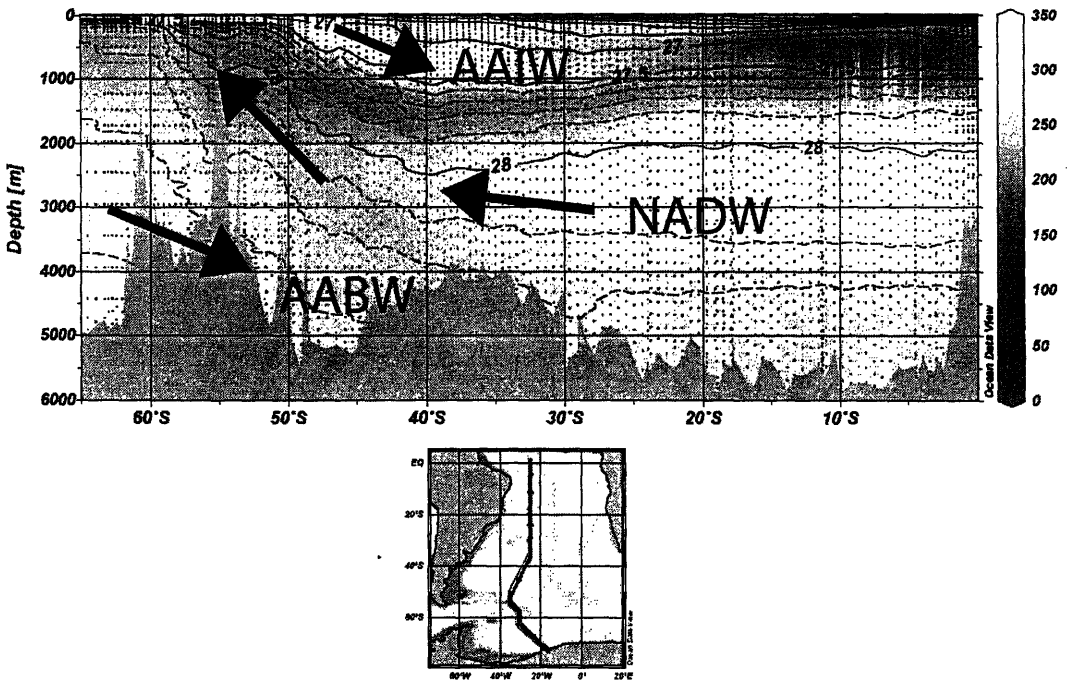

Figure 1-4: Meridional section of neutral density (contour) and oxygen (gray scale) in the Atlantic section. The data is taken from the WOCE hydrographic and bottle data (A-16) and plotted using Ocean Data View. The contour interval for neutral density is 0.5 for solid lines, and is 0.1 for dashed lines. The distribution of oxygen is generally oriented along isopycnals in the Southern Ocean. The newly ventilated Subantarctic Mode Water (SAMW: $26.5 < \gamma_n < 27.0$) and the Antarctic Intermediate Water (AAIW: $27.0 < \gamma_n < 27.5$) are well oxygenated and spread into the northern basins. North Atlantic Deep Water (NADW: $28.0 < \gamma_n < 28.2$) is relatively well oxygenated, and is entrained and mixed with Circumpolar Deep Waters as it enters into the Southern Ocean. The Upper Circumpolar Deep Water (UCDW: $27.5 < \gamma_n < 28.0$) and the Lower Circumpolar Deep Water (LCDW: $28.0 < \gamma_n < 28.2$) are generally oxygen-depleted reflecting the influences of old, deep waters from the Pacific basin. The Antarctic Bottom Water (AABW: $28.2 < \gamma_n$) is ventilated from the continental shelves in the Weddell Sea and the Ross Sea, and also is relatively rich in oxygen.

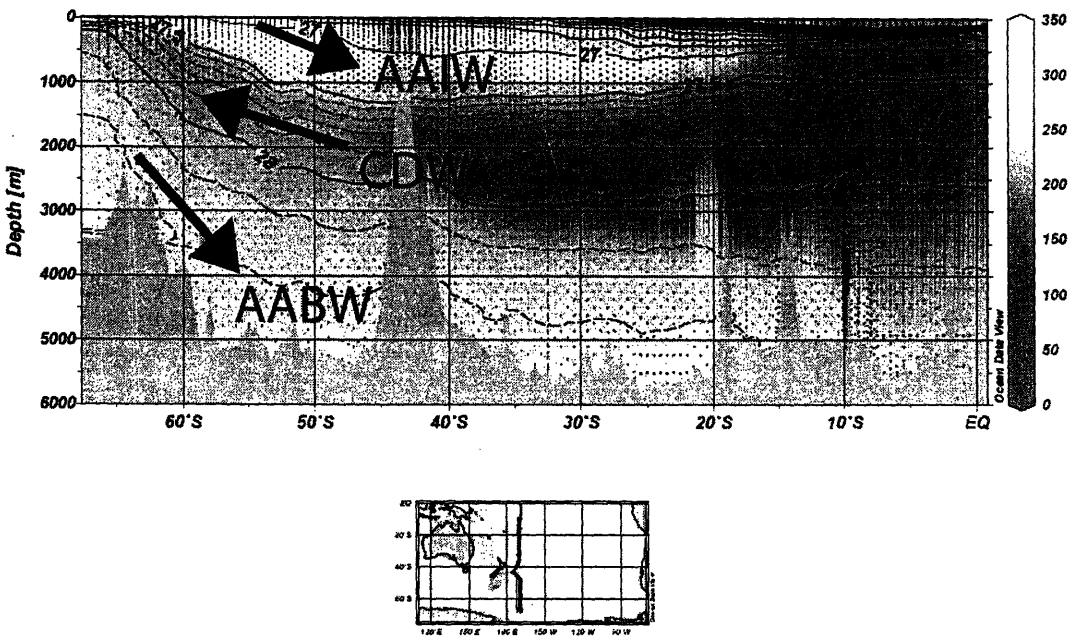

Figure 1-5: Meridional section of neutral density (contour) and oxygen (gray scale) in the Pacific section. The data is taken from the WOCE hydrographic and bottle data (P-15) and plotted using Ocean Data View. The contour interval for neutral density is 0.5 for solid lines, and is 0.1 for dashed lines. The major difference between the Atlantic and Pacific sector is the difference in the influences of the northern basins. Deep waters in the North Atlantic are relatively new and well oxygenated, in contrast to the old, oxygen-depleted deep Pacific waters.

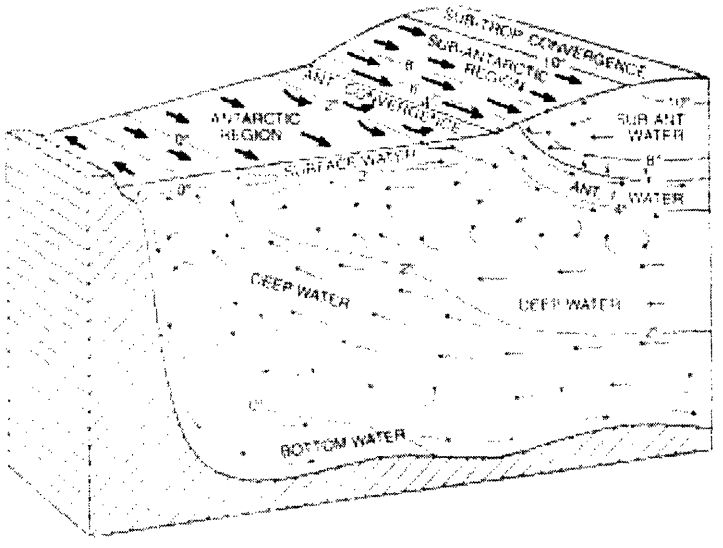

Figure 1-6: A schematic diagram of the meridional overturning circulation reproduced from (Sverdrup et al., 1942). The early researchers inferred the qualitative pattern of the circulation from chemical tracers.

lation in the ACC. The westerly wind drives an equatorward Ekman circulation in the surface layers. The Eulerian mean, meridional overturning circulation, widely known as the Deacon cell, is driven by the surface Ekman transport and geostrophic return flow in the interior ocean supported by the deep topography. The wind-driven upwelling of relatively cold deep waters and downwelling of relatively warm surface waters tend to tilt isopycnals producing the available potential energy of the mean flow. The effect of baroclinic eddies is to extract the potential energy and flatten the isopycnals, which results in the eddy-induced, meridional overturning circulation[2], partially canceling out the wind-driven Eulerian mean circulation (Johnson and Bryden, 1989). Temperature, salinity and other tracers are advected by the residual mean flow, the net effect of the Eulerian mean and the eddy-induced circulation.

Furthermore, there is a thermodynamic constraint that density must be conserved following the residual mean circulation since the diabatic component of eddy fluxes and diapycnal mixing are relatively small away from surface and bottom boundary layers (Marshall, 1997; Speer et al., 2000; Karsten et al., 2002), consistent with the observed distribution of chemical tracers which can be seen to spread along the isopycnal surfaces. Chemical tracers integrate (over time) the effects of a relatively weak, meridional overturning circulation. The distributions of long-lived tracers reflect the pattern of residual mean flow, which gives some sense of overturning circulation shown in Fig.1-4, 1-5 and 1-6. The transport of carbon and nutrients by the residual mean circulation are the key factors in controlling biological productivity, global carbon pumps, and the uptake of anthropogenic CO_2 in the region. In this thesis, I formulate simple models of physical-biogeochemical coupling in the framework of the residual mean theory.

[2]See, for example, (Gill, 1982) for a general review of baroclinic instability theories and the eddy-mean flow interactions.

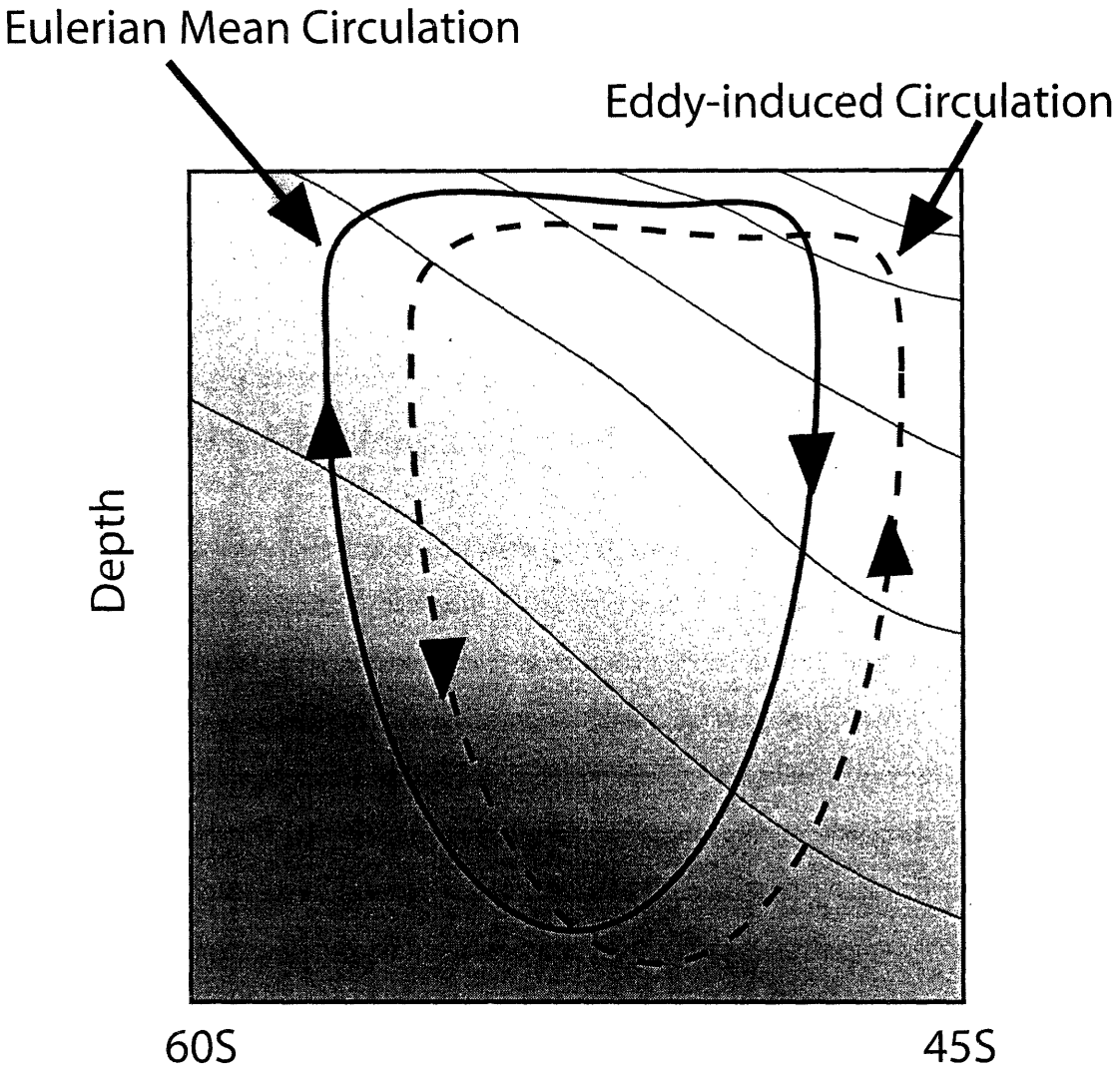

Figure 1-7: A simplified view of the meridional overturning circulation in the Southern Ocean

1.2 The uptake of anthropogenic CO_2

The oceans are the largest sink of fossil fuel CO_2 in the ocean-atmosphere-land system, and recent research indicates that the Southern Ocean is one of the major regions of CO_2 uptake. 7.1 $\pm$ 1.1 PgC (1 PgC = 10^{15} gC) of carbon was emitted annually into the atmosphere during the 1980s due to human activities, and the emission rate continues to rise. Recent studies suggest 2.0 $\pm$ 0.8 PgC were taken up annually into the global oceans during 1980s (Siegenthaler and Sarmiento, 1993; Takahashi et al., 2002). However, the rate at which the oceans absorb anthropogenic CO_2 and its spatial distribution are difficult to determine from direct observations because the anthropogenic perturbations are small compared to the background, naturally-occurring CO_2 fluxes. Furthermore ship-based observations are sparse in time and space. For this reason ocean general circulation and biogeochemical model simulations have been used to provide additional estimates of the distribution and fluxes of anthropogenic CO_2. The Ocean Carbon-cycle Model Inter-comparison Project (hereafter, OCMIP) examined and compared several general circulation model (hereafter, GCM) simulations of anthropogenic tracers(Orr et al., 2001; Dutay et al., 2002). Orr et al. (2001) suggest that the Southern Ocean is a major region of ocean uptake of anthropogenic CO_2 in the models, but also find that it is the region where the models show the largest disagreement in the air-sea CO_2 flux. Fig.1-8 shows simulated, zonally averaged uptake of anthropogenic CO_2 uptake into the global oceans from four OCMIP-1 models. Due to the large surface area of the Southern Ocean, the total CO_2 uptake is the greatest there in most of the models. However, the differences between the models are large, and understanding the processes which cause these differences is crucial for improving current estimates of the CO_2 uptake by the oceans and future climate change. These coarse resolution models typically have horizontal resolution of >100 km, and do not resolve mesoscale eddies whose length scale is on the order of 10 km. Thus the mesoscale eddy fluxes are parameterized. Some recent biogeochemistry models apply the isopycnal thickness diffusion scheme of (Gent and McWilliams, 1990) which includes the advective fluxes of eddies in the sub-grid

scale eddy parameterization, and those models better reproduce the distribution of transient tracers such as CFCs in the Southern Ocean (Robitaille and Weaver, 1995).

The air-sea CO_2 flux is driven by the disequilibrium between the partial pressure of CO_2 in the atmosphere and the sea surface, which is maintained by the interplay between physical circulation, chemical and biological processes. The timescales of air-sea CO_2 equilibration is on the order of a year (Broecker, 1974), suggesting that the air-sea gas exchange is unlikely to be the rate limiting process in the uptake of CO_2 into the surface oceans. Surface waters will reach saturation with atmospheric CO_2 within a few years if the surface layer is stagnant and does not interact with interior ocean. The renewal of surface waters by the upwelling and entrainment of thermocline waters is required to maintain the surface undersaturation and uptake of anthropogenic CO_2 into the surface oceans. Therefore, the pattern and the magnitude of the residual mean flow can play the central role in determining the uptake of anthropogenic CO_2 through controlling the rate of upwelling and renewal of the surface waters in the Southern Ocean. Mesoscale eddy fluxes and the parameterization of them might be the key process limiting our ability to predict the regional uptake of CO_2.

In chapter 2, I develop zonally averaged model of tracer transport in the ACC based on the residual mean theory, and use the model to estimate the uptake of transient tracers including CFCs, bomb radiocarbon, and anthropogenic CO_2. The simplicity of the model allows us to illustrate the relative roles of lateral advection, entrainment of thermocline waters and isopycnal stirring of tracers in controlling the tracer uptake and its regional variation. Scaling relationships are derived for the sensitivity of tracer uptake for each tracer. Tracer distributions are strongly influenced by the ocean circulation. In turn, observed tracer distributions can help constrain the rates of the meridional overturning circulation.

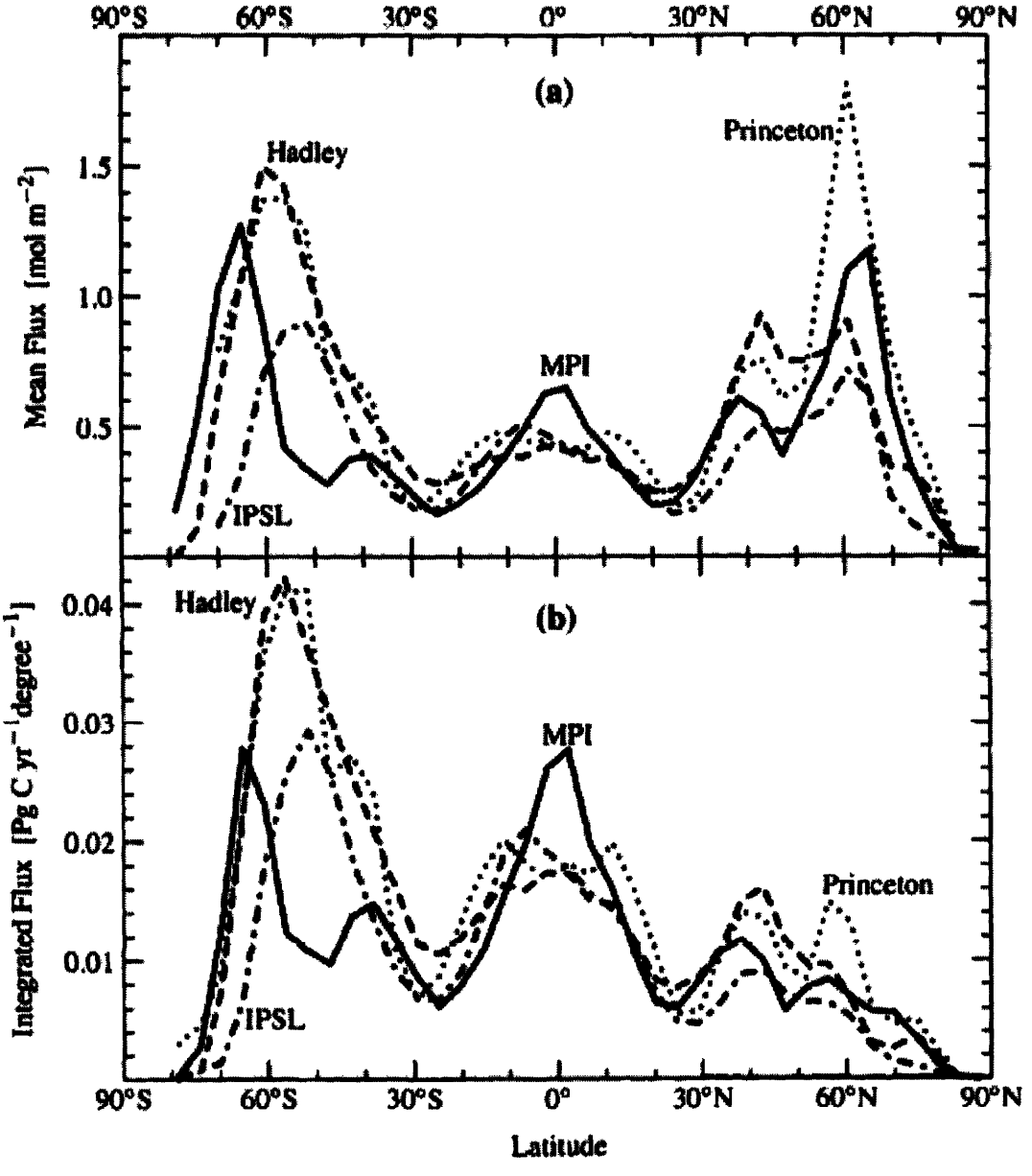

Figure 1-8: Simulated profile of the anthropogenic CO_2 uptake from the OCMIP-1 models. This figure is reproduced from (Orr et al., 2001). These early models do not include advective influences of eddies in their sub-grid scale eddy parameterization.

1.3 Biological pump of CO_2 during the Last Glacial Maximum

The biogeochemistry and physical circulation of the Southern Ocean could have played important roles in past climate changes. Atmospheric partial pressure of CO_2 over the past 420,000 years is reconstructed from polar ice cores (Petit et al., 1999) and revealed that the atmospheric pCO_2 and the polar atmospheric temperatures are tightly coupled with one another. Fig.1-9 shows the variation of atmospheric pCO_2 and polar atmospheric temperature derived from the Vostok ice core. At the Last Glacial Maximum (hereafter, LGM: approximately 12,000 years ago) polar temperatures were cooler approximately by 10°C and atmospheric pCO_2 was lower than the preindustrial condition approximately by 80 ppmv. A number of theories have been suggested to explain the link between the glacial climate and the lowered atmospheric pCO_2.

Some researchers argue that biological pump of CO_2[3] was more efficient during ice ages due to the changes in the biogeochemistry and physical circulation of the Southern Ocean. So-called the "Harvardton Bear" models, which were developed during 1980s by groups at Harvard, Princeton and Bern universities (Sarmiento and Toggweiler, 1984; Siegenthaler and Wenk, 1984; Knox and McElroy, 1984), have shown that a drawdown of sea-surface nutrients in the high latitudes is sufficient to cause a decrease in the atmospheric pCO_2 comparable to those recorded in ice cores. A schematic diagram (Fig.1-10) illustrates how high-latitude surface nutrients may be related to atmospheric pCO_2. The model consists of low-latitude and high-latitude surface oceans, and a deep ocean. At low latitudes, surface nutrients are almost completely utilized, and the export of organic material vertically transfers nutrients and carbon from the surface layer to the deep layer. Due to the density structure of the oceans, the deep waters are ventilated through the polar outcrop, and so chemical

[3]Photosynthesis in the surface ocean converts inorganic carbon and nutrients into organic matter, often accompanied with calcium carbonate structural material. A fraction of the organic matter described as export production, is ultimately transported to, and remineralized within, thermocline and abyssal ocean. Vertical transfer of CO_2 due to the export of organic material is termed as *soft tissue pump* and that of calcium carbonate as *carbonate (hard shell) pump*. The biological pump of CO_2 consists of soft tissue pump and carbonate pump.

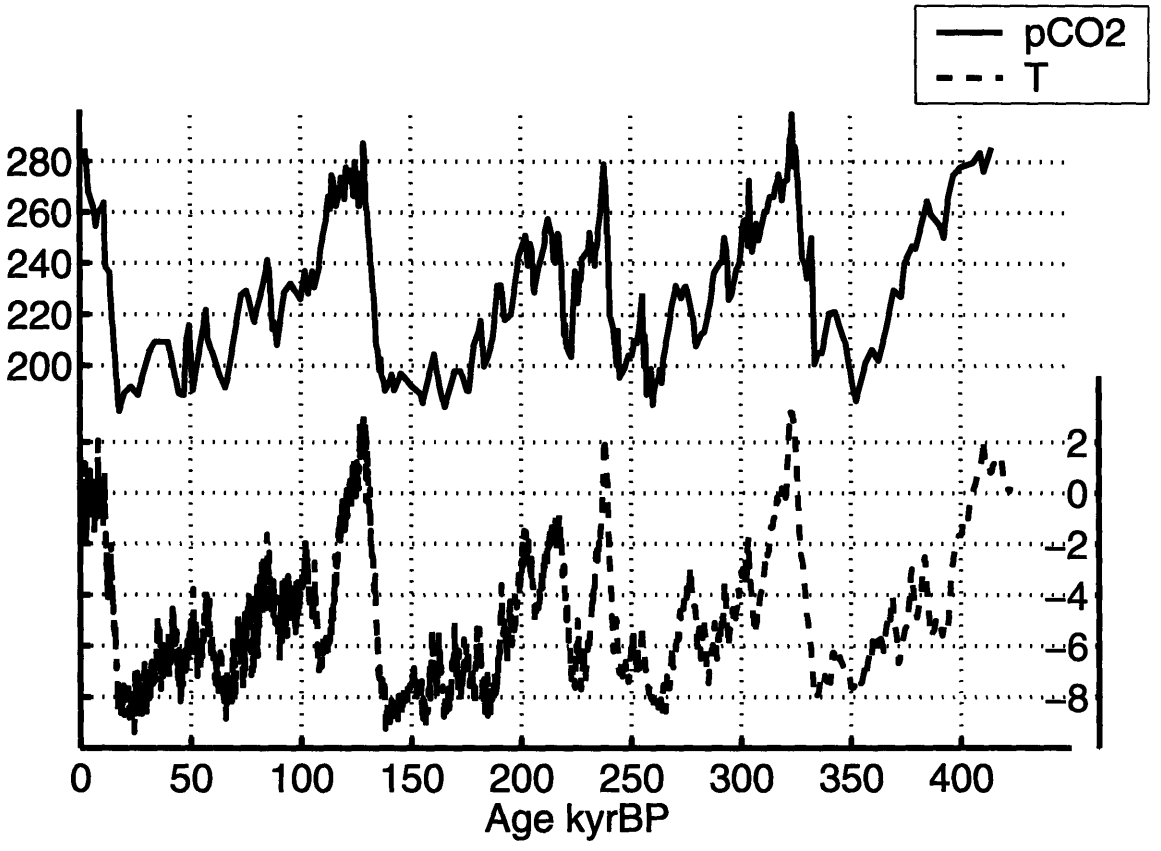

Figure 1-9: Atmospheric pCO_2 and polar atmospheric temperature reconstructed from the Vostok ice cores (Petit et al., 1999). The horizontal axis is the "age" of ice in units of kyr BP (1,000 years before present). The progression of time is conventionally defined from right (old) to left (recent).

properties of high-latitude surface oceans and that of deep waters significantly influence one another[4]. The Southern Ocean is characterized with elevated macro-nutrient concentration in present climate (see Fig.1-11). As the deep waters are entrained into the surface waters, a fraction of CO_2 sequestered by the biological pump at low latitudes is released into the atmosphere. Elevated surface nutrient concentration indicates the inefficiency of the global biological pump. Surface nutrient concentration is set by the competition between the supply of nutrients by the upwelling and the removal by the biological uptake and export. When regional biological uptake is weak relative to the upwelling of nutrients, surface nutrient concentrations become higher, and larger amount of CO_2 is transferred to the atmosphere by outgassing. In the context of these highly idealized box models, there are two processes which can decrease the surface nutrients and suppress the regional outgassing of CO_2 at high latitudes.

- Increased, regional biological uptake and export (Fig.1-10, case 1)
- Decreased upwelling of the deep waters to the surface layer (Fig.1-10, case 2)

The first mechanism could have been supported by the supply of iron to the surface oceans through atmospheric dust deposition (Martin, 1990). Fig.1-11 and 1-12 show the annually-averaged, global distribution of macro-nutrients in the surface oceans. Fig.1-13 and 1-14 shows the distribution in the Southern Ocean. The concentration of phosphate and silicic acid is remarkably high in the polar Southern Ocean. The growth of phytoplankton is not limited by the supply of these macro-nutrients there. The biogeochemistry of the Southern Ocean has been considered as a "high nutrient low chlorophyll" (hereafter, HNLC) condition, where the rate of biological production, normalized by the available macro-nutrient, is relatively low and surface macro-nutrients are not fully utilized. It has been suggested that the biological productivity in the HNLC region could be limited by the supply of micro-nutrients such as iron (Martin and Fitzwater, 1988). In-situ iron addition experiments in HNLC regions

[4]Typically, the "preformed" properties of the deep waters refer to the properties of the polar outcrop at the time of the formation of water masses. As we discuss later in chapter 5, "preformed" nutrients play the central role in the theory of biological pumps.

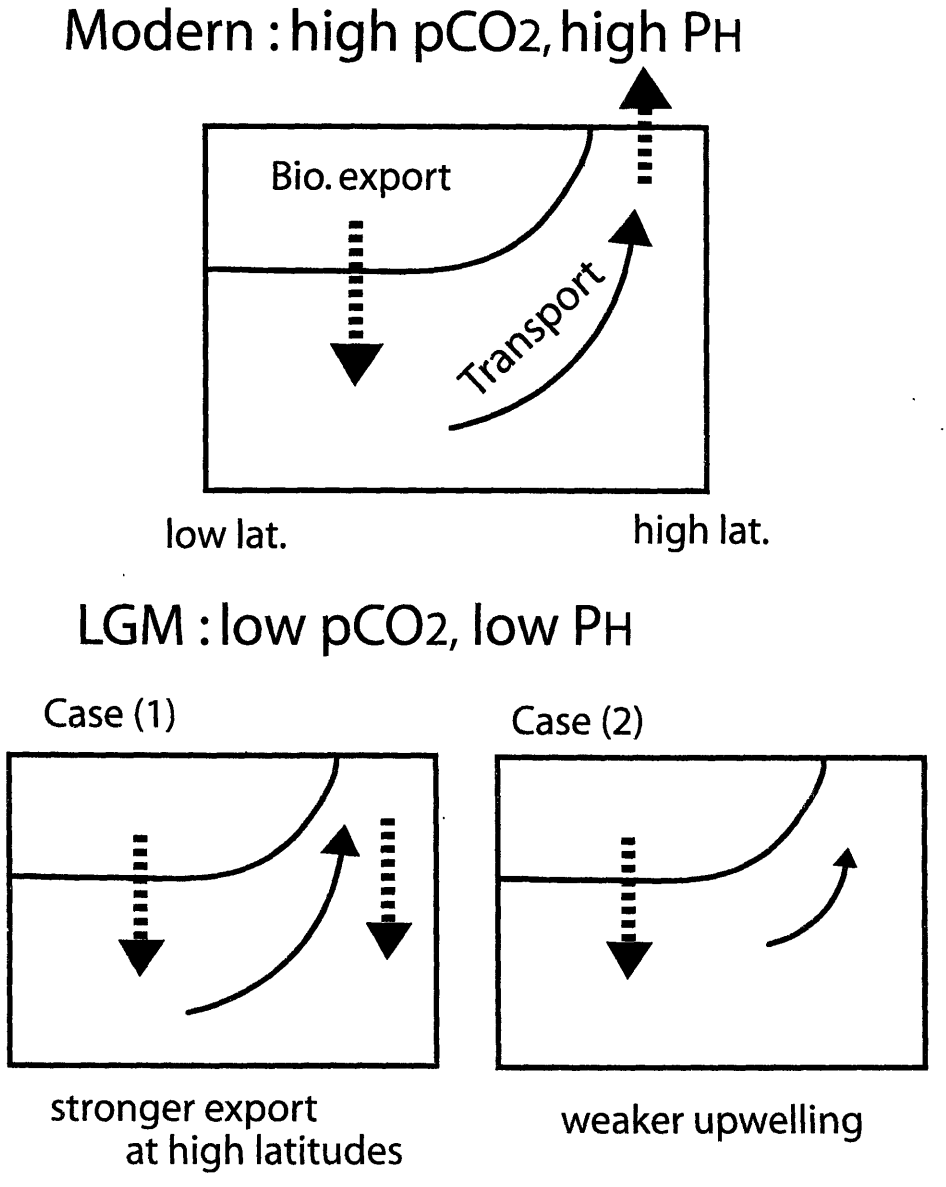

Figure 1-10: Schematic diagrams illustrating the influences of high latitude surface ocean in controlling the efficiency of the biological pump in the global oceans. P_H represents high-latitude surface nutrient concentration. Arrows with dash line represent fluxes of DIC due to chemical and biological processes including biological export and air-sea CO_2 flux. Arrows with solid line represent fluxes of DIC due to physical circulation.

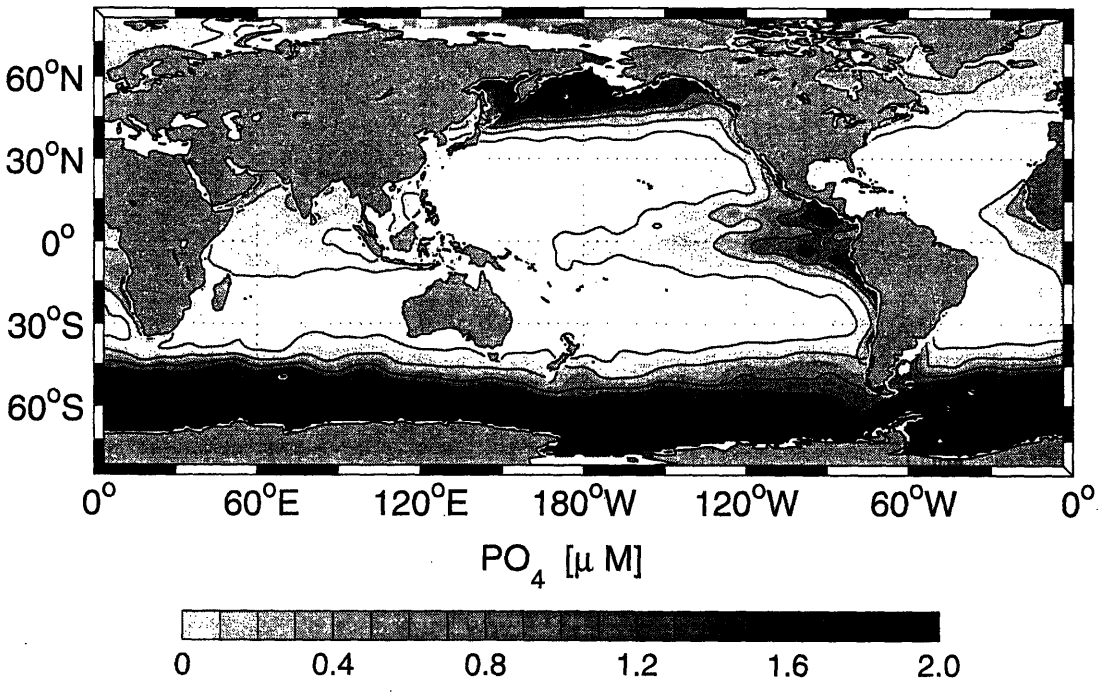

Figure 1-11: Annual mean surface phosphate distribution in the global ocean based on the World Ocean Atlas 2001 (Conkright et al., 2002). Contour interval is 0.4 μ M.

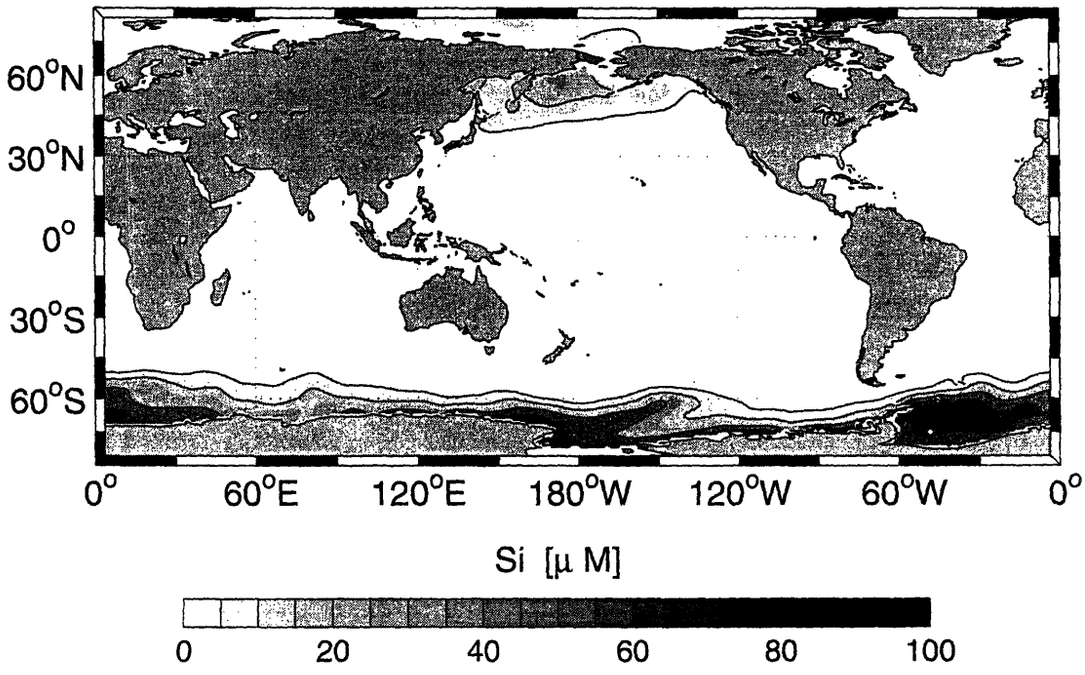

Figure 1-12: Annual mean surface silicic acid distribution in the global ocean based on the World Ocean Atlas 2001 (Conkright et al., 2002). Contour interval is 20 μ M.

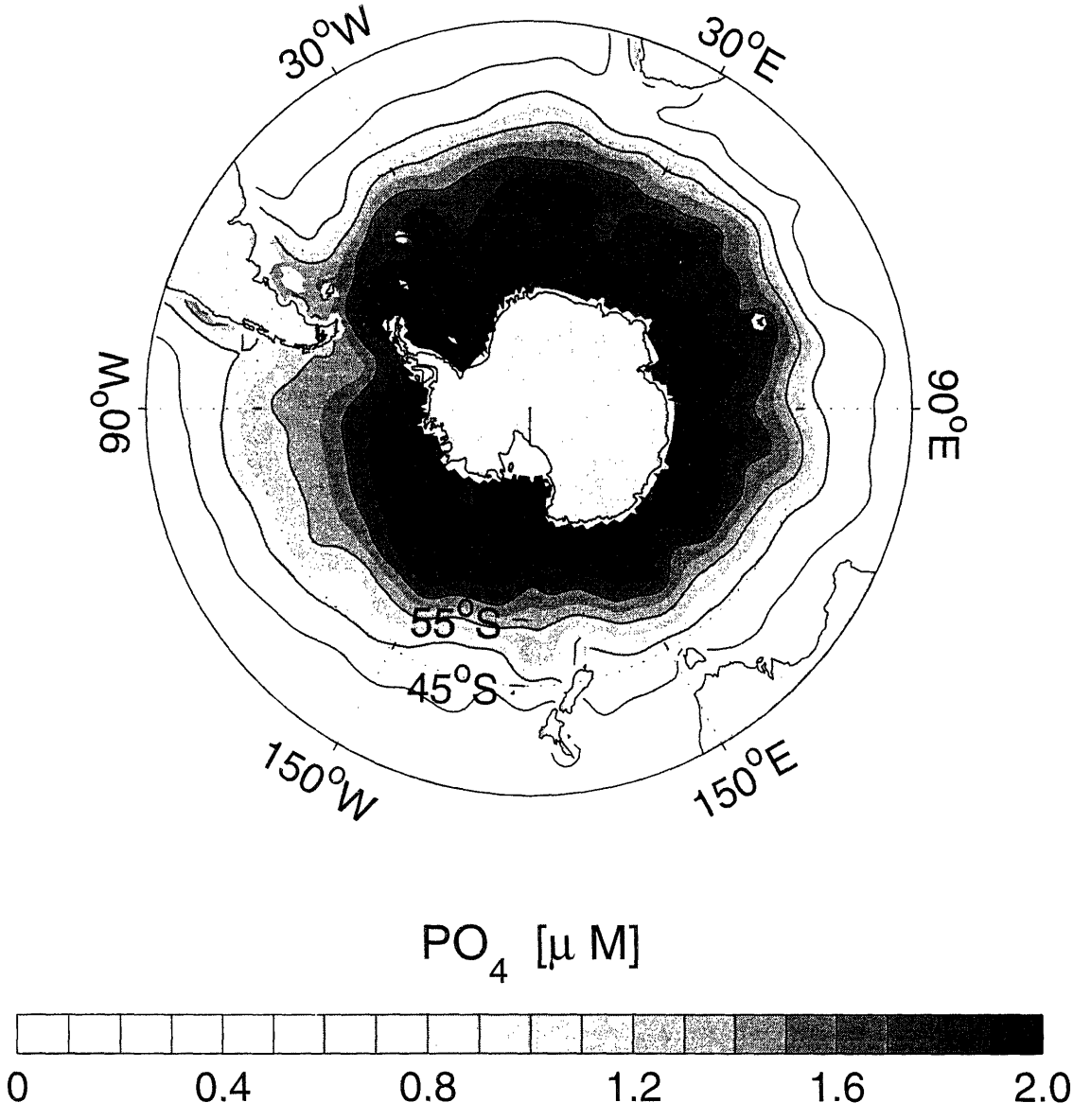

Figure 1-13: Annual mean surface phosphate distribution in the Southern Ocean based on the World Ocean Atlas 2001 (Conkright et al., 2002). Contour interval is 0.4 μ M.

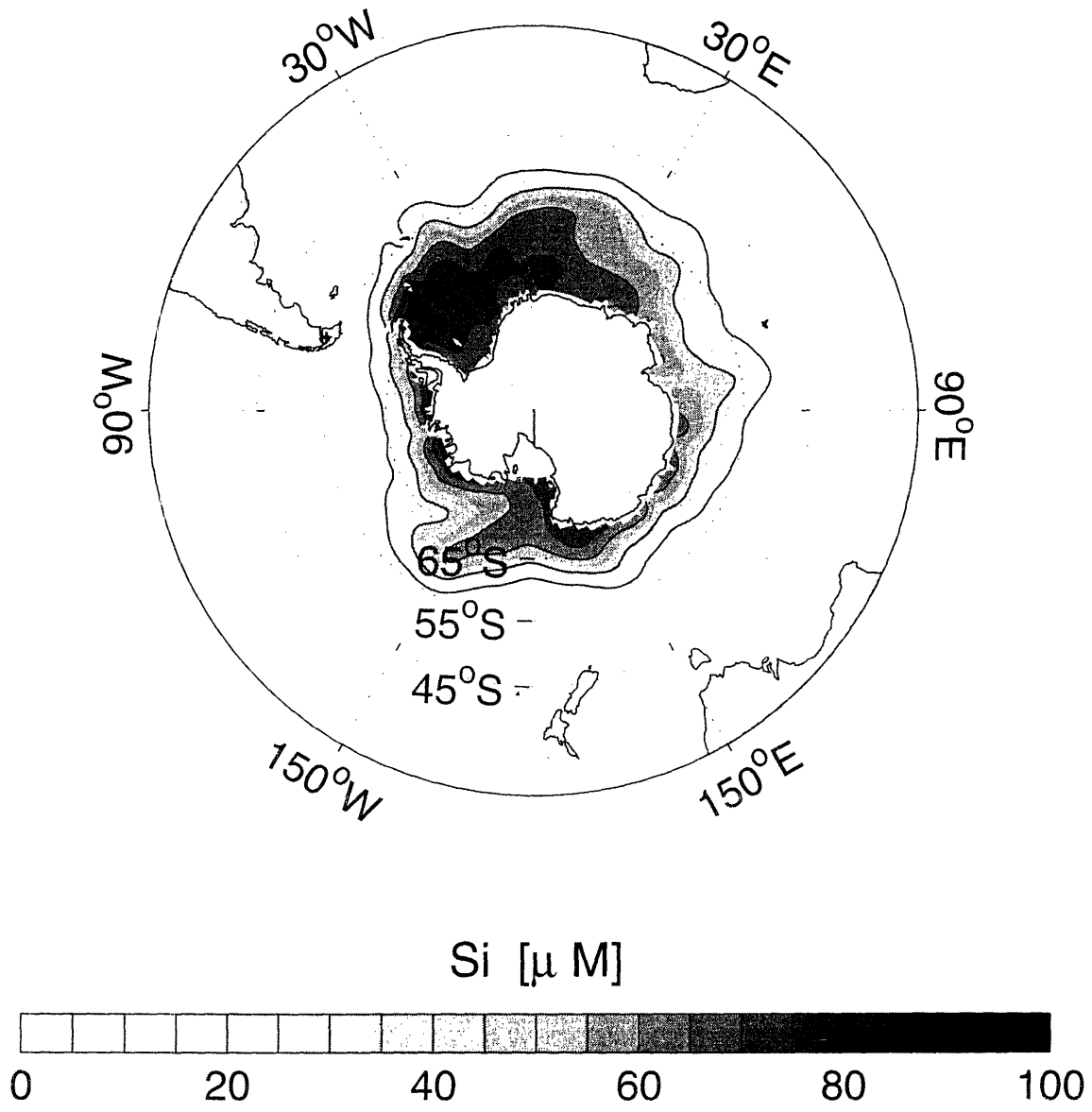

Figure 1-14: Annual mean surface silicic acid distribution in the Southern Ocean based on the World Ocean Atlas 2001 (Conkright et al., 2002). Contour interval is 20 μ M.

revealed that primary production in these regions indeed responds to the addition of iron to the surface waters (Martin et al., 1994; Coale et al., 1996; Boyd et al., 2000) although its impact on the export of organic material out of euphotic layer remains unclear. Increased atmospheric dust deposition during ice ages could have increased local biological productivity, leading to a drawdown of surface nutrients and atmospheric pCO_2 (Martin, 1990).

Since 1990s it has become feasible to combine three-dimensional ocean general circulation models and parameterizations of nutrient and carbon cycles, allowing explorations of the response of carbon cycle to increased rates of nutrient uptake in the surface ocean, mimicking elevated biological export (Sarmiento and Orr, 1991; Archer et al., 2000). These so-called "nutrient depletion" experiments help us to understand the response of carbon cycle to increased utilization of surface nutrients in the context of more realistic, three-dimensional ocean circulation. They find that the sensitivity of atmospheric pCO_2 to the depletion of polar surface nutrients is sensitive to the profile of remineralization in the interior ocean (Sarmiento and Orr, 1991). Moreover, atmospheric pCO_2 is less sensitive to a drawdown of high-latitude surface nutrients in three-dimensional models than in box models, and the drawdown of polar nutrients cannot reproduce the glacial pCO_2 (Archer et al., 2000). It is not yet well understood what ultimately determines the sensitivity of atmospheric pCO_2 to a depletion of polar surface macro-nutrients.

Furthermore, recent development of physical-biogeochemical model has introduced the coupling between ocean carbon cycle and the explicit iron cycle with ecosystem dynamics (Bopp et al., 2003; Parekh et al., 2004a). These models can qualitatively reproduce observed distribution of nutrients in the global oceans. Using these models, the biological productivity and carbon cycle are simulated with elevated atmospheric dust deposition. However, the response of atmospheric pCO_2 to an elevated aeolian dust deposition is significantly smaller than the glacial-interglacial variations of pCO_2 observed in ice cores. Therefore, it seems unlikely that the increased atmospheric dust deposition can be the direct cause of $\sim$ 100 ppmv drawdown of atmospheric pCO_2 during ice ages.

The second mechanism involves changes in the the ventilation of the Southern Ocean. Recent research (Francois et al., 1997; Sigman and Boyle, 2000; Gildor and Tziperman, 2001) suggest that the vertical supply of nutrients significantly decreased during ice ages. They argue that the reduced upwelling of deep waters is caused by the stronger stratification and an equatorward shift of the westerly wind belt. Increasing the stability of water column may suppress convective mixing and decrease the supply of nutrients to the surface layer. Northward migration of the westerly wind belt might weaken the wind stress over the Southern Ocean. Surface wind stress drives near-surface Ekman transport, and to the south of the westerly wind stress maximum, the Ekman transport is divergent and deep waters upwell into the surface layer. Decreasing the surface wind stress weakens the Ekman upwelling and the vertical supply of nutrients. If the supply of nutrient is reduced and the biological productivity is sustained, surface nutrients must be strongly depleted, and the outgassing of CO_2 becomes weaker, leading to a lower atmospheric pCO_2.

The wind-driven Ekman transport partially drives the meridional overturning circulation, however recent research highlights the significant role of mesoscale eddy fluxes leading to the "residual mean" view of the meridional overturning circulation. The representation of physical transport is highly idealized in previous studies of the carbon cycle in the Southern Ocean. In particular, they do not consider the advective influence of mesoscale eddies in the vertical supply of nutrients. The hypothesis of "polar stratification" is challenged by Keeling and Visbeck (2001) that increasing stratification in the Southern Ocean increases the rate of upwelling if the advective influence of mesoscale eddies are included. Theories of baroclinic instability suggest that eddy transports scale with the degree of baroclinicity, which is measured by the slope and the spacing of isopycnal surfaces (Gill, 1982; Pedlosky, 1986; Visbeck et al., 1997). Increasing the stratification decreases the baroclinicity of the region, leading to a weaker eddy-induced transport. Since the Ekman transport is partially compensated by the eddy-induced transport, weakening of the eddy fluxes leads to more pronounced Ekman transport.

Somewhat related to the "polar stratification" hypothesis is the extended sea ice

cover over the Southern Ocean during ice ages (Stephens and Keeling, 2000). The rate of air-sea gas transfer depends on the properties of the sea surface including the fraction of surface area covered by sea ice. The outgassing of CO_2 can be inhibited by extensive sea ice cover during ice ages, leading to the drawdown atmospheric pCO_2. This hypothesis requires near-complete coverage of the surface Southern Ocean by sea-ice for all seasons. Furthermore, sensitivity experiments using three-dimensional ocean biogeochemistry models have shown very low sensitivity of atmospheric pCO_2 to extended sea-ice cover in the Southern Ocean, and increasing sea-ice cover cannot reproduce the glacial pCO_2 in GCMs (Archer et al., 2003).

Toggweiler (1999) alternatively suggest that changes in the circulation and mixing in the Southern Ocean impact on the chemical properties of the global deep waters, and cause the drawdown of atmospheric pCO_2 during ice ages. This model is different from the "Harvardton Bear" models since the drawdown of atmospheric pCO_2 is driven by the reorganization of deep circulation without significant changes in high-latitude surface nutrient concentrations. Surface nutrient concentration of northern North Atlantic is significantly lower than that of the Southern Ocean in modern climate. Thus, deep waters formed in the North Atlantic (NADW) carries relatively low surface nutrients into the deep oceans, and these water masses have relatively greater capacity to sequester CO_2 in the deep oceans than those formed in the Southern Ocean. If the global deep waters are dominated by the waters formed in the North Atlantic during ice ages, atmospheric pCO_2 is significantly decreased by efficient sequestration of CO_2 in the deep waters. Thus this study highlights the role of ventilation of the deep Southern Ocean as a key mechanism in the past variations in atmospheric pCO_2. However, despite its importance, the dynamics of the Southern Ocean is simply prescribed in this theory. Application of a more sophisticated dynamical framework is necessary to evaluate the hypothesized changes in the ocean circulation.

There is important evidence of the glacial-interglacial variations of carbon cycle such as paleo-proxies of export production[5] recorded in sea-floor sediment, which may

[5]Elemental composition of sinking particulate flux can vary depending on the composition of

provide additional constraints on the mechanisms of the drawdown of atmospheric pCO_2 during ice ages. Kohfeld compiled the paleo proxies of export production at the Last Glacial Maximum (Bopp et al., 2003). These proxies include the burial rate of biogenic silica, organic carbon and carbonate, benthic foraminifera accumulation, anthigenic uranium, and excess (Pa/Th) ratio. Fig.1-15 is produced from their compilation paleo data. Paleo proxies have associated assumptions and problems that can complicate their interpretations. Thus the combinations of multiple proxies are used to reduce the uncertainty associated with each proxy type. The reconstruction suggests the overall magnitude of export production (including silica and organic export) was higher during the LGM, relative to the modern condition, to the north of the Polar Front, and lower during the LGM to the south of the Polar Front. Bopp et al.(2003) used a 3-dimensional physical-biogeochemical model to simulate the biological productivity during Last Glacial Maximum (LGM). The model was able to reproduce this pattern including the effects of increased dust deposition, ocean circulation and sea-ice cover for the LGM condition. However, the model itself is complex and the roles of individual processes are not clearly identified. While it may be possible that small changes due to various processes add up and form a strong signal, there may be a simple, zero-order explanation. It is not clear what drives the systematic reorganization of the biological production in the Southern Ocean. Any hypothesis of the glacial-interglacial pCO_2 variations must be consistent with the changes in the pattern of biological productivity there.

In chapter 3, I estimate the biological production and export in the Southern Ocean using an idealized zonally averaged model, and examine the physical processes controlling them using a global ocean physical-biogeochemical model. I consider the relationship between physical transport and macro-nutrient fronts. Simulated nutrient fields illustrate the regimes of nutrient limitation and its relationship with the position of the productivity belt.

In chapter 4, I develop a simple, dynamical model of the Southern Ocean to

phytoplankton species. In this thesis "silica export" refers to the silica content of sinking particulate flux. Similarly, "organic export" and "carbonate export" refer to the sinking particulate flux of organic material and calcium carbonate respectively.

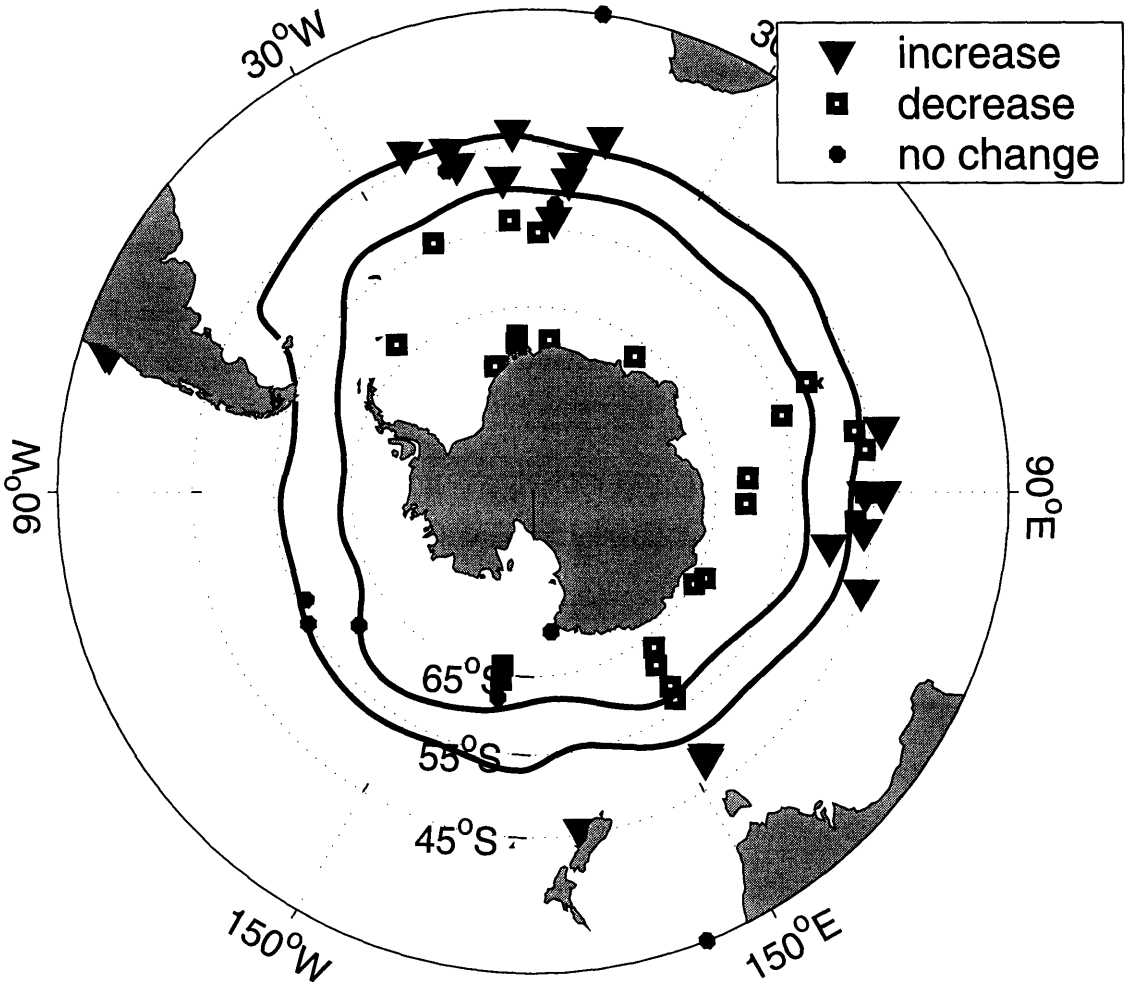

Figure 1-15: Reconstructed export production for the LGM minus today (Bopp et al., 2003). This figure shows whether the export was higher at LGM (triangle), lower at LGM (square), or remained the same (circle). The two solid lines are the mean latitudes of the Polar Front and the Subantarctic front.

calculate the possible changes in the pattern of export production, and illustrate what might control the observed changes in the spatial pattern of biological productivity during the LGM. The position of the Antarctic Circumpolar Productivity Belt could play a central role in the glacial-interglacial variation of the biological productivity.

In chapter 5, I develop a simple theory of the biological pump in the global oceans, relating the polar surface nutrients and atmospheric pCO_2 in a clear and transparent way. The theory can be applied to a wide range of models, and predict the possible range of atmospheric pCO_2 with various rates of biological uptake of macro-nutrients in the surface oceans. These results can provide new insights into the mechanisms which ultimately control the efficiency of biological pumps in a climate with increased aeolian dust deposition over the Southern Ocean.

Chapter 2

What Controls the Uptake of Transient Tracers in the Southern Ocean ?

We apply 'residual mean' theory of tracer transport, in which eddy transfer plays a fundamental role, to develop scalings and idealized numerical models of the Southern Ocean uptake of transient tracers. The streamline-averaged numerical model, which represents transport in the meridional plane, captures the observed distributions of CFC11, bomb-$\Delta^{14}C$, and anthropogenic CO_2. The model reproduces the observed relationship between CFC11 and bomb-$\Delta^{14}C$ and suggests that the upper branch of the residual overturning flow in the Southern Ocean is about 11 Sv, supporting previous inferences based on the observed buoyancy distribution and air-sea buoyancy fluxes. Scale analysis suggest that the limit of fast air-sea gas exchange is applicable to CFC11, for which the surface concentration is close to equilibrium and cumulative ocean uptake is largely determined by physical transport processes. In the slow gas exchange limit, applicable to bomb-$\Delta^{14}C$, the surface concentration is far from equilibrium and the cumulative uptake is most sensitive to the parameterization of the gas transfer coefficient. Anthropogenic CO_2 falls between those two limit cases and is sensitive to both transport processes and the gas transfer coefficient. Sensitivity studies using the streamline-averaged model suggest that uncertainties in

air-sea buoyancy fluxes in current climatologies result in significant uncertainty in estimates of Southern Ocean uptake of anthropogenic CO_2 based on circulation and biogeochemistry models driven by, or brought into consistency with the climatological fluxes. This uncertainty is sufficient to explain a significant amount of the spread in a recent model comparison study.

The main content of this chapter has been published as (Ito et al., 2004). Section 2.2.1 and 2.4 are newly added to this chapter.

2.1 Introduction

Atmospheric CO_2 has been rising rapidly due to anthropogenic emissions, but its rate of increase is mediated by uptake into the oceans and the terrestrial biosphere. Likewise, CFC11 has rapidly increased in the past several decades from zero to about 260 pptv. Atmospheric $\Delta^{14}C$ peaked in the 1960s due to the nuclear tests (Fig. 2-1). The signature of these tracers has been observed in the global oceans through ship-based measurements during the WOCE (World Ocean Circulation Experiment) and JGOFS (Joint Global Ocean Flux Study) and observations continue. The distributions of these transient tracers have some significant differences reflecting the contrast in their respective input functions (atmospheric trends) and air-sea gas exchange rates. Here we use idealized models to help understand and illustrate the mechanisms that control the distribution and fluxes of these tracers. In turn, tracer observations provide a means to test models of Southern Ocean circulation and quantify the overturning circulation in the region.

The uptake of anthropogenic CO_2 by the Southern Ocean is the subject of intense research. Its distribution has been evaluated using observations of biogeochemical properties and age tracers (Gruber et al. 1996; Gruber 1998; Sabine et al. 1999). McNeil et al. (2003) estimate the anthropogenic CO_2 inventory using its relationship to the CFC age distribution. The rate at which the oceans are absorbing anthropogenic CO_2 is difficult to determine directly from observations because the perturbations are small relative to background, naturally-occurring fluxes. Furthermore ship-based

observations are sparse in time and space. For this reason ocean general circulation and biogeochemical model simulations have been used to provide additional estimates of the distribution and fluxes of anthropogenic CO_2. The Ocean Carbon-cycle Model Inter-comparison Project (OCMIP) examined and compared several GCM (General Circulation Model) simulations of anthropogenic tracers (Orr et al. 2001; Dutay et al. 2002). Orr et al. (2001) show that the Southern Ocean is a major region of ocean uptake of anthropogenic CO_2 in the models, but also find that it is the region where the models show the largest disagreement in air-sea flux.

In the Southern Ocean, baroclinic eddies play a central role in the transport of momentum, buoyancy and tracers (Johnson and Bryden 1989; Gille 1994; Karsten et al. 2002), and yet they are generally unresolved and crudely parameterized in the large scale ocean general circulation models. Robitaille and Weaver (1995) demonstrated that the choice of subgrid-scale parameterization significantly impact modeled CFC distributions, favoring the Gent and McWilliams (1990) (hereafter, GM90) scheme. Matear (2001) showed that the uptake of anthropogenic CO_2 is also sensitive to the numerical schemes and eddy parameterizations employed, particularly in the Southern Ocean. Caldeira and Duffy (2000) also demonstrate that isopycnal stirring significantly contributes to the northward transport of anthropogenic CO_2 in the Southern Ocean of an ocean model.

To better understand and interpret the tracer distributions, and the simulations of them, we must closely examine key processes that control the tracer transport and air-sea flux of CO_2 in the region. Surface westerlies drive equatorward Ekman transport which is in part balanced by poleward, eddy-induced transport of properties: the net result is the "residual circulation".

Recent studies show that the residual circulation can be diagnosed from surface momentum and buoyancy fluxes (Marshall 1997; Speer et al. 2000; Karsten and Marshall 2002). These studies employ the Transformed Eulerian Mean (Andrews and McIntyre 1976) which reformulates the tracer transport equation in terms of residual circulation. In this study we examine the transport of anthropogenic tracers in the Southern Ocean using a simple dynamical model of the ACC based on residual mean

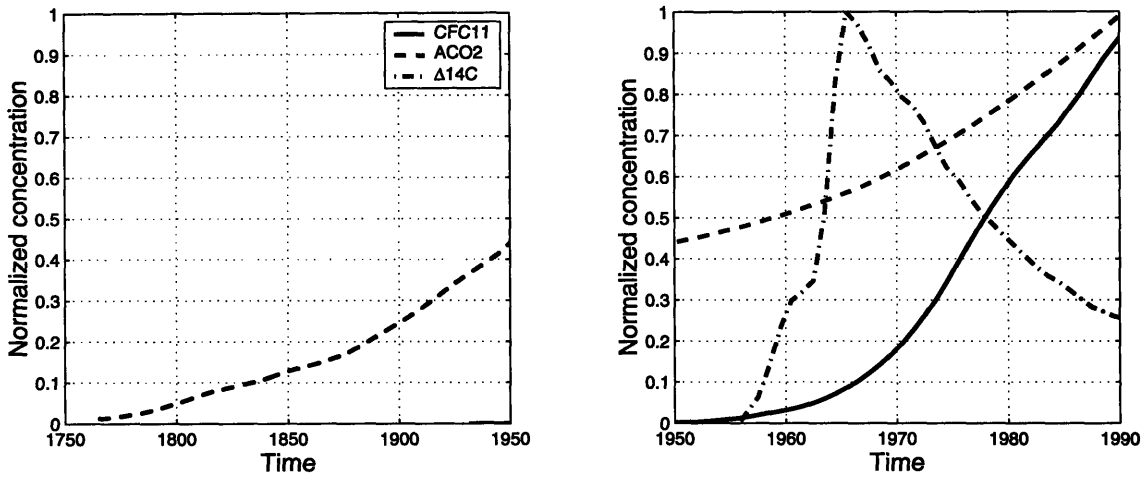

Figure 2-1: (Left) : The time history of anthropogenic CO_2 between 1750 and 1950. (Right) : The time history of CFC11, anthropogenic CO_2 and bomb-induced $\Delta^{14}C$ between 1950 and 1990. The vertical axis is the normalized atmospheric concentration. Atmospheric CO_2 has the longest anthropogenic perturbations.

theory. We consider three transient tracers: CFC11, anthropogenic CO_2, and bomb-$\Delta^{14}C$. The modeled distributions of CFC11 and bomb-$\Delta^{14}C$ are compared with observed distributions to evaluate the theoretical interpretations. Sensitivity studies with the model indicate the key factors controlling the distributions of these tracers and their fluxes.

2.2 Physical transport

The analysis presented here is based on streamline-averaged fields in which velocities and tracer concentrations are averaged along mean streamlines. Fig. 2-2 (a) shows geostrophic streamlines, $\Psi_g = g\overline{h}/f$, in the ACC determined from the 4-year time averaged, large-scale (2° horizontal resolution) dynamic sea surface height data from TOPEX-POSEIDON following Karsten and Marshall (2002). The latitude of the ACC varies with longitude, and is strongly influenced by bottom topography (Gille 1994). Therefore, taking a simple zonally averaged view (i.e. averaging along latitude circles) obscures the meridional tracer distribution and transport across the meandering jet of the ACC. Hence, hereafter, geostrophic streamlines are assumed to be the meridional coordinate. Fig. 2-2 (b) depicts streamline-averaged potential density as

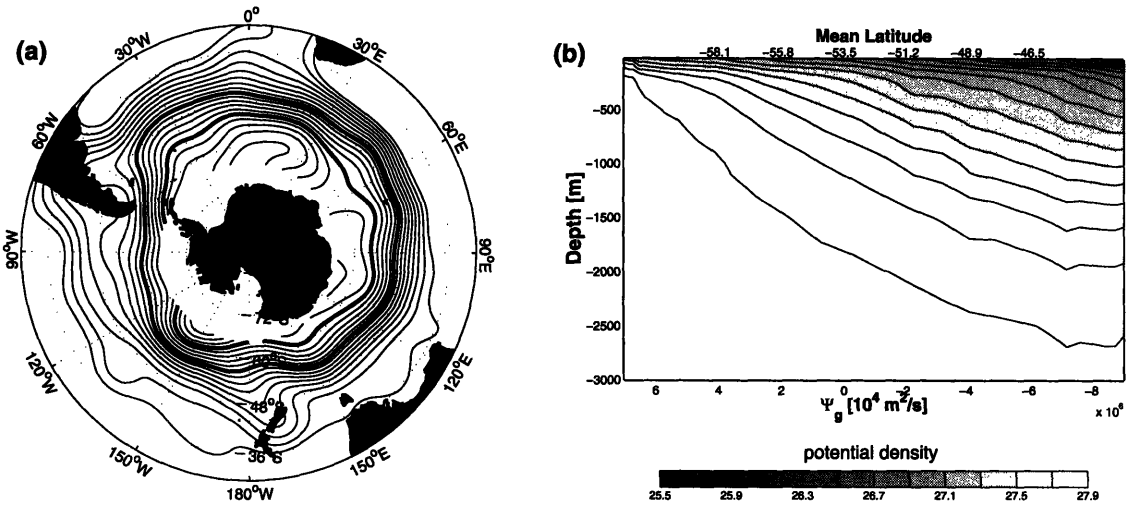

Figure 2-2: Geostrophic streamlines (a), and zonally averaged potential density field from Levitus climatology (b). The geostrophic streamlines are calculated from the 4 year time-averaged field of TOPEX-POSEIDON data. The contour interval is $10^3[m^2s^{-1}]$. The potential density data is from Levitus climatology (Levitus 1994).

a function of depth (using World Ocean Atlas data; Levitus 1994) showing isopycnals sloping up toward Antarctica.

The significance of using the streamline-averaged framework can be illustrated using tracer observations. Fig. 2-3 (a) through (f) shows the distribution of observed pCFC11 in the Atlantic, Indian and Pacific sector of the ACC. The distribution of pCFC, which is the concentration of CFC11 normalized by the solubility, is clearly correlated with the structure of the Circumpolar Current. In Fig. 2-3(a,c,e), pCFC11 is plotted in latitude-depth coordinates. Here the spatial pattern of pCFC11 is significantly different between the three sections due to the meandering of the ACC and the fact that the tracer distribution is tightly coupled to the frontal structures. When the same data is plotted in the streamline coordinate, as shown in Fig. 2-3(b,d,f), the pCFC11 distribution becomes remarkably similar between the three sections. This correspondence motivates us to use a streamline-averaged tracer transport model since the observed tracer distribution is quasi-two-dimensional in that coordinate system.

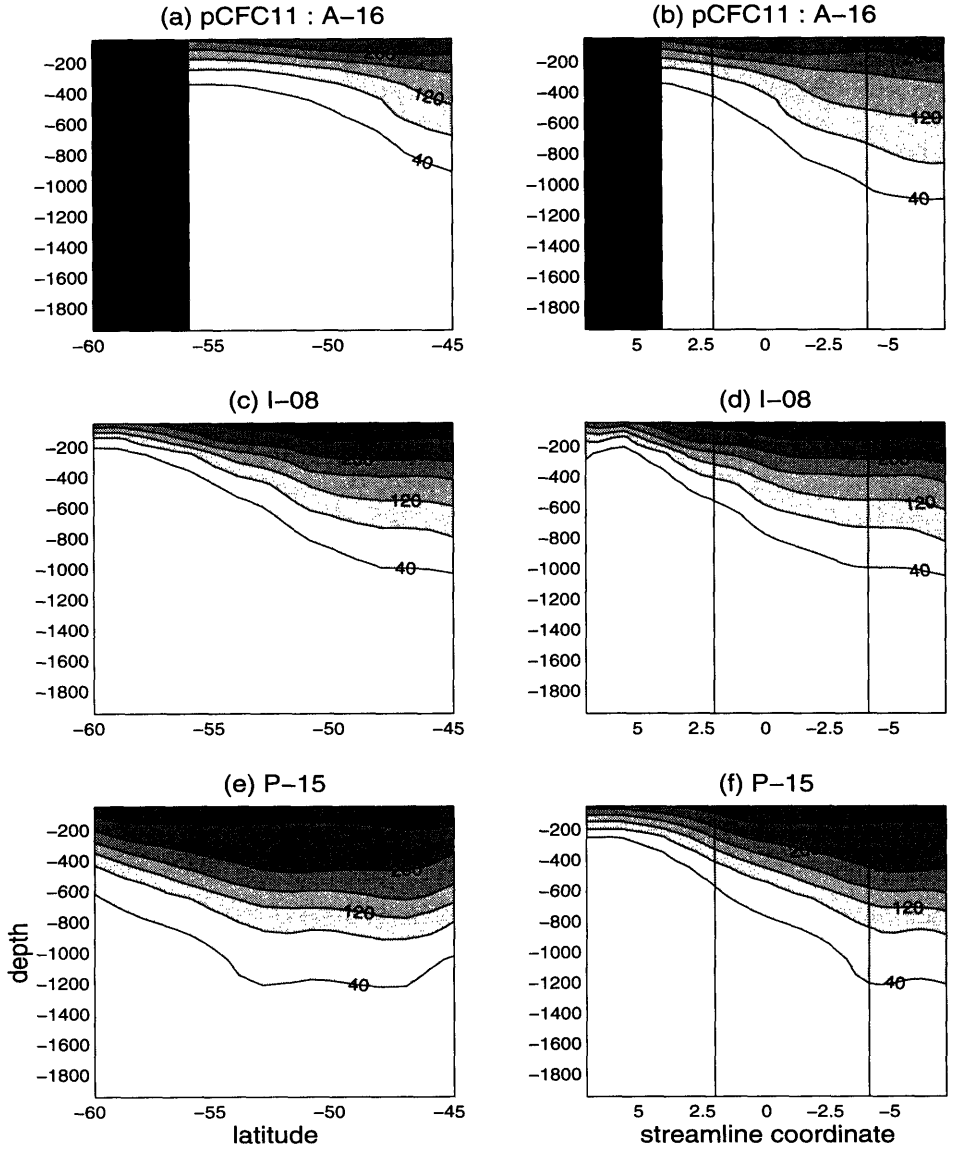

Figure 2-3: Observed pCFC11 distribution from WOCE (left column) in the latitude coordinate, and (right column) in the streamline coordinate. The units are in pptv, and the tracer data is obtained from WOCE line A-16 for (a,b), I-08 for (c,d) and P-15 for (e,f). The units for streamlines are $10^4 m^2 s^{-1}$ in (b,d,f). The two vertical lines in (b,d,f) marks the position of the Polar Front and the Subantarctic Front.

2.2.1 Climatology of surface wind stress and buoyancy flux

Fig.2-4 shows climatological surface wind stress pattern based on the NCEP-NCAR reanalysis project (Kalnay et al., 1996). Eastward momentum is added to the surface ocean with significant zonal variability. Zonal averages presented here are based on streamline-averaged fields in which velocities and tracer concentrations are averaged along mean streamlines shown in Fig.1-3. The latitude of the ACC varies with longitude, and is strongly influenced by bottom topography (Gille, 1994; Marshall, 1995). The maximum input of zonal momentum occurs in the Atlantic and Indian sector of the ACC. Fig.2-4 (b) shows climatological wind stress pattern in the streamline coordinate.

Fig. 2-5 shows climatological surface buoyancy distribution based on time mean NCEP-NCAR reanalysis data. The buoyancy is determined from time mean SST. Meridional gradient is primarily controlled by the SST variations in the latitudes of the ACC, and we neglect Salinity component. The magnitudes of the zonal fluctuations are much smaller than that of the mean meridional gradient, and in the streamline coordinate, the Atlantic and Indian sectors of the ACC are warmer than the Pacific sector because of the meandering of the ACC.

Fig. 2-6 show climatological surface buoyancy flux pattern based on the long-time mean NCEP-NCAR reanalysis data. The buoyancy flux is calculated based on the radiative fluxes, sensible heat fluxes and latent heat fluxes. The freshwater component is not included in the data presented here. Fig.2-6 reveals that the ACC is warmed by the surface fluxes with largest heating occurs in the Atlantic and Indian sector of the ACC reaching up to $3 \cdot 10^{-8}$ $m^2 s^{-3}$.

In summary the surface ocean receives eastward momentum from the westerly wind, and receives buoyancy (heat) by air-sea fluxes. In the following section I illustrate a zonally-averaged, diagnostic model of the meridional overturning circulation of the ACC driven by these surface fluxes.

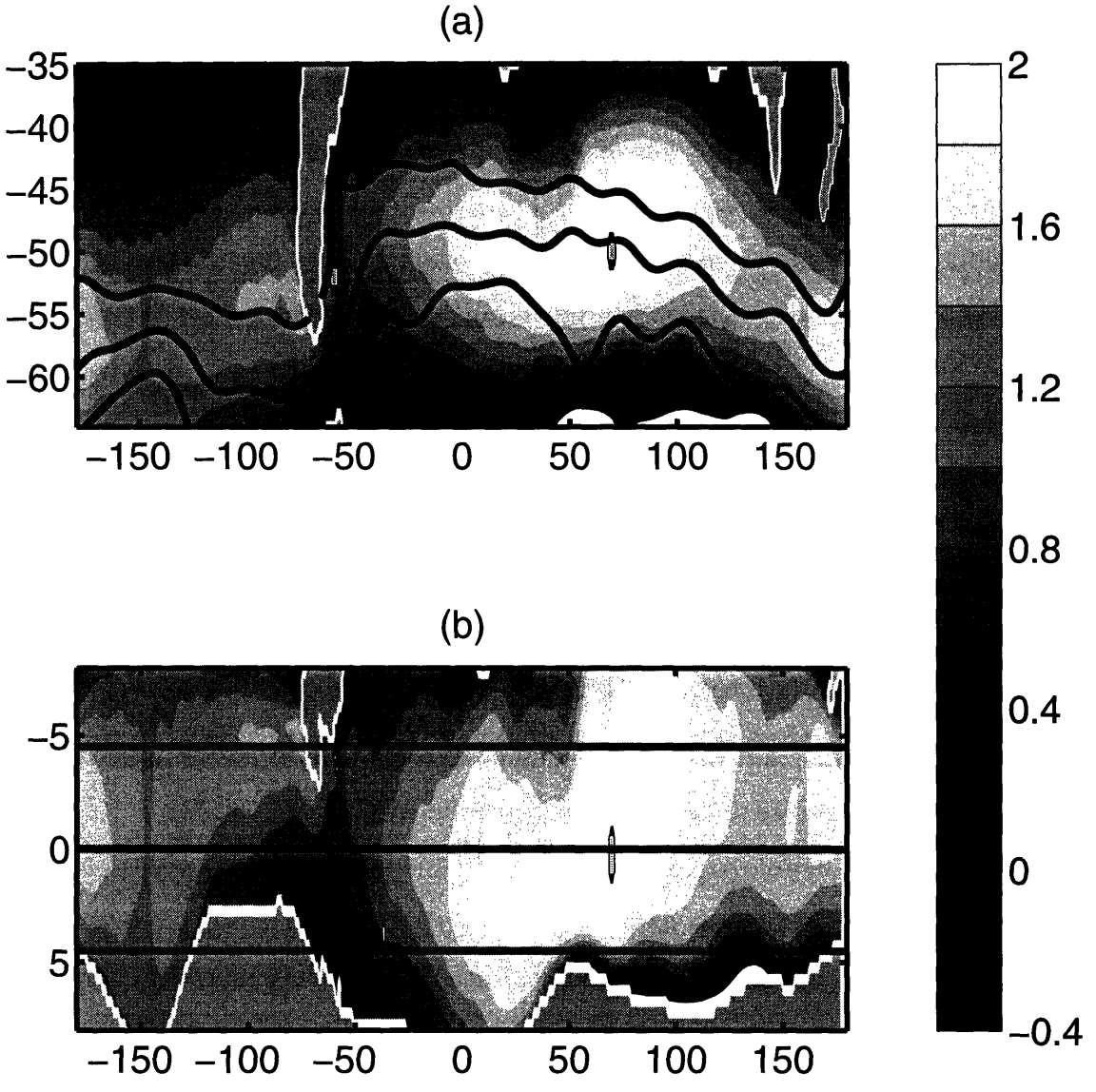

Figure 2-4: Climatological surface wind stress plotted in (a) the longitude - latitude coordinate and (b) the longitude - streamline coordinate. The data is taken from long-time mean NCEP-NCAR reanalysis. The units are in 10^{-1} N m^{-2}.

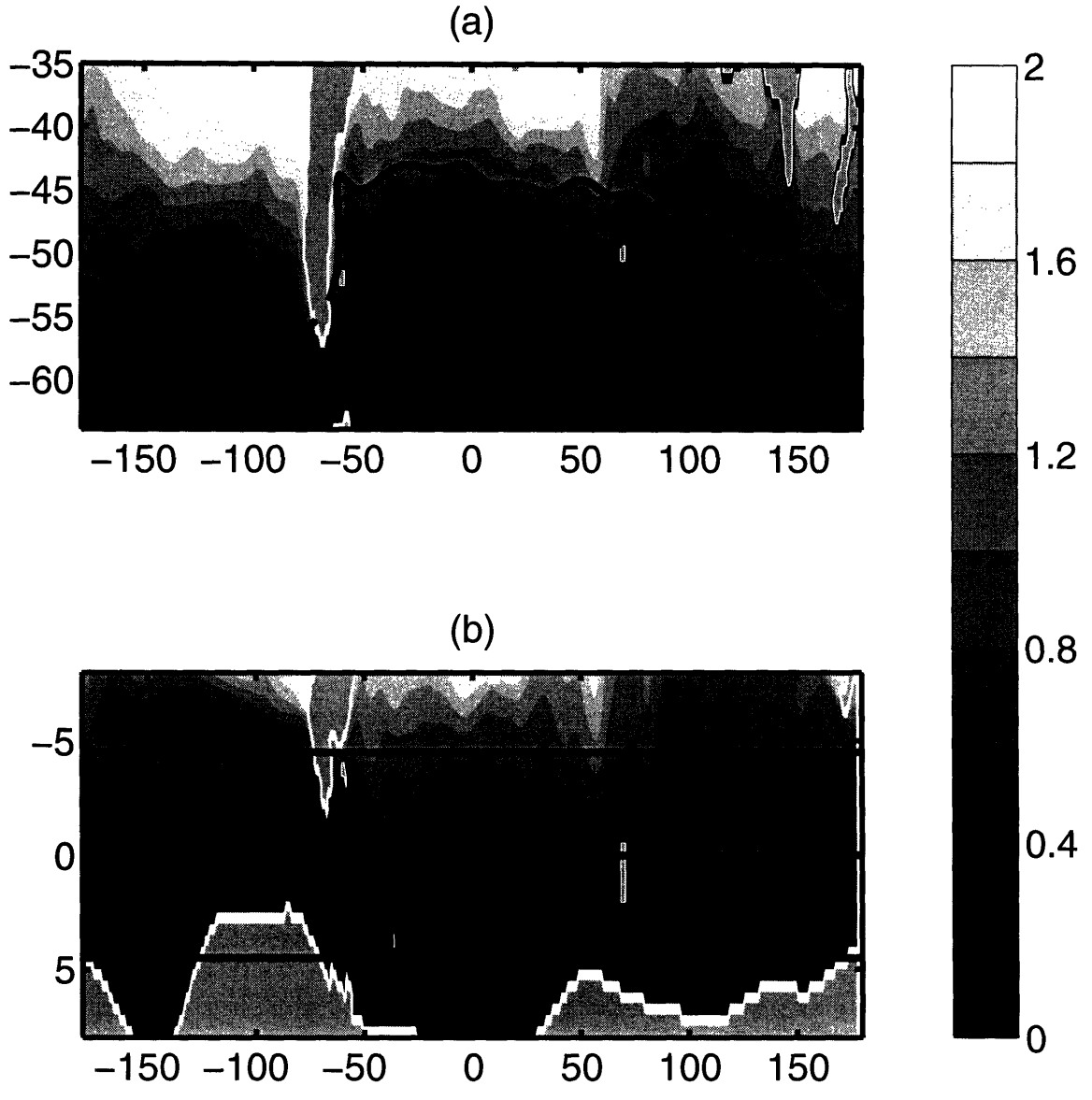

Figure 2-5: Climatological surface buoyancy plotted in (a) the longitude - latitude coordinate and (b) the longitude - streamline coordinate. The data is taken from long-time mean NCEP-NCAR reanalysis. The units are in 10^{-2} m s^{-2}.

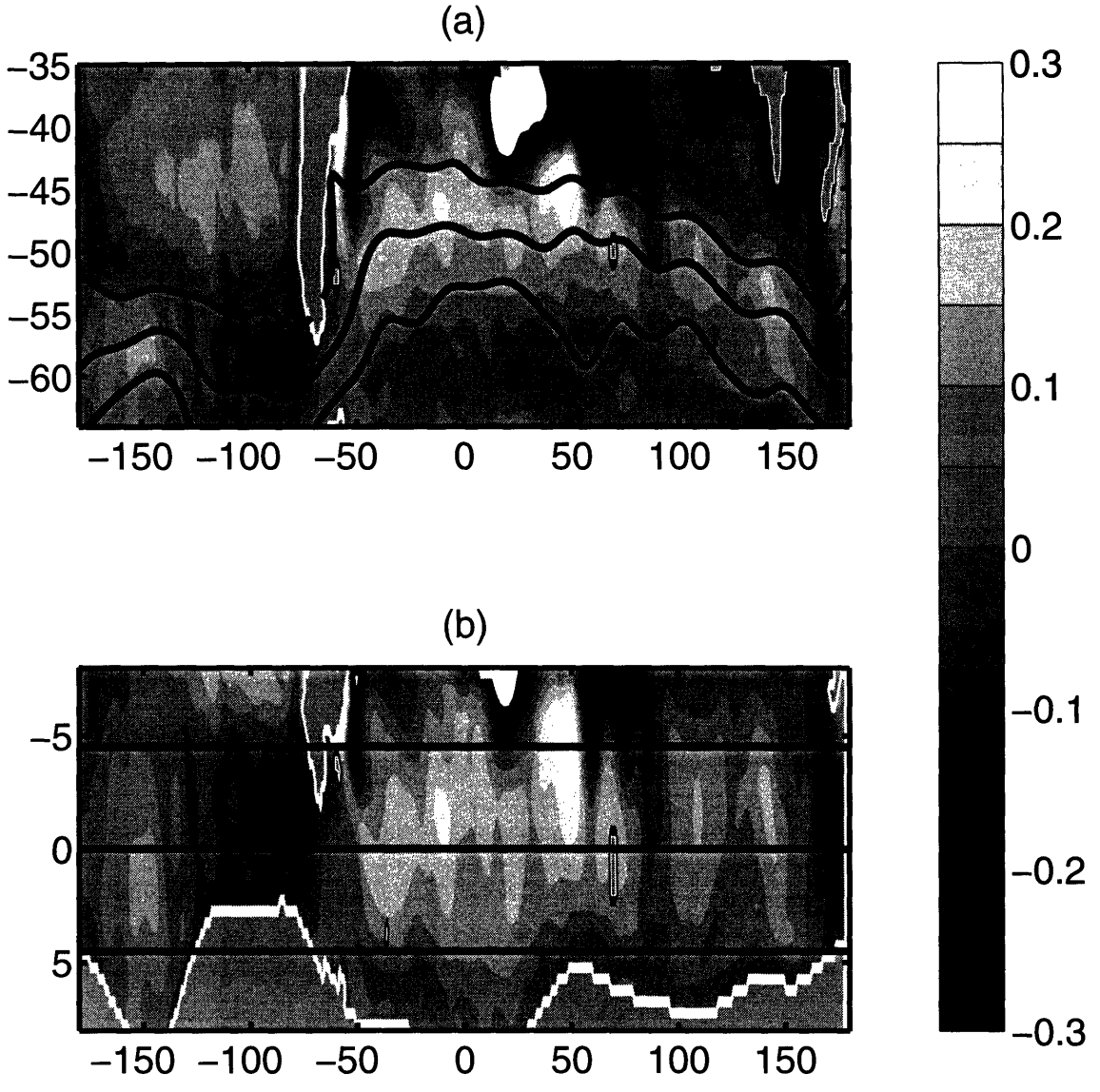

Figure 2-6: Climatological surface buoyancy flux plotted in (a) the longitude - latitude coordinate and (b) the longitude - streamline coordinate. The data is taken from long-time mean NCEP-NCAR reanalysis. The units are in 10^{-7} m^2 s^{-3}.

2.2.2 Transport by the 'residual mean' circulation

We formulate the two-dimensional circulation model following (Karsten and Marshall 2002; Marshall and Radko 2003) based on residual mean theory (Andrews and McIntyre 1976; Held and Schneider 1999). We define the streamline averaged concentration, $\overline{C}(y,z)$ — hereafter just C — in the streamline coordinate where the y-coordinate is mapped on to the corresponding value of Ψ_g. The zonally averaged prognostic equation for tracers is

$$\frac{\partial C}{\partial t} + v_{res}\frac{\partial C}{\partial y} + w_{res}\frac{\partial C}{\partial z} = \nabla \cdot \mathbf{K}\nabla C - \frac{\partial F}{\partial z} \tag{2.1}$$

where $\mathbf{K}$ is the isopycnal diffusion tensor following Solomon (1971). The air-sea gas flux, F, is parameterized as restoring toward equilibrium with the overlying atmosphere under current physical conditions: $F = -\lambda h(C - C_{at})$. Here λ is the inverse timescale for air-sea gas equilibration which is linearly related to gas transfer velocity. C_{at} is the saturated concentration in equilibrium with the atmospheric partial pressure. This form can be applied to each of the gases discussed here, with some approximation (Broecker and Peng 1974). In Table 2.1 we define the saturated concentrations, C_{at} for each tracer, and detailed definitions of chemical constants can be found in an appendix. Approximate formulae and values for the air-sea gas exchange timescales of each tracer are given in Table 2.2.

In eq. (2.1), tracers are advected by the residual mean flow, (v_{res}, w_{res}) in streamline coordinates. It combines the effects of wind-driven and eddy-induced circulation. Fig. 2-7 illustrates, schematically, the dynamical balances in the ACC following Marshall (1997). The Eulerian mean flow, $\overline{\Psi}$, is the Deacon cell driven by the equatorward directed Ekman flow due to the surface westerly wind. The poleward return flow at depth is assumed to be in geostrophic balance with the zonal pressure gradient supported by bottom topography. $\overline{\Psi}$ is partially compensated by the eddy-induced flow, Ψ_{eddy}, driven by baroclinic eddy transfer. The residual mean flow, Ψ_{res}, is the net

transport, the sum of $\overline{\Psi}$ and Ψ_{eddy}:

$$\Psi_{res} = \overline{\Psi} + \Psi_{eddy} \tag{2.2}$$

$$\overline{\Psi} = -\frac{\tau_s}{\rho_0 f} \tag{2.3}$$

$$\Psi_{res}|_{-h}\frac{\partial \bar{b}}{\partial y} = \tilde{B}_s \tag{2.4}$$

Here $\overline{\Psi}$ is the Ekman transport set by the surface wind stress forcing, τ_s, as in (2.3). We diagnose the residual circulation, Ψ_{res}, from the surface buoyancy forcing following Marshall (1997): the residual stream function at the base of surface mixed layer, $\Psi_{res}|_{-h}$, is determined by the steady state buoyancy balance. In eq. (2.4), the surface buoyancy fluxes and the diapycnal eddy fluxes are combined into a diabatic flux, $\tilde{B}_s = B_s - \int_{-h}^{0} \frac{\partial}{\partial y}\overline{v'b'}\,dz$, (Marshall 1997; Marshall and Radko 2003) where B_s is the air-sea buoyancy flux; the combined effect of heat and freshwater exchanges. Thus Ψ_{res} and $\overline{\Psi}$ can, in principle, be diagnosed from surface wind stress and buoyancy forcing.

Marshall and Radko (2003) present simple solutions for the ACC and its overturning stream function based on (2.2)-(2.4). Ψ_{eddy} is parameterized, following GM90, as proportional to the isopycnal slope, s_ρ. In addition, following Visbeck et al. (1997) (hereafter, V97), the eddy transfer coefficient is also set proportional to s_ρ. Thus:

$$K = k|s_\rho|, \tag{2.5}$$

where k is a coefficient of eddy closure. The eddy induced stream function is thus parameterized as:

$$\Psi_{eddy} = -k{s_\rho}^2 \tag{2.6}$$

Using (2.2)-(2.6) the isopycnal slope can be expressed in terms of patterns of external physical forcing:

$$|s_\rho| = \sqrt{-\frac{\tau_s}{k\,f\,\rho_0} - \tilde{B}_s\left(k\frac{\partial \bar{b}}{\partial y}\right)^{-1}} \tag{2.7}$$

	$CFC11$	CO_2	$\Delta^{14}C$
C_{at}	$k_{CFC11}\, pCFC$	$\frac{DIC_0}{pCO_{20}Bu}(pCO_2 - 278\,[ppm])$	$\Delta^{14}C_{atm}$

Table 2.1: Simple formulae for saturated concentrations of CFC11, anthropogenic CO_2 and bomb-$\Delta^{14}C$. k_{CFC11} is the solubility of CFC11. DIC_0 and pCO_{20} are preindustrial distribution of DIC and pCO_2 in the surface ocean. Bu is the Buffer factor. Detailed derivations are presented in appendix.

	$CFC11$	CO_2	$\Delta^{14}C$
λ	$\frac{K_W}{h}$	$\frac{K_W k_{CO_2} pCO_{20} B_u}{hDIC_0}$	$\frac{K_W k_{CO_2} pCO_{20}}{hDIC_0}$
$O(1/\lambda)$	1 (month)	1 (year)	10 (years)

Table 2.2: Air-sea gas exchange timescales following Broecker and Peng (1974). K_W is the gas transfer coefficient, and B_u is the Buffer factor. k_{CO_2} is the solubility of CO_2. See appendix for detailed definitions of these parameters. We parameterize the gas transfer coefficient, K_W, following Wanninkhof (1992) with idealized profiles of temperature, salinity, and surface wind.

Note the simple, square-root relationship between surface wind stress and isopycnal slope, a consequence of the choice of eddy parameterization following V97.

The method of characteristics allows one to map a prescribed surface buoyancy distribution down into the interior. We calculate the depth of each isopycnal layer by horizontal integration of the slope of the isopycnal as it dips down into the thermocline. We assume that diapycnal mixing is negligible in the ocean interior, allowing us to set the residual stream function, Ψ_{res}, to be constant on each isopycnal surface. We integrate from the base of the surface mixed layer where eq.(2.4) sets the boundary condition for Ψ_{res}, and the isopycnal slope is calculated by eq.(2.7). Here, we set the mixed layer depth to a constant, $h = 200$ m, and the eddy closure parameter, $k = 1 \cdot 10^6$ m^{2}s^{-1} as in Marshall and Radko (2003).

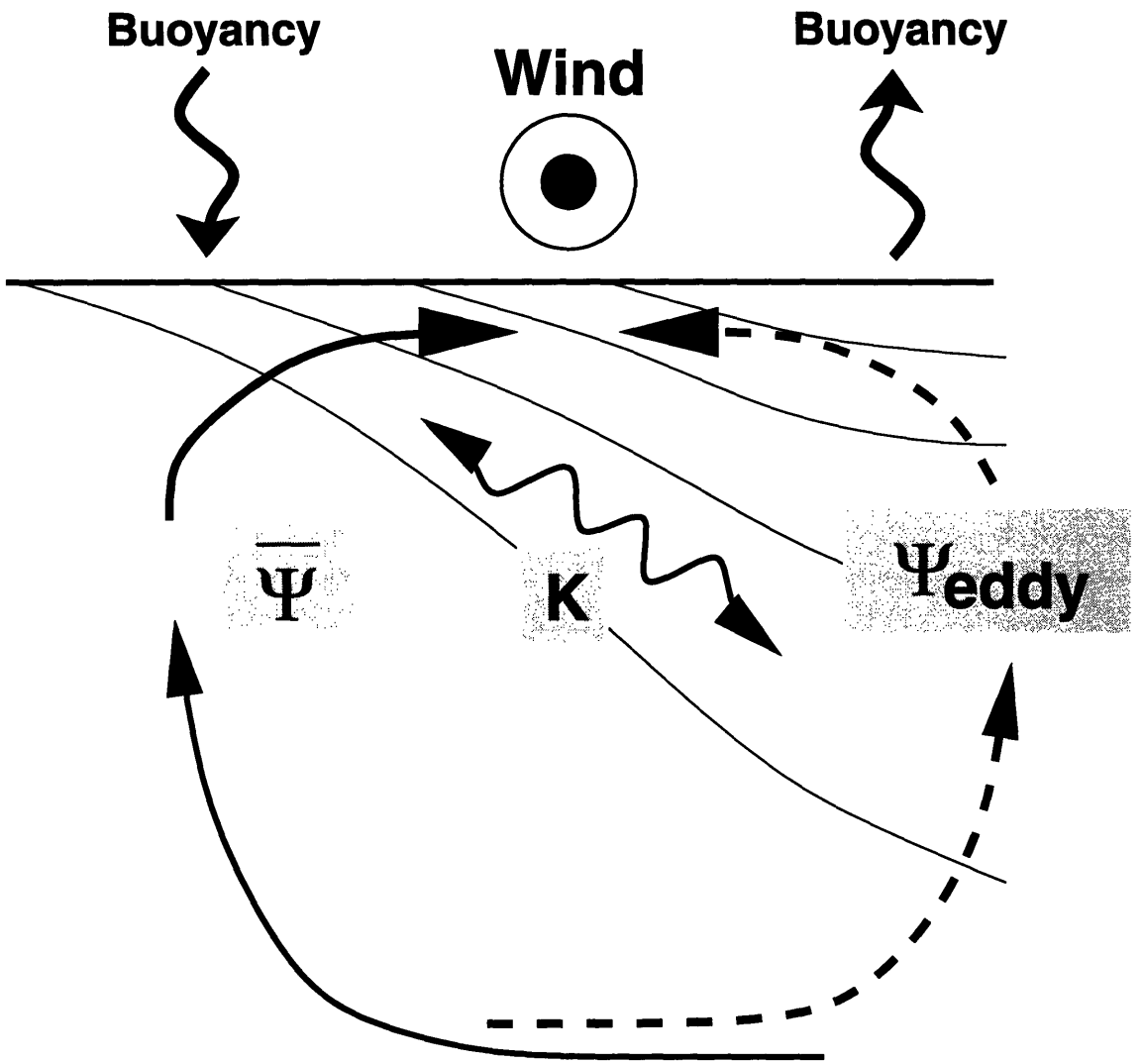

Figure 2-7: A schematic diagram showing the dynamical balance in the ACC. Eulerian mean flow and eddy-induced flow are shown as solid lines and dashed lines. They can be diagnosed from surface physical forcing including wind stress and buoyancy fluxes.

2.2.3 Forcing functions and solutions

Fig. 2-8 shows the streamline-averaged thermal component of the analyzed surface buoyancy flux from several climatologies including the NCEP-NCAR reanalysis (Kalnay et al., 1996), da Silva Surface Marine Data (da Silva and Young, 1994) and the SOC climatology (Josey et al., 1999). These datasets are not in quantitative agreement in the Southern Ocean, but they show a common qualitative structure with a positive buoyancy input into the mixed layer to the south of the ACC. From eq.(2.4), this is suggestive of equatorward residual advection at the surface. There is a decrease in air-sea buoyancy flux to the north of the ACC implying subduction of water masses there (Marshall 1997; Karsten and Marshall 2002). The large differences in amplitude of the buoyancy flux climatologies will manifest themselves as large uncertainties in the intensity of the residual flow estimates based on them. In this paper, for simplicity, we use surface heat flux and surface temperature as a measure of buoyancy forcing. The freshwater component of the air-sea buoyancy flux is even more uncertain and is not used in this analysis. In contrast, the wind stress forcing seems more consistent between climatologies (Fig. 2-8).

Based on the climatologies in Fig. 2-8 we construct an idealized profile of surface buoyancy and wind forcing, approximately an average of the three data sets. Applying eq.(2.2) through (2.7), we calculate the interior buoyancy distributions, residual circulation, and isopycnal eddy diffusivity as outlined in the previous section. In the solution (Fig. 2-9) Circumpolar Deep Water (CDW) upwells to the south of the ACC, moves equatorward at the surface and subducts into the thermocline near the polar front, forming Antarctic Intermediate Water (AAIW). The maximum Ψ_{res} is about 11 Sv and the pattern of residual flow is broadly similar to the circulation estimated by Karsten and Marshall (2002) who diagnose eddy fluxes directly from satellite sea surface height data. The implied isopycnal eddy transfer coefficient in this solution has a peak value of 1250 $m^2\,s^{-1}$ to the north of the ACC and decreases away from it. The particular choice of k modulates the isopycnal slope, s_ρ, and the isopycnal eddy diffusivity, K. Note that our model extends to approximately 60°S and does

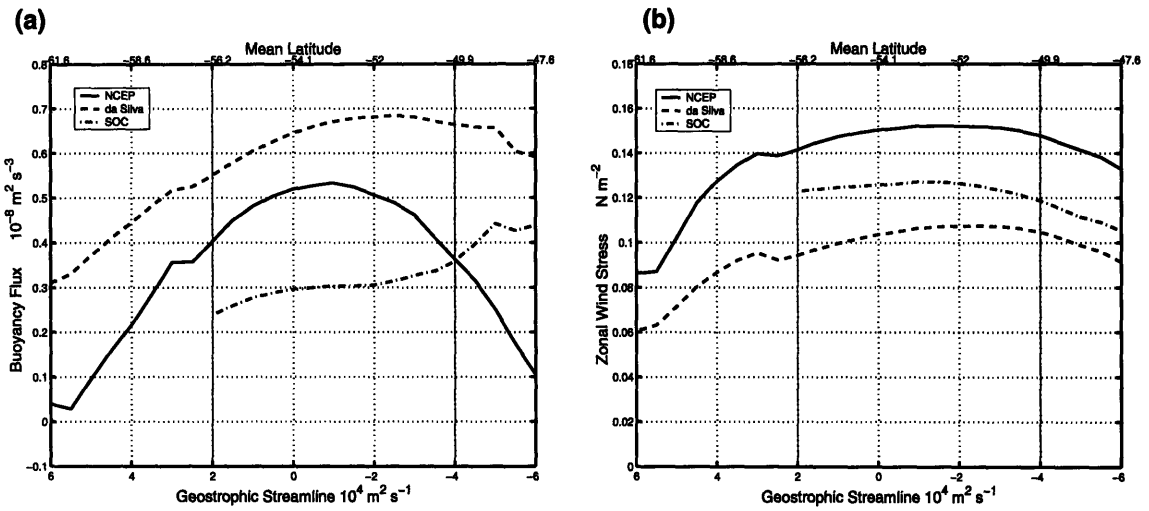

Figure 2-8: Streamline averaged surface fluxes from NCEP-NCAR reanalysis data, the da Silva dataset, and the SOC dataset. (a): the buoyancy flux in units of $m^{-2}s^{-3}$. (b): the surface wind stress in units of N m^{-2}. The horizontal axis is in streamline coordinate, and the two vertical lines marks the position of the Polar Front and the Subantarctic front.

not explicitly represent the formation of Antarctic Bottom Water (AABW).

Baroclinic eddies have a large impact on the resulting tracer distributions through both advective and diffusive (stirring) influences. The eddy-induced flow in (2.6) represents the advective component of baroclinic eddy transfer shown in Fig. 2-9. Isopycnal stirring in (2.1) is the diffusive component of the same dynamical process. Both are represented in the tracer model based on eq.(2.1).

2.3 What controls the distribution of transient tracers ?

We have developed a numerical model which integrates the tracer equation (2.1), based on the residual mean circulation determined as described in the previous section and illustrated in Fig. 2-9. The model has a horizontal resolution of 1° and 15 vertical levels from the surface to 3000 m and advective transport is discretized using a second order finite difference scheme. The tracer model is integrated from 1765 to 1990 for anthropogenic CO_2, CFC11 and bomb-$\Delta^{14}C$, forced by the atmospheric transients

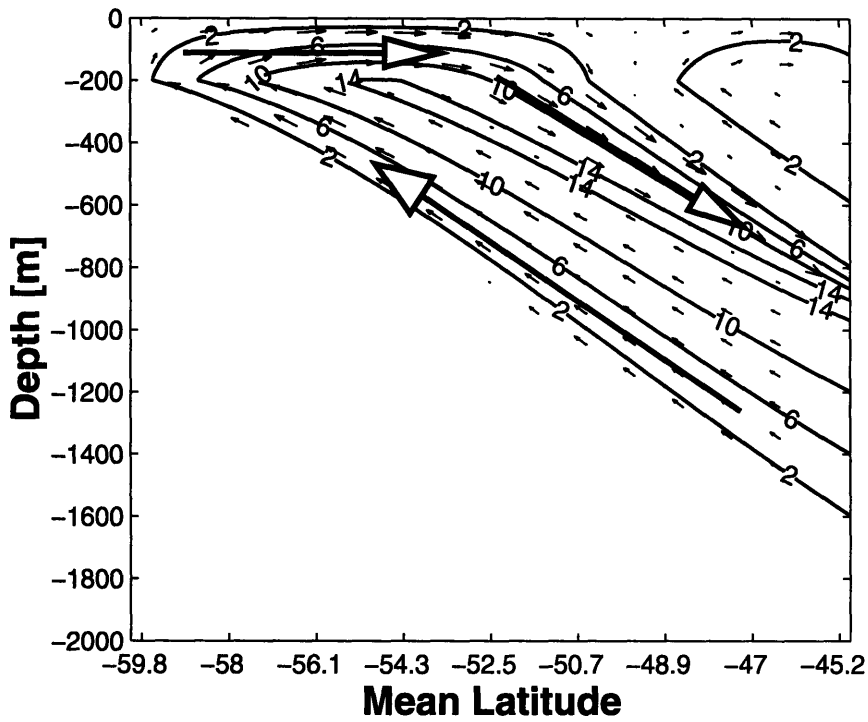

Figure 2-9: The residual stream function calculated using the idealized surface wind stress and buoyancy fluxes using the method of characteristics. The units are in Sv.

depicted in Fig. 2-1. The air-sea gas transfer coefficient, K_W, is a function of the wind speed according to Wanninkhof (1992).

Fig.2-10(a,b) shows the modeled distributions of CFC11 and associated pCFC11 in 1994. The corresponding observations from the WOCE Indian section, I-08, along $\sim 90°$E, are shown in Fig. 2-10(c,d). Similarly, Fig.2-11(a) and 2-11(b) respectively show modeled and observed (I08) distributions of bomb-Δ^{14}C. The observed distribution is determined using the potential alkalinity method of Key and Rubin (2002).

Comparison of modeled and observed fields must be carried out with caution because the modeled fields are streamline-averaged whereas the observations are from a particular section. However, examination of several WOCE sections across the ACC in streamline coordinates reveals rather similar distributions of CFC11 (Figs. 2-3 b,d,f) suggesting that qualitative comparison of the model and observations may be useful.

We find a reasonable agreement between the modeled and observed distributions of CFC11 and bomb-Δ^{14}C. The magnitude of the tracer concentrations and their large scale gradients are captured by the zonally averaged model. The modeled CFC11 and bomb-Δ^{14}C distributions have slightly shallow penetration depths compared to the observations. This is because tracer transport is essentially isopycnal in the interior and the modeled isopycnals are slightly too shallow. At the surface CFC11 is close to saturation, and its meridional gradient reflects the variation of the solubility which is largely controlled by SST. Hence, pCFC11 does not exhibit a surface gradient. Surface bomb-Δ^{14}C is slightly over-estimated compared to that diagnosed from the WOCE I-08 section.

We also evaluate the modeled distributions in terms of the relationships between CFC11 and bomb-Δ^{14}C (Fig. 2-12). The observed sections show two modes of correlation between the tracers. Figure 2-12 shows a positive correlation in the thermocline and a negative correlation in the surface layer along the WOCE I-08 line. This pattern of tracer relationship is common to all the available sections in the ACC. What processes control this pattern of correlations and do the modeled tracers reflect it?

Our simple model can indeed reproduce the general patterns of observed correla-

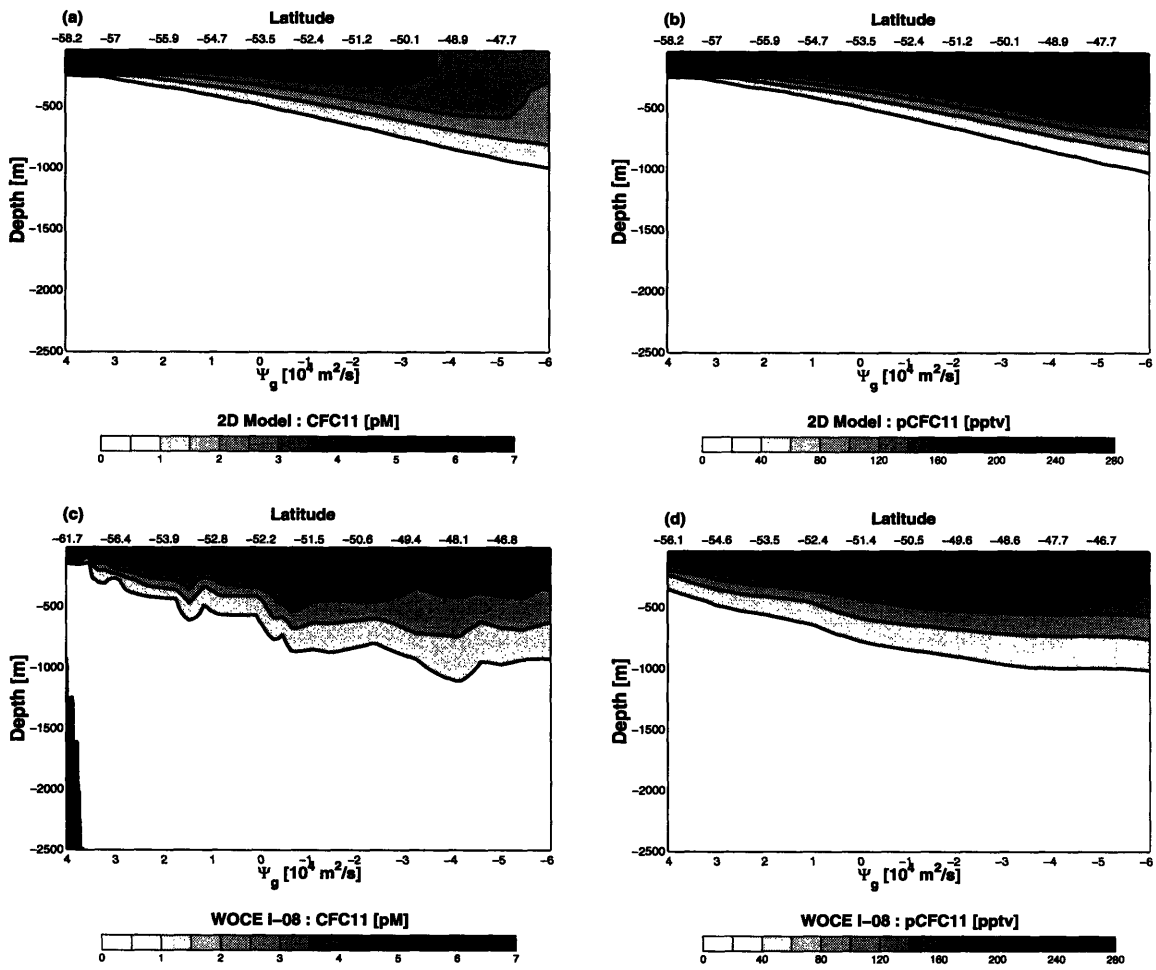

Figure 2-10: Simulated and observed distribution of CFC11 and its associating pCFC11. (a,b): the distribution of simulated CFC11 and pCFC11. (c,d): the distribution of observed CFC11 and pCFC11 from a WOCE Indian section, I-08. The modeled fields are taken for the model year 1994 which roughly corresponds to the periods of WOCE Indian section (I-08).

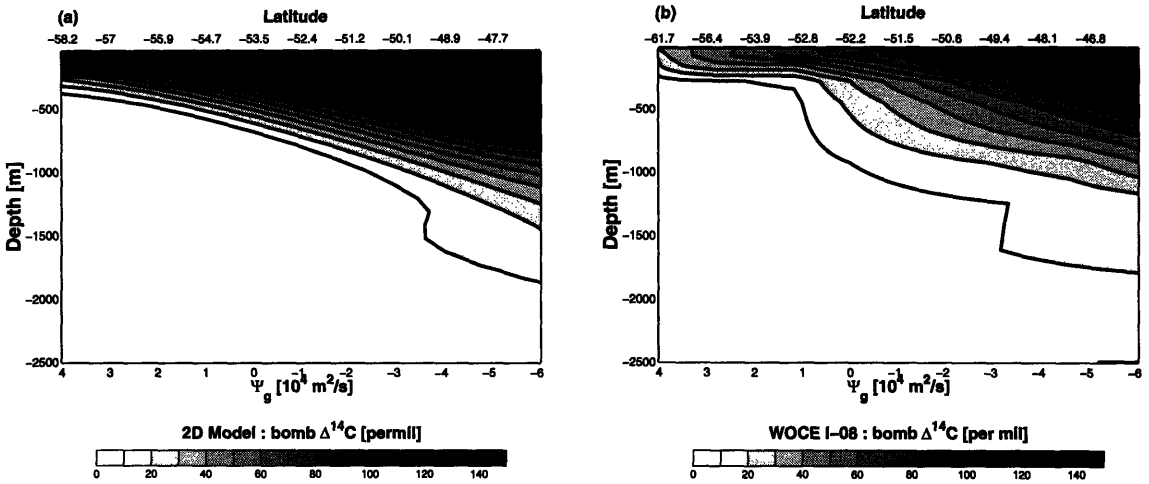

Figure 2-11: Simulated and observed distribution of bomb-$\Delta^{14}C$. (a): the modeled distribution. (b): the observed distribution along the WOCE Indian section (I-08). Bomb-$\Delta^{14}C$ distributions are separated from natural $\Delta^{14}C$ using the potential alkalinity method of Key and Rubin (2002).

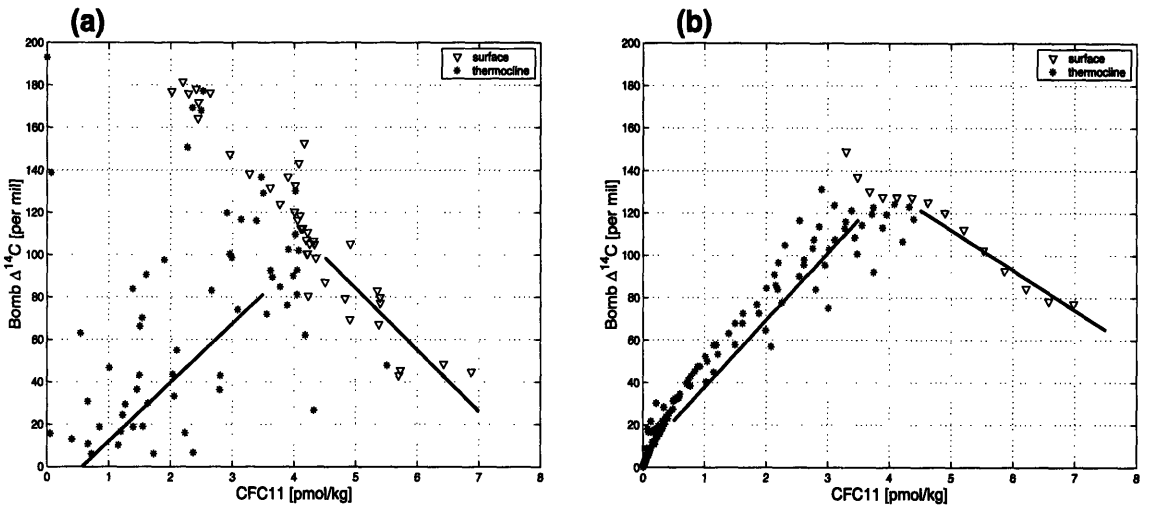

Figure 2-12: Scatter diagram of CFC11 and bomb-$\Delta^{14}C$ in the Southern Ocean to the south of 45S. (a): The diagram is based on the WOCE line I-08. (b): The diagram is based on modeled distributions from the tracer model. Solid lines are the least-square fit to the data. In the surface layer, CFC11 and bomb-$\Delta^{14}C$ distributions are negatively correlated. Below the surface layer, the correlation becomes positive. The model captures the gross pattern of the correlation.

tion between CFC11 and bomb-Δ^{14}C and shows that the residual circulation plays an important role in controlling the correlation at the surface. The meridional gradients of CFC11 and bomb-Δ^{14}C are of opposite sign in the surface layer. This is because CFC11 and bomb-Δ^{14}C have very different air-sea equilibration timescales, λ (Broecker and Peng, 1974), and different spatial variations in solubility.

CFC11 has a monthly timescale for air-sea equilibration, $O(\lambda_{CFC11}) = 10^{-7}$ s^{-1} (see Table 2.2), and its solubility increases polewards due to temperature dependence. Fig. 2-13 schematically illustrates the large scale distribution and controls on CFC11 in the 1990's. We may assume a fast gas-exchange limit for CFC11 such that surface waters are very close to equilibrium. The concentration decreases along isopycnals reflecting the surface source and increasing atmospheric mixing ratio.

In contrast, bomb-Δ^{14}C has a decadal timescale for air-sea exchange, $O(\lambda_{\Delta^{14}C}) = 10^{-9}$ s^{-1}, and decreases polewards in the surface Southern Ocean because upwelling of uncontaminated waters are advected equatorwards more rapidly than they can accumulate bomb-Δ^{14}C from the atmosphere. Fig. 2-14 schematically depicts the controls on bomb-Δ^{14}C. We assume a limit for bomb-Δ^{14}C in which the air-sea gas exchange is much slower than the physical transport and surface waters may be far from solubility equilibrium: $C \ll C_{at}$. To the south of the polar front, where deep water upwells, the surface bomb-Δ^{14}C concentration is determined by a competition between air-sea flux and upwelling. An equatorward advection and accumulation of bomb-Δ^{14}C is consistent with positive buoyancy fluxes into the ocean shown in Fig. 2-8.

The sign of isopycnal gradients of CFC11 and bomb-Δ^{14}C are the same in the thermocline because the only source of these tracers is from the atmosphere.

Anthropogenic CO_2, to be discussed in more detail later, falls between these two tracers with an equilibration timescale on the order of one year (Table 2.2).

Since the residual circulation has a significant control on the surface bomb-Δ^{14}C distribution, but not on that of CFC11, their relative distributions provide a clear, qualitative measure of the residual flow. The streamline-averaged model successfully captures the relative distributions between CFC11 and bomb-Δ^{14}C and helps to il-

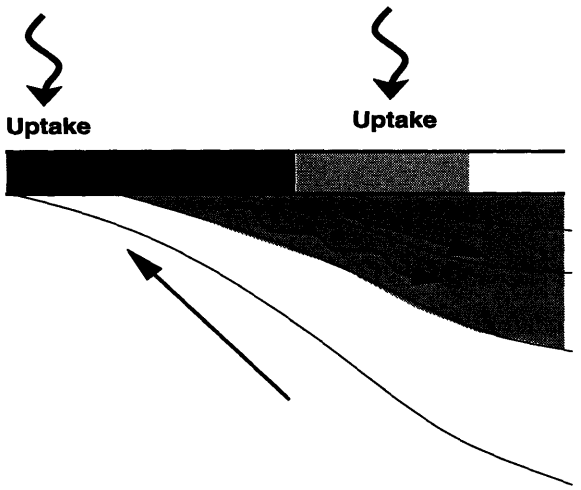

Figure 2-13: Schematic diagram of the uptake of CFC11. Large scale upwelling drives strong uptake of CFC11 to the south of the ACC and isopycnal stirring drives another peak the uptake in the north of the ACC. In between, there is a region of minimum uptake due to the equatorward advection and heating of surface waters.

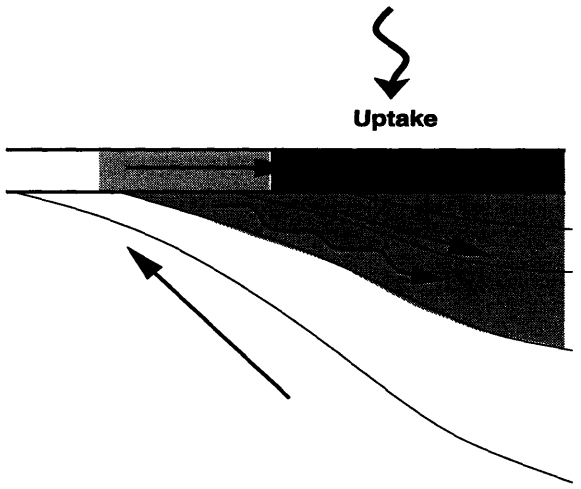

Figure 2-14: Schematic diagram of the uptake of bomb-$\Delta^{14}C$. The gas transfer coefficient controls the uptake. The maximum uptake occurs where the surface wind is at a maximum. In contrast the surface distribution of bomb-$\Delta^{14}C$ reflects the large scale circulation. The surface gradient in the concentration of bomb-$\Delta^{14}C$ is due to equatorward residual flow.

lustrate the controlling mechanisms.

We can use tracer-tracer relationships to examine more complex, three- dimensional general circulation and biogeochemistry models. In particular the correlation of the surface CFC11 and bomb-$\Delta^{14}C$ provides a point of comparison with observations. Fig. 2-15 shows the relationship between CFC11 and bomb-$\Delta^{14}C$ in a coarse-resolution three-dimensional configuration of the MITgcm (Marshall et al., 1997a,b) used for tracer simulations in OCMIP (e.g. Dutay et al 2002). This particular configuration parameterizes subgrid-scale eddy transfers using GM90 and isopycnic eddy stirring with a uniform diffusivity. The model is forced with seasonally varying wind stress and buoyancy forcing. Comparing Figs. 2-15 and 2-12 shows that this particular model set-up does not capture the sharp contrast in surface and thermocline gradients seen in the data and the streamline-averaged model. This is because the simulated residual overturning circulation is very weak in the Southern Ocean (Fig.2-16), and the wind-driven and eddy-induced transport almost cancel one another out and the thermocline in the model's ACC is mainly ventilated by isopycnal eddy stirring.

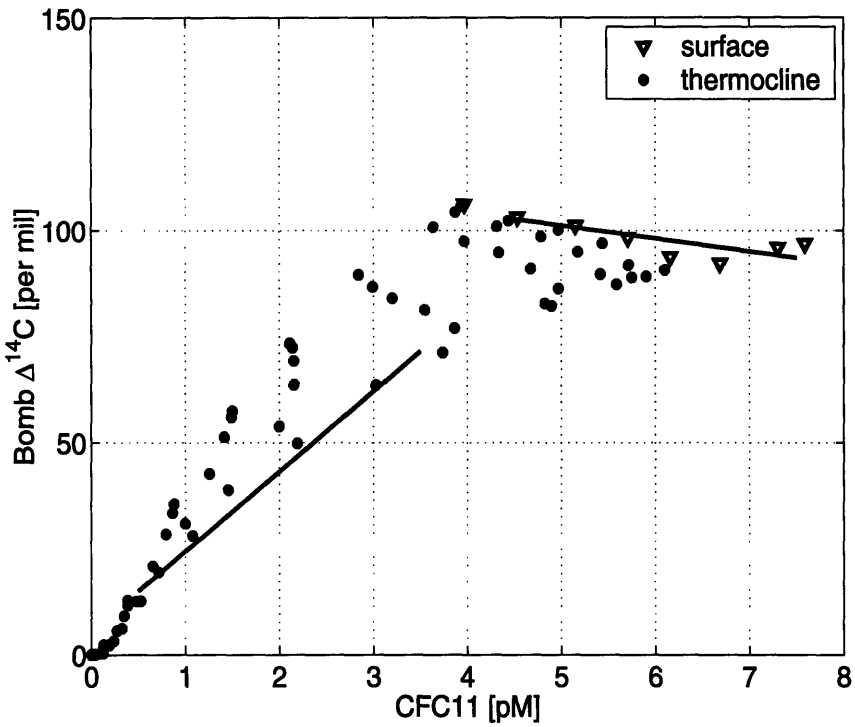

Figure 2-15: Scatter diagram of CFC11 and bomb-$\Delta^{14}C$ in the Southern Ocean to the south of 45S calculated in the MITgcm. The diagram is based on the simulated distribution at the location of the WOCE line I-08. The model does not reproduce the observed pattern of the correlation in the surface layer.

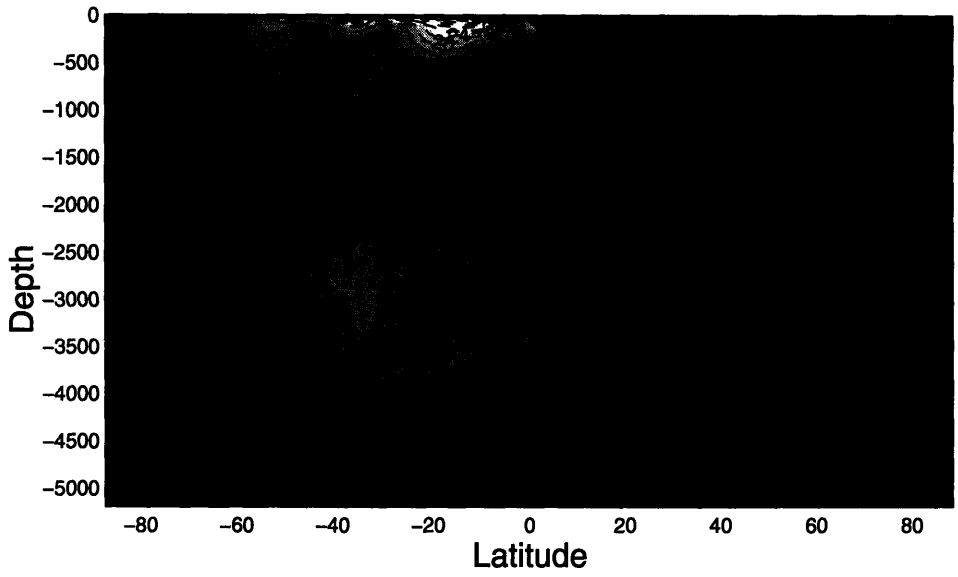

Figure 2-16: Simulated meridional overturning circulation diagnosed from the OCMIP run of MITgcm. The residual mean circulation, Ψ_{res}, plotted here is based on the annual mean, net transport including Eulerian mean flow and eddy-induced circulation parameterized using GM90.

2.4 Tracer-based estimate of the residual mean circulation

Significant differences in the CFC11-bomb Δ^{14}C relationship are found between the OCMIP run and the observations. Physical transport by the residual mean circulation could be the critical factor in affecting the distribution of these tracers in the Southern Ocean. To illustrate and better understand the relationship between the intensity of the meridional overturning circulation and the tracer-tracer relationship, I calculate the sensitivity of the correlation between the two tracers to the intensity of the residual mean circulation in a suite of numerical experiments. Then I suggest that the observed tracer-tracer relationship could constrain the rates of meridional overturning circulation in the ACC which is not directly measurable.

Numerical experiments with the simple 2D model and more complicated general circulation model illustrate the relationship between the rate of the residual mean circulation and the magnitude of the slope of the surface trend of the CFC11-bomb Δ^{14}C diagram introduced in the previous section. Here I define Δ as a measure of the correlation between the two tracers in the surface waters.

$$\Delta = \frac{\partial \Delta^{14}C}{\partial CFC11} \qquad \text{surface layer} \tag{2.8}$$

Sensitivity of Δ to the variations in Ψ_{res} is evaluated in a suite of sensitivity experiments. Table 2.4 summarizes the configuration and the forcing of the simple 2D model and the GCM runs.

I first simulate the distribution of CFC11 and bomb $\Delta^{14}C$ using the simple 2D model. The intensity of the circulation, Ψ_{res}, is varied from 0 Sv to 18 Sv with an interval of 1 Sv. 19 sensitivity runs are conducted to calculate the response of Δ to the variations in Ψ_{res}. The spatial pattern of Ψ_{res} is held constant taking the idealized profile shown in Fig.2-9. The results are plotted in Fig.2-17 indicating the significant variation in simulated Δ in response to the variation in Ψ_{res}. Δ varies from -3 to -33 permil pM^{-1} for the range of Ψ_{res} between 0 and 18 Sv. Standard deviation in Δ is

Model (domain)	Wind stress forcing	Buoyancy forcing	Eddy param. (A_I m^2s^{-1})	Vertical diff. (K_V m^2s^{-1})
2D Model (regional)	Idealized (annual mean)	Idealized, fixed BF	V97 (800 to 1300)	Adiabatic (0)
MIT-01 (global)	TRE89	Fixed HF, FH and Restoring SST, SSS	GM90 (1000)	Enhanced bottom ($3{\cdot}10^{-5}$ to $3{\cdot}10^{-4}$)
MIT-02 (global)	TRE89	Fixed HF only and Restoring SST, SSS	GM90 (1000)	Uniform ($3{\cdot}10^{-5}$)

Table 2.3: Comparison of the numerical models. TRE89 represents the monthly climatology of (Trenberth et al., 1989). BF, HF and FH represent buoyancy flux, heat flux and fresh water flux respectively. V97 and GM90 represent the eddy parameterization of (Visbeck et al., 1997) and (Gent and McWilliams, 1990). A_I and K_V represent the isopycnal eddy diffusivity and the vertical turbulent diffusivity.

on the order of 3 permil pM^{-1}.

Then I also simulate the distribution of CFC11 and bomb $\Delta^{14}C$ using MITgcm. Two model runs are made with different surface boundary condition. These experiments are configured as the OCMIP run presented in the previous section, except that the surface boundary condition is different. The two experiments shown here use the monthly climatological wind stress of (Trenberth et al., 1989).

The buoyancy forcing of the first experiment (MIT-01) includes prescribed climatological heat flux and freshwater flux in addition to the restoring of SST and SSS toward monthly climatology. Furthermore, the MIT-01 run includes enhanced vertical turbulent diffusion coefficient in the bottom layer, driving a relatively intense bottom circulation. The simulated meridional overturning circulation for this run is shown in Fig.2-18. The near-surface residual mean circulation in the ACC (55S, -220m) is 8.5 Sv in this particular calculation.

The buoyancy forcing of the second experiment (MIT-02) is the same as that of MIT-01 except that the freshwater flux is simply parameterized as the restoring

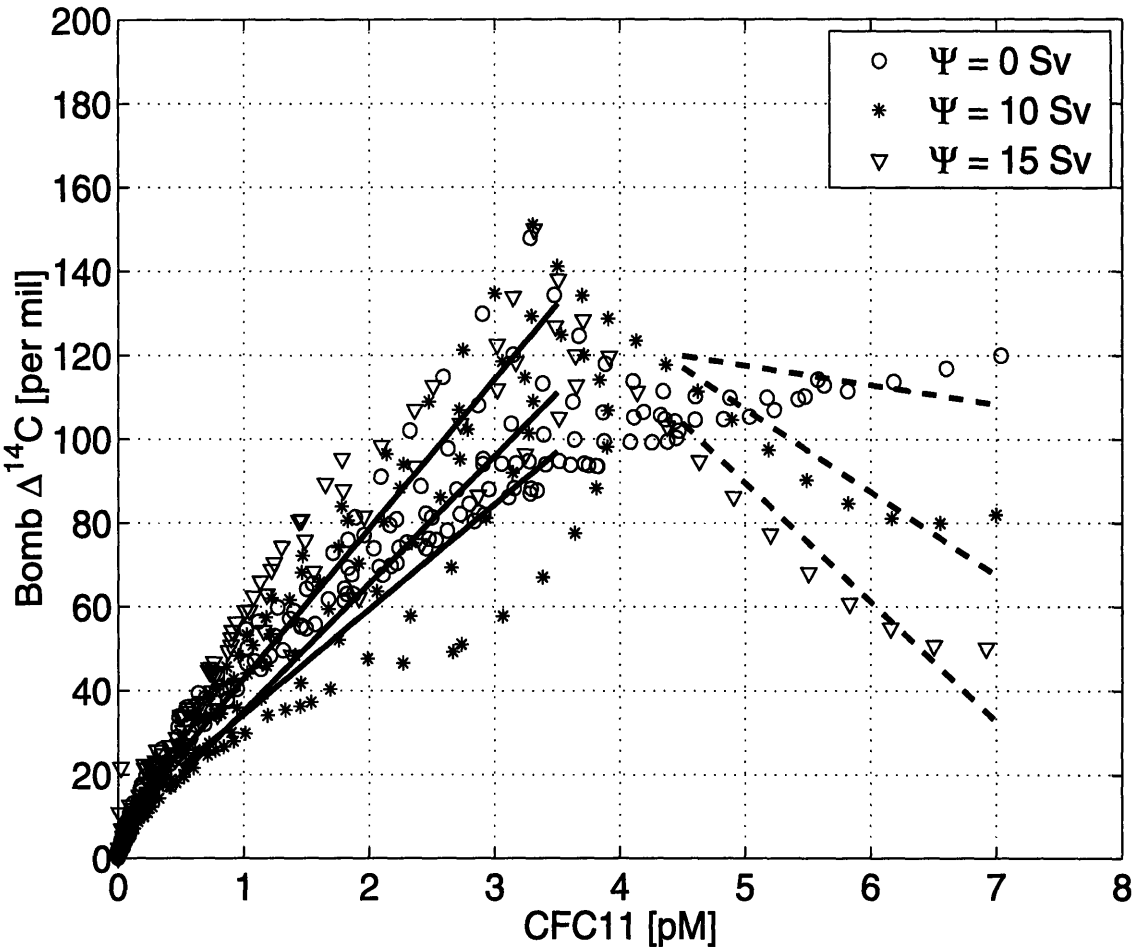

Figure 2-17: The CFC11-bomb $\Delta^{14}C$ scatter diagram from a subset of sensitivity experiments with the zonally averaged model. Three cases are presented here for Ψ_{res} = 0, 10 and 15 Sv. The slope of the surface trend, Δ, changes significantly in response to the variation in Ψ_{res}.

of SSS toward monthly climatology, and this run does not include enhanced vertical turbulent diffusion coefficient in the bottom layer. The simulated meridional overturning circulation for this run is shown in Fig.2-19. Comparing this run with MIT-01, the bottom circulation is significantly weaker, and in the Southern Ocean, the near-surface residual mean circulation at (55S, -220m) is only 3.0 Sv.

Simulated Δ is calculated from the meridional sections from the two GCM runs. Fig.2-20 and 2-21 show the simulated, surface CFC11-bomb $\Delta^{14}C$ relationship in the Atlantic, Indian and Pacific section of the model. The magnitude of Δ does not significantly vary between the sections within each experiment. In the MIT-01 run, the zonal average of Δ is -17.5 permil pM^{-1} with standard deviation of 3.2 permil pM^{-1} from the 128 meridional sections. In the MIT-02 run, the zonal average of Δ is -13.5 permil pM^{-1} with standard deviation of 3.2 permil pM^{-1}. The magnitude of Ψ_{res} is greater in the MIT-01 run and so is that of Δ, qualitatively supporting the simple relationship predicted by the 2D model.

How does the simulated sensitivity of Δ from the 2D model and the GCM compare quantitatively? Fig.2-22 summarizes the results for the relationship between Ψ_{res} and Δ from all sensitivity experiments. Dashed lines represent the relationship predicted by the 2D model with $\pm$ 1 standard deviation. The two circular points show the results from the GCM runs, which have qualitatively similar tendency to the sensitivity of the 2D model. (See also Table 2.4). I also show the observed Δ from the WOCE data. The observed Δ includes significant uncertainty due to the method of separating bomb $\Delta^{14}C$ signal from the large, natural $\Delta^{14}C$ signal (Rubin and Key, 2002) and due to the natural variability in the hydrographic sections. Even so, the magnitude of observed Δ is significantly greater than that simulated by the GCMs. If the sensitivity of the simple 2D model is taken as a reference, $\Psi_{res} \sim 14$ Sv is inferred from the observed Δ. which is broadly consistent with independent estimates of Ψ_{res}. (See, for example, section 2.2.3).

In summary I examined the hypothesis that the CFC11-bomb $\Delta^{14}C$ relationship in the near-surface Southern Ocean can predict the residual mean circulation using a suite of numerical experiments. I quantified the relationship between the intensity of

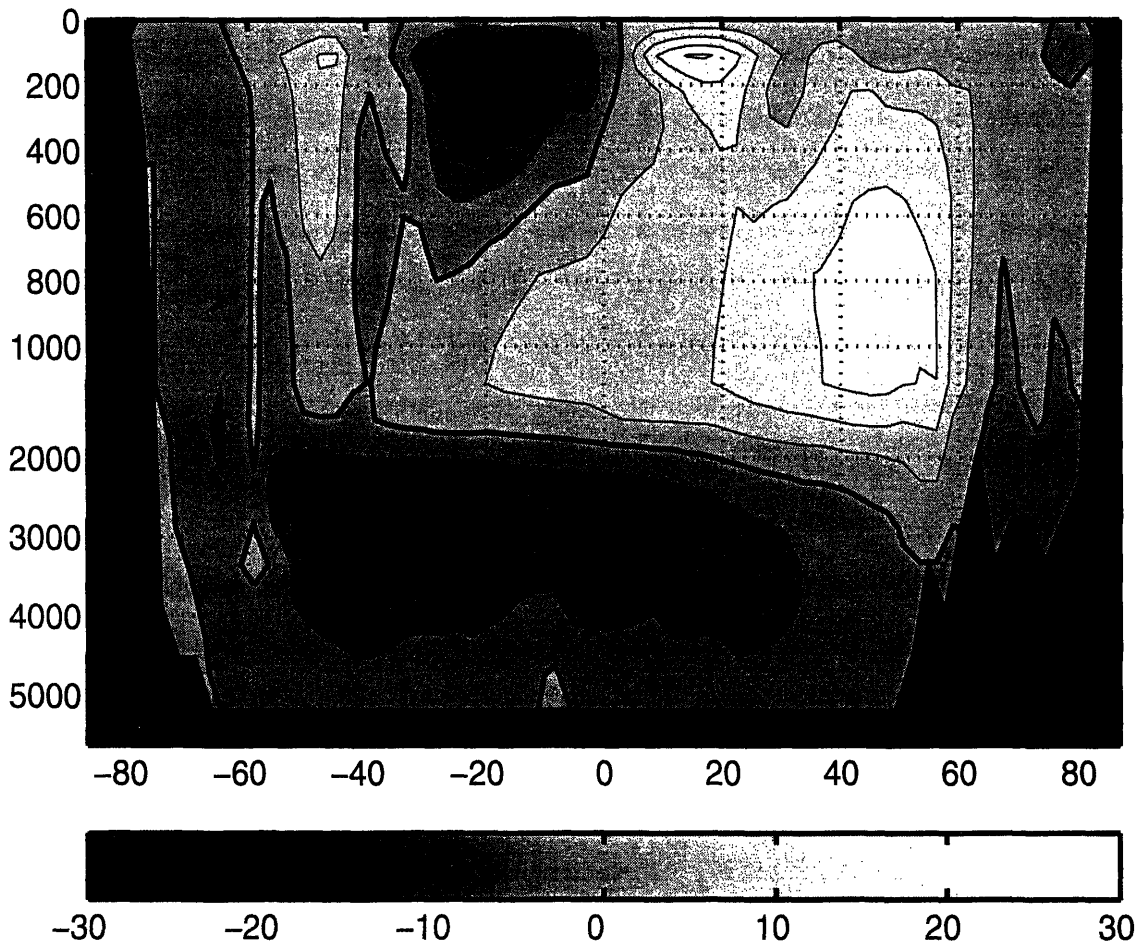

Figure 2-18: Simulated meridional overturning circulation diagnosed from the sensitivity calculation using MITgcm (MIT-01). The residual mean circulation, Ψ_{res}, plotted here is based on the annual mean, net transport including Eulerian mean flow and eddy-induced circulation parameterized using GM90. The contour interval is 5 Sv.

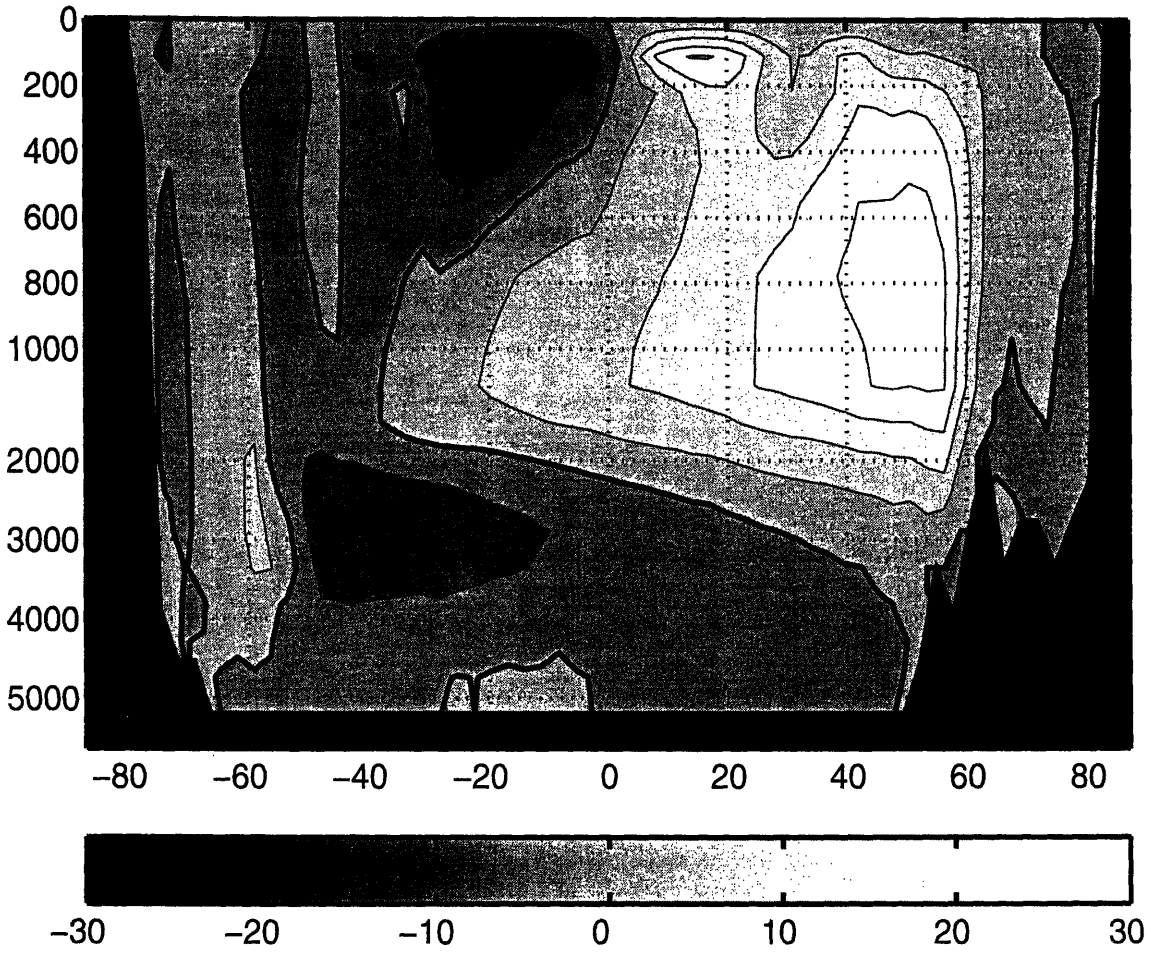

Figure 2-19: Simulated meridional overturning circulation diagnosed from the sensitivity calculation using MITgcm (MIT-02). The residual mean circulation, Ψ_{res}, plotted here is based on the annual mean, net transport including Eulerian mean flow and eddy-induced circulation parameterized using GM90. The contour interval is 5 Sv.

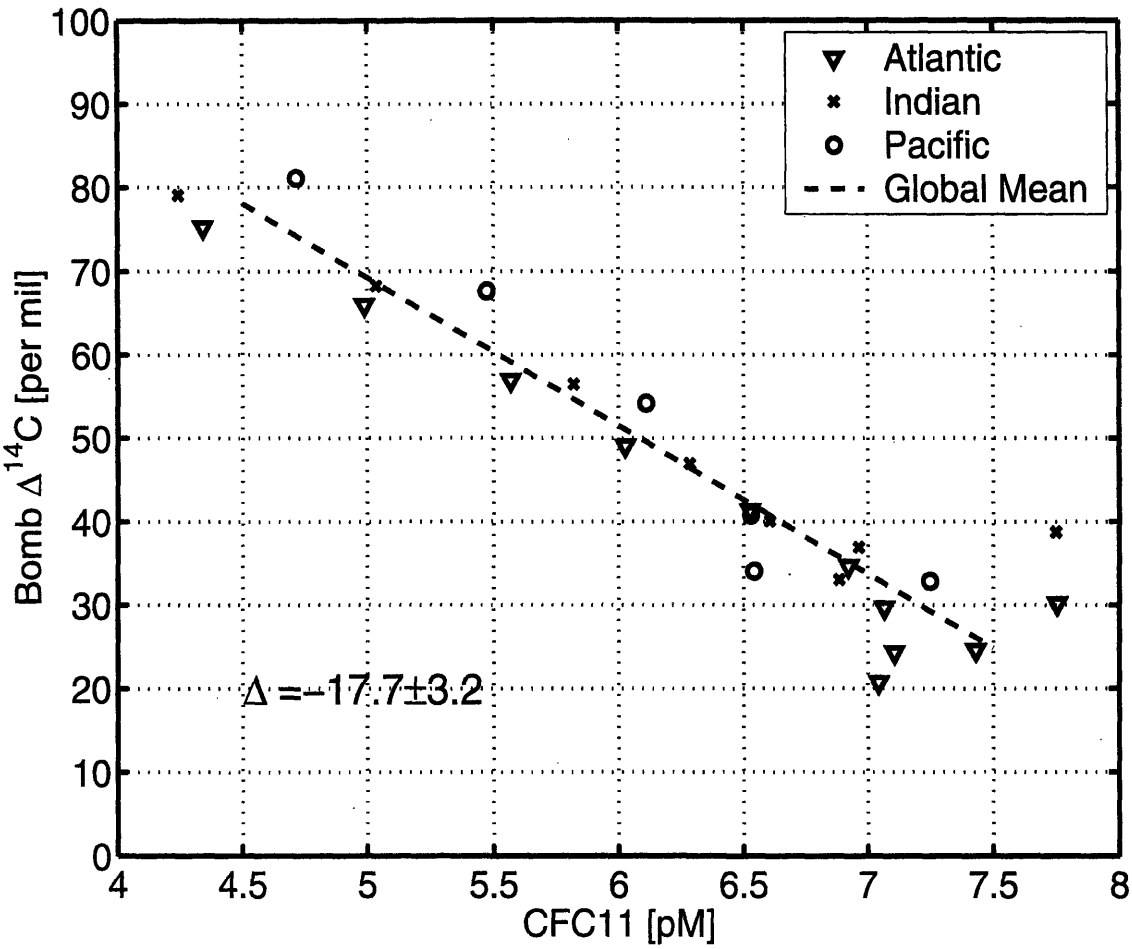

Figure 2-20: Scatter diagram of CFC11 and bomb-$\Delta^{14}C$ in the Southern Ocean to the south of 45S calculated in the MITgcm (MIT-01). The diagram is based on the simulated distribution in the Atlantic (30W), Indian (90E) and Pacific 150(E) sections. The dashed line represents the zonally-averaged tracer distributions.

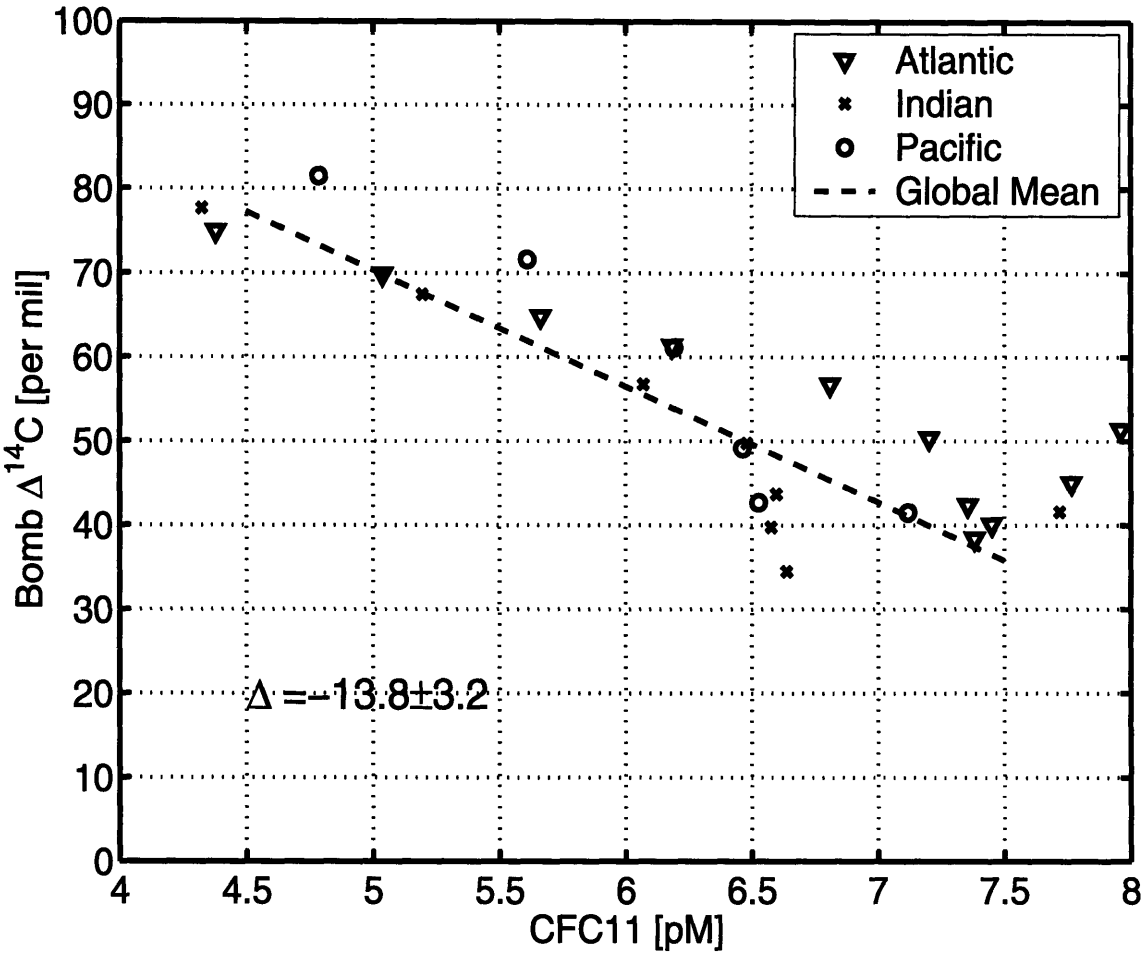

Figure 2-21: Scatter diagram of CFC11 and bomb-$\Delta^{14}C$ in the Southern Ocean to the south of 45S calculated in the MITgcm (MIT-02). The diagram is based on the simulated distribution in the Atlantic (30W), Indian (90E) and Pacific 150(E) sections. The dashed line represents the zonally-averaged tracer distributions.

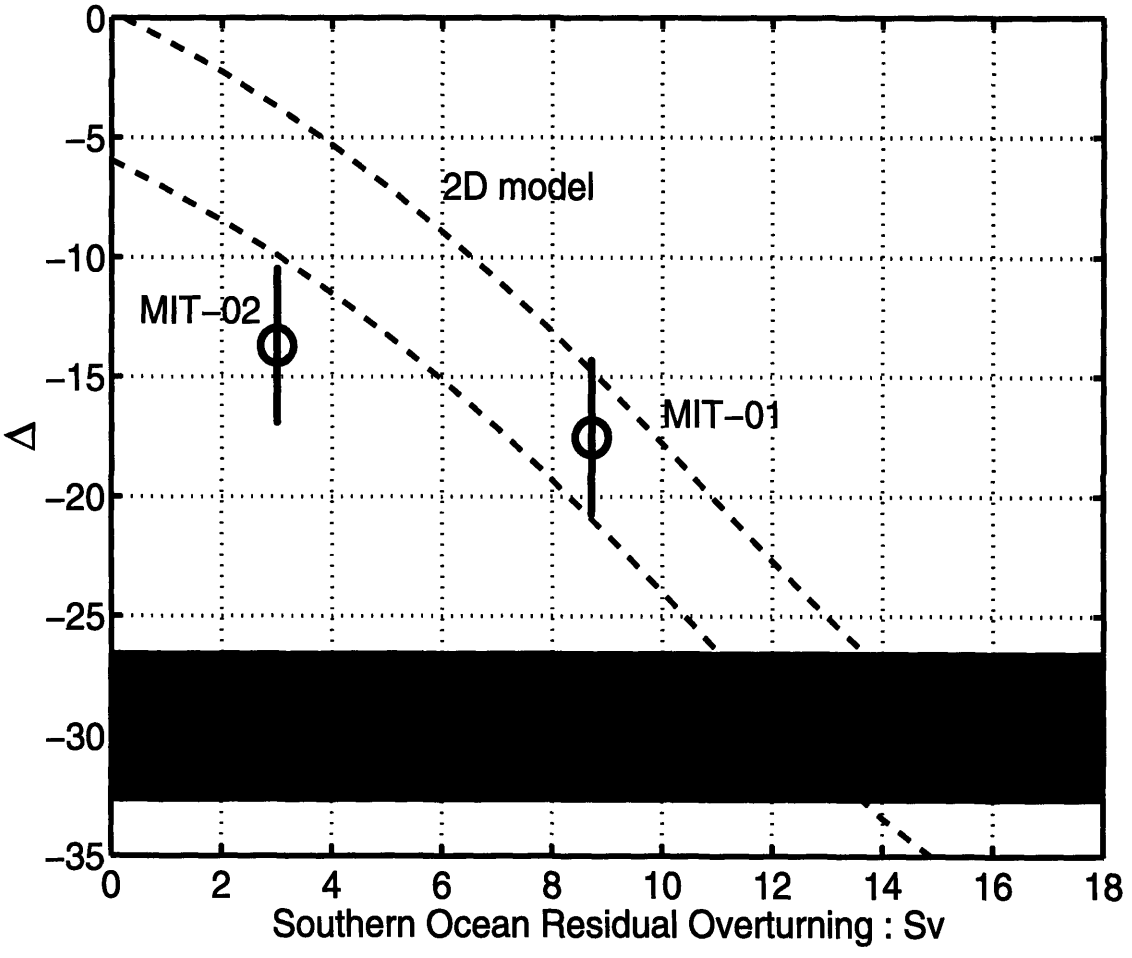

Figure 2-22: Synthesis of the results from the simple 2D model, GCMs and observations (WOCE). The vertical axis is the slope of the CFC11-bomb $\Delta^{14}C$ diagram for the surface ocean in units of per mil pM^{-1}. Dashed lines represent results from the 2D model. The gray region is the value inferred from observation. The two circles represent the value calculated from the two GCM experiments.

Model	Ψ_{res} at 55S	Δ	std(Δ)
2D Model	Prescribed (0 to 18 Sv)	(-3 to -33)	3.0
MITgcm 01	8.5 Sv	- 17.5	3.2
MITgcm 02	3.0 Sv	- 13.5	3.2

Table 2.4: Summary of the sensitivity experiments. std(Δ) represents the standard deviation of Δ. For the simple 2D model, std(Δ) is based on the inverse of the eigenvalues of the Hessian matrix. For GCMs, std(Δ) is based on the standard deviation of Δ from 128 meridional sections simulated in the model.

the residual mean circulation and the correlation between CFC11 and bomb $\Delta^{14}C$. Due to the leading order contribution of eddy processes and the vast surface area of the Southern Ocean, it is very difficult to directly measure the residual mean flow in the region. However, transient tracers integrate the effects of physical transport, and may provide a useful constraint. The simple 2D model suggest that the magnitude of Δ significantly varies with Ψ_{res} indicating a possibility for constraining Ψ_{res} with observed tracer-tracer relationship. The sensitivity experiments with MITgcm support the idea that the magnitude of Ψ_{res} and the slope of the surface CFC11-bomb $\Delta^{14}C$ relationship are correlated. There are only two GCM runs presented here, and it is necessary to include more sensitivity experiments from GCMs to better constrain the relationship between Δ and Ψ_{res}. It is a subject of on-going study to include GCM experiments using different models including a subset of the OCMIP models.

2.5 What controls the uptake of the transient tracers ?

In the previous section we discussed the controls on the distribution of transient tracers in the Southern Ocean. In this section we consider the controls on the air-sea tracer flux using scaling arguments and sensitivity experiments with the streamline-averaged model. How are the large scale patterns of uptake of CFC11, bomb-$\Delta^{14}C$, and anthropogenic CO_2 controlled in the model? What is the rate-limiting process in the uptake of these tracers? How are these fluxes affected by changes in the physical forcing?

We first examine the time-averaged tracer balance in the surface layer. We integrate the tracer equation, (2.1), over the depth of the mixed layer and estimate the relative magnitude (s^{-1}) of each term:

$$\begin{array}{cccccccc} \frac{\partial C}{\partial t} & + v_{res}\frac{\partial C}{\partial y} & + \frac{\Lambda w_{res}|_{-h}}{h}(C - C_{th}) = -\frac{Ks_\rho}{h}\left(\frac{\partial C}{\partial y}\right)_{\rho,-h} & + \frac{\partial}{\partial y}K\frac{\partial C}{\partial y} & -\lambda C & + \lambda C_{at} & \\ O(\frac{C}{T}) & O(\frac{\Psi_{res}C}{hL}) & O(\frac{\Psi_{res}C}{hL}) & O(\frac{KHC}{hL^2}) & O(\frac{KC}{L^2}) & O(\lambda C) & O(\lambda C^{at}) \\ 10^{-9} & 10^{-8} & 10^{-8} & 10^{-8} & 10^{-9} & \lambda & \lambda\frac{C^{at}}{C} \end{array} \tag{2.9}$$

The third term on the LHS represents entrainment and is only active when the water is upwelling: Λ is 1 when w_{res} is positive, and is 0 otherwise. C_{th} represents the tracer concentration in the upper thermocline. The first term on the RHS is due to isopycnal stirring at the base of the mixed layer and $(\partial C/\partial y)_{\rho,-h}$ represents the isopycnal tracer gradient just below the mixed layer. The second term on the RHS is the divergence of horizontal, diapycnal eddy fluxes assuming that eddy transfer is directed horizontally in the mixed layer. We are interested in interannual to decadal timescales and it is appropriate to assume that local accumulation in the mixed layer is negligible compared to physical transport.

The relative magnitudes of the terms in (2.9) are estimated using the following

parameter values: The magnitude of the residual circulation can be estimated from (2.4), $\Psi_{res} \sim B_s L \Delta b^{-1}$. For a buoyancy change across the ACC, $\Delta b = 7 \cdot 10^{-3}$ m s^{-2}, a surface buoyancy flux, $B_s = 5 \cdot 10^{-9}$ m^2 s^{-3} and the meridional scale of ACC, $L = 10^6$ m, we find $O(\Psi_{res}) = 0.7$ m^2 s^{-1}. We also assume a thickness of the surface mixed layer, $O(h) = 10^2$ m, and a thermocline depth, $O(H) = 10^3$ m. The gross magnitude of isopycnal eddy diffusivity is $O(K) = 10^3$ m^2 s^{-1}. Combining these parameters, we arrive at our estimates of the surface transport terms shown in (2.9). We see that the residual flow and isopycnal stirring are of comparable magnitude, but diapycnal eddy fluxes are an order of magnitude smaller than other terms.

2.5.1 CFC11

Fig. 2-23 shows the cumulative uptake of CFC11 in the streamline-averaged model and its sensitivity to buoyancy fluxes (represented by Ψ_{res}), wind stress (represented by $\overline{\Psi}$), and gas transfer coefficient. We define the cumulative air-sea fluxes, $FT(y,t)$, thus;

$$FT(y) = \int_{t_0}^{t_1} \lambda \, h \, (C_{at} - C) \, dt \tag{2.10}$$

where $t_0 = 1750$ is the initial time of the model integration and $t_1 = 1990$ is the end time.

In each panel of Fig. 2-23 solid lines represent the control run which are carried out with the standard set of physical parameters. In the sensitivity runs, depicted by dashed lines, parameters are varied while the spatial patterns are kept fixed. Thus we only examine sensitivities to the magnitude of the physical forcing, not its spatial structure.

The cumulative uptake of CFC11 exhibits two peaks in the control run at around 60°S and 48°S. What controls the spatial patterns of the uptake? In short, the larger peak to the south of the ACC is due to upwelling of cold, deep water and higher solubility. The secondary peak to the north of the ACC is due to enhanced isopycnal stirring. Using simple theory and scaling analysis we will illustrate which processes dominate the spatial patterns and magnitude of the cumulative uptake.

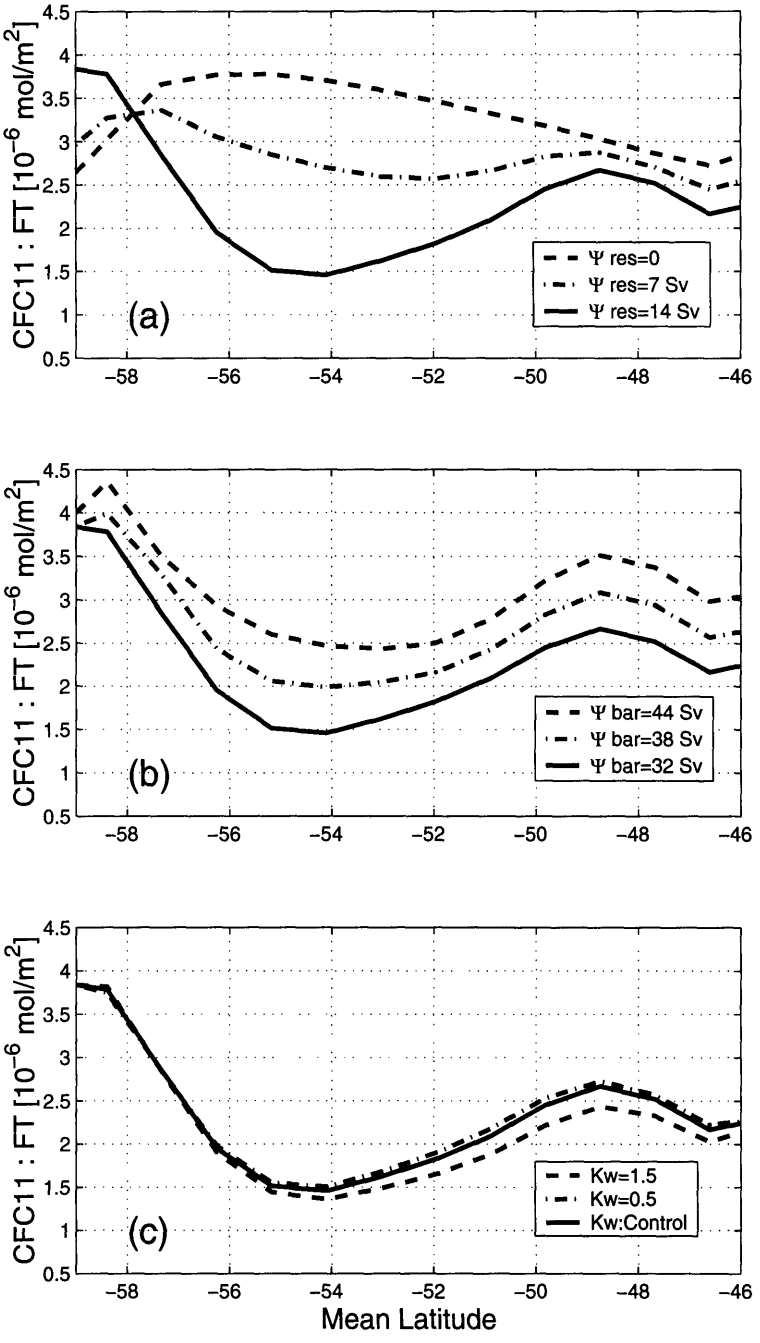

Figure 2-23: Cumulative uptake of CFC11. Three panels are for the sensitivities to Ψ_{res} (a), $\overline{\Psi}$ (b), and K_W (c). For control runs we use a standard set of physical parameters. For sensitivity runs, we modified the physical parameters by multiplying a constant to the profiles of buoyancy fluxes, wind stress, or gas transfer coefficient. Control simulation uses $\Psi_{res} = 14(Sv)$ and $\overline{\Psi} = 32(Sv)$.

We consider the tracer balance in the surface layer shown in (2.9). We assume a fast gas exchange limit for $CFC11$ which has a short air-sea equilibration timescale (order one month) relative to the timescales of physical transport. Adopting this value for λ in (2.9) and we find the leading order balance is dominated by air-sea gas exchange. Hence

$$C \sim C_{at} \tag{2.11}$$

and so the surface distribution of CFC11 is controlled by atmospheric pCFC11 and the temperature dependent solubility.

At the next order (i.e. retaining the next order of terms in the balance) we find that the small deviation from equilibrium — $\Delta C \equiv C - C_{at}$ — is controlled by the physical transport:

$$\Delta C = -\frac{1}{\lambda}\left[v_{res}\frac{\partial C_{at}}{\partial y} + \frac{\Lambda w_{res}|_{-h}}{h}(C_{at} - C_{th}) + \frac{Ks_\rho}{h}\left(\frac{\partial C_{at}}{\partial y}\right)_{\rho,-h}\right] \tag{2.12}$$

The air-sea gas exchange, $F = -\lambda h \Delta C$, is now controlled by physical transport, residual flow and isopycnal stirring. Note that in this fast exchange limit, the uptake of CFC11 becomes insensitive to the gas transfer coefficient.

We now consider three idealized cases in which the air-sea gas exchange is balanced by a combination of the three processes in (2.12): (a) entrainment of thermocline waters, (b) horizontal advection and (c) isopycnal stirring:

(a) Entrainment.

Consider a balance between entrainment and air-sea fluxes, a regime that is relevant to the south of the ACC (around 58°S), where there is large scale upwelling in the residual flow and entrainment of deep waters. Assuming that the upwelling waters are depleted in transient tracers ($C_{th} \ll C_{at}$), we obtain a simple expression for the local uptake:

$$F \sim \frac{w_{res}|_{-h}}{h} C_{at} = \frac{\partial \Psi_{res}}{\partial y}\frac{C_{at}}{h} \tag{2.13}$$

The uptake depends on the upwelling rate of the residual circulation, which is also linearly related to the meridional gradient of the surface buoyancy forcing – see (2.4).

Thus, the uptake rate is related to the surface buoyancy flux in this region. Fig. 2-23 shows the meridional distribution of the cumulative uptake of CFC11 from the streamline-average numerical model. Each of the three panels depicts the result from the control run (solid line) and two sensitivity studies relating to changes in (a) Ψ_{res}, the residual flow, here related to buoyancy forcing, (b) $\overline{\Psi}$, the wind-driven circulation (Deacon Cell), and (c) K_W the gas transfer coefficient. Fig. 2-23(a) illustrates that the spatial pattern of cumulative uptake is very sensitive to Ψ_{res} and hence to the pattern of buoyancy forcing. The uptake to the south of the ACC is reduced with weaker residual flow because upwelling of deep water is reduced, and consistent with the scaling in (2.13).

(b) Horizontal Advection.

Near the polar front (around 53°S), Fig. 2-9 shows a maximum in the equatorward, surface residual flow. Here, the horizontal advection in the mixed layer could play an important role in controlling uptake. Assuming a local balance between uptake and horizontal advection by the residual flow, we have:

$$F \sim v_{res}\frac{\partial C_{at}}{\partial y} = \frac{\Psi_{res}}{h}\frac{\partial C_{at}}{\partial y} \tag{2.14}$$

Depending on the direction of the flow, meridional advection might supersaturate or undersaturate the surface concentration. This parameterization of the surface flux is analogous to the potential solubility model of Keeling et al. (1993) and Murnane et al. (1999). The sign of $(\partial C_{at}/\partial y)$ is negative in the ACC due to the equatorward increase in SST. The residual stream function, Ψ_{res}, is positive (i.e. northward) here and so eq.(2.14) suggests local outgassing in the equatorward residual flow: Cold, CFC11-rich water is advected and warmed, moving toward supersaturation, and the ocean uptake is small.

The sensitivity experiment shown in Fig. 2-23(a) reveals that the uptake of CFC11 near the polar front, around 53°S, is highly sensitive to the variations in Ψ_{res} which is linearly related to surface buoyancy flux. Hence a 50% decrease in the residual flow causes a comparable increase in the local uptake, consistent with the linear

relationship predicted by (2.13) and (2.14).

We note that the observed climatological distribution of buoyancy flux has significant uncertainty (> 50%, see Fig. 2-8) illustrated by the difference between the climatologies. This implies a comparable uncertainty in the regional patterns of air-sea flux of CFC11 determined with any model forced by these physical data sets.

(c) Isopycnic Stirring.

To the north of the ACC, the surface wind is intense and surface buoyancy fluxes suggest that the residual flow is weak. Here it is likely that isopycnic stirring dominates the physical transport. For this regime we may assume a local balance between isopycnal stirring and air-sea flux of CFC11.

$$F \sim \frac{K s_\rho}{h}\left(\frac{\partial C_{at}}{\partial y}\right)_{\rho,-h} = \frac{\Psi_{eddy}}{h}\left(\frac{\partial C_{at}}{\partial y}\right)_{\rho,-h} \tag{2.15}$$

Here, isopycnal stirring depends on the product of isopycnal diffusivity, isopycnal slope, and tracer gradient at the base of the mixed layer. In this regime, eq.(2.15) suggests that uptake is linearly related to the eddy-induced circulation, Ψ_{eddy}, which depends on surface wind stress, surface buoyancy fluxes, and the specific choice of eddy transfer parameterization. From (2.2)-(2.6), the eddy-induced transport is $\Psi_{eddy} = \Psi_{res} - \overline{\Psi}$. Note that Ψ_{eddy} and $\overline{\Psi}$ tend to cancel out one another. Thus, the magnitude of Ψ_{eddy} and the diffusive flux increases with stronger wind and greater $\overline{\Psi}$. Eq.(2.15) also predicts that the uptake associated with the diffusive fluxes decreases with Ψ_{res} (which reflects buoyancy forcing). This prediction is supported by sensitivity studies with the numerical model shown in Fig. 2-23(a) and (b).

In summary; in the control run of the numerical model (Fig. 2-23(a), solid line) we find two major regions of uptake of CFC11 in the Southern Ocean. The first is to the south of the ACC, due to large scale upwelling and high solubility, the second is due to the intensified isopycnal stirring to the north of the polar front. The region of minimum uptake in between is due to equatorwards residual flow. These regimes are schematically illustrated in Fig. 2-13. The sensitivity of uptake in these regimes is also consistent with the idealized scalings derived from (2.11) and (2.12) in the fast

gas exchange limit.

2.5.2 Bomb $\Delta^{14}C$

Fig. 2-24 shows the streamline-averaged, cumulative uptake of bomb-$\Delta^{14}C$ and its sensitivity to buoyancy fluxes (Ψ_{res}), wind stress ($\overline{\Psi}$), and gas transfer coefficient. The cumulative flux is defined in (2.10). The numerical model suggests that uptake of bomb-$\Delta^{14}C$ is only sensitive to the gas transfer coefficient (Fig. 2-24(c)) and the spatial pattern of the uptake reflects that of K_w.

For bomb-$\Delta^{14}C$, the air-sea gas exchange is much slower than the physical transport. In this limit, surface water may be far from the solubility equilibrium, $C \ll C_{at}$. Then, the leading order balance in (2.9) is

$$F = \lambda h C_{at} \tag{2.16}$$

This approximation has its limitations in the subtropics where the surface concentration approaches C_{at} in the 1990s – the significance of this assumption can be seen in the numerical experiments. Since we assume that atmospheric concentration is spatially uniform, spatial patterns of the uptake are controlled by the profile of gas transfer coefficient, K_w, which, in the numerical experiments, is a function of windspeed following Wanninkhof (1992).

Fig. 2-24 shows that variations in Ψ_{res} (buoyancy forcing) and $\overline{\Psi}$ (wind-stress forcing) have relatively small impact on the *uptake*, even though the large scale *distribution* of bomb-$\Delta^{14}C$ is very sensitive to the surface residual flow (Section 3). Fig. 2-24(a) shows that the meridional profile of uptake is largely set by that of the surface wind forcing, but we observe enhanced uptake to the south of the ACC due to the upwelling of uncontaminated, deep waters. When the residual flow is switched off, $\Psi_{res} = 0$, the spatial pattern of the uptake becomes even more closely resembles the surface wind profile. The uptake to the north of 55°S is slightly increased when the residual flow, Ψ_{res}, is reduced because of changes in isopycnal diffusivity and surface distributions. Likewise, in Fig. 2-24(b) with greater $\overline{\Psi}$, the overall uptake

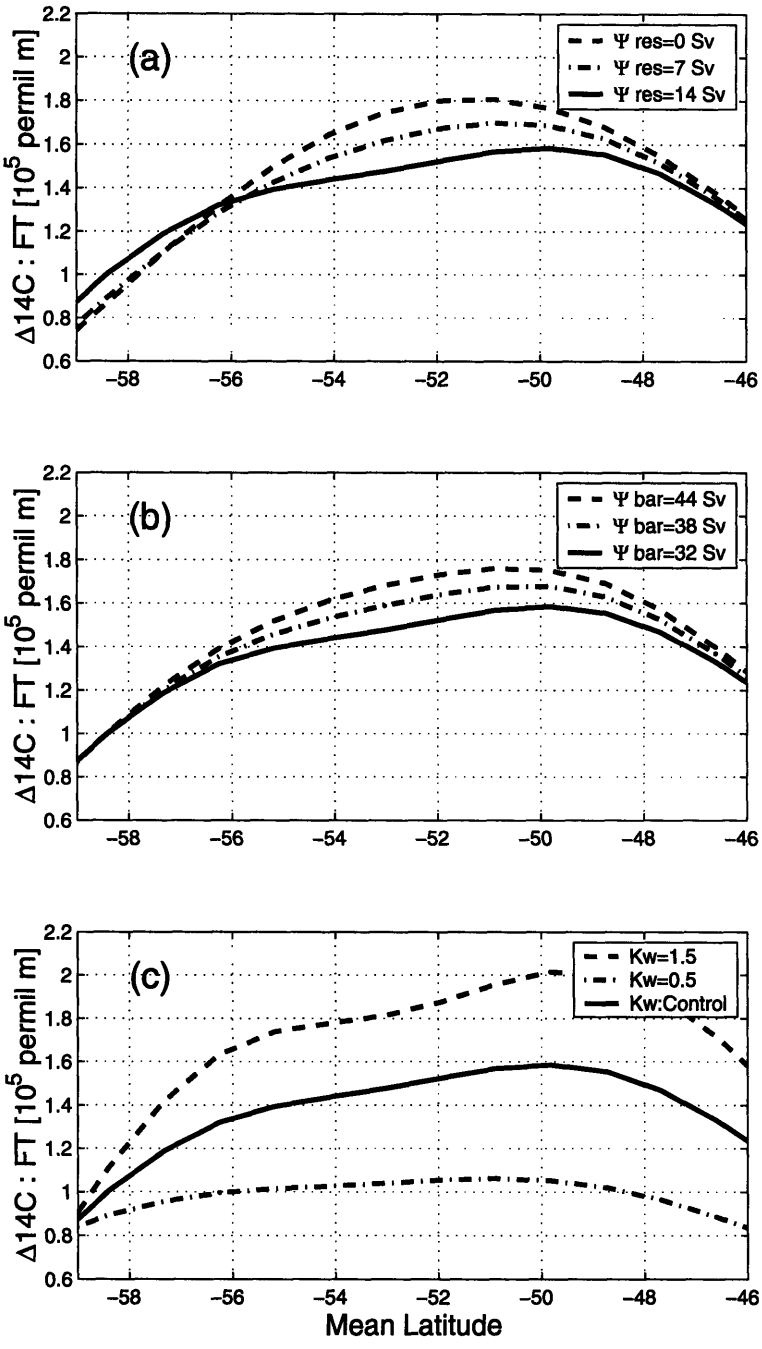

Figure 2-24: Cumulative uptake of bomb-$\Delta^{14}C$ between 1950 and 1990. Three panels are for the sensitivities to Ψ_{res} (a), $\overline{\Psi}$ (b) and K_W (c). The uptake has units of $[permil\, m]$, and is plotted as a function of mean latitude. Solid lines represent the control run.

is slightly increased due to enhanced isopycnal eddy diffusivity. However, the gross magnitudes and spatial patterns are strongly controlled by the meridional profile of gas transfer velocities, K_W (Fig. 2-24(c)) and the sensitivity of modeled uptake is greater when the gas transfer coefficient is small. In summary, the modeled oceanic uptake of bomb-Δ^{14}C is most sensitive to the gas transfer coefficient, even though its regional distribution is sensitive to the residual flow. This is consistent with the simple scalings for the slow gas transfer regime.

2.6 Anthropogenic CO_2

In the previous section we examined the fast- and slow-gas exchange limits which are appropriate for CFC11 and bomb-Δ^{14}C respectively. Of special interest, however, is the role of the Southern Ocean in the uptake of anthropogenic CO_2. The timescale for air-sea equilibration of CO_2 is on the order of one year, and so falls between the limit cases. Fig. 2-25 shows the distribution of anthropogenic CO_2 in the 1990's from the streamline-averaged model and as derived from WOCE-era ocean observations. The observational estimate is from the Indian sector (90°E) of the gridded data of the Global Ocean Data Analysis Project using the ΔC^* method of Sabine et al. (1999). There is a correspondence between the simulated and observed distributions in the streamline coordinate: in both cases the distribution lies somewhat between that of CFC11 and bomb-Δ^{14}C, as might be expected.

Fig. 2-26 shows the meridional distribution of the cumulative oceanic uptake of anthropogenic CO_2 in the model and its sensitivity to changes in physical forcing. It is sensitive to all of the physical parameters discussed here: buoyancy forcing (determining residual flow), wind-stress forcing (determining eddy transfers) and air-sea gas transfer coefficient. Anthropogenic CO_2 has characteristics of both CFC11 and bomb-Δ^{14}C since its gas exchange timescale lies somewhat between the two extreme cases. The gas transfer timescale for CO_2 is comparable to the timescale of physical transport and so scaling suggests that the leading order balance must include both influences.

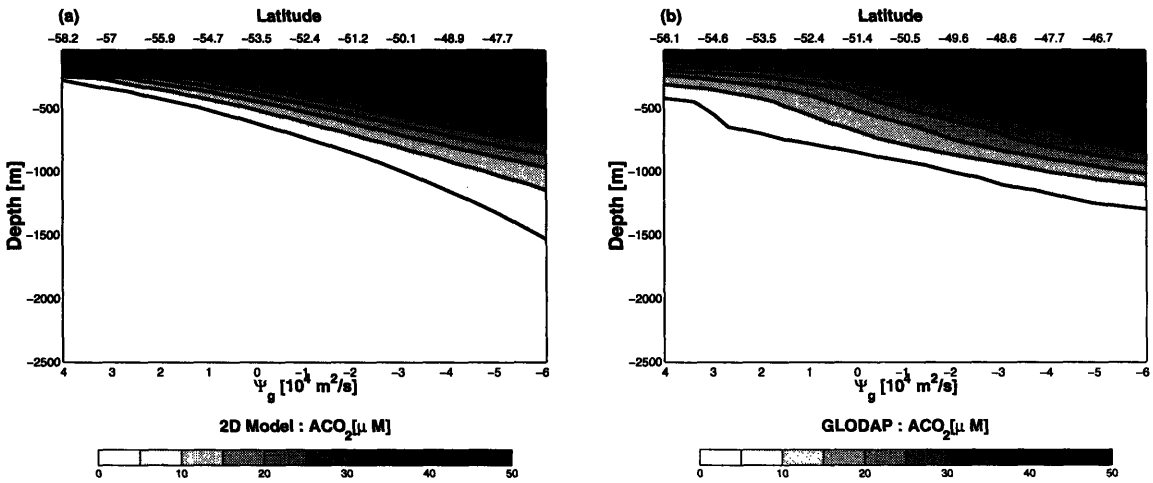

Figure 2-25: Modeled and observationally-derived fields of anthropogenic CO_2. (a): the simulated distribution using the 2D model. (b): the observationally-derived distribution calculated by Sabine et al. (1999). The observational data is obtained from Global Ocean Data Analysis Project, and the plot (b) is reproduced with a permission.

There are two peaks in the modeled uptake of anthropogenic CO_2, around 58°S and 48°S in the control run, reminiscent of CFC11 (compare Figs. 2-23 and 2-26). What controls the pattern of the modeled oceanic uptake? The peak to the south of the ACC is due to upwelling of deep, uncontaminated water. The peak to the north of the ACC is due to enhanced isopycnal stirring, keeping surface concentrations low, and a stronger gas transfer coefficient there. Using simple theory and scaling analysis, we will illustrate two regimes of modeled cumulative uptake which are reflected in the regional model.

First, to the south of the ACC (around 58°S), there is large scale upwelling as shown in Fig. 2-9. The upwelling deep waters are essentially free of anthropogenic CO_2, driving surface partial pressures down. We hypothesize that the entrainment term is likely to control the air-sea flux in that region and consider a local balance between entrainment and air-sea fluxes. The upwelling waters are depleted in transient tracers ($C_{th} \ll C$) so a simple expression describes the local uptake:

$$\frac{w_{res}}{h} C \sim -\lambda (C - C_{at}) \tag{2.17}$$

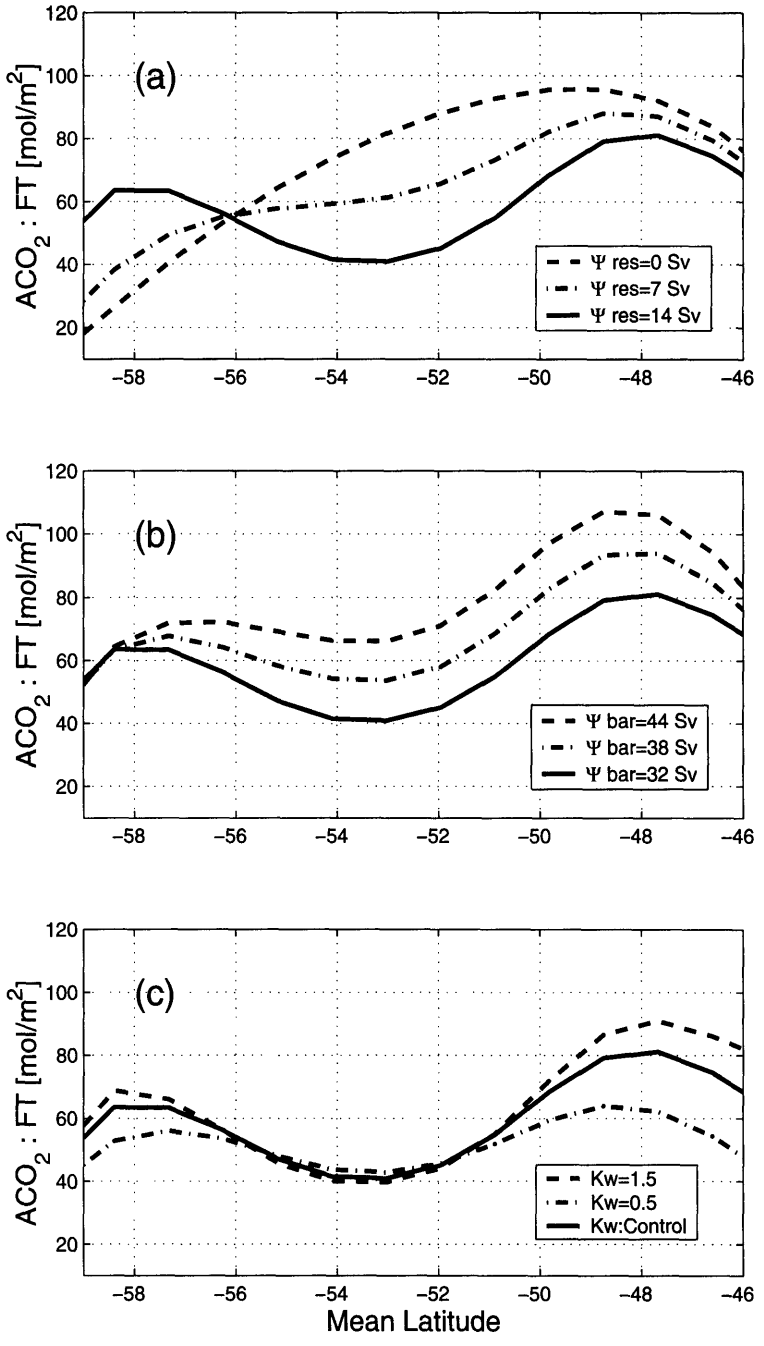

Figure 2-26: Cumulative uptake of anthropogenic CO_2 between 1765 and 1990. Three panels are for the sensitivities to Ψ_{res} (a), $\overline{\Psi}$ (b) and K_W (c). The unit of CO_2 flux is in $[mol/m^2]$, and is plotted as a function of mean latitude. Solid lines represent the control run.

We define a non-dimensional parameter, $W \equiv \frac{w_{res}}{h\lambda}$ which represents the competition between the rate of large scale upwelling and the rate of gas transfer. Solving for C and for the uptake, $F = -\lambda h\,(C - C_{at})$, we find

$$C \sim C_{at}(1+W)^{-1}, \tag{2.18}$$

$$F \sim \lambda h C_{at}\left(\frac{W}{1+W}\right) \tag{2.19}$$

The relationships for anthropogenic CO_2 fall between the limit cases of CFC11 and bomb-$\Delta^{14}C$. In the fast gas exchange limit, $W \ll 1$, eq.(2.18) and (2.19) become identical to (2.11) and (2.13). Similarly, in the slow gas exchange limit, $W \gg 1$, eq.(2.19) becomes identical to (2.16). The concentration and uptake of anthropogenic CO_2 depend on the balance between the upwelling rate and the gas transfer coefficient. To the south of the ACC the uptake rate is thus closely related to Ψ_{res}, as illustrated by the sensitivity experiments in Fig. 2-23(a). A 50% decrease in Ψ_{res} leads to a 40% decrease in the cumulative uptake, consistent with (2.19) when $W \sim 0.3$. Fig. 2-25 shows that the surface concentration to the south of the ACC is indeed low, partly due to the large scale upwelling of deep waters with low anthropogenic CO_2 concentration there. However, the latitudinal variation of the Buffer factor also contributes to the low anthropogenic CO_2 concentration in this region. The effective solubility of anthropogenic CO_2 depends on both solubility of CO_2 and the Buffer factor, reflecting the seawater carbonate chemistry. The net effect of these influences is an increase in effective solubility of anthropogenic CO_2 with temperature. Thus, warmer water has greater CO_2 uptake capacity at a given rate of atmospheric pCO_2 increase.

A second anthropogenic CO_2 peak emerges to the north of the ACC at around 48°S where eddy transfers are vigorous. Here we can identify a second regime in which there is a local balance between isopycnal stirring and air-sea fluxes:

$$\frac{Ks_\rho}{h}\left(\frac{\partial C}{\partial y}\right)_{\rho,-h} \sim -\lambda(C - C_{at}) \tag{2.20}$$

Caldeira and Duffy (2000) simulated anthropogenic CO_2 uptake in the Southern Ocean using a general circulation model, and described the northward isopycnal stirring of CO_2 as indicated by (2.20). Using (2.5) and (2.6) to relate eddy-induced flow and isopycnic eddy diffusivity, we define a non-dimensional parameter, $D \equiv \frac{\Psi_{eddy}}{\lambda h L}$, which represents the competition between the rate of isopycnal stirring and the rate of gas transfer. We solve for C and the uptake, $F = -\lambda h (C - C_{at})$:

$$C \sim C_{at}(1+D)^{-1}, \tag{2.21}$$

$$F \sim \lambda h C_{at} \left(\frac{D}{1+D}\right) \tag{2.22}$$

These relationships are in a form similar to (2.18) and (2.19), except here D is controlled by Ψ_{eddy} and not Ψ_{res}. Again, these relationships become identical to the solutions for uptake of CFC11 and bomb-$\Delta^{14}C$ in the fast and slow gas exchange limits respectively. The rate of uptake is controlled by the competition between the rate of gas transfer and Ψ_{eddy}. Fig. 2-26(b) shows that the modeled, overall magnitude of the cumulative uptake does indeed increase with stronger wind stress (which leads to stronger eddy transfers if buoyancy distribution and fluxes are held constant). Contrast this with Fig. 2-26(a), in which the cumulative uptake decreases with stronger buoyancy flux.

The cumulative uptake of anthropogenic CO_2 increases with faster gas transfer coefficient, but the sensitivity is not uniform in space. The regions of strong uptake around 58°S and 48°S are sensitive to the gas transfer coefficient while other regions are not (Fig. 2-26c). This is consistent with (2.19) and (2.22) which suggest that the cumulative uptake in these peak regions should increase with faster gas transfer coefficient. At high values of gas transfer coefficient, sensitivity decreases since surface waters move closer to saturation and the system shifts to the fast gas exchange limit.

The uptake of anthropogenic CO_2 is sensitive to both the parameterization of the gas transfer coefficient and the climatological distribution of buoyancy fluxes which determines the residual flow. Hence the uncertainty in the modeled uptake of anthropogenic CO_2 is greater than that of CFC11 and bomb-$\Delta^{14}C$, which represent limit

cases which are insensitive to gas transfer coefficient and buoyancy fluxes (residual flow) respectively. The differences between published climatologies (Fig. 2-8) suggest that the major sources of uncertainty lies in the buoyancy fluxes (> 50%) and residual flow, with smaller differences between wind climatologies and hence the gas transfer coefficient ($\sim$ 10%). If we simply assume that these uncertainties in the forcing linearly project onto the uptake, we expect an uncertainty in modeled uptake of anthropogenic CO_2 on the order of 60%, simply because of uncertainties in the surface physical forcing data sets.

In a comparison of modeled uptake of anthropogenic CO_2 using several general circulation models Orr et al. (2001) find model-to-model differences on the order of 70% in the Southern Ocean. In that study (OCMIP), a consistent profile of the gas transfer coefficient was used by all models, but the buoyancy forcing and parameterization of subgrid-scale eddies differ between the models. Our analysis suggests that much of the model-to-model difference in the Southern Ocean CO_2 fluxes in the OCMIP models could simply be attributable to the choice of surface boundary conditions for buoyancy and the resulting differences in Ψ_{res} in the models which use Gent and McWilliams (1990) type eddy transfer parameterizations. Those models, which do not explicitly account for eddy-induced advection, might be expected to have introduced an uncertainty of O(1) in Ψ_{res} in the Southern Ocean where eddy-induced flow plays a dominant role.

In Fig. 2-26, the cumulative uptake of anthropogenic CO_2 south of 56°S increases with stronger buoyancy fluxes, but it decreases to the north indicating that the net CO_2 uptake has only a weak dependence on the buoyancy fluxes despite strong regional sensitivities. The spatially integrated cumulative uptake (between 60°S and 46°S) is 27.8 PgC in the control run, increasing by less than 10% when Ψ_{res} is reduced by 50%, although the spatial patterns of the uptake are very different (Fig. 2-26a). This is due to a partial compensation between advection and eddy stirring. The diffusive transport is reduced when the residual circulation is intense, and vice versa, because the isopycnal tracer gradient decreases with stronger residual flow. Overall, the net uptake is smaller with greater Ψ_{res}, as suggested by (2.22).

2.7 Summary and Discussion

We have developed simple scalings which relate the Southern Ocean uptake of transient tracers to the physical forcing. The scalings are rooted in residual mean theory and a streamline-averaged view of the ACC. We have considered the influence of surface buoyancy fluxes, wind stress, and gas transfer coefficient on three transient tracers; namely CFC11, bomb-$\Delta^{14}C$ and anthropogenic CO_2. In addition to scaling arguments, we have developed an explicit two-dimensional (streamline-averaged) numerical model of the meridional tracer transport in the vicinity of the ACC, again rooted in residual mean theory. We use the numerical model to test the simple scalings and to perform sensitivity studies illustrating the uncertainties in modeled ocean tracer uptake due to uncertainties in forcing data sets.

The relationships of ocean tracer distributions and oceanic uptake to the physical forcing are sensitive to the timescale of air-sea gas exchange. There is a large separation in the respective gas exchange timescales of CFC11 and bomb-$\Delta^{14}C$, so they have very different sensitivities to the three physical parameters.

2.7.1 Tracer distributions

Since CFC11 equilibrates rapidly, its surface distribution reflects solubility and atmospheric partial pressure but is not significantly impacted by the residual flow or isopycnal mixing. Bomb-$\Delta^{14}C$ equilibrates slowly and the surface distribution reflects the upwelling of uncontaminated deep waters and the accumulation of tracer in the northward flowing residual circulation. Hence the contrasting gradients of CFC11 and bomb-$\Delta^{14}C$ in the surface Southern Ocean reflect the strength of the residual flow, which cannot be directly observed. It also provides a useful diagnostic by which the strength of the residual flow in numerical models may be compared. In the thermocline, however, both tracers simply reflect advection and mixing down from the surface. The ability of the streamline-averaged model to qualitatively reproduce observed features provides support for the application of the residual mean theoretical approach.

2.7.2 Ocean uptake

The behavior of CFC11 is well represented by the fast gas exchange limit in the mixed layer tracer balance. The oceanic uptake of CFC11 largely reflects upper ocean transport processes (illustrated in Fig.10). The spatial pattern of the cumulative air-sea flux is sensitive to the strength of the residual flow which controls the rate at which deep, uncontaminated waters are supplied to the surface. The residual flow is, in turn, controlled by the pattern of air-sea buoyancy fluxes since the heat budget and water mass transformation rates must be consistent. Isopycnal eddy transfer also plays a significant role in promoting uptake of CFC11 by keeping surface water partial pressures low. The vigor of eddy stirring is largely controlled by the surface wind-stress, since eddy activity must, to zero-order, counteract the wind-driven Deacon Cell. In contrast, bomb-Δ^{14}C reflects a slow gas exchange limit. As a consequence the uptake of bomb-Δ^{14}C is mainly controlled by the gas transfer coefficient (illustrated in Fig.11). The pattern of uptake fundamentally depends on the profile of surface wind speed. Variations in isopycnal eddy diffusivity and residual flow can also impact the uptake of bomb-Δ^{14}C, but their effects are somewhat moderate.

In this idealized model, while the spatial pattern of the cumulative uptake of CFC11 and anthropogenic CO_2 are highly sensitive to residual flow, Ψ_{res}, the spatially integrated uptake is not. It has been noted that the uptake of anthropogenic CO_2 in the three-dimensional, general circulation and biogeochemistry models of the OCMIP study, show considerable variations in spatial pattern in the Southern Ocean (Orr et al. 2001), and yet, the simulated global uptake from those models agrees relatively well (to within 20%). We suggest that model-to-model differences in the spatial patterns of the anthropogenic CO_2 uptake is likely due to the differences in the representation of Ψ_{res} (in those models with GM90-type eddy transfer parameterizations).

2.7.3 Residual mean circulation

The uptake and transport of tracers are sensitive to the water mass transformations and residual mean flow, Ψ_{res}, and observed transient tracer distribution reflects the pattern and the magnitude of the residual flow. Thus these tracers can be used to constrain the magnitude of Ψ_{res} and evaluate the simulated physical transport of numerical models.

Residual mean flow in the surface layer must also be consistent with surface buoyancy distribution and buoyancy fluxes (Marshall, 1997). However, climatological buoyancy fluxes in the Southern Ocean presently have large uncertainties, witnessed by the variations between data climatologies (Fig. 2-8). Hence, even if the buoyancy fluxes are imposed in numerical ocean models, this uncertainty is reflected in the modeled tracer uptake. Our sensitivity studies suggest that this factor alone is sufficient to explain much the model-to-model difference in southern ocean anthropogenic CO_2 uptake in the OCMIP models. (Though this may be a significant factor, we do not suggest that it is the only one - the OCMIP models differ greatly in choice of sub-grid scale eddy transfer parameterizations and physical boundary conditions at the surface).

In this study we applied spatially varying isopycnal eddy transfer coefficients, following Visbeck et al. (1997), in contrast to most current general circulation and biogeochemistry models, in which spatially homogeneous isopycnal mixing coefficients are assumed. If the diffusivity is assumed to be constant, the isopycnal slope is linearly related to the wind stress. The isopycnal eddy flux at the base of the mixed layer in (2.9) scales with the product of the isopycnal slope and the eddy diffusivity, and so the diffusive transport responds linearly to the wind stress. It is coincidental that the isopycnal eddy flux has linear dependence on the wind stress for both cases: eddy parameterization based on uniform diffusivity and that based on spatially varying diffusivity of Visbeck et al.(1997) results in the same linear sensitivity of tracer uptake to the wind stress.

Thus far, we have treated surface wind stress and gas transfer coefficients as

independent variables in order to illustrate model sensitivities in a transparent way. In reality, both depend on the wind speed at the sea surface, and are not independent. A stronger surface wind will enhance both the uptake of CFC11 and that of bomb-$\Delta^{14}C$. However, different processes control the increase in uptake of these two tracers. The uptake of CFC11 is enhanced by the increase in isopycnal eddy diffusion and the uptake of bomb-$\Delta^{14}C$ increases because of the greater gas transfer velocities. For anthropogenic CO_2, both isopycnal diffusivity and gas transfer velocities will enhance uptake, since its intermediate equilibration timescale make it sensitive to both effects.

The models and scalings presented here are deliberately idealized and simplified to provide clearer insights. However, this leads to the omission of some processes which are also significant in the region. Notably the polar regions of the Southern Ocean are partially ice covered, affecting buoyancy and tracer fluxes. Also there are regions of significant deep water formation also affecting the regional uptake of tracers by the ocean. These processes are certainly worthy of closer study and are omitted here to focus on processes associated with upwelling regions and the formation of intermediate and mode waters.

In brief, we have applied residual mean theory to develop scalings and idealized numerical models of the uptake of transient tracers in the Southern Oceans. The streamline-averaged numerical model captures the observed distributions of CFC11, bomb-$\Delta^{14}C$ and anthropogenic CO_2 and their relationships to one another, suggesting that there is a residual overturning flow of about 11 Sv in the Southern Ocean. Sensitivity studies with the model suggest that the uncertainties in air-sea buoyancy fluxes in current climatologies impose significant uncertainty in estimates of Southern Ocean uptake of anthropogenic CO_2 from current circulation and biogeochemistry models which are driven by, or seek to be consistent with, the climatological fluxes.

Chapter 3

The Antarctic Circumpolar Productivity Belt

3.1 Introduction

The Southern Ocean is characterized by high surface macro-nutrient concentrations as shown in Fig.1-13 and 1-14, indicating that the biological productivity is not limited by those macro-nutrients. Hence the availability of iron may play important roles in limiting biological productivity in the region. Lateral gradient of macro-nutrient is coupled to the Southern Ocean fronts. The concentration of silicic acid changes sharply across the Polar Front ($\sim$ 55S) while the concentration of phosphate remains unchanged. Phosphate concentration sharply decreases near the Subantarctic Front ($\sim$ 50S).

A series of ship-based survey, which are carried out during Antarctic Environment and Southern Ocean Process Study (AESOPS) of US Joint Global Ocean Flux Study (JGOFS), revealed complex structures of the biological uptake and the export in the Southern Ocean (Honjo et al., 2000; Buesseler et al., 2002). Seasonal variations of the sinking particulate flux have been observed, and the yearly maximum of the sinking flux occurs in the austral summer reflecting the seasonal bloom of phytoplankton. Elemental composition of sinking particulate flux changes meridionally across the ACC reflecting the community structure. Diatoms are phytoplankton which uses silica to

build cell walls, whereas cocolithophores, a typical nano-phytoplankton, uses calcium carbonate for the structural material. Intense diatom blooms are observed near the Polar Front during spring and summer accompanied with large silica export. To the south of the ACC, the sinking flux contains more silica relative to calcium carbonate reflecting diatom-dominated community structure. To the north of the ACC, sinking particulate flux contains less silica relative to calcium carbonate reflecting the chemical composition of shells from the nano- and pico-phytoplankton dominated community.

The spatial structure of the biological productivity in the Southern Ocean can be characterized as the "Antarctic Circumpolar Productivity Belt", a figurative term describing the zonal belt of high biological productivity in the Southern Ocean (Schlitzer, 2002). This pattern of export production is identified by ship-based observations (Honjo et al., 2000; Buesseler et al., 2002), satellite-based observations (Moore and Abbott, 2000) and inverse calculations (Schlitzer, 2002). Fig.3-1 shows the distributions of organic export in Southern Ocean based on an inverse calculation fitting modeled tracer distribution to climatology. Moore and Abbott (2000) examined the ocean color data from SeaWifs and suggest that enhanced primary production are coupled to the Southern Ocean fronts. Ship-based observations of export production are qualitatively consistent with the satellite data, where enhanced export production is found near the Polar Front (Honjo et al., 2000; Buesseler et al., 2002). The magnitude of the observed sinking particulate flux in sediment traps significantly varies over the latitudes of the ACC. The maximum of the silica export is located on the southern flank of the ACC near the Polar Front. The organic export has a broader peak, and its magnitude is greater than the global mean by a factor of two (Honjo et al., 2000). These observations motivate following questions.

- What is the significance of iron limitation in controlling the biological productivity and the observed macro-nutrient fronts?

- What sets the position and the magnitude of the Antarctic Circumpolar Productivity Belt?

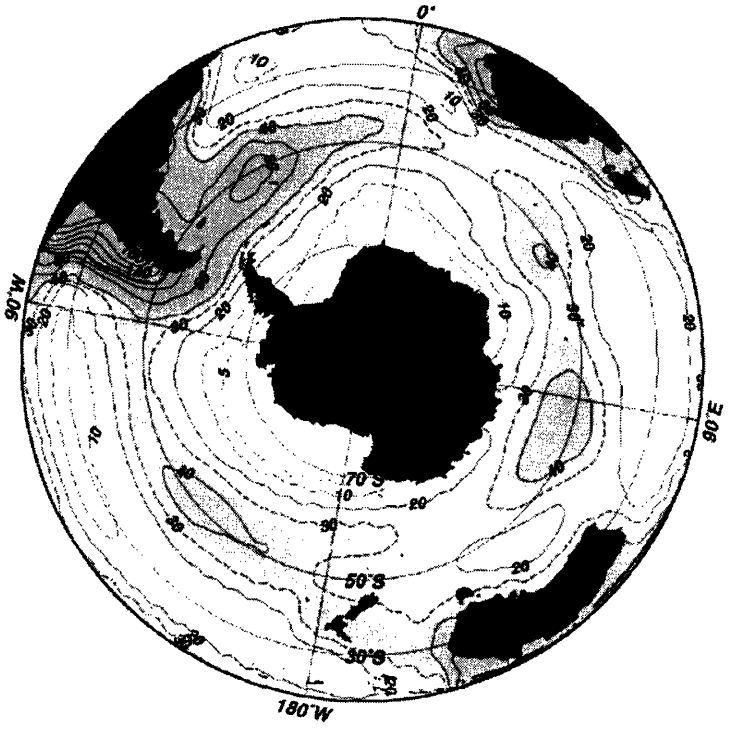

Figure 3-1: Annually averaged organic export. The data is derived from an inverse calculation fitting modeled, large-scale tracer distribution to climatology. The data is taken from Schlitzer (2000). Organic export is in units of gC m^{-2} yr^{-1}.

- Can we develop a conceptual framework for understanding physical and biogeochemical controls on the Antarctic Circumpolar Productivity Belt?

While observational grounds for describing the biogeochemistry of the Southern Ocean are growing, the mechanisms which determine the structure of biological productivity are not yet well understood. In this chapter, I empirically determine the meridional structure of the export production (i.e. sinking particulate flux) using an inverse method, and illustrate mechanisms which control the pattern using a physical-biogeochemical model.

In section 3.2, I apply the simple 2D tracer model developed in chapter 2 in combination with simple biogeochemical parameterizations to estimate the export production in the Southern Ocean. I take an inverse approach where the model is brought into consistency with the observed, streamline-averaged macro-nutrient fields based on the World Ocean Atlas 2001 (Conkright et al., 2002). Export of biogenic silica is inferred from the method of least squares. It reproduces a meridional profile of export production qualitatively similar to the observations.

In section 3.3 I examine a coupled physical-biogeochemical model of the circulation and biogeochemistry of the Southern Ocean, and develop a conceptual framework for understanding what controls the magnitude and the spatial pattern of the biological productivity there. There have been major advances in such biogeochemical models, including increased complexity of ecosystem models and the addition of explicit iron cycle (Archer and Johnson, 2000; Lefevre and Watson, 1999; Parekh et al., 2004a; Parekh et al., 2004b). I use the MITgcm configured for the global ocean with a coarse resolution with NPZD ecosystem component and phosphorus, silica, and iron cycles. We develop a simple theoretical framework for understanding the structure of the biogeochemistry using a diagnostic tracer, Fe*, and suggest that the maximum in the biological productivity emerges at the regime transition from iron-limited Antarctic zone to the macro-nutrient limited Subantarctic zone. In Section 3.4, we discuss implications to the physical-biogeochemical interactions in the Southern Ocean and conclude.

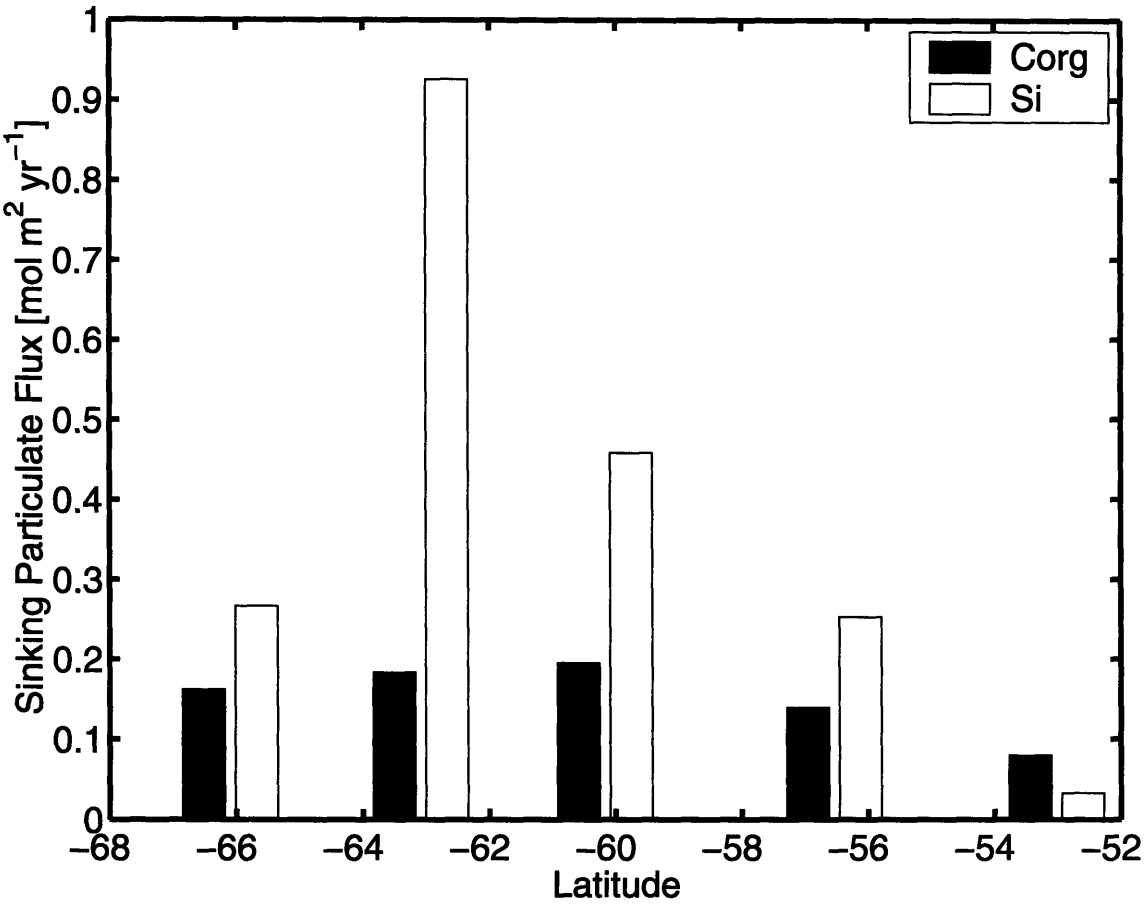

Figure 3-2: Observed sinking particulate flux of organic carbon and biogenic silica at the depth of $\sim$ 1000m. The data is based on the mooring deployed in the Pacific sector of the ACC during 1996 and 1998 (Honjo et al., 2000).

3.2 Estimating export production with inverse methods

In this section I empirically determine the export of biogenic silica using an idealized, zonally-averaged tracer model developed in chapter 2. The tracer transport model is applied to the transport of silicic acid to infer the rates of silica export and remineralization. The new aspect of this study is the combination of the matrix formulation of the tracer transport (Khatiwala et al., 2004) and the method of least squares. From a mathematical perspective, the meridional profile of silica export is treated as independent model variables, which are adjusted to minimize the cost function, a quadratic measure of the misfit between the observations and the model fields. See chapter 3 of (Wunsch, 1996), for a review of the subject. The resulting optimal solutions are used to explore the relationship between the residual mean circulation and the cycling of nutrients in the Southern ocean.

Typically "export production" refers to sinking particulate flux which is vertically transported out of the euphotic layer and remineralize within the interior ocean. Silica export has been diagnostically estimated with ocean circulation models by bringing the modeled surface nutrients toward climatology through a Newtonian relaxation term in the surface layers (hereafter, this method is referred as the Newtonian relaxation method) (Gnanadesikan, 1999). This method was first developed by Najjar (1990) for organic export and has been widely used including OCMIP-2. Due to its simplicity, several empirical constants are required for this approach. For example, the timescale for the Newtonian relaxation is typically set on the order of 30 days, which has little physical and biogeochemical basis.

The dissolution rates of biogenic silica increases with temperature which affects the vertical, e-folding scale of sinking particulate flux of silica. A temperature-dependent dissolution scheme has been used to calculate remineralization in the interior ocean in (Gnanadesikan, 1999), where the vertical length scale of particulate silica flux varies from 200m in the tropical waters to 5000m in the polar waters. In this study, the vertical profile of particulate silica flux, F_{Si}, is parameterized using a power function

following (Martin et al., 1987).

$$F_{\mathrm{Si}}(z) = F_{\mathrm{Si},z_m}\left(\frac{z}{z_m}\right)^{-\beta} \qquad (z < z_m) \tag{3.1}$$

where z_m is the depth of the euphotic layer which is prescribed to 225m, and β sets the vertical length scale of the remineralization. In section 3.2.2, β is set to a uniform constant of 0.15 which corresponds to the vertical length scale of $\sim$ 5000m. Then, in section 3.2.5, the meridional profile of β is allowed to vary. F_{Si,z_m} is the magnitude of particulate silica flux at the base of the euphotic layer. In the euphotic layer, silicic acid is consumed at the rate of $F_{Si,z_m} z_m^{-1}$ representing the silica uptake and the production of sinking silica flux.

In the following sections, I develop a new approach to constrain an ocean biogeochemistry model using the method of least squares and to infer the rates of export production. The method allows us to estimate the magnitude and the spatial profile of β as well as F_{Si,z_m}, which was not possible with the Newtonian relaxation method. Furthermore this method can quantify uncertainties associated with the optimal solutions, and it is possible to include *a priori* estimates of the model variables. Observed particulate silica flux in sediment traps (shown in Fig.3-2) can also be used to constrain the model. The resulting solution can give insights into the role of the residual mean circulation in the supply of nutrients to the euphotic layer.

3.2.1 The matrix formulation of the biogeochemical model

First I consider the transport of silicic acid and constrain the export of biogenic silica using the simplest possible setting. The equation for the transport of silicic acid can be written as

$$\frac{\partial \mathrm{Si}}{\partial t} = \left(-v_{res}\frac{\partial}{\partial y} - w_{res}\frac{\partial}{\partial z} + \nabla\cdot\mathbf{K}\nabla\right)\mathrm{Si} - \frac{\partial F_{\mathrm{Si}}}{\partial z} \tag{3.2}$$

where F_{Si} is defined in eq.(3.1). For the residual mean circulation I use an idealized profile of Ψ_{res} shown in Fig.2-9. The model domain is limited to the ACC between 45S and 60S and between the surface and the depth of 3000 m. Open boundary conditions

are applied at the northern and southern boundary and the bottom. Here the tracer concentration is set to the annual-mean climatology. The transport equation (3.2) is discretized using 2nd order finite difference scheme and the model equation (3.2) is expressed in the matrix formulation introduced by (Khatiwala et al., 2004).

$$\frac{d\mathbf{x}}{dt} = \mathbf{A}_I\mathbf{x} + \mathbf{B}\mathbf{x}_b + \mathbf{b}_{bio} \tag{3.3}$$

The tracer field is represented as a vector, $\mathbf{x}$. Each element of $\mathbf{x}$ is the concentration of Si at the corresponding grid box. The physical transport is expressed as a square matrix, $\mathbf{A}_I$, representing the first term on the RHS of eq.(3.2). The biological (source - sink) term is represented as a vector, $\mathbf{b}_{bio}$. The boundary condition includes the boundary matrix, $\mathbf{B}$, and the boundary tracer vector, $\mathbf{x}_b$. It can be shown that $\mathbf{A}_I$ is full-rank and is invertible. Here we use the annually-averaged physical transport which does not vary in time. It is possible to calculate the steady state solution by inverting the transport matrix, $\mathbf{A}_I$. The steady state tracer distribution, $\mathbf{x}_S$, can be calculated as

$$\mathbf{x}_S = -\mathbf{A}_I{}^{-1}(\mathbf{B}\mathbf{x}_b + \mathbf{b}_{bio}) \tag{3.4}$$

The biological (source - sink) vector consists of the convergence of the particulate flux parameterized following eq.(3.1), which is a linear function of the silica export, F_{Si,z_m}. Then $\mathbf{b}_{bio}$ can be defined as $\mathbf{b}_{bio} = \mathbf{E}\mathbf{p}$. Each element of $\mathbf{p}$ consists of silica export, F_{Si,z_m}, at corresponding latitudes. $\mathbf{E}$ maps $\mathbf{p}$ onto the biological (source - sink) vector, $\mathbf{b}_{bio}$, taking into account the vertical derivative of sinking silica flux.

$$\mathbf{p}_j = F_{\mathrm{Si},z_m} \tag{3.5}$$

$$\mathbf{E}_{ij} = \begin{cases} 0 & (y_i \neq y_j) \\ -\frac{1}{z_{k+1}-z_k}\left[\left(\frac{z_{k+1}}{z_m}\right)^{-\beta} - \left(\frac{z_k}{z_m}\right)^{-\beta}\right] & (y_i = y_j) \end{cases} \tag{3.6}$$

where F_{Si,z_m} is the sinking particulate flux of silica at the base of the euphotic layer, z_m. j is the index for latitude grid and k is the index for depth. i describes the mapping between the two dimensional grid (j,k) to the column vector (i). Note that

$\mathbf{E}$ depends on β which is assumed to be a uniform constant for here. Mathematically, eq.(3.4) can be re-written as

$$\mathbf{x}_S = \mathbf{M}\mathbf{p} + \mathbf{x}_0 \tag{3.7}$$

where $\mathbf{x}_0 = -\mathbf{A}_I{}^{-1}\mathbf{B}\mathbf{x}_b$ and $\mathbf{M} = -\mathbf{A}_I{}^{-1}\mathbf{E}$. The second term, $\mathbf{x}_0$, is completely determined by the physical transport and the boundary condition and represents the distribution of silicic acid in the limit of vanishing biological export.

3.2.2 The least squares problem

Here I infer the silica export vector $\mathbf{p}$ by fitting $\mathbf{x}_S$ to $\mathbf{x}_{obs}$. Here the "observation", $\mathbf{x}_{obs}$, is the annually and zonally averaged silicic acid distribution based on the World Ocean Atlas 2001 (Conkright et al., 2002). I define the cost function, J_{obs}, which is a quadratic measure of the model-data misfit.

$$J_{obs} = \frac{1}{2}(\mathbf{x}_S - \mathbf{x}_{obs})^T\mathbf{W}(\mathbf{x}_S - \mathbf{x}_{obs}) \tag{3.8}$$

where $\mathbf{W}$ is the weight matrix for the differences between the observation, $\mathbf{x}_{obs}$, and its model counterparts, $\mathbf{x}_S$. Here $\mathbf{W}$ is defined as a diagonal matrix with each element with the magnitude of $(\mathrm{N}\ \mathrm{Si}_0^2)^{-1}$ where Si_0^2 is set to 10 $\mu\mathrm{M}^2$ representing a typical magnitude of the variance for the silicic acid distribution in the Southern Ocean. N is the total number of grid points of the model. We seek for the optimal solution of the export of biogenic silica, F_{Si,z_m}, through minimizing the cost function.

The cost function, J_{obs}, can be rewritten using the steady state solution shown in eq.(3.7). Furthermore, *a priori* estimate of silica export, $\mathbf{p}_0$, can also be included in the total cost function, J.

$$\begin{aligned} J_{obs} &= \frac{1}{2}(\mathbf{M}\mathbf{p} + \mathbf{x}_0 - \mathbf{x}_{obs})^T\mathbf{W}(\mathbf{M}\mathbf{p} + \mathbf{x}_0 - \mathbf{x}_{obs}) \\ J_{prior} &= \frac{1}{2}(\mathbf{p} - \mathbf{p}_0)^T\mathbf{W}_p(\mathbf{p} - \mathbf{p}_0) \\ J &= J_{obs} + J_{prior} \end{aligned} \tag{3.9}$$

The total cost function is the sum of two components; J_{obs} and J_{prior}. J_{obs} measures the magnitude of the model-data misfit, and J_{prior} measures the magnitude of the differences between the best-fit silica export and its *a priori* estimate. $\mathbf{W}_p$ is the weight matrix for the misfit between the best-fit values for $\mathbf{p}$ and its *a priori* estimate $\mathbf{p}_0$.

Here I use $\mathbf{p}_0$ based on the sediment trap data plotted in Fig.3-2 in which there are five data points across the latitude band of the ACC at the depth of $\sim$ 1000 m. The data is interpolated onto the meridional grid points based on the streamline coordinate (the streamline coordinate is defined in chapter 2) to produce a smooth profile of $\mathbf{p}_0$. The magnitude of particulate silica flux is scaled with a factor of $10^{0.15}$ to represent the particulate flux at the depth of 100 m following eq.(3.1).

$\mathbf{W}_p$ is defined as a diagonal matrix with each diagonal elements set to $\alpha(\mathrm{L}\ \mathrm{p}_0^2)^{-1}$ where α is an arbitrary constant and p_0^2 is the variance of $\mathbf{p}_0$. L is the number of surface grid points of the model. The magnitude of α represents the confidence in $\mathbf{p}_0$ relative to the observations, $\mathbf{x}_{obs}$. For example, we could assume that the sediment trap data contain relatively large uncertainty ($\alpha \ll 1$) or relatively small uncertainty ($\alpha \gg 1$). Since the actual magnitude of the errors in the sediment trap data is not clear, we use a range of scaling factor, α, and explore the response of the resulting solutions.

The optimal solution is obtained by taking the stationary point of J with respect to $\mathbf{p}$.

$$\begin{aligned} \frac{\partial J}{\partial \mathbf{p}} &= \mathbf{M}^T\mathbf{W}(\mathbf{M}\mathbf{p} + \mathbf{x}_0 - \mathbf{x}_{obs}) + \mathbf{W}_p(\mathbf{p} - \mathbf{p}_0) = 0 \\ \mathbf{p} &= (\mathbf{M}^T\mathbf{W}\mathbf{M} + \mathbf{W}_p)^{-1}(\mathbf{M}^T\mathbf{W}(\mathbf{x}_{obs} - \mathbf{x}_0) + \mathbf{W}_p\mathbf{p}_0) \end{aligned} \tag{3.10}$$

In the limit case where one has little confidence in the *a priori* estimate ($\alpha \ll 1$), this solution leads to the classical least square problem ($\mathbf{W}_p = \mathbf{0}$). In another limit case where one has little confidence in the observations of the silica distribution, ($\alpha \gg 1$), the solution leads to $\mathbf{p} = \mathbf{p}_0$.

I calculated the optimal solution with varying α over a wide range from $\alpha =$

10^{-3} to 10^3. Fig.3-3 shows the optimal solutions for the export of biogenic silica, $\mathbf{p}$, with $\alpha = 10^{-3}$, 1, and 10^3 as determined by eq.(3.10). A detailed discussion on the significance of error bars can be found in section 3.2.4. The zero-order structure of the silica export is independent of the particular choice of α. All of the optimal solutions reveal the peak in the silica export in the southern flank of the ACC, which is a robust feature of the solution. This pattern is qualitatively consistent with the position of the "Antarctic Circumpolar Productivity Belt" inferred from remotely sensed chlorophyll data (Moore and Abbott, 2000) and direct observation of sinking particulate flux (Honjo et al., 2000; Buesseler et al., 2002). Detailed structures of the optimal silica export vary in response to changing α. When α is much smaller than 1, the optimal solution for $\mathbf{p}$ is completely determined by the constraints provided by the observed silicic acid distribution and the transport model. When α is much greater than 1, the optimal solution is dominated by *a priori* estimate, $\mathbf{p}_0$ as expected. When α is comparable to 1, the optimal silica export reflects the combination of the observed silica distribution and *a priori* estimate.

Fig.3-4 shows the best-fit estimates of the distribution of the silicic acid with $\alpha = 10^{-3}$, 1, and 10^3. The zero-order structure of the modeled silica distribution is independent of the particular choice of α. The distribution near the surface is most affected by changing the silica export. The distribution in the interior ocean is largely set by the physical transport including residual mean flow and eddy stirring which are oriented along isopycnals.

Fig.3-5 shows the two components of the cost function for the optimal solution over the wide range of α. When α is smaller than 1, the total cost function is dominated by the component due to the data-model misfit. When α is similar to 1, the magnitudes of J_{obs} and J_{prior} becomes similar to one another. When α is larger than 1, the total cost function is dominated again by the the component due to the data-model misfit. In this case the optimal solution is dominated by *a priori* estimate, $\mathbf{p}_0$, and J_{prior} becomes small even though it scales with α.

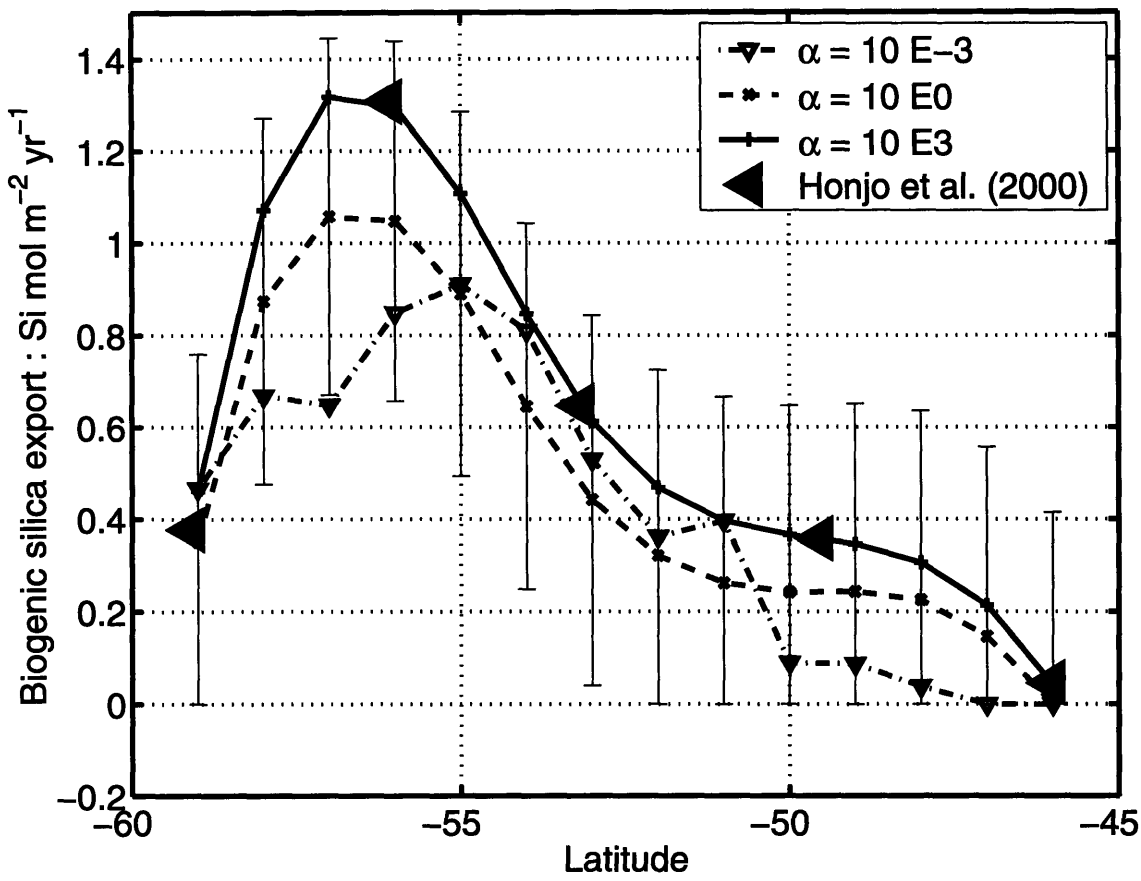

Figure 3-3: Optimal solutions for the export of biogenic silica evaluated at the depth of 100 m. Three solutions are presented with varying magnitudes of α. *A priori* estimates of silica export is calculated from the data provided by (Honjo et al., 2000). The magnitude of error bars are adjusted to prohibit negative solution since each element of $\mathbf{p}$ must be positive.

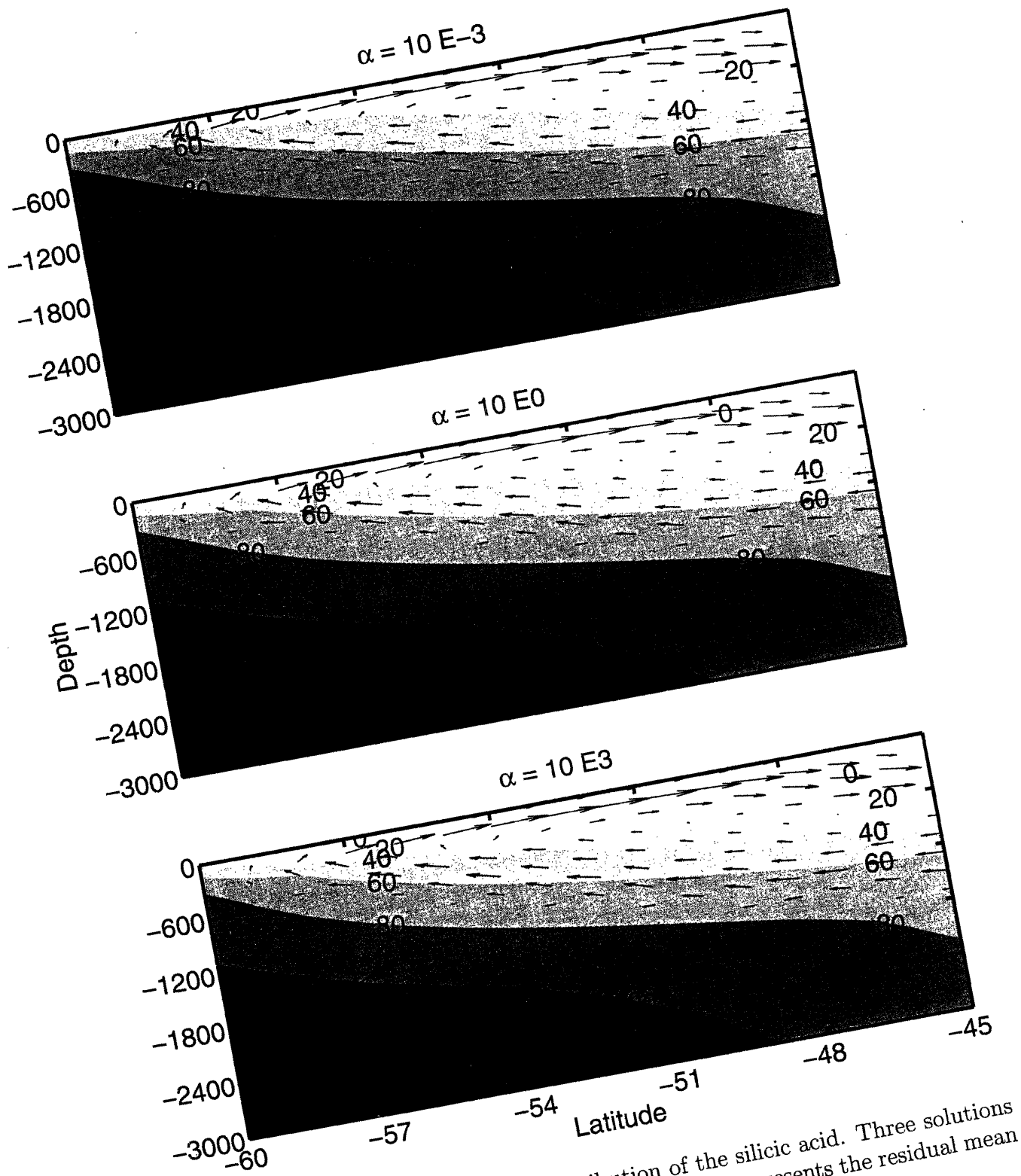

Figure 3-4: Optimal solutions for the distribution of the silicic acid. Three solutions are presented with varying magnitudes of α. Vector plot represents the residual mean circulation which are used in the tracer transport model.

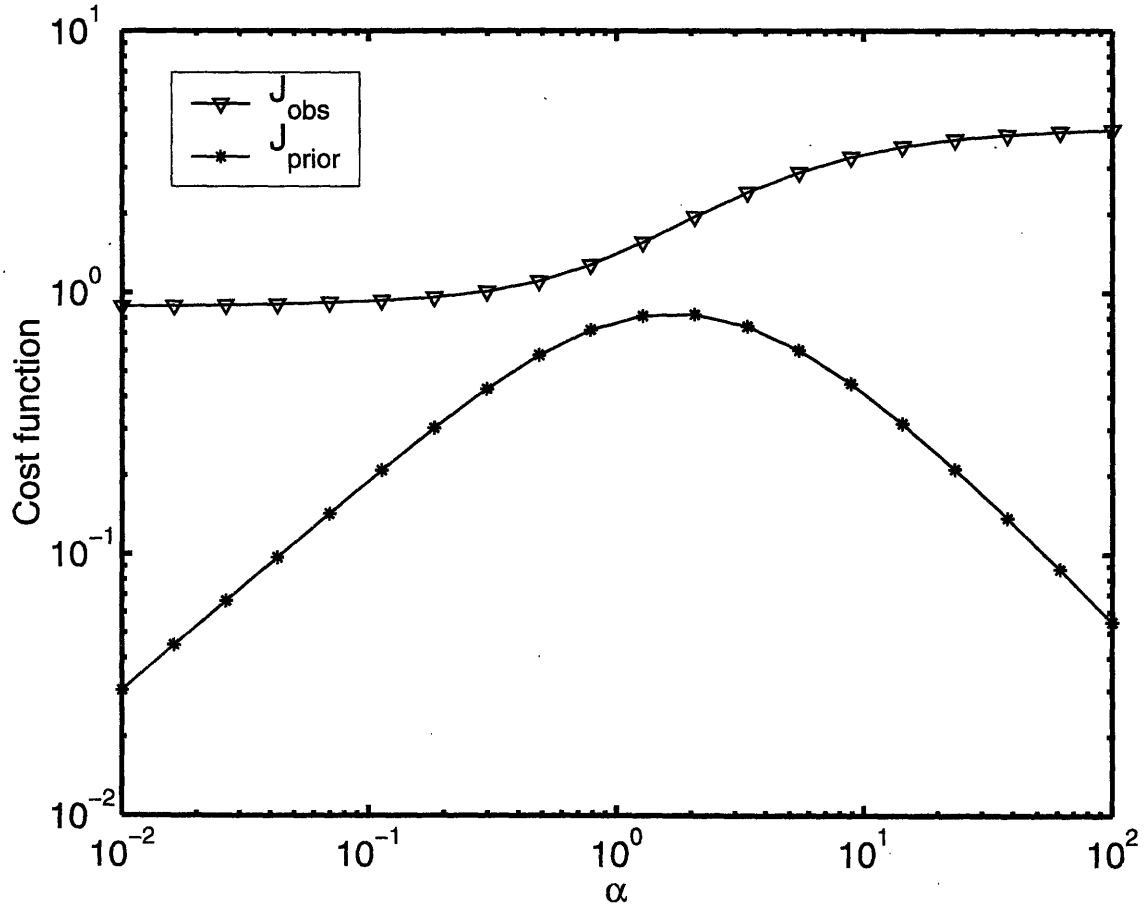

Figure 3-5: Variation of the magnitude of the two components of the cost function with varying α.

3.2.3 Physical and biogeochemical interpretations

I have empirically estimated silica export in the latitude band of the ACC using the method of least squares in the context of the zonally-averaged tracer transport model. The physical transport is based on the residual mean theory in which the mesoscale eddy fluxes plays critical role. No assumptions were made in terms of the mechanisms controlling the biological productivity. The spatial profile of silica export is simply adjusted to minimize the quadratic measure of the differences between the observed silicic acid distribution and its model counterpart. Thus the optimal solution does not directly provide mechanistic understanding of the processes controlling the biological productivity. It simply estimates the pattern of the silica export which is required to bring the model fields close to the observations.

The optimal solutions were examined and explored over a wide range of the weighting parameter. In all cases, the inferred silica export has its maximum on the southern flank of the ACC; a robust feature of the optimal solutions. The magnitude of the silica export is comparable to the sediment trap data of Honjo et al. (2000) within the range of estimated errors (which is discussed in section 3.2.4). A number of studies suggest that the biological productivity in the Southern Ocean is characterized with the circumpolar belt of high biological productivity, the "Antarctic Circumpolar Productivity Belt". The silica export calculated from the least squares method shows the significance of the productivity belt in the zonal average.

Diagnosis of the optimal solution allows us to examine the role of physical transport in the supply of silica to the euphotic layer. The transport model includes the advective fluxes due to residual mean circulation and the diffusive fluxes due to isopycnal eddy stirring. Fig.3-6 shows the separation of the silica tendency into advective component, $-J(\Psi_{res}, Si)$, and diffusive component, $\nabla \mathbf{K} \nabla Si$. Overall, advective tendency and diffusive tendency have similar magnitudes but the pattern of these tendency terms differ significantly. To the south of the ACC where the deep water upwells ($\sim$ 56S), the residual mean flow and the isopycnal eddy stirring are both important for the supply of silica for biological uptake. To the north of the

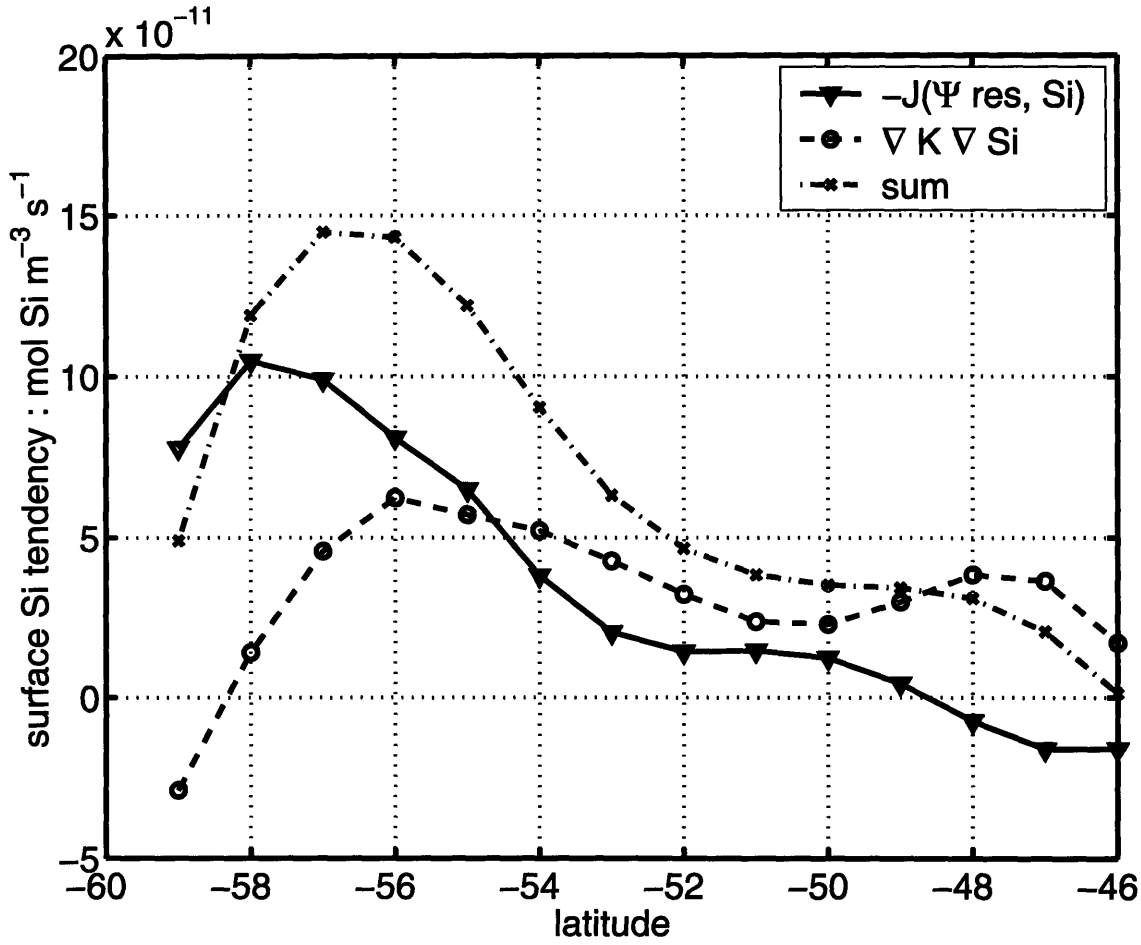

Figure 3-6: Comparison of the two tracer tendency terms; advective tendency, $-J(\Psi_{res}, Si)$, and diffusive tendency, $\nabla \mathbf{K} \nabla Si$. In this particular case, α is set to 1. The net effect of physical transport is the sum of these two terms and it balances the uptake of silica in the surface layer of the model.

ACC where the subduction occurs ($\sim$ 48S), the silica export becomes weak and the primary silica supply is through the isopycnal eddy stirring. This pattern is analogous to the uptake of transient tracers discussed in chapter 2, in which the tracer transport is mainly controlled by residual mean flow to the south of the ACC and is dominated by isopycnal eddy stirring to the north.

3.2.4 Uncertainty analysis

It is a significant advantage of the least squares method to be able to estimate the uncertainties in the optimal solution, which is impossible for the simple Newtonian relaxation method. Fig.3-3 includes error bars associated with the uncertainty in the observed silica distribution and *a priori* estimate of particulate silica flux. The magnitude of these errors can be estimated by combining the model matrix, **M**, and uncertainties in observations and *a priori* estimate.

The second derivative of the cost function is typically used to estimate the uncertainty of the optimal solution.

$$\frac{\partial^2 J}{\partial \mathbf{p}^2} = \mathbf{H} = \mathbf{M}^T \mathbf{W} \mathbf{M} + \mathbf{W}_p \tag{3.11}$$

The first term reflects the component of the cost function involving the data-model misfit, and the second term reflects the component due to the confidence in *a priori* estimate. The matrix, **H**, is called the Hessian matrix. It can be shown that the error-covariance matrix for the optimal solution for **p** is given by the inverse of **H** (Thacker, 1989).

The Hessian matrix defines the shape of the cost function, which determines the ability of the model and observation to constrain silica export. If the cost function has a deep minimum, the second derivatives is large and the error bar becomes small. Error bars shown in Fig.3-3 are determined by the square-root of the diagonal elements of the inverse of **H**. The size of the error bars can indicate the possible range of optimal solutions due to uncertainties in the observations which are used to constrain the silica export.

3.2.5 Numerical solution using the adjoint method

In the previous sections, the least squares method was applied to a linear model of the silica cycling to find the optimal profile of silica export which minimizes the quadratic measure of the difference between the observed silicic acid data its model counterpart. In this section I optimize the profile of β, which defines the vertical profile of remineralization of silica in the interior ocean, as well as the silica export. The parameterization of the sinking particulate flux in eq.(3.1) takes the form of a non-linear function with respect to β, so the model becomes non-linear if β is considered as a model variable. The fundamental idea of the least squares method, which is to minimize cost function by adjusting model variables, can be applied to constrain non-linear models, but the optimization must be carried out numerically. The model variables are systematically adjusted to minimize the cost function using an iterative method. The gradient of the cost function with respect to the model variables is the key to finding the optimal solution efficiently. The gradient of the cost function is provided by the adjoint equations, and this method is often called the adjoint method. A significant advantage of this method is to be able to constrain variables of non-linear models.

The biological (source-sink) vector, $\mathbf{b}_{bio}$, is a non-linear function of β which controls the depth scale of remineralization. I define the "remineralization" vector, $\mathbf{q}$, whose elements are meridional profile of β. $\mathbf{b}_{bio}$ depends on the profile of silica export, $\mathbf{p}$, and the parameter setting the depth scale of remineralization, $\mathbf{q}$.

$$\mathbf{b}_{bio} = \mathbf{b}_{bio}(\mathbf{p}, \mathbf{q}) \tag{3.12}$$

Here the purpose of the least squares method is to adjust $\mathbf{p}$ and $\mathbf{q}$ to minimize the cost function as defined in eq.(3.8). The adjoint equations can be derived by adding the residuals of the model equation to the cost function with the Lagrange multiplier vector, $\mathbf{r}$. Here I take the form of the steady state model based on eq.(3.3), and

append the product of $\mathbf{r}$ and the model equation to the cost function.

$$J_A = \frac{1}{2}(\mathbf{x}_S - \mathbf{x}_{obs})^T \mathbf{W}(\mathbf{x}_S - \mathbf{x}_{obs}) \tag{3.13}$$

$$+\mathbf{r}^T (\mathbf{A}_I \mathbf{x}_S + \mathbf{B}\mathbf{x}_b + \mathbf{b}_{bio}(\mathbf{p}, \mathbf{q})) \tag{3.14}$$

For simplicity, I do not include the contributions from *a priori* estimates of $\mathbf{p}$ and $\mathbf{q}$ in the cost function. This newly defined cost function includes the term involving the Lagrange multiplier, and is defined as J_A to avoid confusion with the original cost function in the previous section. The least squares solution corresponds to the condition in which the gradient of cost function vanishes.

$$\frac{\partial J_A}{\partial \mathbf{r}} = \mathbf{A}_I \mathbf{x}_S + \mathbf{B}\mathbf{x}_b + \mathbf{b}_{bio}(\mathbf{p}, \mathbf{q}) = 0 \tag{3.15}$$

$$\frac{\partial J_A}{\partial \mathbf{x}_S} = \mathbf{W}(\mathbf{x}_S - \mathbf{x}_{obs}) + {\mathbf{A}_I}^T \mathbf{r} = 0 \tag{3.16}$$

$$\frac{\partial J_A}{\partial \mathbf{b}_{bio}} = \mathbf{r} \tag{3.17}$$

The first equation (3.15) is the condition for the steady state of the model. The second equation (3.16) is the adjoint equation which determines the Lagrange multiplier vector, $\mathbf{r}$. As the third equation (3.17) indicate, the Lagrange multiplier vector, $\mathbf{r}$, provides the gradient of cost function with respect to the biological (source-sink) vector, $\mathbf{b}_{bio}$.

In the minimization algorithm, the initial guess for the model variables, $\mathbf{p}$ and $\mathbf{q}$, must be specified. In this example, I initially set $\mathbf{p} = \mathbf{0}$ for the silica export vector, and set each element of $\mathbf{q}$ to 0.15 for the remineralization vector. Given these model variables, the steady state solution, $\mathbf{x}_S$, can be calculated using eq.(3.15).

$$\mathbf{x}_S = \mathbf{x}_0 - {\mathbf{A}_I}^{-1} \mathbf{b}_{bio}(\mathbf{p}, \mathbf{q}) \tag{3.18}$$

where $\mathbf{x}_0 = -{\mathbf{A}_I}^{-1}\mathbf{B}\mathbf{x}_b$. Then the adjoint equation (3.16) can be solved for the Lagrange multiplier, $\mathbf{r}$, and the gradient of the cost function with respect to $\mathbf{p}$ and $\mathbf{q}$

is calculated using the Jacobian matrices, $\left(\frac{\partial \mathbf{b}_{bio}}{\partial \mathbf{p}}\right)$ and $\left(\frac{\partial \mathbf{b}_{bio}}{\partial \mathbf{q}}\right)$.

$$\mathbf{r} = \left(\mathbf{A}_I^T\right)^{-1} \mathbf{W} \left(\mathbf{x}_{obs} - \mathbf{x}_0 + \mathbf{A}_I^{-1} \mathbf{b}_{bio}(\mathbf{p}, \mathbf{q})\right) \tag{3.19}$$

$$\frac{\partial J_A}{\partial \mathbf{p}} = \mathbf{r}^T \left(\frac{\partial \mathbf{b}_{bio}}{\partial \mathbf{p}}\right) \tag{3.20}$$

$$\frac{\partial J_A}{\partial \mathbf{q}} = \mathbf{r}^T \left(\frac{\partial \mathbf{b}_{bio}}{\partial \mathbf{q}}\right) \tag{3.21}$$

Jacobian matrices relate the Lagrange multiplier vector, $\mathbf{r}$, to the gradient of J_A with respect to control variables, $\mathbf{p}$ and $\mathbf{q}$ (i.e. meridional profile of silica export and the depth scale of remineralization). These Jacobian matrices can be calculated from the definition of $\mathbf{b}_{bio}$. Once the gradient of the cost function is calculated in eq.(3.20,3.21), the control variables ($\mathbf{p}$ and $\mathbf{q}$) are adjusted using the Conjugate-Gradient decent algorithm (Press et al., 1992) to find a better combination. Then eq.(3.18) through (3.21) are repeated such that the cost function is iteratively reduced toward its minimum.

Fig.3-7 shows the modeled distribution of silicic acid from the first 4 iteration cycles illustrating the improvements of the modeled silicic acid field. The solution with the first guess is characterized by elevated silicic acid concentration near the surface due to the lack of biological uptake of silica in the first guess. After the first iteration, the silica export is adjusted to reduce the near-surface anomaly. Fig.3-8 shows the estimated silica export from the first 4 iteration cycles. The first guess is $\mathbf{p} = \mathbf{0}$, and the $\mathbf{p}$ rapidly becomes similar to the analytic solution (with fixed β) after a few iterations, revealing a peak in the silica export on the southern flank of the ACC. It is interesting to note that the numerical solution is somewhat smoother than the analytic solution, and the optimal solution for the remineralization vector, $\mathbf{q}$, is dominated by the initial guess. Adjustments of β through the iterative procedure is very small relative to the magnitude of the initial guess. The data does not strongly constrain the magnitude of β, perhaps because of the fact that much of the biogenic silica exported from the euphotic layer reaches the bottom and dissolves at the sea floor. Therefore small variations in the magnitude of β does not affect the cost

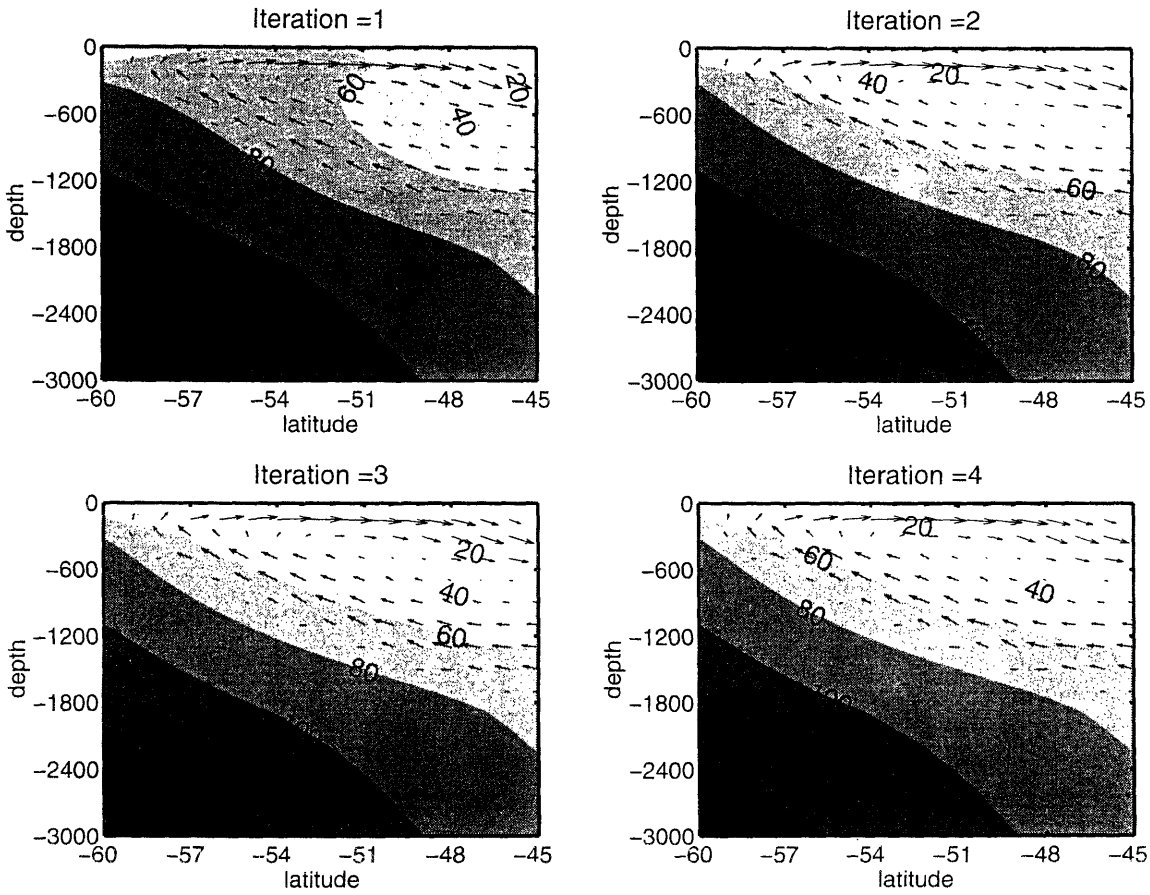

Figure 3-7: Distribution of the modeled silicic acid from the first 4 iteration cycles of the optimization using the adjoint method. The vector plots represent the residual mean circulation. The system reaches very close to the the optimal solution after a few iterations.

function as long as the depth scale of remineralization is comparable to the depth of the ocean.

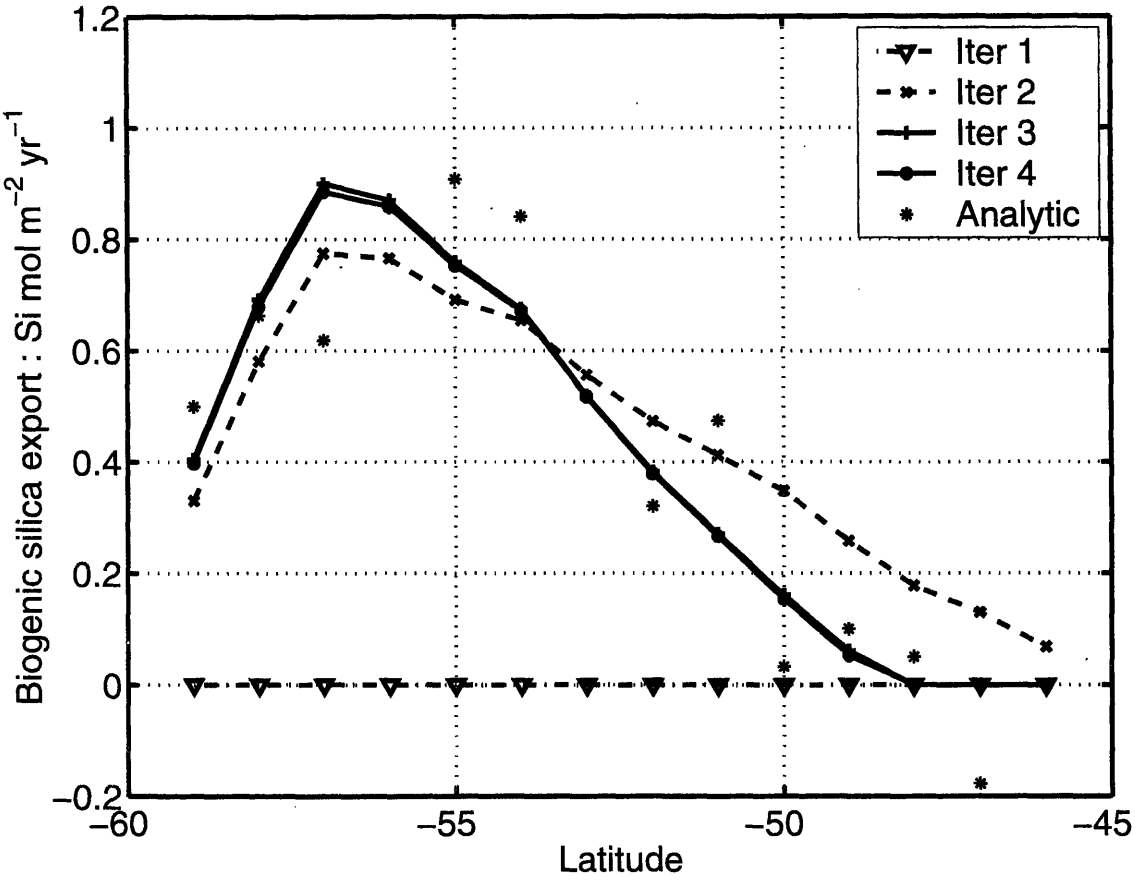

Figure 3-8: The profile of the silica export of biogenic silica from the first 4 iteration cycles of the optimization using the adjoint method. The initial guess is set to $\mathbf{p} = \mathbf{0}$. The analytic solution is taken from the case with $\alpha = 0$.

3.2.6 A sensitivity study : $\Psi_{res} = 0$

The simplicity of the model allows us to investigate what aspect of the model leads to the presence of an Antarctic Circumpolar Productivity Belt. The physical transport is driven by the residual mean circulation and isopycnal eddy stirring in the model. In section 3.2.3, the supply of silica to the surface layer is separated into contributions from the residual mean flow and isopycnal eddy stirring. Advective transport by the residual mean flow is a major source of silica to the south of the ACC, where the elevated silica export is found. To illustrate this point, I re-calculated the optimal solution with the advective transport suppressed in the transport model. The transport matrix $\mathbf{A}_I$ and the boundary matrix $\mathbf{B}$ are re-calculated by setting Ψ_{res} to zero everywhere in the model domain. In this case, the advective transport vanishes and the silicic acid can be transported only through isopycnal diffusive fluxes of eddy stirring.

Fig.3-9 shows the comparison of the optimal solution of the silica export calculated from the two cases; the control case and the "$\Psi_{res} = 0$" case. In the control case, the silica export is calculated with the active residual mean circulation in the transport model. The solution is iteratively determined using the adjoint method initialized with zero silica export, and the *a priori* estimate of silica export is not included in the cost function. The same calculation is repeated with the "$\Psi_{res} = 0$" case, by setting v_{res} and w_{res} to zero while keeping other parameters the same. In the control, the optimal solution reproduces the Antarctic Circumpolar Productivity Belt as illustrated in the previous sections. In the "$\Psi_{res} = 0$" case, the inferred silica export is significantly smaller than that of the control, and it does not reproduce the maximum of the silica export in the southern flank of the ACC. There is a broad silica export near the core of the ACC in the "$\Psi_{res} = 0$" case supported by isopycnal eddy stirring of silica. Clearly, the overturning circulation significantly influences the estimates of the silica export, and I suggest that the residual mean flow is responsible for the maintenance of the relatively large silica export in the Southern Ocean.

In summary, the advective transport by the residual mean circulation is the key

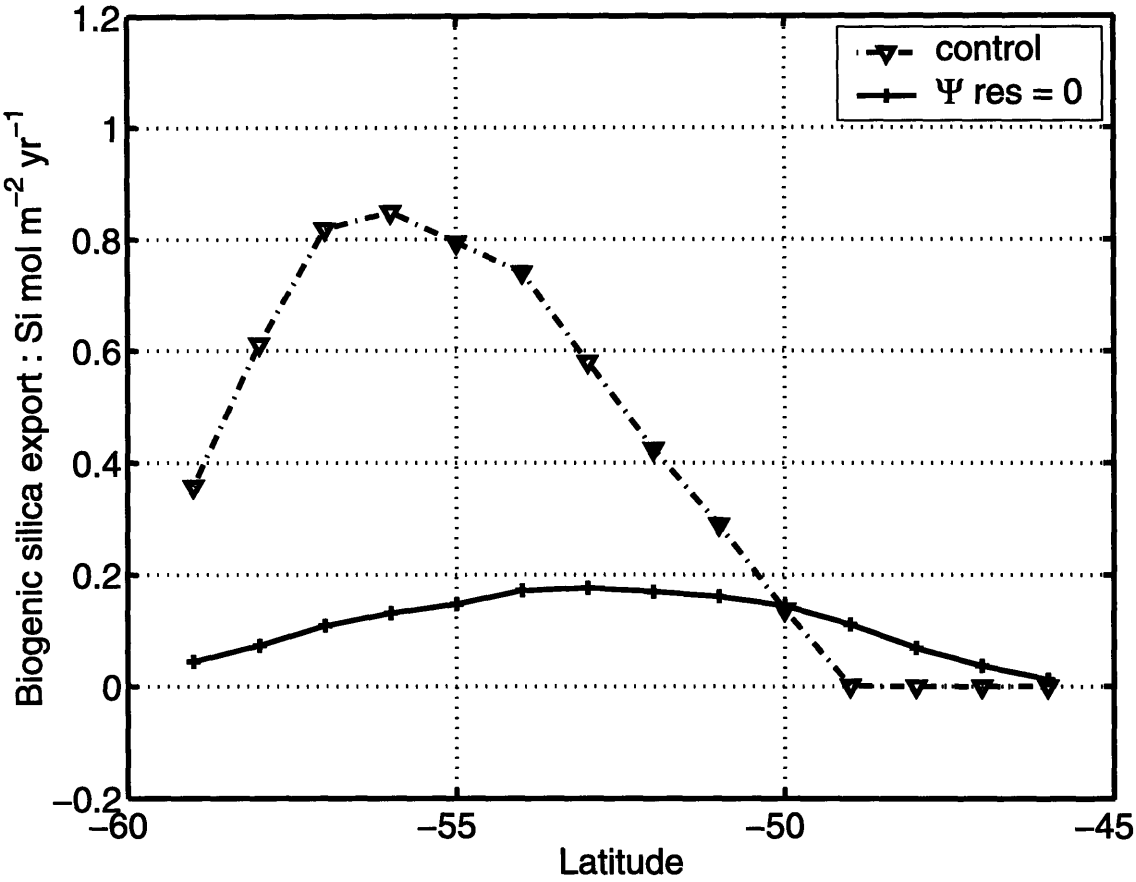

Figure 3-9: Comparison of two optimal solutions. In the control case, the silica export is calculated with the active residual mean circulation in the transport model. The solution is iteratively calculated through the adjoint method initialized with zero silica export. In the "$\Psi_{res} = 0$" case, the silica export is calculated by setting v_{res} and w_{res} to zero.

process in bringing the estimated profile of the silica export close to the observed pattern. The optimal solution can reproduce the Antarctic Circumpolar Productivity Belt reasonably well when the vigorous residual mean flow is included in the transport model. Therefore I argue that the supply of silicic acid through the residual mean circulation is an important process supporting the biological productivity in the Southern Ocean.

3.3 Coupled physical-biogeochemical model

I examine and illustrate the mechanisms controlling the biological productivity in the Southern Ocean using a physical-biogeochemical model (Dutkiewicz et al., 2004) based on MITgcm (Marshall et al., 1997a; Marshall et al., 1997b). The inverse calculations in the previous sections can constrain the pattern and magnitude of the biological productivity in the region, but it does not provide mechanisms controlling the biological productivity. In this section I take a forward-modeling approach where biogeochemical processes are parameterized and simulated in a three dimensional general circulation model. Diagnosis of the simulated biological productivity may provide insights into the processes controlling the magnitude and the spatial pattern of the biological productivity. The biogeochemical model includes an explicit ecosystem dynamics with two functional groups of phytoplankton and an explicit iron cycle component, which is suitable for simulating the biological productivity in the Southern Ocean.

3.3.1 Physical circulation

The model is configured in a global domain at coarse resolution (2.8 $\times$ 2.8 degrees, 15 vertical levels) and is forced with climatological monthly wind stresses (Trenberth et al., 1989), surface heat and freshwater fluxes. There is additional relaxation toward climatological sea surface temperature and salinity. The physical forcing used in this study is the same as the MIT-01 run shown in chapter 2. In these coarse resolution studies, the effect of mesoscale eddy transfers is parameterized following (Gent and McWilliams, 1990) (hereafter, GM90). Vertical mixing in the surface mixed layer of the ocean is represented through a simple convective adjustment scheme. We use a third-order upwind, flux corrected advection scheme for tracers (Dutkiewicz et al., 2001).

The model is spun up to achieve a statistical steady state. The simulated zonal transport through the Drake Passage is approximately 122 Sv, which is somewhat smaller than observed ACC transport. Vertical transport near the base of surface

mixed layer is particularly important for the supply of nutrients to the surface layer where photosynthesis occurs. Fig.3-10 and 3-11 show the simulated, annual mean vertical velocities at 220m depth for the Eulerian mean and the eddy-induced circulation respectively. They have similar magnitudes in the Southern Ocean with opposite signs from one another. Eulerian mean circulation is largely dominated by Ekman transport where the regions of Eulerian mean upwelling and downwelling are separated by the $curl(\tau) = 0$ line.

The net effect of the Eulerian mean circulation and the eddy-induced circulation is the residual mean circulation. Figure 3-12 shows the annual mean, residual mean vertical velocity. The model reproduces the subduction and the formation of the thermocline and intermediate waters on the northern flank of the ACC. The formation of the bottom water occurs near the coast of the Antarctic continent. In between the northern and the southern downwelling regions, the upwelling of the deep water occurs near the latitude band of the ACC but with a significant zonal variability. The simulated meridional overturning circulation in the Southern Ocean (shown in Fig.2-18) is comparable ($\sim$ 13 Sv) to the estimates based on meteorological reanalysis data and those inferred from transient tracers (Ito et al., 2004). The lower cell in the opposing sense reflects the formation of bottom waters in the southern polar region, and their upwelling in the interior. This deep cell ventilates the deep Atlantic basin and much of the Pacific basin.

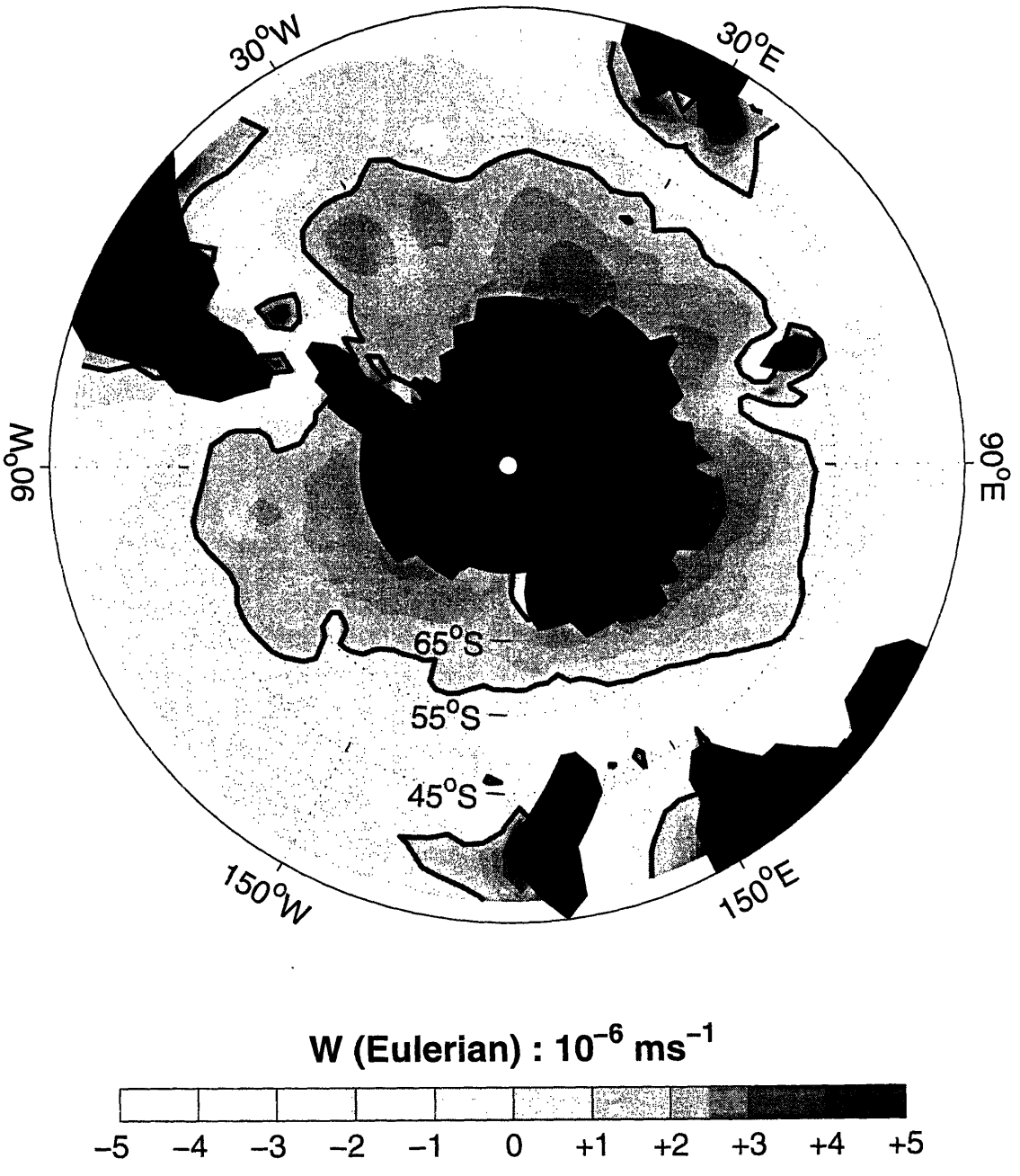

Figure 3-10: Eulerian mean vertical velocity evaluated at the depth of 225m.

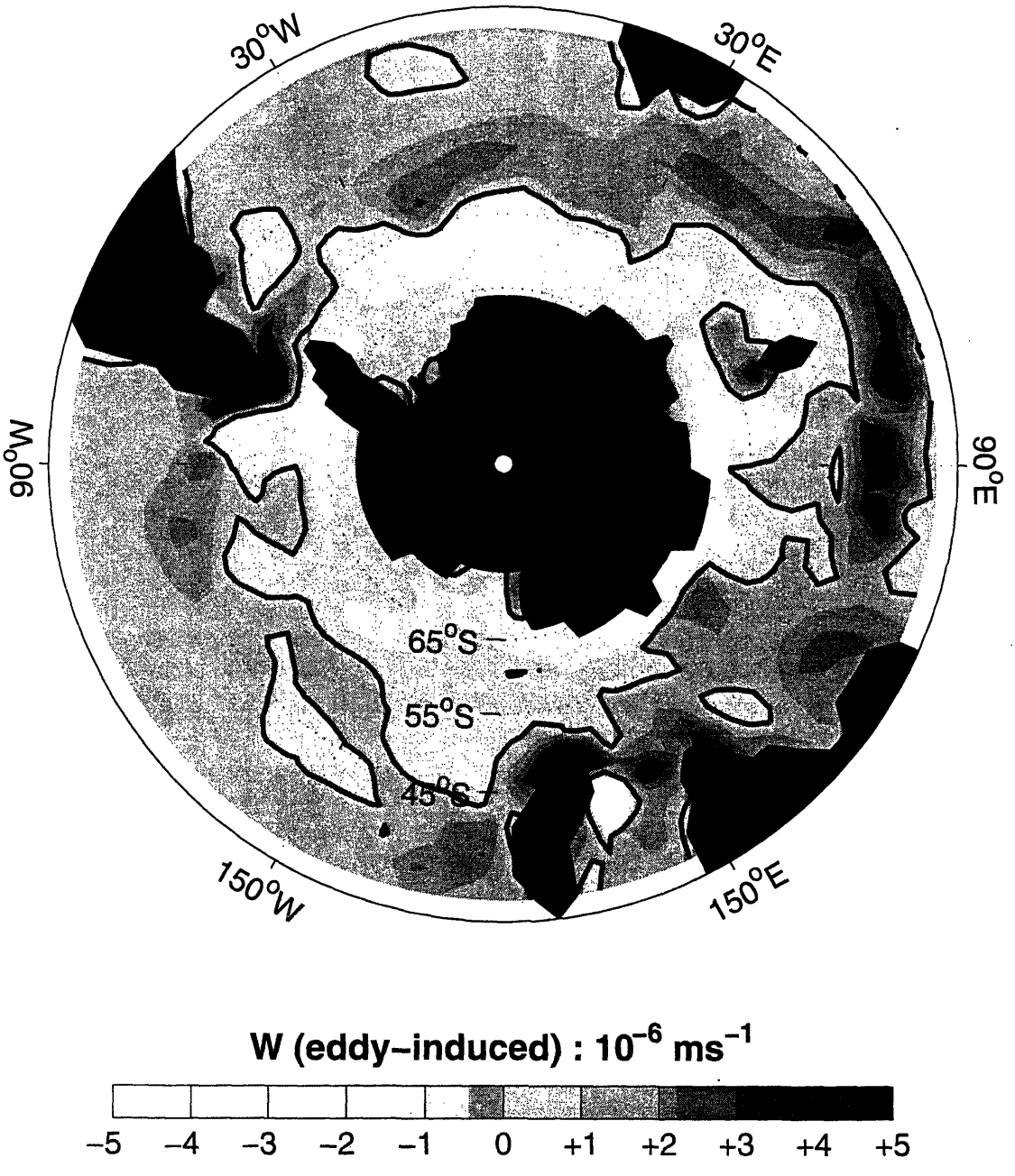

Figure 3-11: Parameterized, eddy-induced vertical velocity evaluated at the depth of 225m.

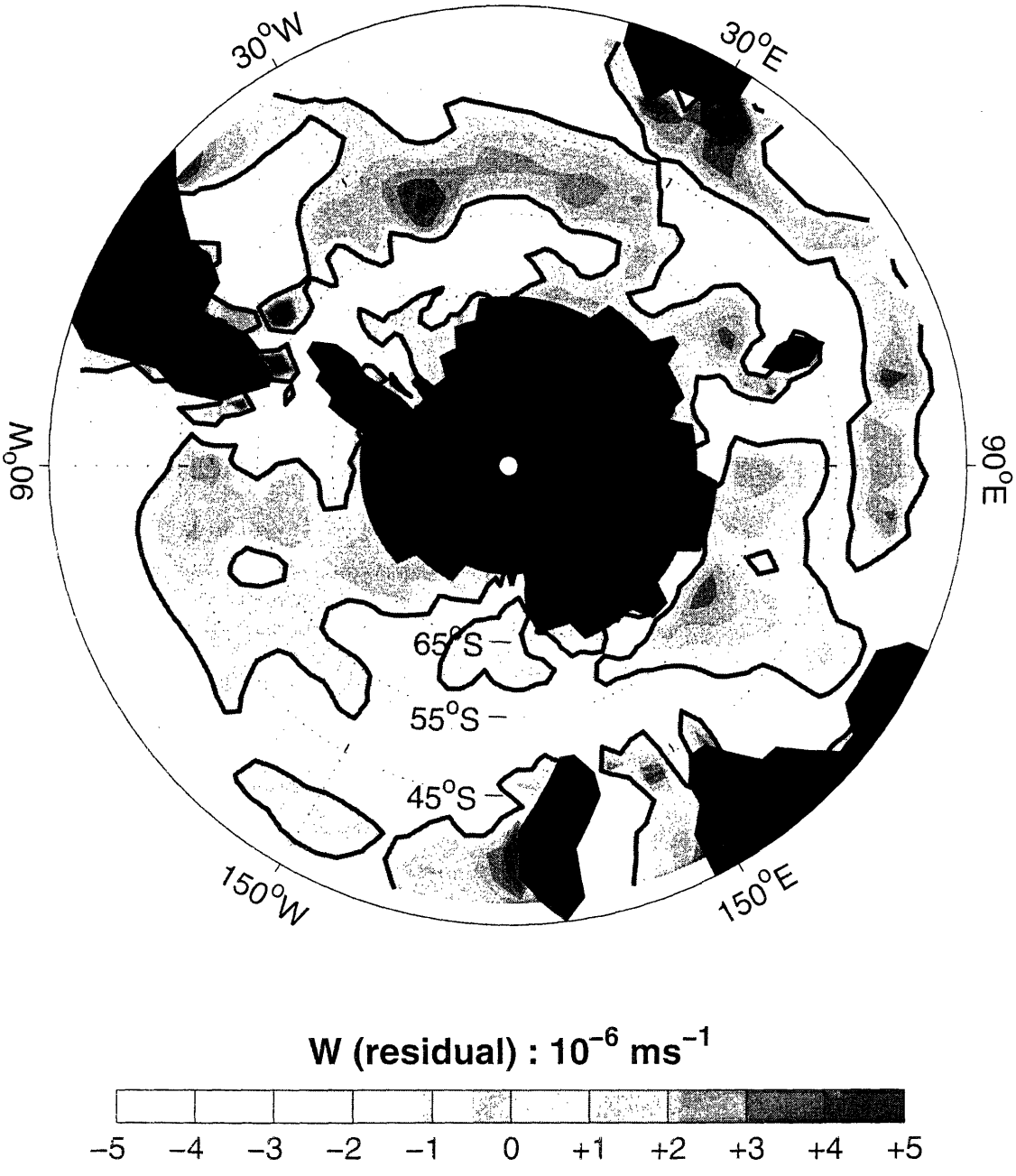

Figure 3-12: Residual mean vertical velocity evaluated at the depth of 225m.

3.3.2 Ecosystem dynamics

We use an intermediate complexity ecosystem model with two phytoplankton functional groups, one zooplankton size-class, two detritus pools and three nutrients: phosphate, silicic acid and iron. Dissolved nutrients, phytoplankton and zooplankton are explicitly transported as passive tracers by the three-dimensional physical circulation of the model.

Here I briefly summarize architecture of the model, which is described in detail by Dutkiewicz (2004). Growth of phytoplankton is limited by light and the availability of essential nutrients using Michaelis-Menton kinetics.

The larger phytoplankton class, representing diatoms, utilizes silicic acid, phosphate and iron, whereas the smaller phytoplankton class, representing nano/pico plankton, utilizes only phosphate and iron. We assume a fixed stoichiometry of nutrient uptake for each phytoplankton size class. The model includes a single zooplankton class which grazes on phytoplankton preferring the smaller size-class. The modeled zooplankton has a fixed mortality rate. Detritus is formed by mortality and excretion, and from sloppy feeding of zooplankton. Detritus is divided into two pools: a dissolved pool which remains suspended in the water column and a particulate pool which sinks vertically with constant speed. The fraction that ends up in each pool differs for each processes of the formation of detritus. Furthermore, the rate at which the pools remineralize differs for each nutrient.

Phosphorus and silica have very long residence time relative to the ventilation timescale of deep oceans. Hence we assume that phosphate and silicic acid are internally recycled within the ocean, and the model does not include external sources and sinks. In contrast, the residence time of iron is on the order of 100 years and we must represent sources and sinks for iron. Iron enters the surface ocean via aeolian deposition, and it is removed from the water column by scavenging onto sinking particles. Complexation, the binding of iron to organic ligands allows iron to remain dissolved in the system, increasing the residence time of iron in the ocean. Here we use the iron parametrization of (Parekh et al., 2004a; Parekh et al., 2004b), which

includes an aeolian source, scavenging and complexation. We assume a uniform ligand concentration of 1 nM and provide an aeolian flux with dust fields generated by an atmospheric circulation model (Mahowald et al., 2003).

3.3.3 What controls the simulated biological productivity?

What controls the biological productivity and its spatial pattern in the Southern Ocean? We examine modeled export production of PO_4 and Si and tracer distributions to gain insights into the possible mechanisms controlling the position and the intensity of the Antarctic Circumpolar Productivity Belt.

Fig.3-13 and 3-14 show the simulated, annual mean export of organic carbon and biogenic silica, calculated as the sum of the sinking particulate flux and the downward flux of dissolved organic material. The simulated export shows a zonal belt of high biological productivity and export in the Southern Ocean, the "Antarctic Circumpolar Productivity Belt", consistent with the inference from the inverse calculations and observations (Honjo et al., 2000; Moore and Abbott, 2000; Buesseler et al., 2002; Schlitzer, 2002).

The export of biogenic silica is dominated by the large phytoplankton which have elevated population on the southern flank of the ACC. The magnitude of the export of biogenic silica has significant zonal variability from 0.5 to 2 mol Si m^{-2} yr^{-1} in the latitude band between 55S and 65S. The largest export is found in the Atlantic and Indian sector of the ACC, and the smallest export is found in the Pacific. The large export in the Indian sector is associated with the regional eddy-induced upwelling.

The export of organic carbon is driven by both small and large phytoplankton, and the productivity belt of organic carbon derived from export of PO_4 using the Redfield ratio is wider in latitude. The magnitude of the organic carbon export has significant zonal variability from 3 to 7 mol C m^{-2} yr^{-1} in the latitude band between 40S to 60S. The largest export is found in the Indian sector of the ACC, and the smallest export is found in the Pacific.

The meridional profiles of PO_4 and Si change (3-15) from low values in the subtropics to high values in the Southern Ocean. The meridional profile of Fe has opposing variation where the Fe is depleted in the Southern Ocean and increases equatorwards. In the southern flank of the ACC, macro-nutrients including PO_4 and Silicic acid are abundant, and the availability of Fe controls the overall biological productivity in this

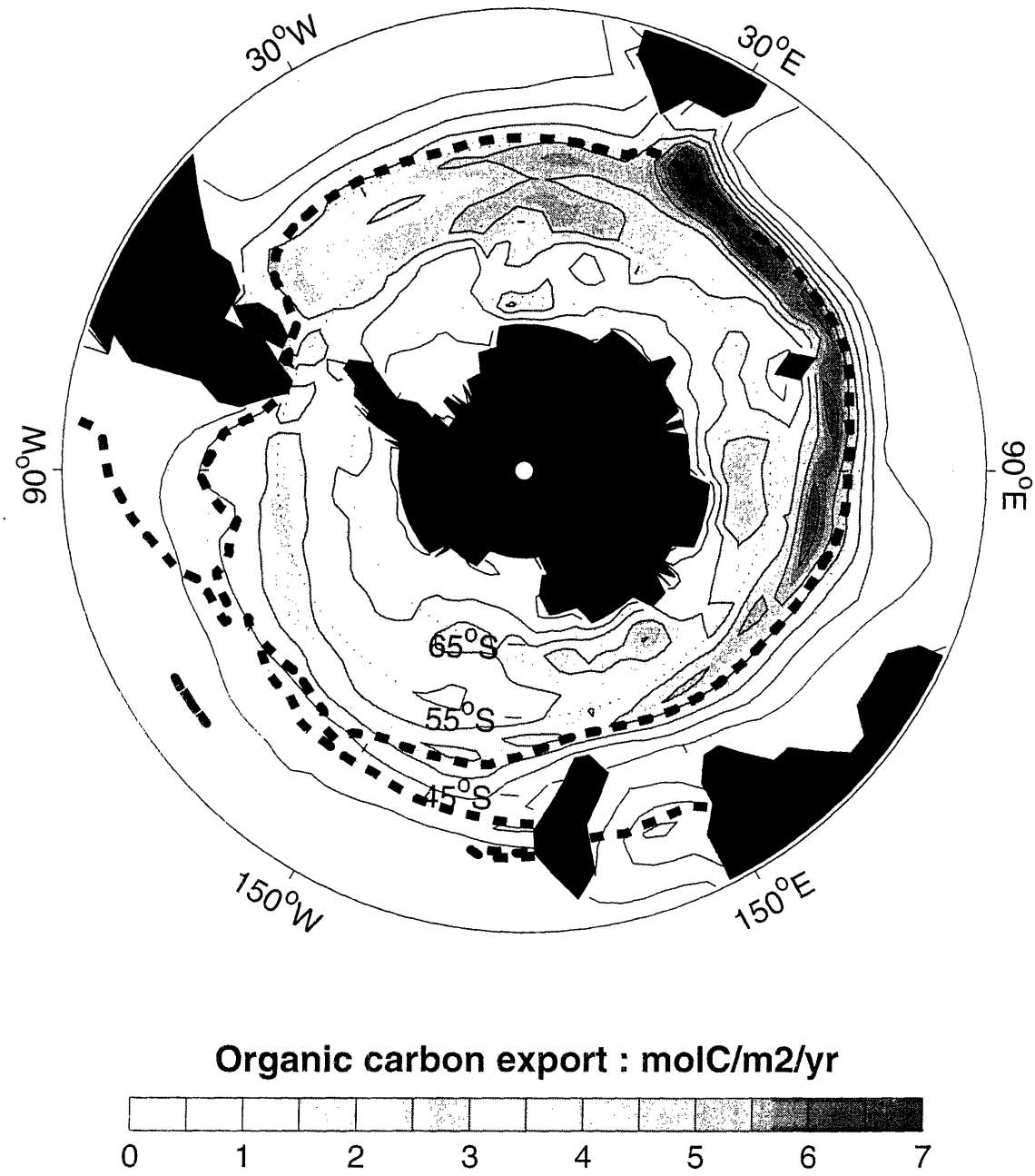

Figure 3-13: Simulated, annual-mean distribution of export production of organic material. The Dash line represents $Fe^*(PO_4) = 0$ contour, marking the position of the Antarctic Circumpolar Productivity Belt.

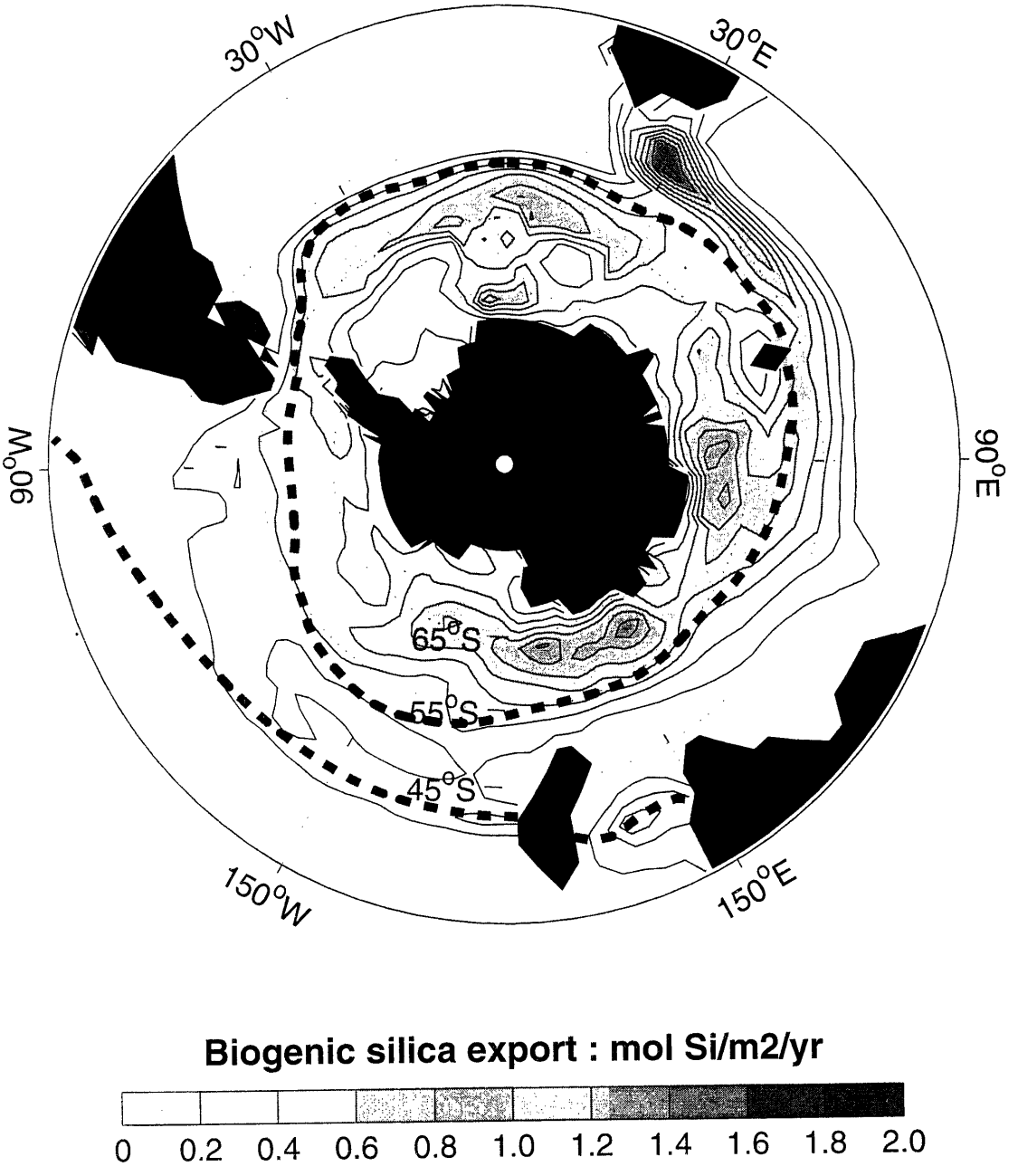

Figure 3-14: Simulated, annual-mean distribution of export production of biogenic silica. The Dash line represents Fe*(Si) = 0 contour, marking the position of the Antarctic Circumpolar Productivity Belt.

region. In the northern flank of the ACC, macro-nutrients decrease toward very low concentrations and the productivity is clearly limited by their availability. In the latitude band of the ACC, the regime of nutrient limitation changes from macro-nutrient limited regime (Subantarctic zone) to micro-nutrient limited regime (Antarctic zone). The lower panel of Fig.3-15 indicates that the biological export is at its maximum at the biogeochemical regime transition. Why is modeled carbon export highest in this transition zone? We suggest that, in the regime transition zone, organisms have relatively good access to both nutrients, having an optimal condition for the phytoplankton growth.

To illustrate this point, we define a diagnostic tracer, Fe*, which tracks the relative magnitude of decoupling between Fe and PO_4 (or Si). Fe* is calculated by subtracting scaled macro-nutrient concentrations from the Fe distribution.

$$Fe^*(\mathrm{P}O_4) = \mathrm{F}e - < R_{\mathrm{P}O_4} > \mathrm{P}O_4 \tag{3.22}$$

$$Fe^*(\mathrm{S}i) = \mathrm{F}e - R_{\mathrm{S}i}\,\mathrm{S}i \tag{3.23}$$

$< R_{\mathrm{P}O_4} >$ represents the averaged biological uptake ratio of Fe:P which differs between functional groups. (The uptake ratio for small phytoplankton, R_S, is set to 10^{-4}, and that for large phytoplankton, R_L, 10^{-3}.) We take the population-weighted average of the uptake ratio to calculate $< R_{\mathrm{P}O_4} >$.

$$< R_{\mathrm{P}O_4} >= \frac{R_S\, Phy_S + R_L\, Phy_L}{Phy_S + Phy_L} \tag{3.24}$$

where Phy_S and Phy_L represents the annual-mean concentration of the small and large phytoplankton respectively. The growth of small phytoplanton does not depend on the availability of silicic acid, and so similar averaging is not required for $R_{\mathrm{S}i}$.

Fig.3-16 and 3-17 shows the annual-mean, surface distribution of $Fe^*(\mathrm{P}O_4)$ and $Fe^*(\mathrm{S}i)$ in the Southern Ocean. The sign of Fe* can illustrate the regime of nutrient limitation. If $Fe^*(\mathrm{P}O_4) \gg 0$, we would expect biological production to be strongly limited by phosphate relative to iron. Similarly, if $Fe^*(\mathrm{S}i) \gg 0$, we would expect

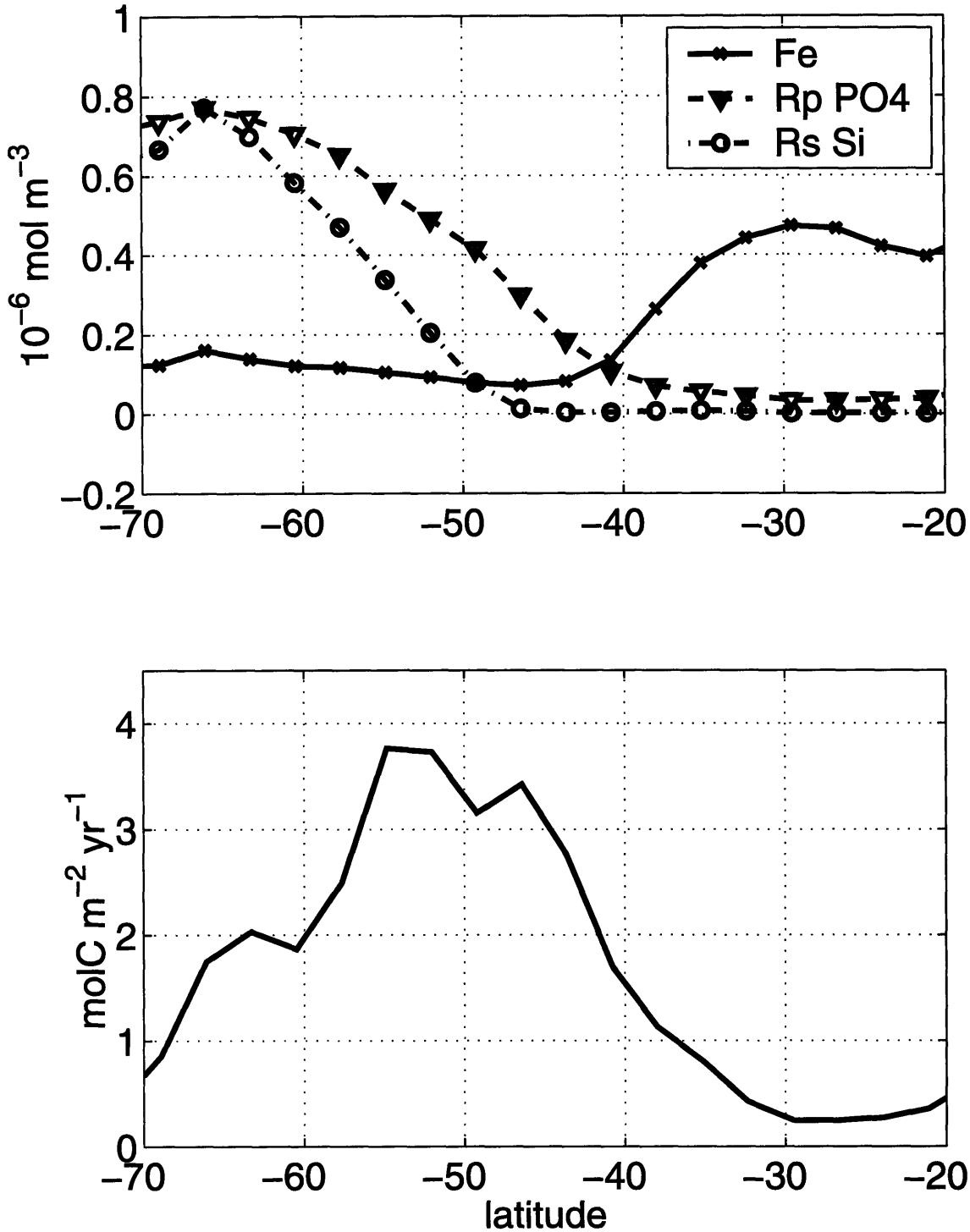

Figure 3-15: (Top) Simulated surface PO_4, Si, Fe distributions in a meridional section in the Atlantic. (Bottom) Simulated profile of export production in a meridional section in the Atlantic. The magnitudes of the concentrations are scaled such that all nutrients become comparable. The scaling factors are set to the uptake ratios of the nutrients specified in the model.

biological production to be strongly limited by silicic acid relative to iron. For example, the North Atlantic receives a large aeolian dust input and the dissolved iron concentration is high relative to the biological requirement for dissolved phosphate or silicic acid, so we find, $Fe^*(PO_4) \gg 0$ and $Fe^*(Si) \gg 0$.

Conversely, if $Fe^*(PO_4) \ll 0$ and $Fe^*(Si) \ll 0$, we would expect biological production to be strongly limited by iron. The Southern Ocean is characterized by low Fe* concentrations showing that organisms are strongly limited by the availability of iron. Subpolar North Pacific. tropical Pacific, and the Southern Ocean are generally low in the modeled Fe* distribution. Dash lines in Fig.3-16 and 3-17 are the Fe*=0 contours, marking the transition between the macro-nutrient limited regime and the micro-nutrient limited regime. The $Fe^*(PO_4) = 0$ contour is approximately at 50S, and the $Fe^*(Si) = 0$ contour is approximately at 55S. Fig.3-13 and 3-14 show that the biogeochemical regime transition marked with dash line roughly corresponds to the position of the simulated productivity belt, where we find the highly enhanced biological productivity.

We suggest that atmospheric dust deposition and the pattern of the residual mean circulation determine the position of the productivity belt. Figure 3-18 schematically illustrates the hypothesis. On the southern flank of the ACC, the large scale upwelling of the residual circulation supplies the nutrients to the surface oceans. While PO_4 and silicic acid accumulate in the interior ocean due to remineralization, Fe is also subject to a sink term, scavenging. The old, upwelling waters are depleted in Fe relative to macro-nutrients due to the integrated effects of scavenging, and the atmospheric dust deposition is very low in the high latitude Southern Ocean. Therefore the organisms are likely to be limited by the availability of iron, and there are observational evidences for iron limitation (Martin et al., 1994; Coale et al., 1996; Boyd et al., 2000). On the northern flank of the ACC, the large scale circulation subducts and forms Antarctic Intermediate Waters and Subantarctic Mode Waters. There is a source of aeolian derived iron into this region originating from Australia and South America. Hence iron concentration increases to the north while silicic acid and phosphate concentrations sharply decrease across the ACC towards the macro-nutrient

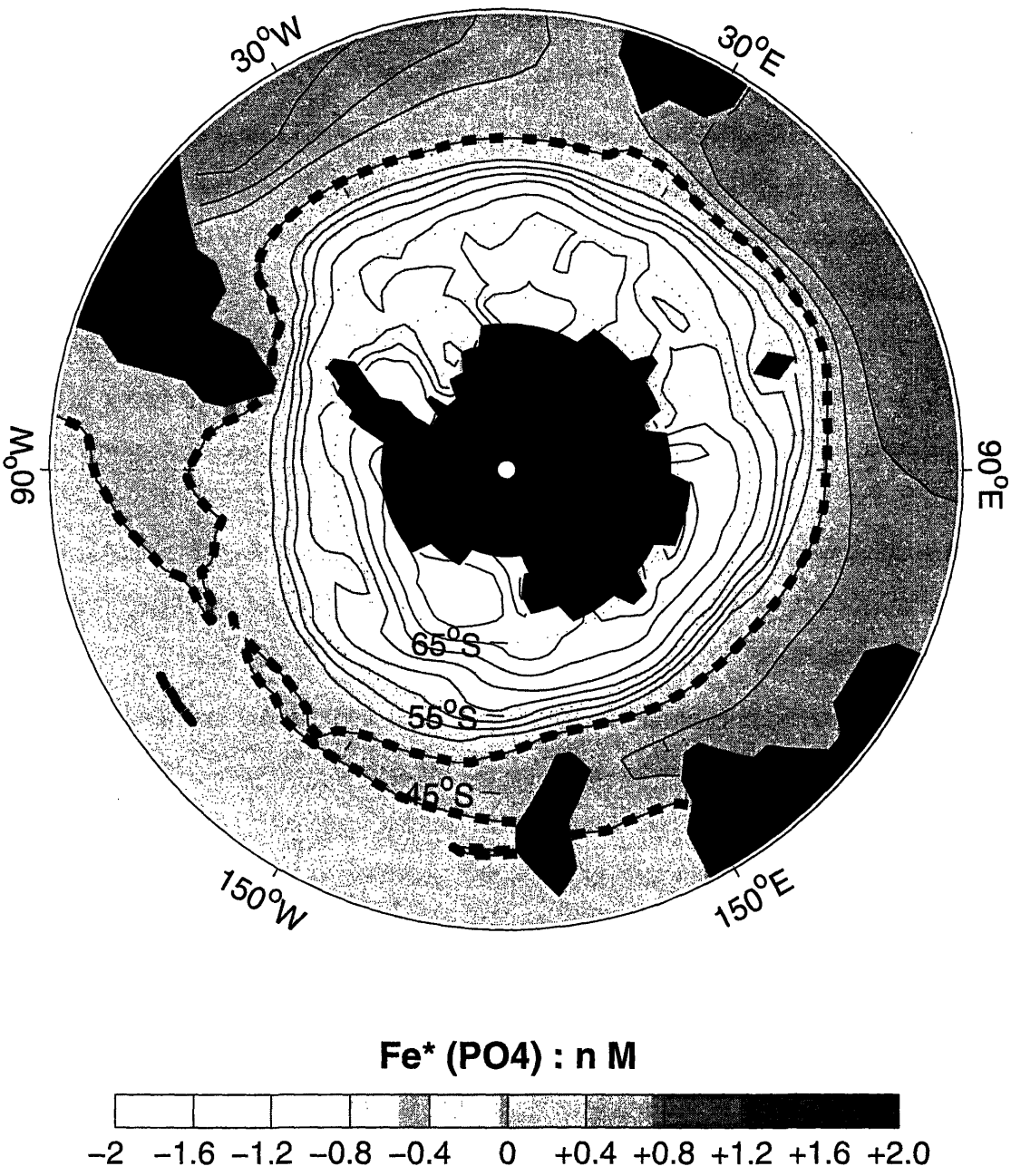

Figure 3-16: Simulated Fe* distribution in (a) the global ocean and (b) the Southern Ocean. The dashed line in (b) and (c) represents the regime transition between iron-limited Antarctic zone and the macro-nutrient limited Subantarctic zone. The simulated productivity belt (c) is close to the regime transition.

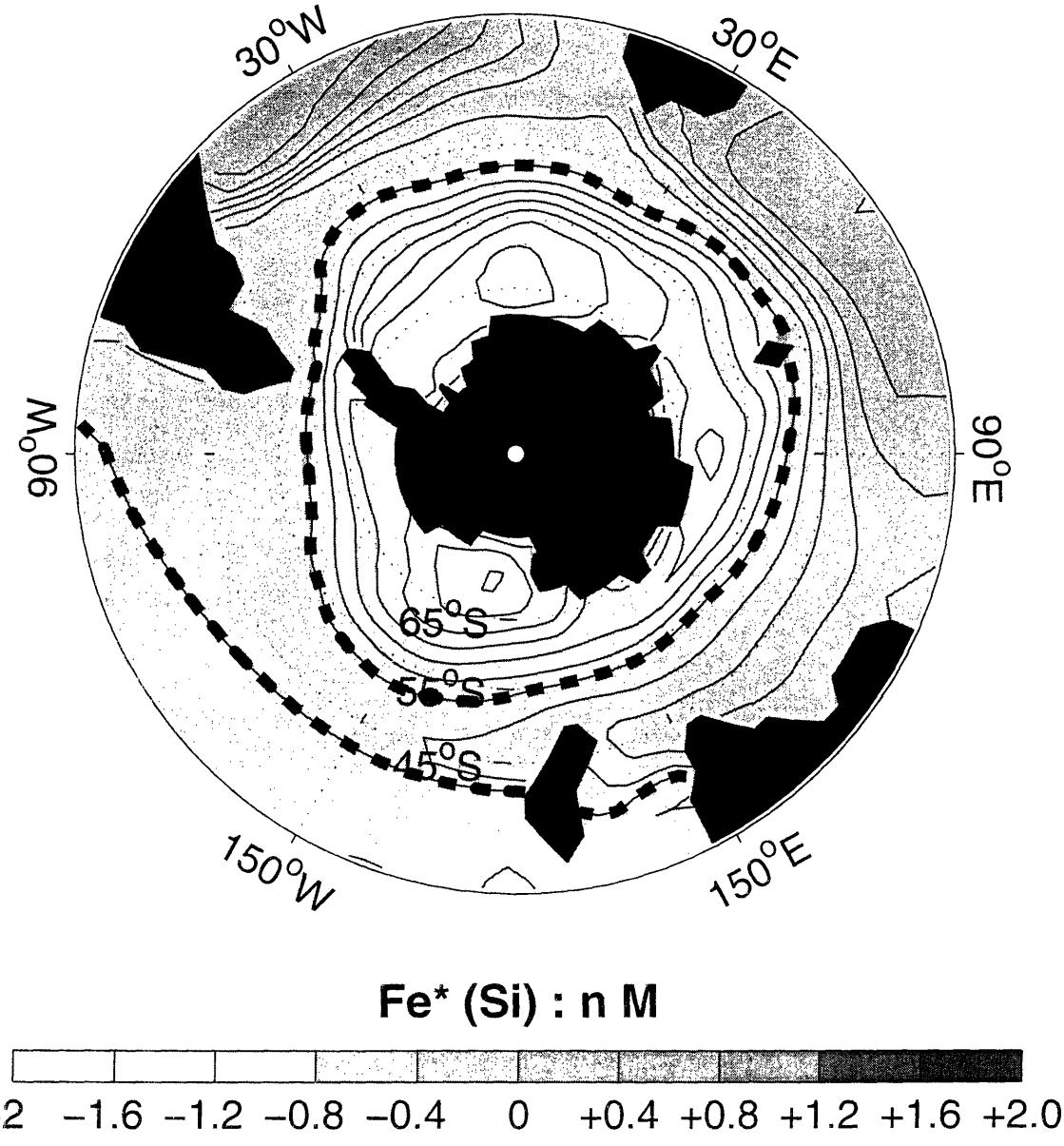

Figure 3-17: Simulated Fe* distribution in (a) the global ocean and (b) the Southern Ocean. The dashed line in (b) and (c) represents the regime transition between iron-limited Antarctic zone and the macro-nutrient limited Subantarctic zone. The simulated productivity belt (c) is close to the regime transition.

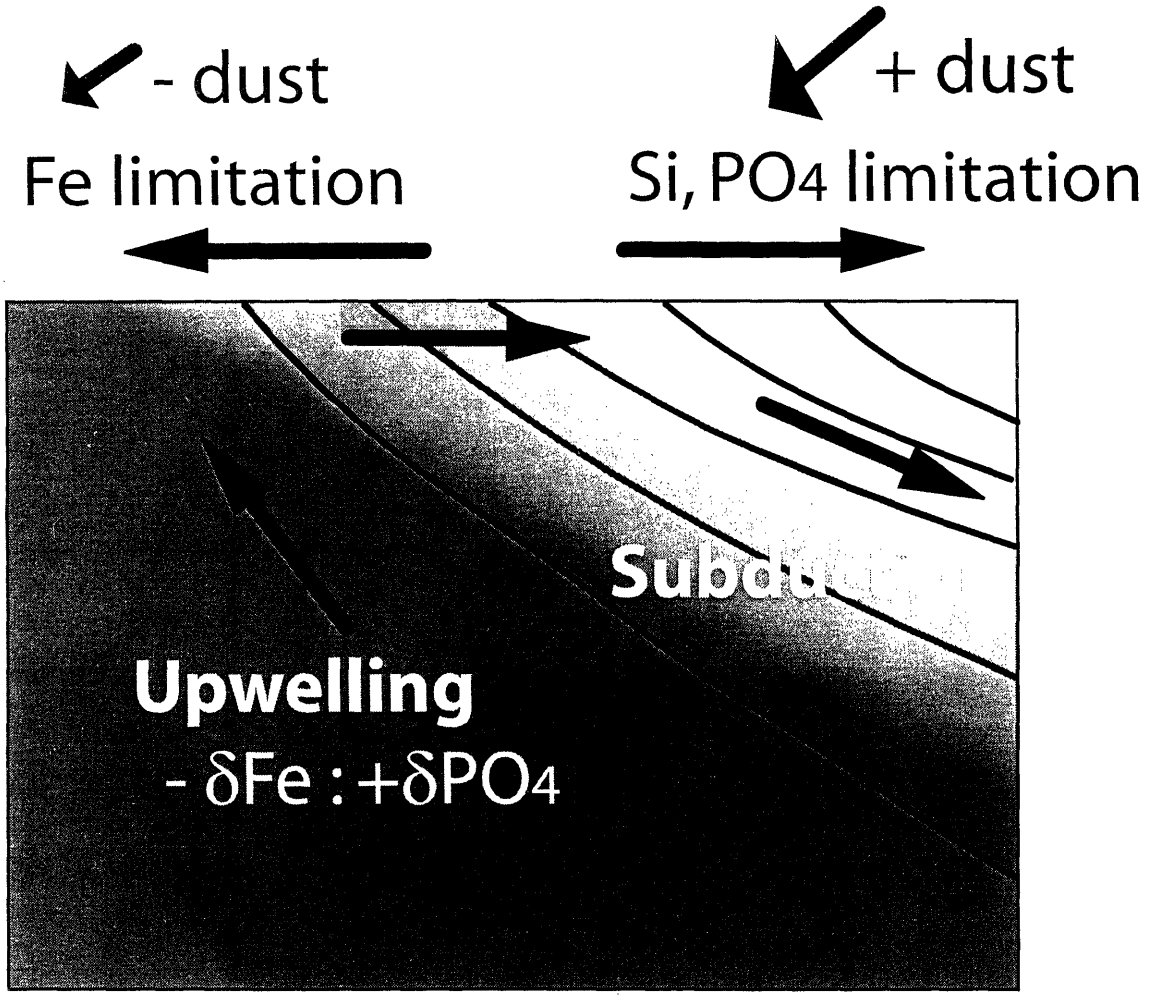

Figure 3-18: Schematic diagram showing the mechanisms controlling the position of the productivity belt.

limited Subantarctic zone. The overturning circulation of the Southern Ocean coupled with the differences in the biogeochemistry of iron and macro-nutrients dictates the location of the biogeochemical transition zone which leads to the formation of the productivity belt.

3.4 Discussion

In this chapter we estimated the magnitude and the spatial pattern of the export production using an inverse method, and illustrated the mechanisms controlling the biological productivity using a coupled physical-biogeochemical model including an

ecosystem of intermediate-complexity. The inverse method and the forward, physical-biogeochemical model together reproduce the band of high biological productivity in the Southern Ocean, "Antarctic Circumpolar Productivity Belt", which is qualitatively consistent with ship-based measurements (Honjo et al., 2000; Buesseler et al., 2002) as well as satellite ocean color data (Moore and Abbott, 2000; Moore and Abbott, 2002).

The Simulated productivity belt is located near the biogeochemical regime transition between iron-limited Antarctic zone and macro-nutrient limited Subantarctic zone where organism have optimal access to both nutrients. The vertical transport of macro-nutrients is driven by the residual mean circulation which is the net effect of Eulerian mean circulation and the eddy-induced circulation. The residual mean circulation upwells in the southern flank of the ACC, and downwells in the northern flank. This pattern of the overturning circulation, combined with the atmospheric dust deposition, controls the position of the regime transition and the productivity belt.

The numerical model can illustrate the regional distribution of small and large phytoplankton, qualitatively consistent with observations (Smith et al., 2000). Diatom-like large phytoplankton dominate the productivity southward of the ACC where silicic acid is available for phytoplankton growth. Small phytoplankton dominates equatorward of the ACC where the lack of silicic acid limits the grow of large phytoplankton. The export of biogenic silica is driven by large phytoplankton and that of organic carbon is controlled by both phytoplankton functional groups.

While the diagnosis of this numerical model is useful for understanding and illustrating the basic structure of the biogeochemistry in this region, we do not claim that the model can fully capture the complexity of physical circulation and ecosystem dynamics there. Mesoscale eddies cannot be resolved at this coarse resolution, and they are parameterized in this model. The uptake ratio between silicic acid and phosphate (and iron) may vary depending on environmental conditions, but they are prescribed in this model. A number of simplifications had to be made to formulate the numerical model which can run on the available computational resources, and we must be

cautious in interpreting the results. However, the intermediate-complexity, coupled physical-biogeochemical model can be used as a powerful tool for understanding some fundamental mechanisms controlling the biogeochemistry in the Southern Ocean. It is left for future studies to examine the role of the spatial and temporal variability of the ACC and mesoscale eddies. Furthermore, more ocean observations and laboratory studies are necessary to better understand and improve the representation of iron cycling and ecosystem dynamics.

Chapter 4

What sets the position of the productivity belt?

4.1 Introduction

Biological productivity in the Southern Ocean is characterized by a circumpolar belt of elevated biological production (Moore and Abbott, 2000; Schlitzer, 2002) known as "Antarctic Circumpolar Productivity Belt". The export of biogenic silica from the surface ocean has a maximum on the southern flank of the ACC based on the inverse calculation using a zonally averaged tracer model in chapter 3. Observations suggest that this elevated export of silica may be controlled by the seasonal bloom of diatoms (Honjo et al., 2000; Buesseler et al., 2002). Observed organic export also has a broad maximum near the ACC. In chapter 3, the large-scale patterns of nutrients and biological production were simulated using a global ocean physical-biogeochemical model, which includes parameterizations of ecosystem dynamics and iron cycling. The model can reproduce the circumpolar maximum in the biological productivity, and the mechanisms controlling the biological production were explored and illustrated through diagnosis of the simulated distribution of nutrients.

The position of the productivity belt is spatially correlated with the transition between the iron-limited Antarctic zone and the macro-nutrient-limited Subantarctic zone, where organisms have relatively good access to both nutrients. A diagnostic

tracer, Fe*, clearly reflects the regime transition (Fe*=0) in the numerical model. The position of the maximum silica export is close to the Polar Front (PF) where the lateral gradient of silica is the greatest, corresponding to the regime transition between iron-limited region (poleward of the PF) and the silica-limited regions (equatorward of the PF).

Kohfeld first suggested that there is a distinct, dipole pattern in the paleo-proxy of biological export in the Southern Ocean at the last glacial maximum (Bopp et al., 2003). Existing sediment records of the sinking particulate material were compiled into a global map showing spatial distributions in the difference of biological production between the LGM and the modern ocean (Fig.1-15, reproduced from the data published by Bopp et al; 2003). Their reconstruction suggests that biological productivity (including silica and organic export) was higher north of the Polar Front during the LGM relative to modern conditions, and was lower south of the Polar Front during the LGM. Bopp et al.(2003) configure a global circulation and biogeochemistry model with LGM physical and geochemical boundary conditions. They find that the reconstructed shift in export during the LGM is qualitatively captured by that model. However, it is not clear what processes in this complex model were responsible. While it may be possible that small changes due to various processes add up and form a strong signal, there may be a simple, zero-order explanation for such a large, coherent signal.

I hypothesize that the observed paleo-productivity proxies reflect changes in the position of the Antarctic Circumpolar Productivity Belt on glacial-interglacial timescales. The schematic diagram shown in Fig.4-1 illustrates the idea. The modern Southern Ocean is characterized by the maximum in export production near the Polar Front (Moore and Abbott, 2000; Moore and Abbott, 2002; Honjo et al., 2000; Buesseler et al., 2002; Schlitzer, 2002). If the position of the productivity belt were to have been at lower latitudes during the LGM, relative to modern conditions, local export production would be higher on the northern flank of the ACC during the LGM, and it would be lower on its southern flank. Thus, an equatorward migration of the productivity belt provides a zero-order explanation for the observed changes in the

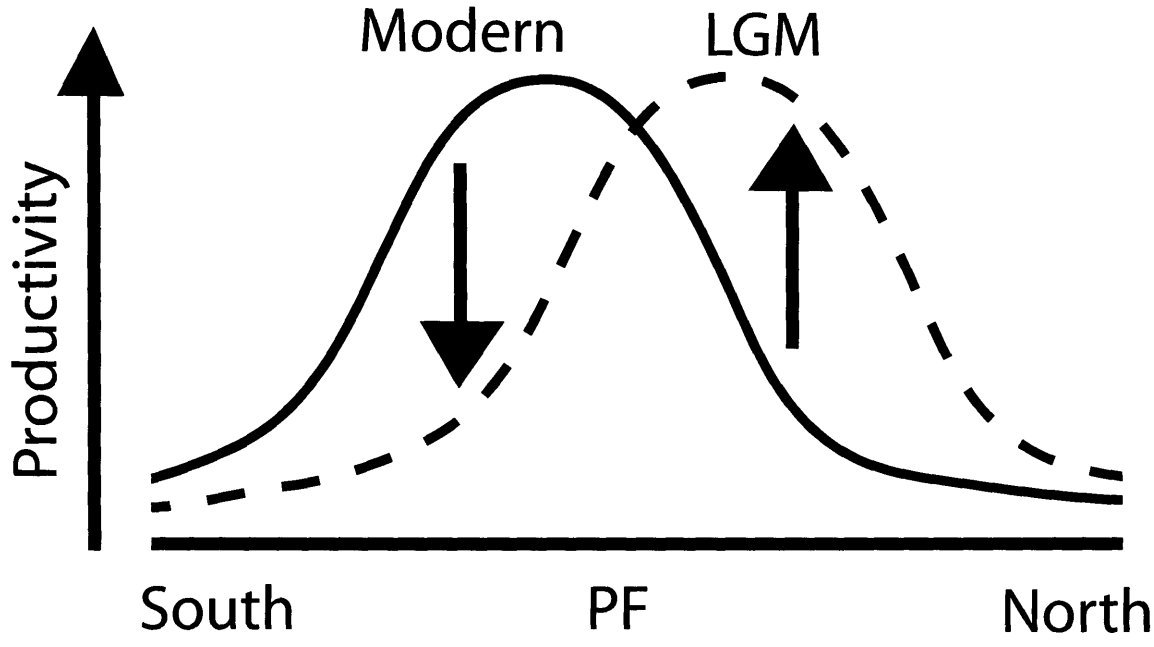

Figure 4-1: The observed pattern of changes in biological productivity between glacial and inter-glacial conditions can be accounted for by a northward shift of the productivity belt during ice ages. The position of the Polar Front in modern conditions is close to the node of the dipole pattern in the paleo-productivity proxies.

paleo-productivity proxies. What, though, might cause such a shift? In this chapter I explore possible shifts in the productivity belt due to the changes in the physical environment.

4.2 Aeolian iron supply and the position of the productivity belt

Polar ice core records reveal an anti-phase relationship between atmospheric pCO_2 and dust deposition on polar ice caps over glacial-interglacial timescales (Petit et al., 1999). High atmospheric pCO_2 and low dust deposition are found during warm periods, and low atmospheric pCO_2 and high dust deposition are found during ice ages. The response of biological productivity to increased dust deposition has been a focus of recent research (Martin et al., 1994; Coale et al., 1996; Boyd et al., 2000). In this section I consider the response of the position of the productivity belt to variations in atmospheric dust deposition.

Dutkiewicz et al.(2004) illustrated the simulated response of biological production to variations in dust deposition in a physical-biogeochemical model similar to the one discussed in chapter 3. In a suite of sensitivity experiments, increasing atmospheric dust deposition globally leads to an expansion of the oligotrophic regions. Increased aeolian dust input to the upwelling, iron-limited regions increases local productivity, and depletes local surface macro-nutrient concentrations. Since the surface Ekman transport across the gyre boundary is a major supply of macro-nutrients to the subtropical gyres (Williams and Follows, 2003), depleting surface macro-nutrients in the Southern Ocean diminishes the inventory of macro-nutrient in the subtropical thermocline and subtropical productivity in general. As a result, the boundary between the iron-limited regime and the macro-nutrient limited regime will move poleward and global dust deposition increases. Fig.4-2 illustrates schematically such a poleward shift of the biogeochemical regime transition in response to increased atmospheric dust deposition over the Southern Ocean.

In summary, an increased dust deposition during ice ages is unlikely to explain the observed equatorward shift in the position of the productivity belt. Increased dust deposition will increase the area of the macro-nutrient limited regime, and the transition between the iron-limited regime and the macro-nutrient limited regime will migrate poleward. One might expect, then, that the position of the productivity belt,

dictated by the regime transition, would also migrate poleward. The inferred change in biological production is then in the opposite direction to the pattern suggested by paleo-productivity proxies.

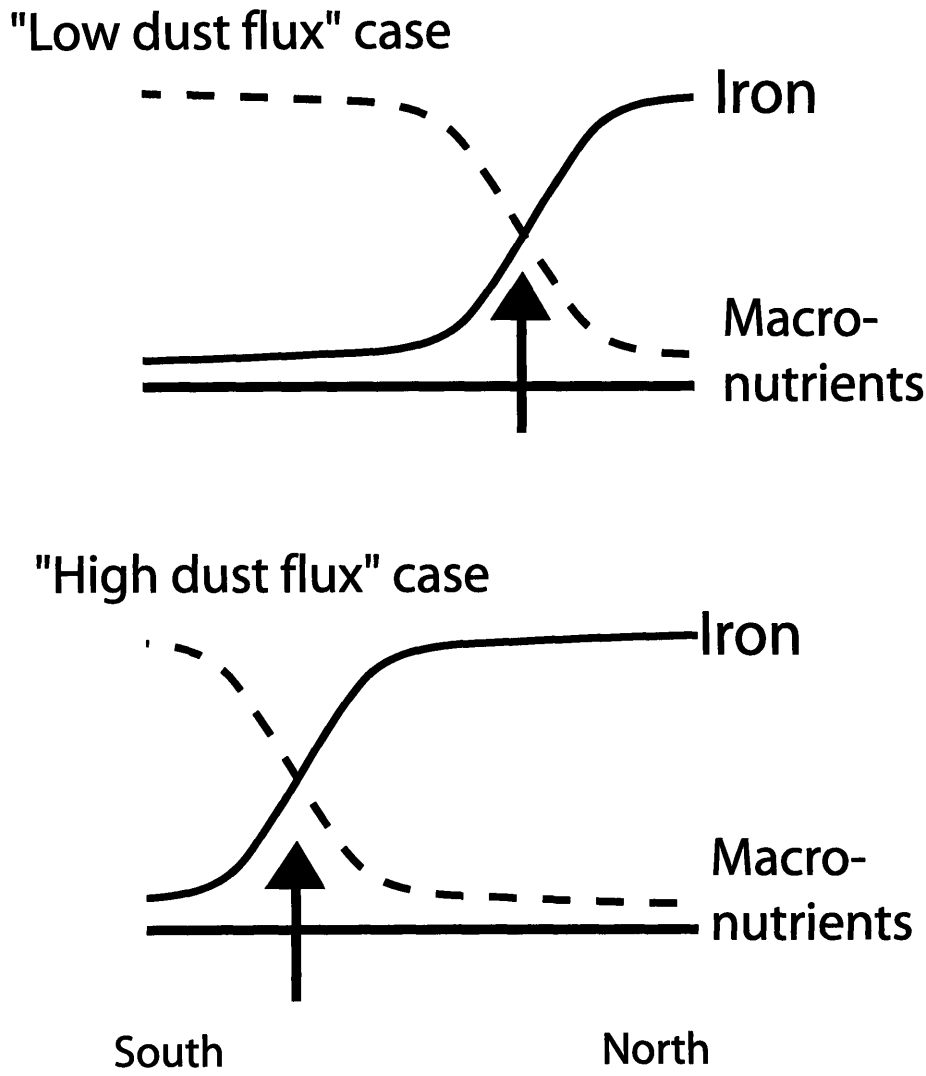

Figure 4-2: Schematic diagram showing the response of the surface nutrient distribution and the position of the productivity belt in the Southern Ocean. The arrows point to the position of the transition between iron-limited and macro-nutrient limited regimes.

4.3 Changes in the ocean circulation

Intensity and spatial patterns of upwelling play important roles in controlling the supply of nutrients to the surface ocean and the structure of biological productivity. The southern flank of the ACC is generally enriched in macro-nutrients due to the supply by upwelling of deep waters, and biological productivity is limited by the availability of iron. The northern flank of the ACC is generally depleted in macro-nutrients due to the absence of vertical supply of macro-nutrients, and biological productivity is limited by the availability of macro-nutrients.

The meridional overturning circulation was inferred from the climatological surface buoyancy flux for the modern ocean in chapter 2. Fig.2-9 shows that the residual mean vertical velocity changes its sign near the Polar Front where the upwelling of deep waters occurs on the southern flank of the ACC, and the subduction of intermediate and thermocline waters occurs in the northern flank. How is this pattern of the meridional overturning circulation influence the position of the productivity belt? In chapter 3, I showed that the position of the productivity belt is close to the transition between iron-limited and macro-nutrient limited regimes marked with $Fe^*=0$. In this section, I develop a simple theory describing the distribution of Fe^* in the Southern Ocean, and use it as a tool to illustrate the impact of physical circulation on the position of the productivity belt. I consider potential changes in the intensity and spatial pattern of the residual mean circulation.

Tracer observations suggest that there are two overturning cells in the Southern Ocean (Fig.4-3). The upper cell involves the upwelling of CDW, equatorward surface flow, and the formation of AAIW. The lower cell comprises upwelling of CDW, poleward surface flow, and the formation of AABW. To the south of the ACC where the CDW upwells into the surface layer, Fe^* is strongly negative reflecting the properties of the old, deep water. In the upper cell, the surface residual mean flow carries the newly upwelled water northward. As the water parcel move northward, macro-nutrients are depleted due to biological uptake and export. Similarly iron is consumed by biological uptake but aeolian iron input can partially resupply iron to the surface

waters. Fe* increases downstream of residual mean flow in the upper cell. The latitude where Fe* changes its sign is therefore determined by the position of the upwelling and the intensity of the surface residual flow. The position of the productivity belt will migrate northward if the upwelling region moves northwards. Alternatively, if the surface residual mean flow intensifies, the productivity belt migrates northward due to the stronger northward advection. The surface Fe* distribution in the upper cell can be illustrated using a highly idealized one-dimensional model of the surface layer in the ACC.

$$v_{res}\frac{\partial Fe^*}{\partial y} = D - S \tag{4.1}$$

where D is the rate of iron input due to the atmospheric deposition and S is the rate of the scavenging sink of iron. Fe* is not affected by biological sources and sinks. Assuming that D and S is uniform constant, we can integrate eq.(4.1) and solve for the position (y) where Fe* = 0.

$$y = y_0 + \left(\frac{-Fe_0^*}{D-S}\right) v_{res} \tag{4.2}$$

y represents the position of the productivity belt (Fe* = 0) and y_0 is the latitude of the upwelling region. Fe_0^* is the concentration of Fe* in the upwelling region, and is typically on the order of -1 nM. In this highly idealized example, the position of the productivity belt is linearly related to the intensity of the surface residual flow. The intensity of the upper cell circulation can be constrained by the air-sea buoyancy flux for modern climate (Speer et al., 2000; Marshall and Radko, 2003), and the tracer distributions are indeed consistent with the circulation inferred from the observed air-sea buoyancy fluxes (Ito et al., 2004). In the following sections, I use a simple parameterization of residual mean circulation to speculate possible changes in (1) the intensity of the surface residual flow in the upper cell, and (2) the position of the upwelling region. Then I discuss implications to the biological productivity during the LGM and possible interpretation of the paleo-productivity proxies.

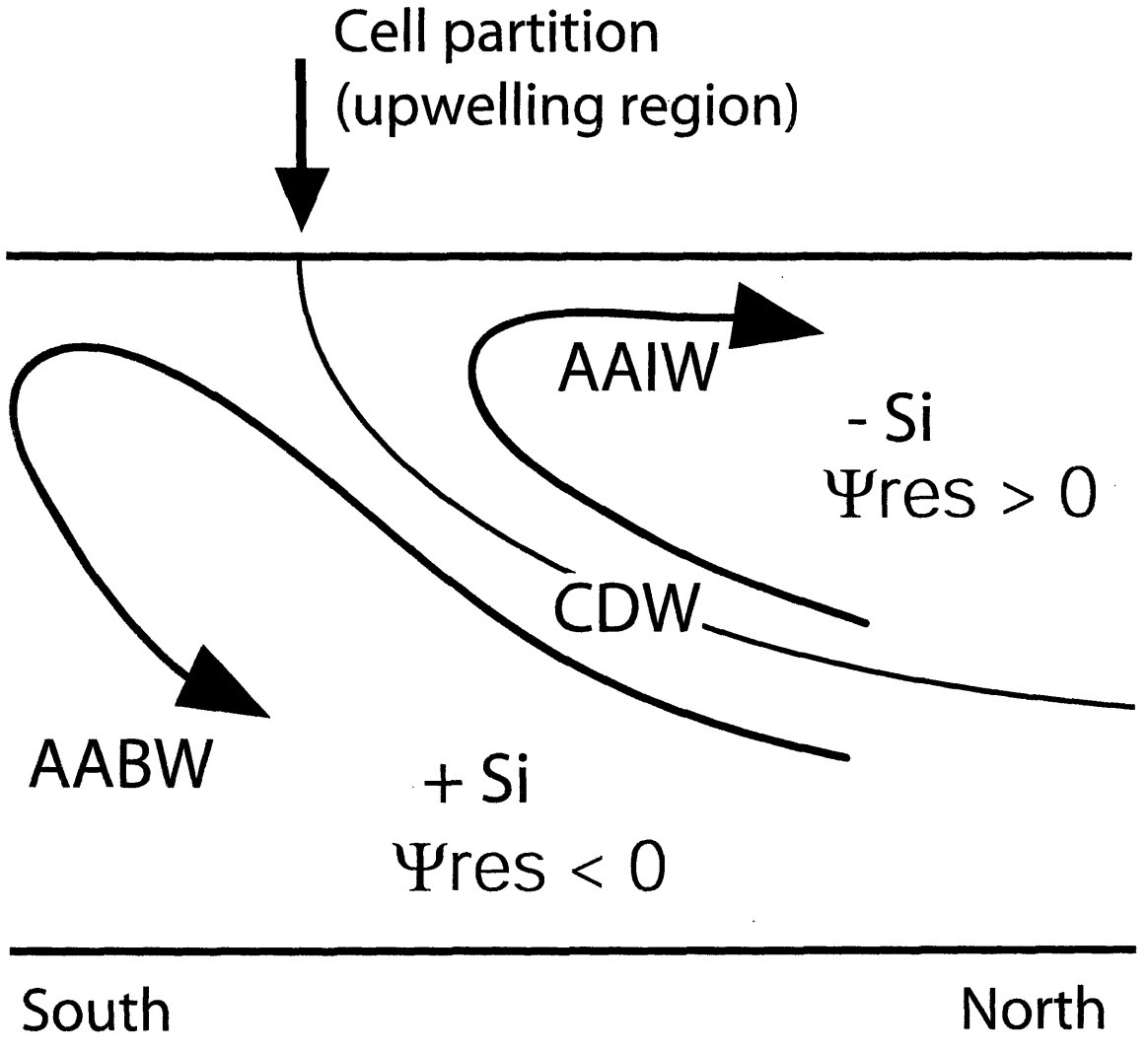

Figure 4-3: Schematic diagram showing the two-cell structure of the meridional overturning circulation in the Southern Ocean. Ψ_{res} changes its sign between the two cells: Ψ_{res} is positive in the upper cell, and negative in the lower cell.

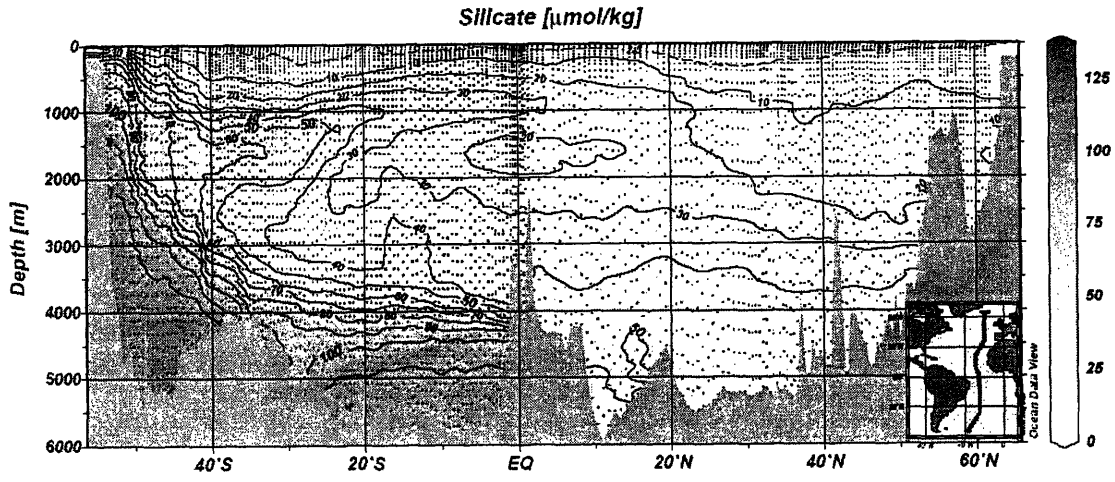

Figure 4-4: Observed silicic acid distribution in WOCE section, A-16.

4.3.1 Intensity of the surface residual flow

Antarctic ice core record shows that the atmospheric dust deposition on polar ice cap was greater during ice ages (Petit et al., 1999), and it has been interpreted that glacial climate had been dryer and windier. What is the impact of stronger wind stress over the ACC on the position of the productivity belt? If the stronger wind can intensify the surface residual mean flow, it could account for the northward shift of the productivity belt. Here I use a highly idealized parameterization of residual mean circulation to derive scalings for the intensity of the surface residual flow. Following the discussion in chapter 2, I parameterize the Eulerian mean circulation as the Ekman transport, and apply isopycnal thickness diffusion scheme for the mesoscale eddy fluxes.

$$\overline{\Psi} = -\frac{\tau_s}{\rho f} \tag{4.3}$$

$$\Psi_{eddy} = -K\left(\frac{\Delta z}{\Delta y}\right) \tag{4.4}$$

where τ_s is the surface wind stress over the ACC, and K is the isopycnal eddy diffusivity which is a uniform constant. $\frac{\Delta z}{\Delta y}$ represents the slope of isopycnal, expressed as a ratio between the depth of the subtropical thermocline, Δz, and the meridional length scale of the ACC, Δy, which is set to the width of the Drake Passage. Ventilated thermocline theory suggests that the depth of the subtropical thermocline is determined by curl of the surface wind stress (Luyten et al., 1983).

$$\Delta z \propto \sqrt{w_{ek}} \tag{4.5}$$

Stronger wind stress intensifies the eddy-induced circulation through the deepening of the subtropical thermocline. Assuming that the Ekman pumping increases with the overall amplitude of the wind stress, stronger wind stress deepens the subtropical thermocline and increases the slope of isopycnal.

$$\overline{\Psi} \propto \tau_s \tag{4.6}$$

$$\Psi_{eddy} \propto -\sqrt{\tau_s} \tag{4.7}$$

Thus the net effect of stronger wind stress is to increase residual mean flow. If the magnitude of the surface wind stress is doubled, the Eulerian mean circulation will increase by a factor of 2, whereas the eddy-induced circulation will increase by a factor of 1.4. Therefore, the net effect will be dominated by the greater increase in the Eulerian mean circulation. The sensitivity of the residual mean flow to the surface wind stress is sensitive to the parameterization of the eddy diffusivity. If the eddy diffusivity is also a linear function of the isopycnal slope, the Ψ_{eddy} will be a linear function of the wind stress. The sensitivity of the residual mean flow to the wind stress will be smaller in this case. Even so, stronger wind stress is likely to increase the residual mean circulation in a reasonable range of parameters. Fig. 4-5 illustrates the sensitivity of the residual mean flow to the surface wind stress with varying eddy parameterization. n represents the power-law relationship of the eddy-induced circulation.

$$\Psi_{eddy} = -k_n \left(\frac{\Delta z}{\Delta y}\right)^n \tag{4.8}$$

where k_n is a constant for eddy closure, which is adjusted such that the magnitude of the residual mean circulation is set to 15 Sv for the control case. Residual mean flow increases with the surface wind stress in all cases but the sensitivity significantly vary depending on n. Considering the relationship (4.2), stronger wind stress can shift the productivity belt northwards through the intensification of the surface residual flow. If we consider the case with n=1, a 50% stronger wind stress can increase the residual mean flow by 65%. It could shift the productivity belt northward on the order of 650 km based on this simple calculation.

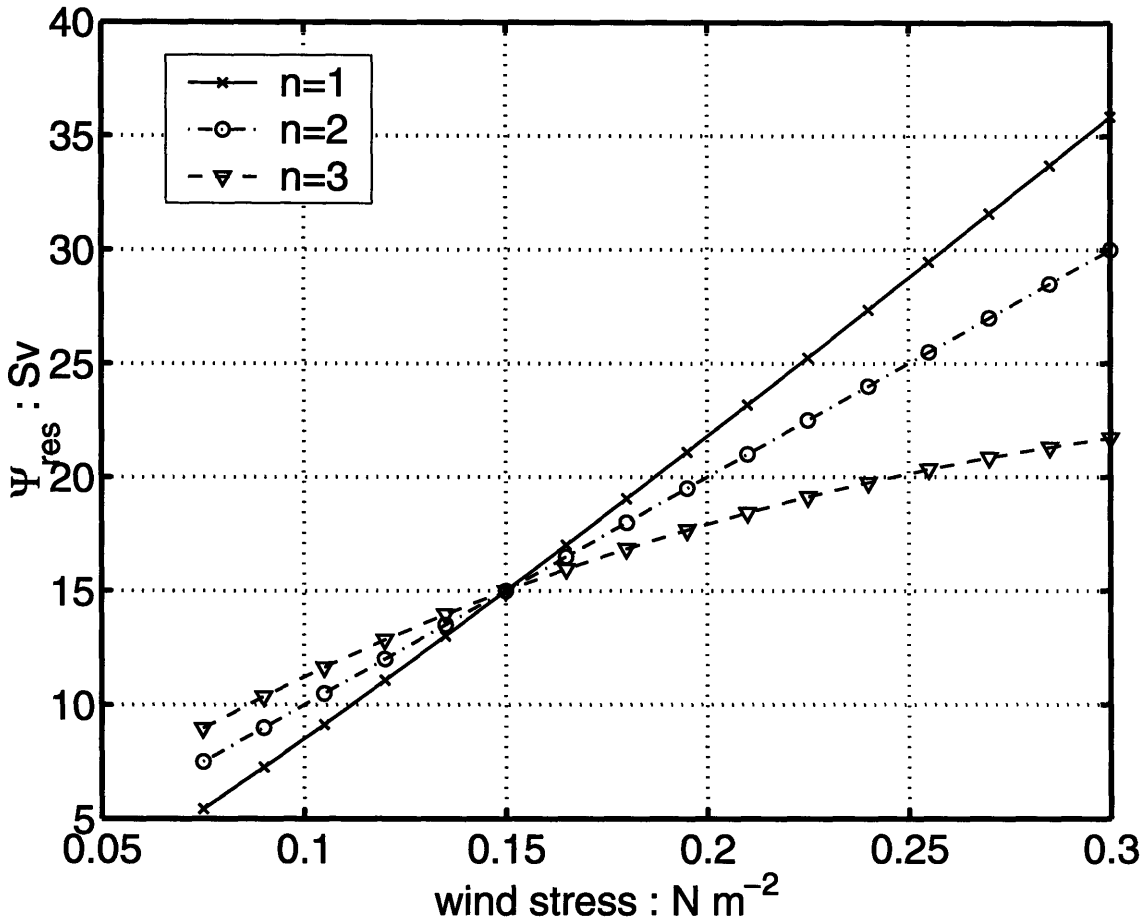

Figure 4-5: Sensitivity of the surface residual mean flow to the surface wind stress.

4.3.2 What controls the position of the cell partition?

Here I develop an idealized, zonally averaged model of the meridional overturning circulation to illustrate the possible change in the upwelling region. The theory is building on Transformed Eulerian Mean theory (Andrews and McIntyre, 1976), somewhat similar to the model described in chapter 2. The zonally and temporally averaged buoyancy equation can be written as

$$\mathbf{v_{res}} \cdot \nabla \bar{b} = -\nabla \cdot \mathbf{F}^{\dagger} + S + B \tag{4.9}$$

where residual mean circulation, $\mathbf{v_{res}} = \overline{\mathbf{v}} + \mathbf{v}^{\star}$, is the sum of the Eulerian mean flow and the eddy-induced flow. (See chapter 2 for detailed definition of $\mathbf{v_{res}}$) The eddy induced velocity is defined as $\mathbf{v}^{\star} = \mathbf{i} \times \nabla \Psi_{eddy}$. Here $\mathbf{F}$ represents the diabatic component of the eddy fluxes, and S represents small-scale diapycnal mixing. B is air-sea buoyancy fluxes at the surface. Eddy-resolving simulations of an idealized circumpolar current (Karsten et al., 2002) show that the eddy buoyancy flux in the interior ocean is closely aligned with isopycnal surfaces, so that $\mathbf{F}^{\dagger} \sim \mathbf{0}$. If we assume an adiabatic condition in which the eddy buoyancy flux is directed entirely along $\bar{b}$ surfaces and S is negligibly small, we can write:

$$\mathbf{v}^{\dagger} \cdot \nabla \bar{b} = J(\Psi_{res}, \bar{b}) = 0 \qquad \text{interior} \tag{4.10}$$

This relationship puts strong constraints on the meridional overturning circulation. The residual mean flow, $\mathbf{v}^{\dagger}$, is perpendicular to the mean buoyancy gradient, and the residual mean stream function, $\Psi_{res} = \overline{\Psi} + \Psi_{eddy}$, becomes parallel to the isopycnal surfaces, $\Psi_{res} = \Psi_{res}(\bar{b})$ (see Fig.1-6).

The upper cell circulation involves the upwelling of the Circumpolar Deep Water (CDW) and the formation of the Antarctic Intermediate Water (AAIW), and can be estimated from buoyancy fluxes in the surface layer, which balance the near-surface residual circulation (Marshall and Radko, 2003). The upper cell is generally characterized by a positive residual circulation, $\Psi_{res} > 0$, and the sign of Ψ_{res} changes

at the division with the lower cell. I examine the processes which set the partitioning, $\Psi_{res} = 0$, and by association, the position of the productivity belt, and how it might vary with prescribed physical parameters such as surface wind stress and stratification.

Here I assume that the surface buoyancy distribution is prescribed as a linear function of latitude, and the buoyancy distribution at the northern boundary is specified as an exponential function of z. This is supported by observations presented in (Karsten and Marshall, 2002). Then, calculating the $\Psi_{res} = 0$ surface reduces to a boundary value problem. We now summarize the assumptions made in calculating the position of the cell partition.

- Surface boundary condition is specified as $\bar{b}(y, -h_m)$, which is a linear function of y.

- Northern boundary condition is specified as $\bar{b}(L_y, z)$, which is an exponential function of z.

- The position of the isopycnal corresponding to the cell partition, $\Psi_{res}(\bar{b}) = 0$, must connect the surface and northern boundary conditions.

4.3.3 Model domain and the Eulerian mean circulation

The model (Fig.4-6) consists of a zonally re-entrant channel with a longitudinal extent, L_x = 20,000 km, a latitudinal extent, L_y = 2,000 km, and a depth, H = 4 km. The channel has an open boundary to the north ($y = L_y$), the sea surface is at $z = 0$, sea floor is at $z = -H$, and a bottom boundary layer is prescribed between $-H < z < -h_b$.

The zonal current is forced with a spatially uniform wind-stress, τ_s, over the ACC[1]. The wind stress decays within a thin, surface Ekman layer. Eulerian mean,

[1]Here I use the highly idealized, uniform wind stress. This assumption is later evaluated with a version of the model with spatially varying wind, and the results are qualitatively similar to the uniform-wind model.

zonally-averaged zonal momentum equation on a f-plane can be written as

$$-f\overline{v} = -\frac{1}{\rho_0}\frac{\Delta p}{L} + \frac{1}{\rho_0}\frac{\partial \tau_s}{\partial z} \tag{4.11}$$

Here we neglect Reynolds stresses and nonlinear acceleration terms. The zonal current is blocked by a prescribed bottom topography similar to Drake Passage in the Southern Ocean, which supports a zonal pressure gradient below the topographic depth, $-h_t$. Δp is determined such that the vertical integral of the zonal pressure gradient balances the surface wind stress.

$$\Delta p = \frac{\tau_s L}{H - h_t} \tag{4.12}$$

Here Δp is assumed to be independent of z below the topographic depth, thus, the geostrophic transport is determined by the surface wind stress. the Eulerian mean meridional velocity can be calculated from eq.(4.11) for three depth ranges separately.

$$\overline{v} = \begin{cases} -\frac{\tau_s}{\rho_0 f h_m} & -h_m \leq z < 0 \\ 0 & -h_t \leq z < -h_m \\ \frac{\tau_s}{\rho_0 f (H-h_t)} & -H \leq z < -h_t \end{cases} \tag{4.13}$$

The Eulerian mean, meridional velocity is directed southward below the topographic depth. The zonal pressure gradient below the topographic depth must ultimately balance the surface momentum input from the surface wind stress. Likewise, the poleward, deep Eulerian mean circulation balances the equatorward Ekman transport in the surface ocean.

Considering continuity in the meridional plane, we define an Eulerian mean overturning stream function, $\overline{\Psi}$, as the vertical integral of the meridional velocity, $\overline{v}$,

shown in eq.(4.13).

$$\overline{\Psi} = \begin{cases} -\overline{\Psi}_0 \frac{z}{h_m} & -h_m \leq z < 0 \\ \overline{\Psi}_0 & -h_t \leq z < -h_m \\ \overline{\Psi}_0 \left(1 + \frac{z+h_t}{H-h_t}\right) & -H \leq z < -h_t \end{cases} \tag{4.14}$$

where $\overline{\Psi}_0$ is defined as $-\frac{\tau_s}{\rho_0 f}$.

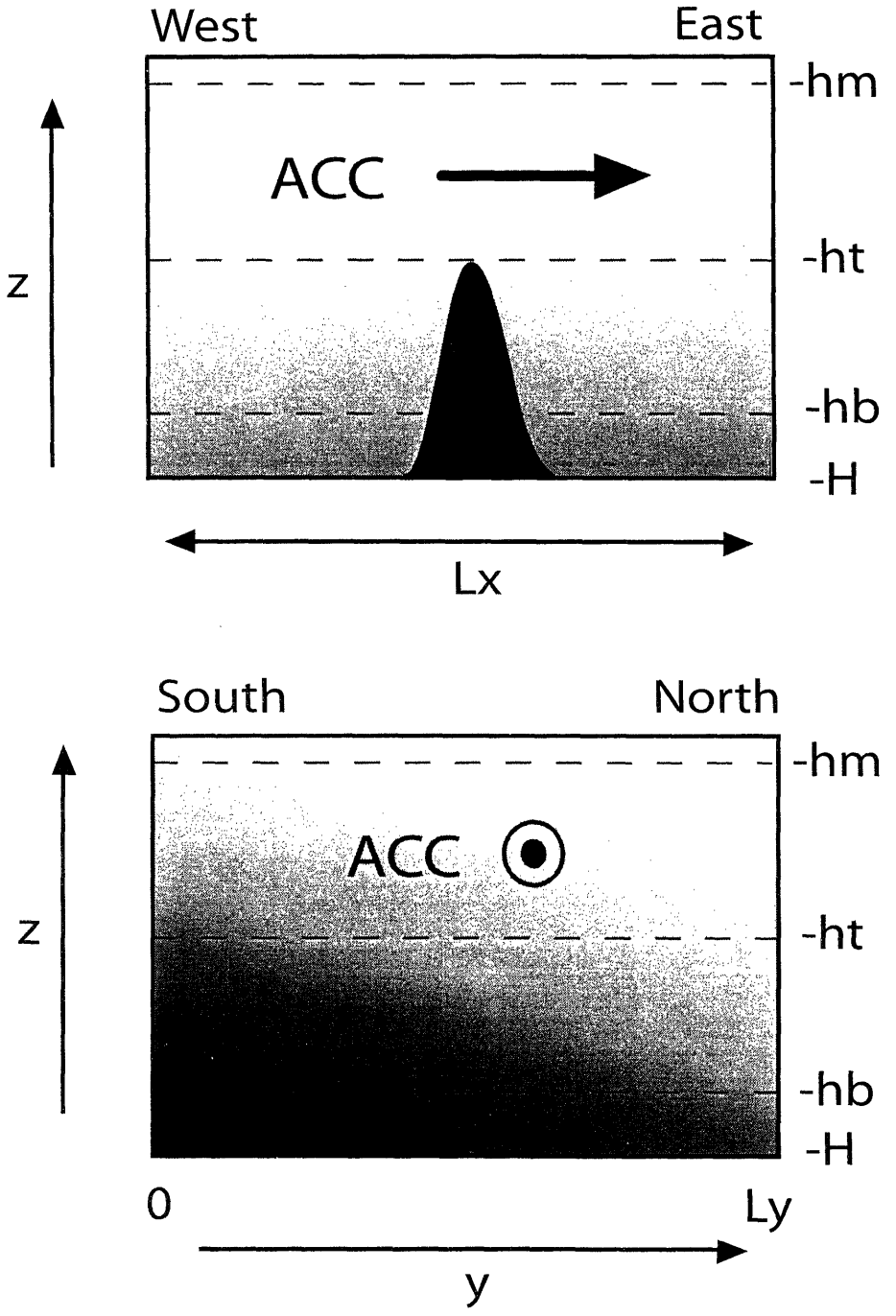

Figure 4-6: Schematic diagram of the model architecture. The model has an idealized bottom topography below the depth of $-h_t$, and the effect of the topography on the circulation is parameterized as a zonal pressure gradient in the zonally-averaged momentum equation.

4.3.4 Method of solution

Here we parameterize the eddy induced circulation using an isopycnal thickness diffusion scheme (GM90) such that $\Psi_{eddy} = K\, s_b$, where s_b is the slope of isopycnals. The residual mean circulation is the sum of Eulerian mean circulation and the eddy-induced circulation, $\Psi_{res} = \overline{\Psi} + \Psi_{eddy}$. The position of the cell partition is determined by solving for the particular condition $\Psi_{res} = 0$. The isopycnal slope in the interior ocean on the $\Psi_{res} = 0$ surface is

$$s_b(\Psi_{res} = 0) = \left(\frac{\partial z}{\partial y}\right)_{\bar{b},\Psi_{res}=0} = -\frac{\overline{\Psi}}{K} \tag{4.15}$$

In this special case ($\Psi_{res} = 0$) the isopycnal slope is completely determined by the ratio between the Eulerian mean circulation and the isopycnal eddy diffusion coefficient. The surface buoyancy distribution is prescribed as an idealized linear profile, and the northern buoyancy distribution has a exponential profile. We assume that the dynamics of the subtropical gyres essentially sets z^*, the e-folding depth scale for the stratification at the northern boundary. Thus the boundary condition are

$$\bar{b}(y, -h_m) = b_1 + \frac{b_2}{L_y} y \qquad \text{surface} \tag{4.16}$$

$$\bar{b}(L_y, z) = b_1 + \frac{b_2}{1-\gamma}\left(e^{\frac{z+h_m}{z^*}} - \gamma\right) \qquad \text{north} \tag{4.17}$$

$$\gamma \equiv e^{\frac{-h_b+h_m}{z^*}}$$

where b_1, b_2 and γ are constants. The e-folding depth scale for the stratification in the northern boundary, z^*, essentially determines the stratification in the ACC. Fig.4-7 shows the profile of the northern boundary condition (eq.4.17) with varying z^*. We solve the boundary condition problem defined by eq.(4.15) through (4.17).

Above the depth of the topography ($z > -h_t$), the Eulerian mean circulation, $\overline{\Psi}$, is a uniform constant, and the slope of $\Psi_{res} = 0$ surface is also a uniform constant following eq.(4.15). Here we define y_m as the latitude where $\Psi_{res} = 0$ surface intersects the base of the surface mixed layer, and z_m as the depth where $\Psi_{res} = 0$ surface

intersects the northern boundary. Then the isopycnal slope determined by y_m and z_m.

$$\frac{z_m}{L_y - y_m} = \frac{\overline{\Psi}}{K} \tag{4.18}$$

Since $\Psi_{res} = 0$ surface coincides with an isopycnal surface, it must satisfy boundary conditions, eq.(4.16) and (4.17).

$$\frac{y_m}{L_y} = \frac{1}{1-\gamma}\left(e^{\frac{z_n + h_m}{z^*}} - \gamma\right) \tag{4.19}$$

Combining these two equations, y_m and z_m are determined as a function of only two parameters, $\eta \equiv \frac{\overline{\Psi}_0}{K}$ and z^*. The former depends on the surface wind stress and the eddy diffusivity, and the latter depends on the stratification of the northern boundary condition.

Below the depth of the topography ($z < -h_t$), the Eulerian mean circulation, $\overline{\Psi}$, is no longer a uniform constant, and these equations are slightly modified. I numerically solve the model equations (4.18, 4.19), and the solution for y_m and $z(y, y_m)$ are plotted in Fig.4-8 and 4-9. In Fig.4-8 and 4-9 we illustrate the sensitivity of the position of the cell partition to variations in η (Fig.4-8) and z^* (Fig.4-9). These solutions illustrates the sensitivity of the position of the cell partition to the changes in the prescribed physical forcing including the wind stress and the stratification. In the following sections, I describe the physical mechanisms which could shift the position of the cell partition, thus the position of the productivity belt.

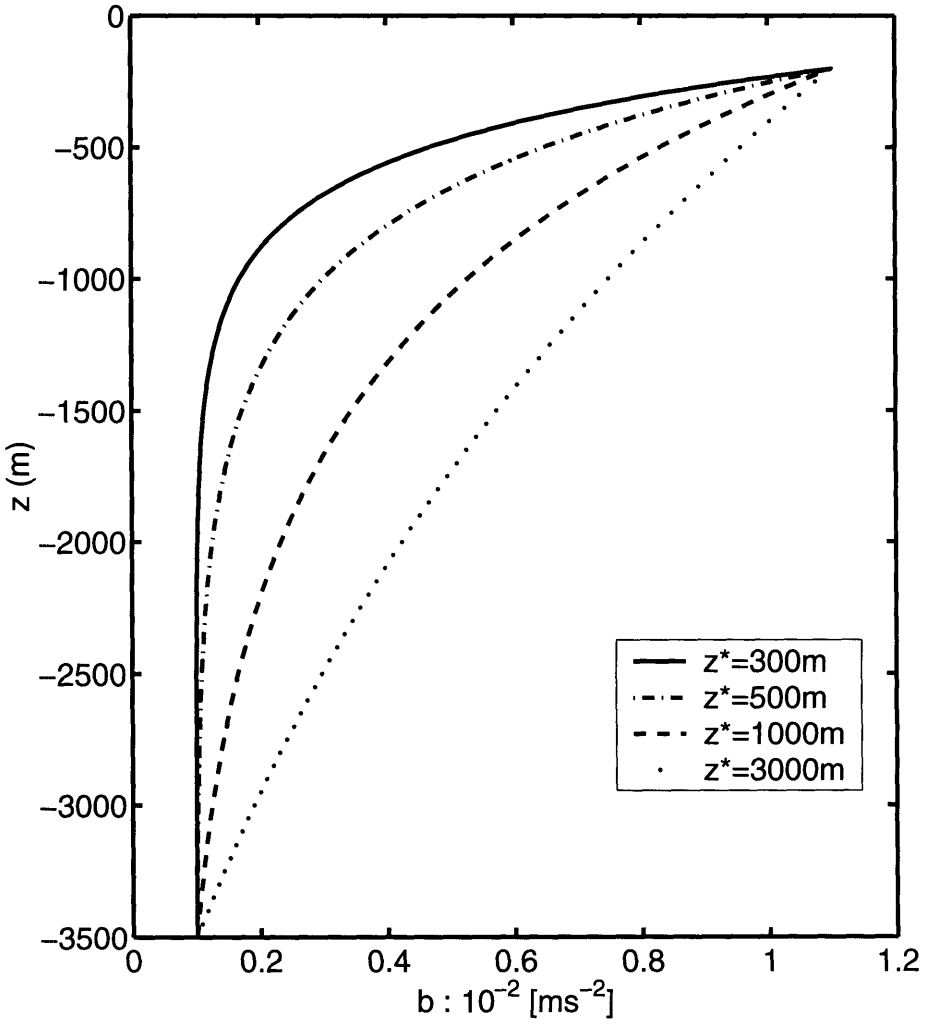

Figure 4-7: The northern boundary condition, $g(z)$, with varying z^*.

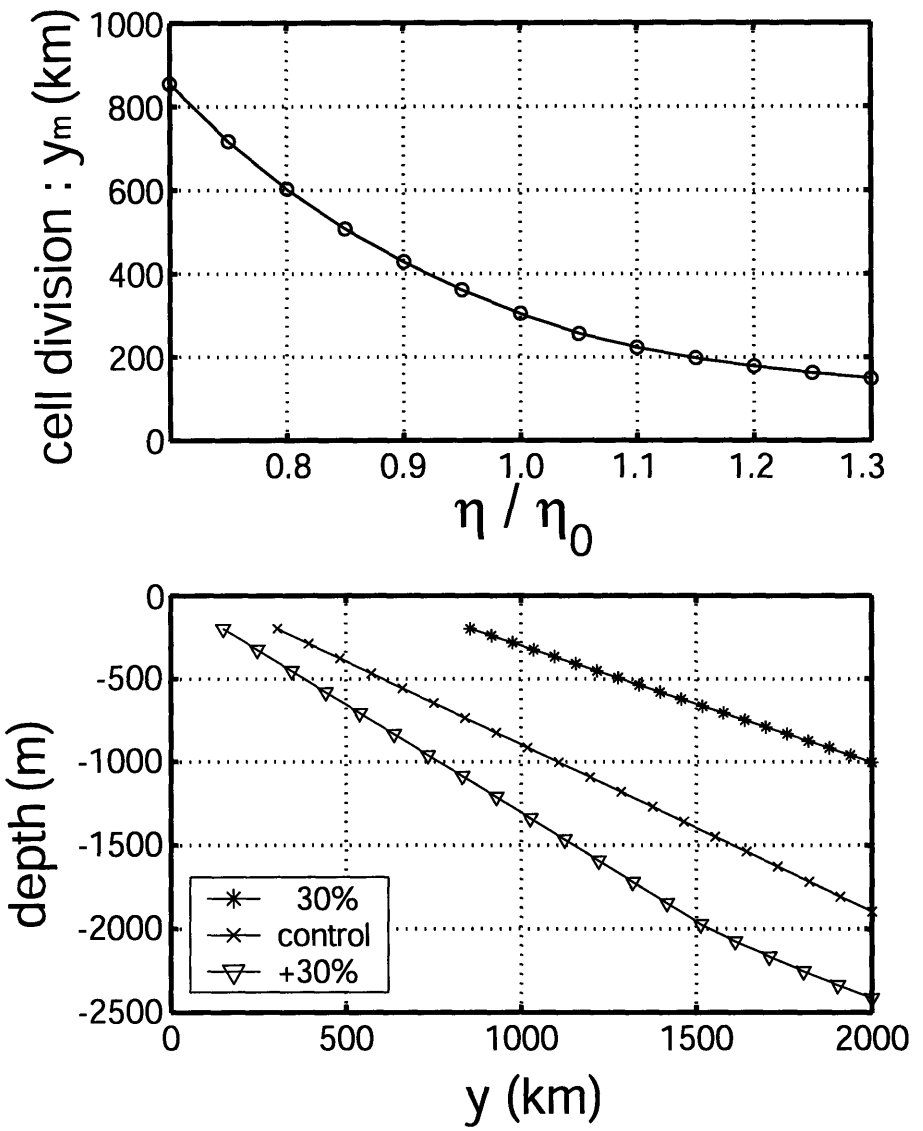

Figure 4-8: Sensitivity of y_m to variation in η. η_0 represents the value for the control run, $\eta_0 = 10^{-3}$. (a) The solution for y_m as a function of η. (b) The position of the cell partition for three cases: the case with a 30% reduction in η, the control run, and the case with a 30% increase in η

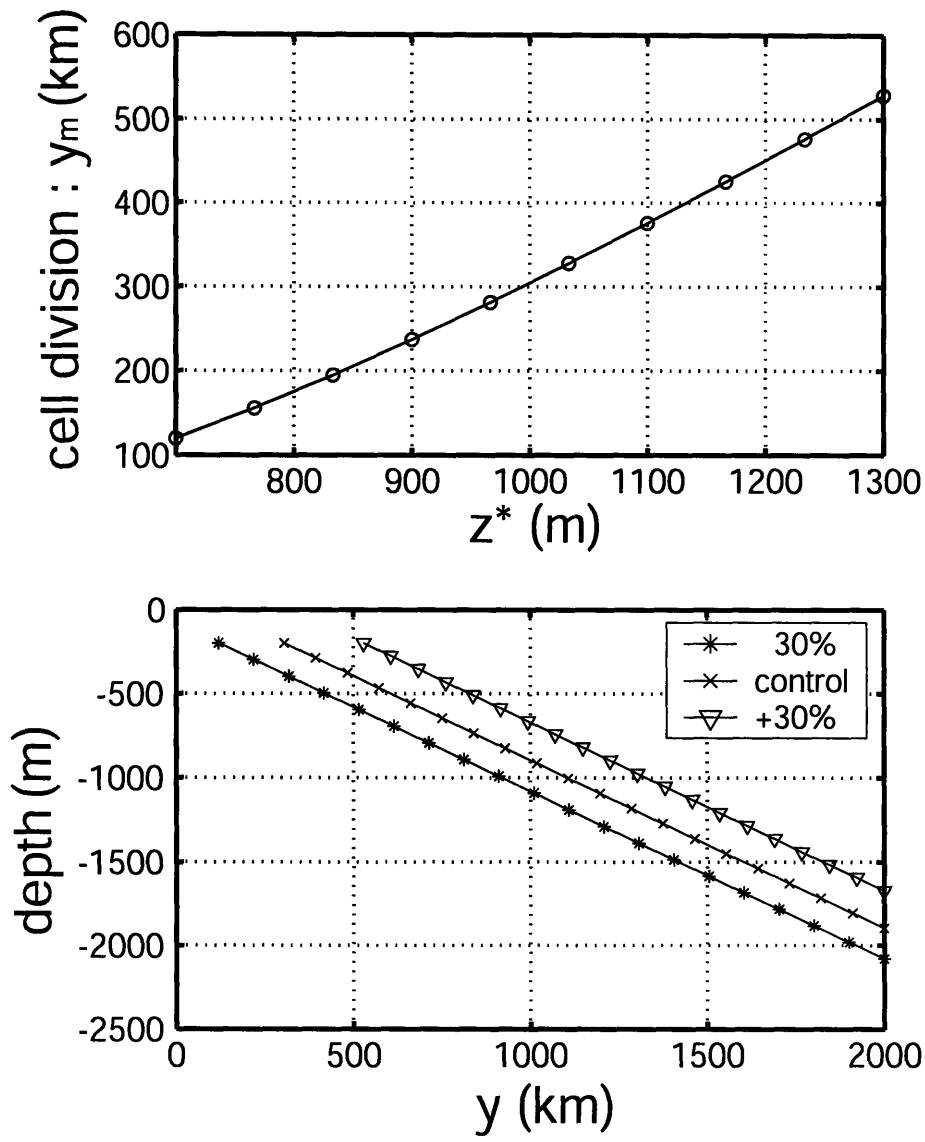

Figure 4-9: Sensitivity of y_m to variation in z^*. (a) The solution for y_m as a function of z^*. (b) The position of the cell partition for three cases: the case with a 30% reduction in z^*, the control run, and the case with a 30% increase in z^*

4.3.5 Sensitivity of y_m to η

We first discuss the effect of the dimensionless parameter, η, on the position of the cell partition. η is defined as the ratio between the wind-driven, Eulerian mean circulation, $\overline{\Psi}_0$ and the eddy diffusivity, K, and it represents the magnitude of the slope of the isopycnal in the limit of $\Psi_{res} = 0$. The boundary value problem of eq. (4.18, 4.19) requires that the slope of isopycnal, η, which is dictated by the surface wind stress, must meet the hydrographic structure imposed by the boundary conditions.

Fig.4-8(a) indicates that y_m decreases with η, and the relationship is not linear where the sensitivity is larger when η is smaller. Fig.4-8(b) shows the position of the cell partition $z(y, y_m)$ with variations in η. As η becomes smaller, the cell partition moves northward and upward, and the upper cell becomes smaller and the lower cell becomes larger. The cell partition is very sensitive to the magnitude of η. The position of the cell partition is determined by the boundary value problem (4.18, 4.19). The buoyancy distribution at the northern boundary is prescribed as an exponential function of z, stratification becomes weak in the deep ocean, and imposed isopycnal slope becomes steeper. Thus, increasing surface wind stress and η leads to the deepening of the cell partition. Reducing the magnitude of η by 30% leads to the northward shift of the cell partition by approximately 500 km. In contrast, increasing the magnitude of η by 30% shifts the cell partition southwards by only 150 km.

The definition of Ψ_{res} can give a clear, physical interpretation for the sensitivity of the cell partition. In the upper water column ($-h_t < z$),

$$\begin{aligned} \Psi_{res} &= \overline{\Psi} + \Psi_{eddy} \\ &\sim K\left(\eta - \frac{z^*}{L_y}\right) \end{aligned} \tag{4.20}$$

The relative magnitude of $\overline{\Psi}$ and Ψ_{eddy} determine the sign of Ψ_{res} and the position of the cell partition. Increasing η essentially increases the relative magnitude of the Eulerian mean circulation, and tends to increase Ψ_{res}. Therefore, the regions affected by the upper cell circulation increases. Fig.4-8(b) clearly indicates that the cell partition moves downward and southward as η increases.

Paleo-productivity proxies suggest that the position of the productivity belt could have been shifted northward during the LGM, relative to the modern condition. The position of the cell partition migrates northwards when the surface wind stress is reduced. It is not clear if the surface wind stress over the Southern Ocean could have been significantly weaker during the LGM condition. In the following section, I consider the sensitivity to the depth of the subtropical thermocline, z^*, which also influence the position of the productivity belt.

4.3.6 Sensitivity of y_m to z^*

Stratification of the northern boundary could be determined by the depth of the subtropical thermocline. It significantly affects the position of the cell partition. We essentially set the buoyancy structure of the ACC through the boundary conditions. The stratification is expressed in terms of z^* which is the e-folding depth scale for $\bar{b}_n$ as shown in eq.(4.16). A small z^* indicates a shallower subtropical thermocline and increased stratification. Fig.4-9(a) indicates that y_m increases with z^*. Fig.4-9(b) shows the position of the cell partition $z(y, y_m)$ as determined by the variation in z^*. As z^* becomes larger, the cell partition moves northward and upward, and the upper cell becomes smaller and the lower cell becomes larger. The stratification imposed by the northern boundary condition sets the spatial profile of the isopycnal slope in the model. Isopycnal slope becomes steeper in the deep ocean, and when z^* is large, the isopycnal slope generally becomes steeper. Since the slope of Ψ_{res} surface is dictated by the wind stress (η) and do not vary with z^*, the cell partition must migrate upward and northward. Increasing z^* by 30% leads to the northward shift of the cell partition by approximately 220 km. The definition of Ψ_{res} as shown in eq.(4.20) can provide a physical interpretation for the sensitivity of the cell partition. Eddy-induced circulation, Ψ_{eddy}, is determined by the eddy diffusivity and the slope of isopycnals.

$$\Psi_{eddy} = K\, s_b \sim -K\frac{z^*}{L_y} \tag{4.21}$$

By increasing z^*, the isopycnal slope increases, and the eddy-induced flow is intensified. Note that the isopycnals are tilted downward to the north in the ACC, and so the sign of Ψ_{eddy} is always negative. The regions affected by the upper cell circulation decreases as z^* increases. Fig.4-9(b) clearly indicates that the cell partition moves upward and northward as z^* increases.

The partitioning between the two cells can vary significantly depending on the variations in the surface wind stress and the stratification in the ACC. Fig.4-10 shows the sensitivity of y_m to the combined variations in η and z^*. Both parameters are varied over $\pm$ 30% of the control values. Within this rage of the parameters, the

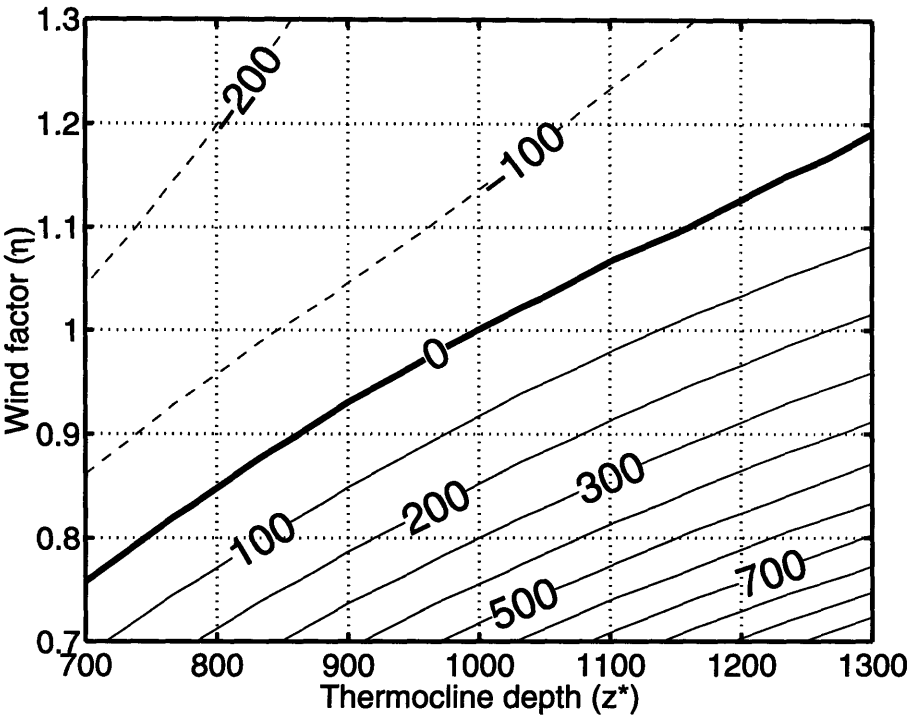

Figure 4-10: A schematic diagram for the response of the cell partition to η and z^*. The contour represents relative displacement of the position of the cell partition.

potential displacement of the cell partition is expected to be more than 700 km, which could impact on the deep circulation on the global scale. As we discuss in the following section, variations in the surface wind and the thermocline depth could result in the reorganiztion of the meridional overturning circulation and the position of the productivity belt.

4.4 Implications for the Last Glacial Maximum

In this chapter, we discuss possible mechanisms for the changes in the biological productivity due to varying physical environment. These results have significant implications for potential changes in the position of the productivity belt over glacial-interglacial timescales. I assumed that the glacial climate had been windier due to an elevated dust deposition in the polar ice core records. However, it is difficult to infer quantitative change in the surface wind speed over the Southern Ocean. Atmospheric GCM simulation of the ice ages has been carried out in the Paleoclimate Model Intercomparison Project (hereafter, PMIP) (Joussaume and Taylor, 2000). Changes in simulated surface momentum drag between the LGM and modern condition from a subset of PMIP simulations are examined (Wyputta et al., 2000). They argue that the ensemble mean of the surface wind stress over the Southern Ocean was weaker during the LGM. However, there are significant model-model differences in the surface wind speed over the Southern Ocean. These differences can be due to differences in the sub-grid scale parameterization for clouds and precipitation as well as differences in the model formulation and resolutions. These atmospheric GCMs, on ensemble average, can qualitatively reproduce pressure and wind distributions of modern climate, however, significant model-model differences are found (Gates et al., 1998). Furthermore, the modeled wind stress field is highly sensitive to the specification of SST (whether prescribed from CLIMAP or computed as a response to the heat budget of ocean mixed layer). Thus it is difficult to infer a systematic change in the wind stress based on these atmospheric GCM simulations. Here I discuss some possible changes in the physical environment during the LGM based on the observed, polar ice core records.

- Increased aeolian dust deposition
- Increased surface wind stress
  $\longrightarrow$ changes in the intensity of the surface residual flow
  $\longrightarrow$ changes in the latitude of upwelling region

An elevated dust deposition during ice ages is unlikely to explain the observed pattern of the paleo-productivity proxies. The paleo-productivity proxies suggest that the productivity belt could have shifted equatorward during the LGM relative to the modern ocean. When atmospheric dust deposition is increased uniformly on the global scale, it will increase the area of the macro-nutrient limited regime, and the transition between the iron-limited regime and the macro-nutrient limited regime will shift poleward (Dutkiewicz et al., 2004). Likewise, the position of the productivity belt will shift poleward, and the inferred changes in the biological production have opposite sign from the pattern suggested by the paleo-productivity proxies.

In chapter 3, the simulated maximum of the export production is found at the regime transition between the iron-limited and macro-nutrient limited regions, marked by Fe*=0. Thus I focused on the physical processes which impact on the latitude where Fe* changes its sign in the Southern Ocean. Eq.(4.2) illustrate that the position of the upwelling region and the intensity of the surface residual flow impact on the position where Fe* = 0.

First, I consider an idealized model of the residual mean flow to explore the sensitivity of the intensity of the residual mean flow to the intensity of the surface wind stress. Assuming the spatial pattern of the wind stress remains the same, a stronger wind stress leads to stronger Ekman transport and eddy-induced circulation. These effects partially compensate one another. For reasonable range of parameters, the increase in the Ekman transport dominates over the eddy-induced circulation and the residual mean flow increases with stronger wind. The sensitivity depends on the parameterization of eddy-induced transport. In the case with constant eddy diffusivity, a 50 % increase in the surface wind stress can lead to northward shift of the productivity belt on the order of 650 km. The response becomes smaller if the eddy diffusivity is a function of the isopycnal slope. The response of the productivity belt is significant and the intensification of the surface residual flow could be the leading order mechanism for the northward shift of the productivity belt.

Secondly, we explored the possible change in the position of the upwelling region by calculating the partition between the upper cell and the lower cell using the

simple dynamical model. Fig.4-11 schematically illustrates the response of the cell partition to variations in η and z^*. Increasing η or reducing z^* lead to a southward and downward shift of the cell partition. Sensitivity calculations suggest that significant displacement of the cell partition (on the order of 500 km) is possible over $\pm 30\%$ variations in η and z^*. Note that the sensitivity shown in Fig. 4-10 is based on a constant eddy diffusivity. The magnitude of the sensitivity can change if the eddy diffusivity is allowed to vary with isopycnal slope. The result of the sensitivity study indicates that the upwelling region shifts northward if the surface wind stress is weaker and/or the subtropical thermocline is deeper. Considering that the depth of the subtropical thermocline is also influenced by the Ekman pumping rate in the subtropical region, the weaker wind stress and deeper thermocline is not consistent with one another. If the surface wind stress was stronger during the LGM, the depth of the thermocline will be deeper. In this case, the influences of the perturbations in the wind stress and the thermocline depth partially cancel out one another such that the net effect on the position of the upwelling region is small. In the case with constant eddy diffusivity, a 50 % increase in the wind stress can lead to a southward shift of the upwelling region approximately by 100 km only. The response is relatively small due to the compensating effects of the perturbations in the Ekman transport and the eddy-induced circulation.

One could ask if other paleoclimate proxies might be consistent with these changes in the ocean circulation (see Table 4.1). Francois et al. (1997) argued that the rate of upwelling in the Southern Ocean was weaker due to increased stratification. Furthermore, Gildor and Tziperman (2001) argued that the cooling of North Atlantic Deep Water due to northern hemisphere glaciation is transported southward by the thermohaline circulation, increases the stratification, and reduces the vertical mixing in the Southern Ocean. This argument is based on the nitrogen isotope record preserved in Southern Ocean sediments. Such paleoceanographic information seems contradictory to the intensification of the residual mean flow, however, their argument erroneously makes a connection between the rate of upwelling and the stratification. An increased stratification (i.e. shallower thermocline) leads to weaker eddy-induced

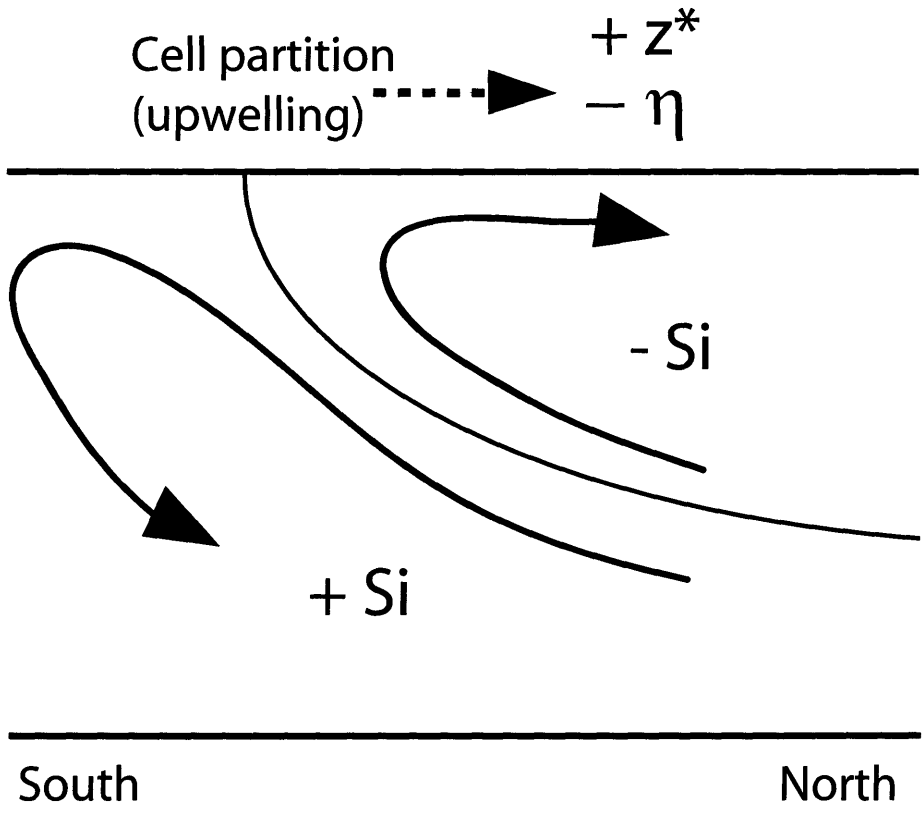

Figure 4-11: A schematic diagram for the response of the cell partition to η and z^*

circulation and stronger upwelling (Keeling and Visbeck, 2001). An increased stratification cannot explain the weaker upwelling rates. Moreover, it is difficult to explain a shallower thermocline in the presence of stronger wind stress during the LGM. On the other hand, the hypothesis presented in this thesis cannot explain increased nitrate utilization to the south of the polar front.

How can we reconcile the increased nitrate utilization and the northward shift of the productivity belt? The uptake ratio of diatoms between silica and nitrate could change depending on the availability of iron (Hutchins and Bruland, 1998; Boyle, 1998). Brzezinski et al. (2002) argue that the increased iron concentration decrease the Si:NO_3 uptake ratio leading to the depletion of nitrate in the high latitude Southern Ocean during the LGM. This effect has not been considered in this study, and it can help explain the increase in nitrate utilization during the LGM. Alternatively, Sigman and Boyle (2000) speculated that the rate of upwelling in the Southern Ocean was weaker during the LGM because the westerly wind could have migrated equatorward. If the westerly wind could have migrated equatorward in the LGM relative to the modern climate, what would be the response of the Eulerian mean circulation and the eddy-induced circulation? First, an equatorward shift in the westerly wind could decrease the wind stress over the ACC, leading to a weaker Eulerian mean transport. Secondly, an equatorward shift in the westerly wind could have deepen the subtropical thermocline by increasing the Ekman pumping in the subtropical gyres, leading to stronger eddy-induced circulation. Combining these changes, the rate of upwelling could be somewhat weaker and the position of the upwelling region could have shifted northward during the LGM. It could shift the productivity belt northward through the northward shift of the upwelling region. However, the intensity of the residual mean circulation could be slightly weakened, partially canceling out the effect of the shift in the upwelling region. It is difficult to quantitatively evaluate the net effects of these compensating changes on the position of the productivity belt since the possible range of variation in the wind stress pattern is not well understood. However, the northward shift of the westerly wind belt could reconcile the weakened upwelling rate and the northward shift of the productivity belt, which are inferred from the

paleoceanographic proxies.

In this study, the intensity of the meridional overturning circulation is calculated based on local forcing by the Southern Ocean winds. The dynamical theory includes an open boundary condition connecting the circumpolar ocean to the northern basins. Can a remote forcing (e.g. from the North Atlantic) significantly modify these results? Upper cell circulation closes with the formation of the deep waters in the northern North Atlantic, which is not included in the simple model. Thus the theory implicitly assumes that the deep water upwelling into the Southern Ocean must be supplied from elsewhere. If deep convection and formation of deep waters in the North Atlantic are significantly suppressed, it might significantly change the two cell structure of the meridional overturning circulation in the Southern Ocean (Bryan, 1986; Marotzke and Willebrand, 1991). However, we suggest that the rate of upwelling in the Southern Ocean is likely to be set locally through the interplay of the Ekman transport and the mesoscale eddy fluxes.

Finally, one could ask if the assumption of the uniform wind stress could affect the model results, however, in a slightly more complicated version of the model with spatially varying wind, the sensitivity of the cell partition to variations in η and z^* is qualitatively similar to the result presented here. In summary, a simple model of the meridional overturning circulation is developed in this chapter, which can give useful insights into the paleoclimate proxies by providing a simple relationship between the surface wind stress to the meridional overturning circulation. In a climate with stronger surface wind, we expect that the intensity of the residual mean flow increases, and the position of the upwelling region remains at the similar latitudes. These changes could shift the productivity belt northwards. A controversial aspect of this hypothesis is the interpretation of the nitrogen isotope data. The northward shift of the productivity belt could be reconciled with the increased nitrate utilization in the Southern Ocean through the northward shift of the westerly wind belt or change in the Si:N uptake ratio of diatoms during the LGM.

Table 4.1: Some paleo-proxies for physical and biogeochemical changes in the Southern Ocean during the LGM

Proxy	Interpretation	Reference
Ice core $\delta^{18}O$	Lower atmospheric temperature	Petit et al. (1999)
Ice core dust	Increased windiness and aridity	Petit et al. (1999)
Foraminiferal $\delta^{18}O$	Similar SST gradient between Holocene and the LGM	Matsumoto et al. (2001)
Sediment Pa/Th	Similar flux of NADW entering into the Southern Ocean	Yu et al. (1996)
Opal burial rate	Increased silica export (north of PF) Decreased silica export (south of PF)	Kumer et al. (1993) Francois et al. (1997)
C_{org} burial rate	Increased organic export (north of PF) Decreased organic export (south of PF)	Kumer et al. (1995) Anderson et al. (1998)
Sediment Pa/Th	Increased sinking particles (north of PF)	Kumer et al. (1993)
Sediment $\delta^{15}N$	Lower surface nitrate (south of PF) Increased stratification	Francois et al. (1997)

Chapter 5

The role of the Southern Ocean in the global carbon cycle

Polar ice core records reveal a strong coupling between the climate and the carbon cycle (Petit et al., 1999). The relationships between atmospheric temperature, pCO_2 and dust deposition are significant in the last four glacial cycles over the last 420,000 years. High atmospheric pCO_2 and low dust deposition are found during warm periods, and low atmospheric pCO_2 and high dust deposition are found during cold, ice ages. Simple box models developed in 1980s showed that atmospheric pCO_2 is sensitive to the "preformed" nutrient concentration which is connected to the high latitude surface oceans where deep isopycnals outcrop (Sarmiento and Toggweiler, 1984; Siegenthaler and Wenk, 1984; Knox and McElroy, 1984). Depleting the surface macro-nutrients in high latitudes can explain the glacial pCO_2 in these simple box models. A possible mechanism for depleting the preformed nutrient in the LGM is to utilize the surface nutrients in the Southern Ocean with enhanced atmospheric dust deposition (Martin, 1990).

In this chapter, I develop a new theory relating atmospheric pCO_2 and the efficiency of the soft tissue pump of CO_2 in the ocean, measured by P*, a quasi-conservative tracer. P* is inversely correlated with preformed phosphate, and its global average represents the fraction of nutrients transported by the export and remineralization of organic material. This view is combined with global conserva-

tion constraints for carbon and nutrients leading to a theoretical prediction for the sensitivity of atmospheric pCO_2 to changes in globally averaged P*. The theory is supported by sensitivity studies with a more complex, three-dimensional numerical simulations. The numerical experiments suggest that the ocean carbon cycle is unlikely to approach the theoretical limit where globally averaged $P^* = 1$ (complete depletion of preformed phosphate) because the localized dynamics of deep water formation, which may be associated with rapid vertical mixing timescales, preclude the ventilation of strongly nutrient depleted waters. Hence, in the large volume of the deep waters of the ocean, it is difficult to significantly reduce preformed nutrient (or increase P*) by increasing the efficiency of export production. This mechanism could ultimately control the efficiency of biological pumps in a climate with increased aeolian iron sources to the Southern Ocean. Using these concepts I discuss implications to the glacial-interglacial variations in atmospheric pCO_2 and the possible range of pCO_2 variation due to the utilization of surface macro-nutrients in the Southern Ocean.

5.1 Introduction

Photosynthesis in the surface ocean converts inorganic carbon and nutrients into organic matter, often accompanied by calcium carbonate structural material. The living tissues take part in complex ecosystem behavior and local remineralization, but a fraction, described as export production, is ultimately transported to, and remineralized within, thermocline and abyssal ocean. The vertical transport of organic carbon is termed the soft tissue pump and that of calcite, the carbonate pump (Volk and Hoffert, 1985). These biological carbon pumps remove carbon from surface oceans and the atmosphere and store it in the ocean interior, and might play a critical role in the long-term variation of atmospheric CO_2.

Polar ice cores suggest that atmospheric pCO_2 significantly fluctuated between 180 ppm during the cold, glacial periods and 280 ppm during the warm, interglacial periods (Petit et al., 1999). Box model studies (Sarmiento and Toggweiler, 1984;

Siegenthaler and Wenk, 1984; Knox and McElroy, 1984) illustrated that atmospheric CO_2 is highly sensitive to the depletion of high latitude surface nutrients. Following these studies, several possible mechanisms have been suggested for the depletion of high latitude surface nutrients, for example, reduced ocean ventilation (Francois et al., 1997) and increased export production (Kumar et al., 1995) which may be related to changes in iron limitation of phytoplankton organisms in the Southern Ocean (Martin, 1990). However, a recent study based on more complicated, and perhaps more realistic, general circulation models showed that depletion of surface nutrient leads to a weaker response in atmospheric CO_2 and cannot fully reproduce glacial-interglacial changes in atmospheric pCO_2 (Archer et al., 2000). How can we define and quantify the efficiency of biological pumps independent of the types of numerical models? What ultimately controls the efficiency of the biological pumps in the oceans? Can we reconcile the box model and GCM results? First we briefly review the measures by which the efficiency of the biological carbon pumps have been defined.

5.1.1 Vertical gradients of DIC and nutrients

Volk and Hoffert (1985) first defined the biological (and solubility) pumps of carbon, characterizing their relative efficiency in terms of their contributions to the vertical gradient of DIC. For a closed ocean-atmosphere system, increasing the vertical gradient in DIC reduces the DIC concentration in the surface oceans. Since the surface oceans, on global average, are indeed close to equilibrium with atmospheric CO_2, this reduces atmospheric pCO_2. In addition to the biological pumps, vertical gradient of DIC is enhanced by the thermal structure of the ocean and its control on the solubility of CO_2 (solubility pump of CO_2). Cold and dense deep waters are enriched in DIC relative to the warm surface waters. Preindustrial atmosphere contained 280 ppmv of CO_2 as a result of the combined effects of the solubility pump and the biological pumps. For example, box models suggest that atmospheric pCO_2 would rise to approximately 460 ppmv (Sarmiento and Toggweiler, 1984; Volk and Hoffert, 1985) if the effects of the biological pumps were completely removed. When the effects of

both solubility pump and biological pumps were removed by homogenizing the DIC concentration in the oceans, atmospheric pCO_2 would rise up to 720 ppmv (Volk and Hoffert, 1985). The vertical gradient of DIC is an useful measure for interpreting idealized conceptual models. However, this one-dimensional view cannot address the role of the significant horizontal variabilities observed in the real ocean.

5.1.2 Unutilized surface macro-nutrients

The efficiency of the biological carbon pumps has also been related to the budget of macro-nutrients (nitrate or phosphate) in the surface ocean. The presence of inorganic nutrients in the surface waters suggests that the soft tissue pump of carbon is not working at full efficiency. There are large regions of the surface ocean, in particular the high latitude Southern Oceans, where surface macro-nutrients are far from depleted. If the available nutrients were to be consumed in photosynthesis and transferred to the deep ocean as organic matter, they might significantly enhance the storage of carbon in the deep ocean. Classical box model studies indicated that completely depleting the surface nutrients in the Southern Ocean can drive down atmospheric pCO_2 as low as 165 ppmv (Sarmiento and Toggweiler, 1984), approximately 115 ppmv lower than preindustrial condition. They predict that atmospheric CO_2 can change on the order of 300 ppmv between the case with complete utilization of surface nutrients and the case with no biological export and remineralization. Recent studies, in contrast, suggest that drawing down surface nutrients in general circulation and biogeochemistry models has a weaker response in atmospheric CO_2. GCM simulations with a rapid Newtonian damping of surface nutrients result in a decrease of 46-84 ppmv (Sarmiento and Orr, 1991) and approximately 50 ppmv (Archer et al., 2000). These results indicate that the simulated sensitivity of atmospheric CO_2 in GCMs is significantly smaller than that of box models. Inventories of macro-nutrient in the surface ocean are unlikely to be a robust measure of the efficiency of biological pump since the sensitivity depends on the model architecture. Here we develop a new measure of the efficiency of the biological pump, which is independent of the formulation and the spatial resolution of the model.

In section 5.2 we develop a simple mathematical model describing the efficiency of the soft tissue pump in terms of the fraction of nutrients which are "preformed", and predict the sensitivity of atmospheric pCO_2 to the inventory of preformed nutrients. A key element of the theory is the integral constraint on the carbon and nutrient budgets, and partitioning of carbon and nutrients between the "preformed" pool and the "regenerated" pool. In section 5.3 we use an ocean GCM and biogeochemistry model to simulate ocean carbon pumps and partitioning of CO_2 between atmosphere and ocean. We use the numerical model to evaluate theoretical predictions against sensitivity experiments. Furthermore, the sensitivity experiments can illustrate bounds on the potential range of variation in atmospheric CO_2, and we discuss constraints on the role of the biological pumps in controlling atmospheric CO_2 over glacial-interglacial timescales.

5.2 Theory and observations

First we review concepts of preformed and regenerated nutrients and illustrate them using observed tracer distributions from WOCE-JGOFS survey and climatology (World Ocean Atlas 2001). It is possible to define two components in nutrient and carbon concentrations: the "preformed" component and the "regenerated" component. The partitioning between the two pools plays critical roles in setting the efficiency of the soft tissue pump and its control on atmospheric CO_2. Then we develop a simple mathematical model describing the efficiency of the soft tissue pump combining the partitioning of nutrient and carbon with global conservation constraints. The theory, in turn, gives insights into the interpretation of the observations and the quantification of the soft tissue pump.

5.2.1 Preformed and regenerated phosphate

We consider phosphate as a measure of macro-nutrient, and write it as the sum of preformed phosphate and regenerated phosphate.

$$P = P_{pre} + P_{reg} \tag{5.1}$$

When thermocline or deep waters are newly formed, unutilized nutrients are subducted into the interior ocean. The fraction of nutrient in the ocean which was subducted and transported is termed "preformed" nutrient, P_{pre} (Broecker, 1974; Broecker and Peng, 1982; Broecker et al., 1985; Toggweiler et al., 2003a; Sigman and Haug, 2003). In the interior ocean, phosphate is added to the waters through respiration of organic molecules. Clearly the preformed phosphate of the deep waters is closely related to the surface concentration at the outcrop of isopycnals(Broecker et al., 1985). The fraction of phosphate in the ocean which is regenerated by respiration is termed "regenerated" nutrient, P_{reg}.

Regenerated phosphate, P_{reg}, can be estimated using Apparent Oxygen Utilization (AOU), which depends on the observed temperature, salinity and in-situ oxygen distributions (Broecker, 1974; Broecker et al., 1985). In the interior ocean, O_2 is consumed by respiration, and generally, oxygen is increasingly depleted as the water mass accumulates regenerated nutrients. Assuming that oxygen concentration is close to saturation at the surface, we can estimate how much oxygen is consumed by the remineralization of organic molecules.

$$AOU = O_{2,sat}(T,S) - O_2 \tag{5.2}$$

$$P_{reg} = R_{P:O2} AOU \tag{5.3}$$

where $O_{2,sat}$ is the saturated concentration of oxygen which is a function of temperature, T and salinity, S. We assume a fixed stoichiometric ratio between oxygen, phosphate and organic carbon following Anderson (1995). Fig. 5-1 shows the distribution of regenerated phosphate in the Atlantic and Pacific ocean from WOCE lines

A-17 and A-20 for Atlantic, and P-18 for Pacific. Regenerated phosphate generally increases with the "age" of the water due to the accumulation of biogenic phosphate. Newly ventilated NADW contains less regenerated phosphate, P_{reg}, and it has a maximum value in the deep North Pacific.

Fig.5-2 shows the distribution of preformed phosphate in the Atlantic and Pacific section, revealing the contrast between major water masses in the global ocean: the waters formed in the northern North Atlantic (NADW) are relatively low ($\sim$ 0.9 μM) in preformed nutrient. The waters formed in the Southern Ocean are relatively enriched ($\sim$ 1.6 μM), reflecting high surface nutrient concentration of the region of water mass formation. Mode waters in subtropical thermocline are depleted in preformed phosphate (0.6 μM); much lower than the deep waters since they are formed at middle latitudes. In the Antarctic Circumpolar Current, (ACC) deep waters from the northern North Atlantic are mixed with the waters formed in the Southern Ocean.

Fig. 5-3 schematically illustrates the nutrient cycle in the oceans, and offers a qualitative interpretation of the partitioning of phosphate between the "preformed" pool and the "regenerated" pool. Nutrients are supplied to the surface oceans by physical transport such as upwelling of intermediate and deep waters. There are two pathways for nutrients to return back into the interior ocean: (1) through biological export and remineralization (biological path), and (2) through subduction and water mass formation (physical path). The contrast between the two pathways can clearly illustrate the efficiency of the soft tissue pump. The biological path is associated with sequestration of carbons from the surface oceans, which is efficient in driving down atmospheric CO_2. In contrast the biological pumps do not operate through the physical path.

The relative significance of the two pathways can be illustrated using the concept of preformed and regenerated nutrient. The distribution of the regenerated phosphate (shown in Fig.5-1) reflects the integrated effect of phosphate returning to the interior ocean through the "biological" path. Similarly the pattern of the preformed phosphate (shown in Fig.5-2) reveals the amount of phosphate returning to the interior

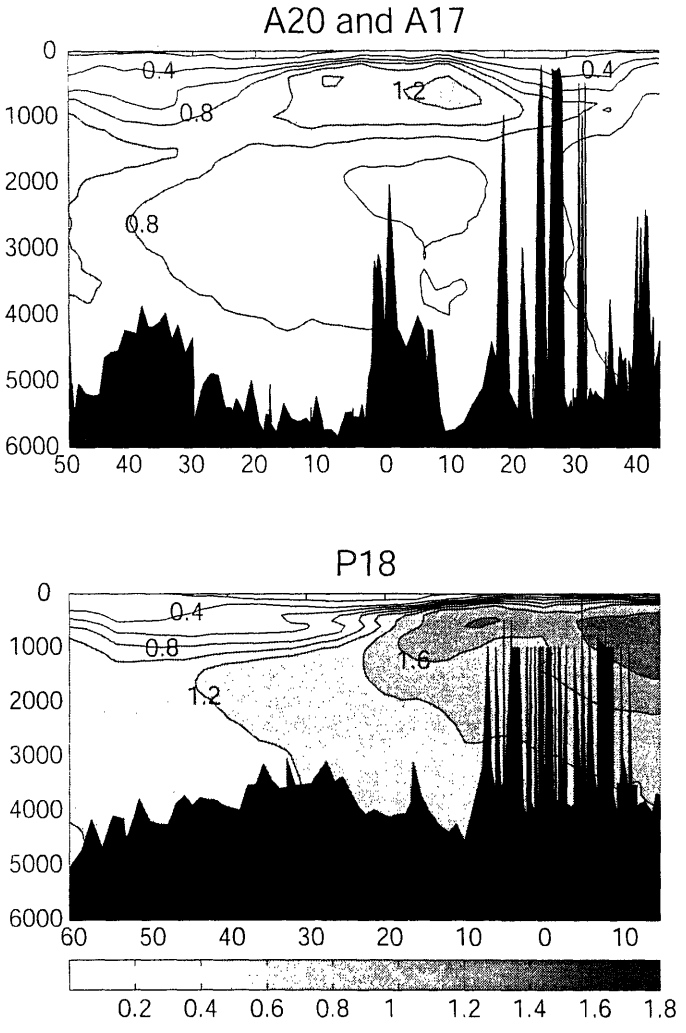

Figure 5-1: Distribution of P_{reg}, regenerated phosphate based on the WOCE-JGOFS survey. (a) WOCE line A-17 and A-20 in the Atlantic Ocean, (b) WOCE line P-18 in the Pacific Ocean. We use in-situ oxygen and hydrographic data to calculate AOU. Observed data is interpolated on to a latitude-depth grid whose horizontal resolution is 1° and vertical resolution is 100 m. While general patterns of AOU clearly indicate the integrated effect of respiration, one has to be cautious about its interpretation. Significant undersaturation of oxygen and other trace gases is observed in the ice-covered surface polar oceans (Weiss et al., 1979; Schlosser et al., 1991), suggesting that preformed oxygen concentration may be lower than saturation particularly in the cold deep waters. If preformed oxygen concentration is undersaturated, AOU overestimates the effect of respiration and so does the regenerated phosphate.

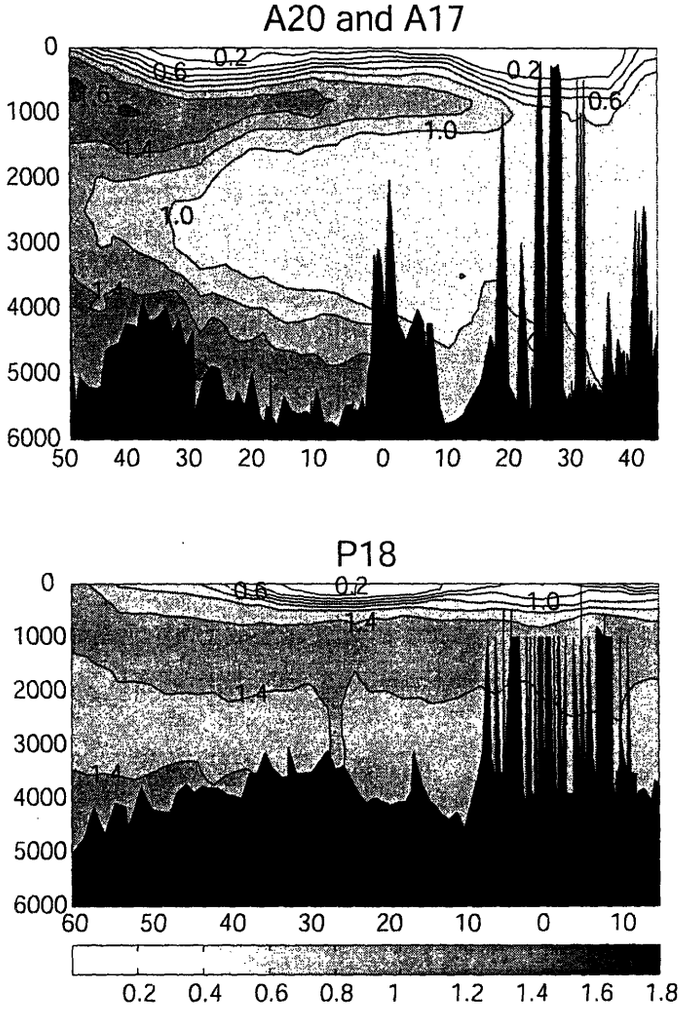

Figure 5-2: Preformed phosphate distribution based on WOCE-JGOFS survey. Data is taken from (a) line A-17 and A-20, (b) line P-18. Waters formed in the Southern Ocean have approximately 1.6 μM of preformed phosphate based on the calculation using AOU (5.2) which may include a bias due to the oxygen disequilibrium. (See caption for Fig.1)

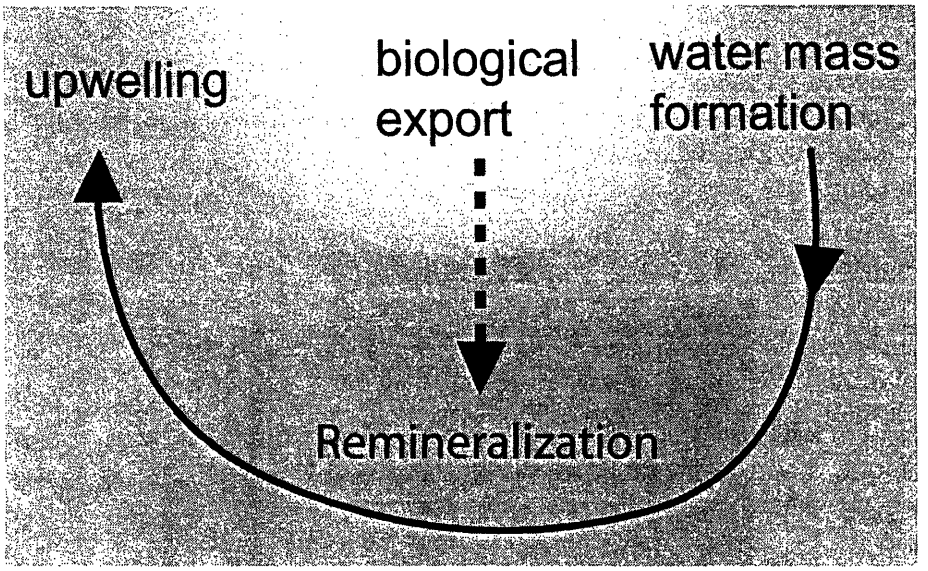

Figure 5-3: A schematic diagram for the major pathways of macro-nutrients in the oceans. The upwelling of nutrient is balanced by (1) biological uptake and export and by (2) subduction and formation of water masses. Here we neglect the effects of riverine input and sedimentary burial.

ocean through the "physical" path.

Let us consider an extreme case in which surface phosphate are totally depleted by biological uptake. All the upwelling phosphate return to the interior ocean through the "biological path". In this limit case the soft tissue pump is working at its maximum efficiency ($P_{pre} = 0$). Another limit case is that there is no biological uptake at all. All the upwelling nutrients return to the interior ocean through the "physical path". This corresponds to the minimum efficiency of the soft tissue pump ($P_{reg} = 0$). There is no regenerated nutrients in the oceans, and all the nutrients are preformed. the biological pump of the real ocean should fall somewhere in between the two limit cases.

Here we define a global metric of the efficiency of the soft tissue pump, $\overline{P*}$, reflecting the fraction of phosphate which is regenerated by respiration in the global ocean. It quantitatively indicates the importance of the biological path in the downwards return of nutrients to the interior ocean.

$$\overline{P*} \equiv \frac{\overline{P_{reg}}}{\overline{P}} \tag{5.4}$$

where $\overline{P}$ is the global mean of P. $\overline{P*}$ can only vary between 0 and 1: $\overline{P*} = 1$ indicates the complete utilization of phosphate in the surface oceans, and $\overline{P*} = 0$ indicates a complete shutdown of the soft tissue pump. We use $\overline{P*}$ as a global measure of the efficiency of the soft tissue pump, which can be calculated from the distributions of phosphate and oxygen in observations and models.

The efficiency of the soft tissue pump of the modern ocean can be readily calculated based on climatological distributions of phosphate and oxygen, using the World Ocean Atlas (Conkright et al., 2002). Applying Eq.(5.2,5.3,5.4) to the climatological distribution of T, S, P and O_2, we find that $\overline{P*}$ is approximately 0.36 indicating that about 36 % of phosphate is in the regenerated pool in the modern ocean. What is the expected range of atmospheric CO_2 associated with the variation in $\overline{P*}$? In the following sections we develop a mathematical model describing the relationship between $\overline{P*}$ and atmospheric pCO_2.

5.2.2 Carbon pump decomposition

First we describe the decomposition of the DIC concentration into carbon pump components. Carbon pump decomposition was first introduced as a tool for detecting anthropogenic CO_2 in the ocean (Brewer, 1978; Chen and Millero, 1979). The approach has been modified and developed into the ΔC^* method used for the same purpose (Gruber et al., 1996; Gruber, 1998; Sabine et al., 1999). In a variation of this approach, Gruber and Sarmiento (2002) also analyzed the carbon pump components of observed tracer fields from the recent WOCE-JGOFS survey and illustrated the processes controlling the vertical gradient of DIC, in which tracer fields are referenced to the global surface mean properties. Here we decompose the carbon pumps based on the partitioning of DIC between the preformed pool and the regenerated pool where tracer fields are referenced to the outcrop of isopycnals.

As for the partitioning of phosphate (5.1), observed DIC concentration, C, can be expressed as the sum of preformed DIC, C_{pre}, and regenerated DIC, C_{reg}.

$$C = C_{pre} + C_{reg} \tag{5.5}$$

C_{reg} can be further divided into a soft tissue component and a calcite component representing the respiration of organic molecules and the dissolution of calcium carbonate structural materials.

$$C_{reg} = C_{calcite} + C_{org} \tag{5.6}$$

$$C_{org} = R_{Corg:PO_4} P_{reg} \tag{5.7}$$

Regenerated phosphate, P_{reg}, and the soft tissue component, C_{org}, are coupled assuming a constant stoichiometric ratio (Anderson, 1995). Preformed carbon concentration, C_{pre}, can be decomposed into the saturated component (i.e. the concentration at equilibrium with preindustrial atmosphere) and ΔC^*.

$$C_{pre} = C_{sat}(T, S, TA_{pref}, pCO_2^{atm}) + \Delta C^* \tag{5.8}$$

ΔC^* therefore contains components due to both anthropogenic CO_2 and air-sea disequilibrium under preindustrial conditions. Here we consider only the preindustrial condition where there is no influence of anthropogenic CO_2, and we use the notation, ΔC, for preindustrial disequilibrium. For example, if surface waters at an outcrop are in complete saturation with overlying atmospheric pCO_2, $\Delta C = 0$. A positive ΔC indicates that the surface waters were outgassing CO_2 into the atmosphere at the time of subduction. Similarly, a negative ΔC indicates uptake. In the following section we combine the carbon pump decomposition, the partitioning of phosphate and the integral constraints for carbon and nutrients to form a new theory for calculating the sensitivity of atmospheric CO_2.

5.2.3 A new theory based on the integral constraints on carbon and phosphate

Here we explore the connection between the soft tissue pump, expressed in terms of $\overline{P*}$, and atmospheric CO_2, and derive a general theory for constraining the efficiency of soft tissue pump. We illustrate the coupling between the preformed phosphate and

atmospheric pCO_2 based on the integrated mass balance of carbon and nutrients in the ocean-atmosphere system. The mass balance constraints are independent of the detailed physical and biogeochemical parameterization, and are generally applicable to models with wide range of complexity. First, we assume that the ocean-atmosphere system is in closed balance so that we may neglect riverine input and sedimentary interactions of nutrients and carbon. Then, we also assume that the timescale for mixing of CO_2 in the atmosphere is rapid relative to relevant oceanic processes, and the atmosphere can be treated as a well-mixed reservoir of CO_2. The global conservation of phosphate and carbon can be stated as following.

$$P_0 = \frac{1}{V}\int_V P\,dxdydz = constant. \tag{5.9}$$

$$C_0 = \frac{1}{V}\left(M\,pCO_2^{atm} + \int_V C\,dx\,dy\,dz\right) = constant. \tag{5.10}$$

M is the total moles of gas in the atmosphere, pCO_2^{atm} is the mixing ratio of atmospheric CO_2. V represents the volume of the global ocean. P and C are the ocean phosphate and dissolved inorganic carbon concentration in units of mol m^{-3}. We assume the conservation of the total amount of phosphate and carbon in the atmosphere-ocean system.

The integral constraint (5.10) and carbon pump components (5.5,5.6,5.8) can be combined to yield an expression for the partitioning of carbon between the atmospheric reservoir and the carbon pumps in the ocean.

$$M\,pCO_2^{atm} + V\,\{\overline{C_{sat}} + \overline{\Delta C} + \overline{C_{org}} + \overline{C_{calcite}}\} = V\,C_0 \tag{5.11}$$

where $V\,C_0$ represents the total amount of carbon in the system, and the overbar indicates globally averaged concentrations. M, V and C_0 are assumed to be constants of the system. It is interesting to consider the sensitivity of atmospheric CO_2 by making a small perturbation to a reasonable mean state. For small perturbations to

the carbon pump components, Eq.(5.11) becomes

$$M\,\delta pCO_2^{atm} + V\,\{\delta\overline{C_{sat}} + \delta\overline{\Delta C} + \delta\overline{C_{org}} + \delta\overline{C_{calcite}}\} = 0 \tag{5.12}$$

Here we will specifically consider the sensitivity of pCO_2^{atm} to the soft tissue pump. For simplicity we assume that a perturbation in the soft tissue pump is decoupled from that of the carbonate pump and the degree of saturation, so, we set $\delta\overline{C_{calcite}} = \delta\overline{\Delta C} = 0$. The relationship between C_{sat} and pCO_2^{atm} are determined by the carbonate chemistry of the sea water. For a simple case where T, S and Alk are held constant, variations in C_{sat} and pCO_2^{atm} can be described using the Buffer factor, $B \sim 10$ (Bolin and Eriksson, 1959).

$$\delta \ln pCO_2^{atm} = B\,\delta \ln C_{sat} \tag{5.13}$$

There are spatial variations in C_{sat} in the surface ocean but the variation of C_{sat} is one order of magnitude smaller than its mean value. Thus it can be shown that $\overline{\ln C_{sat}} = \ln \overline{C_{sat}} + O(\ln \varepsilon^2)$ where $\varepsilon = C_{sat} - \overline{C_{sat}}$, and we assume B to be an uniform constant, set to the global mean value. Then, we find an approximate expression for the global average of (5.13).

$$\delta \ln pCO_2^{atm} = B\,\delta \ln \overline{C_{sat}} \tag{5.14}$$

Using (5.12,5.14) to eliminate C_{sat} from (5.12), we find an expression for the sensitivity of pCO_2^{atm} to $\overline{C_{org}}$.

$$\frac{\delta pCO_2^{atm}}{\delta\overline{C_{org}}} = -\frac{V}{M\,\gamma} \tag{5.15}$$

$$\gamma \equiv 1 + \frac{V\,\overline{C_{sat}}}{B\,M\,pCO_2^{atm}} \tag{5.16}$$

A dimensionless parameter, γ, emerges from the combination of the atmosphere-ocean carbon balance and the carbonate chemistry. It represents the relative size of the oceanic and the atmospheric carbon inventory, where atmospheric inventory

is weighted with the Buffer factor. The second term of RHS in Eq.(5.16) is on the order of 7 for the modern ocean. Therefore, to the leading order approximation, the sensitivity of atmospheric CO_2 to variation in $\overline{C_{org}}$ is independent of the size of the reservoirs.

$$\frac{\delta pCO_2^{atm}}{\delta \overline{C_{org}}} \sim -\frac{B\, pCO_2^{atm}}{\overline{C_{sat}}} \tag{5.17}$$

These relationships (5.15,5.17) are simple expressions for the sensitivity of atmospheric CO_2 to the soft tissue component, $\overline{C_{org}}$, which is directly coupled to the nutrient cycle through Eq.(5.7). Increasing the global inventory of $\overline{C_{org}}$ indicates an increase in the regenerated carbon and phosphate in the interior ocean, enhancing the relative importance of the biological path in the downwards transport of phosphate and carbon illustrated in Fig.5-3. The rate of variation in atmospheric CO_2 with respect to the change in $\overline{C_{org}}$ is set by the partial derivative, $\partial pCO_2^{atm}/\partial \overline{C_{org}}$, which essentially depends on globally averaged Buffer factor and the reference states of $\overline{C_{sat}}$ and pCO_2^{atm}.

Now consider the partitioning of phosphate between the preformed pool and the regenerated pool. Variation in the soft tissue component, $\overline{C_{org}}$, is directly related to the changes in P* through the integral constraint (5.9) and the definition of P* (5.4).

$$\delta \overline{C_{org}} = R_{C:P}\, \delta \overline{P_{reg}} \tag{5.18}$$

$$= R_{C:P}\, P_0 \delta \overline{P*} \tag{5.19}$$

Combining eqs. (5.15) and (5.19), we find

$$\frac{\delta pCO_2^{atm}}{\delta \overline{P*}} = -\frac{V\, R_{C:P} P_0}{M\, \gamma} \sim 312\, ppmv \tag{5.20}$$

which is very similar to Eq (5.15), but directly expressed in terms of the efficiency of the soft tissue pump, $\overline{P*}$, which can only vary between 0 and 1 as long as the total phosphate inventory of the global ocean is conserved. It provides a constraint on the potential variation of atmospheric CO_2 with changes in the soft tissue pump.

Atmospheric CO_2 can vary by approximately 300 ppmv between the minimum and the maximum efficiency of the soft tissue pump ($0 < \overline{P*} < 1$), consistent with previous studies based on box models (Sarmiento and Toggweiler, 1984). (Constants used in this calculation are based on the modern ocean, shown in Table 5.1).

5.2.4 Implications of P* for potential changes in the soft tissue pump

The theory predicts a simple response of atmospheric pCO_2 to perturbations in the inventory of regenerated phosphate, expressed in terms of $\overline{P*}$. Climatological distributions of phosphate and oxygen indicate $\overline{P*} = 0.36$ for the modern ocean (Conkright et al., 2002). If $\overline{P*}$ were to increase up to 0.7, the simple theory suggest that atmospheric CO_2 would be expected to decrease by 100 ppmv, which is similar to the difference in atmospheric pCO_2 between the Last Glacial Maximum (LGM) and the Holocene. What controls the possible range of variation in $\overline{P*}$?

It is possible to consider the efficiency of the soft tissue pump, $P*$, as a quasi-conservative tracer in the ocean based on the preformed phosphate.

$$P* = 1 - \frac{P_{pre}}{P_0} \tag{5.21}$$

Global average of this equation, combined with Eq.(5.1,5.9), becomes identical to Eq.(5.4). P* carries similar information to the preformed phosphate in this formulation, but P* has some notable properties.

- P* cannot be greater than 1.
- P* is conserved in the interior ocean.
- Water masses tend to exhibit distinct P* concentrations.

In the modern ocean, the value of P* in NADW is approximately 0.60, reflecting relatively low preformed phosphate concentration in NADW. The value of P* is low ($\sim$0.15) in AABW, reflecting relatively high preformed phosphate in the Southern

Ocean. Globally averaged P* can be considered as the volume weighted mean of the P* in the water masses in the global ocean. One could consider two possible methods to vary $\overline{P*}$: (1) changing the phosphate concentration at the outcrop of isopycnals (P* of the end members) and (2) changing the large-scale circulation in the oceans and volumetric ratio of various water masses. Both processes can lead to variations in $\overline{P*}$.

Among the hypotheses for the glacial-interglacial variations in atmospheric CO_2, those based on the depletion of high latitude surface nutrients (Martin, 1990; Kumar et al., 1995; Francois et al., 1997) are essentially driven by the first mechanism with the changes in P* of the end members. Alternatively, variations in the ocean circulation could have a large changes in the P* distribution without changing the surface nutrient distribution (Toggweiler, 1999; Toggweiler et al., 2003a), which is the second mechanism. Physical circulation determines the global distribution of P* by mapping surface P* distribution into the interior ocean. In summary the simple theory suggests that global changes in the soft tissue pump and its impact on atmospheric CO_2 can be quantified in terms of $\overline{P*}$. Analysis based on P* provides a simple and comprehensive diagnostic of the soft tissue pump.

In the following section we use an idealized, physical-biogeochemical model as a tool to examine the theory in the context of numerical simulation. The theoretical prediction (5.20) is tested against sensitivity experiments, and the simulated distribution of P* provides useful insights into the mechanisms controlling the bounds on $\overline{P*}$ and atmospheric CO_2.

5.3 Ocean-atmosphere carbon cycle model

In the simple theory, the sensitivity of atmospheric CO_2 to changes in the global inventory of P* in Eq.(5.20) is calculated based on the integral constraints in the ocean-atmosphere system, combined with the carbon pump decomposition and the carbonate chemistry. The theory can be quantitatively tested in the context of numerical simulations. Furthermore it provides a theoretical framework to diagnose and

Table 5.1: Constants used in the theory

Symbol	Units	Value
$\overline{C_{sat}}$	μ mol kg^{-1}	1800
pCO_2^{atm}	ppmv	280
$R_{C:P}$	ND	106
$R_{N:P}$	ND	16
B	ND	10
γ	ND	6.10
V	m^3	$1.37 \cdot 10^{18}$
M	mol	$1.77 \cdot 10^{20}$

interpret the simulated carbon pumps. Here we simulate ocean-atmosphere carbon cycle in an idealized bathymetry such that the model is computationally efficient and the results are easier to diagnose. The aims of the numerical experiments are to:

- Examine and illustrate simulated oxygen, phosphorus and carbon distribution using the concept of carbon pump components and P*.
- Explicitly simulate the response of atmospheric CO_2 to the soft tissue pump, and test the theory such as Eq.(5.20) in a more complex setting.
- Explore the possible variations in P* over a wide range of model parameters.

5.3.1 Model configuration and physical circulation

We use the MIT ocean general circulation and biogeochemistry model (Marshall et al., 1997b; Marshall et al., 1997a; Follows et al., 2002) configured in an interhemispheric, rectangular ocean basin with an open channel in the Southern hemisphere (Fig. 5-

4). Polewards of 40°S, a periodic boundary condition is applied to represent the circumpolar current, which extends to the southern boundary of the model domain (60°S) and down to 2000 m. The model has flat bottom at 3280 m depth, horizontal resolution of 3° and 12 vertical levels. Eddy-induced circulation is parameterized using an isopycnal thickness diffusion scheme (Gent and McWilliams, 1990) with isopycnal diffusivity of 1000 m^2s^{-1}. Small scale diapycnal mixing is parameterized with a uniform, vertical tracer diffusivity of $5 \cdot 10^{-5}$ m^2s^{-1}. The model is forced with an idealized zonal wind stress which has sinusoidal profile broadly similar to the present climate. Salinity is set to a uniform constant (35 psu), and the model density is entirely determined by temperature. SST is restored to a prescribed sinusoidal profile broadly similar to modern ocean climatology, with a timescale of 30 days. There is no seasonal variation in the wind and thermal forcing. The model is initialized with a uniform temperature at rest, and spun up for 5000 years.

Fig. 5-5(a) shows the barotropic stream function of the model at steady state. Wind-driven subtropical gyres are present in both hemispheres, and a weaker, subpolar gyre is also found in the northern hemisphere. In the subpolar southern hemisphere, the circumpolar current transports about 60 Sv. Fig. 5-5(b) shows the Eulerian mean overturning circulation including about 8 Sv of deep water formation in the northern basin, and the wind-driven overturning circulation in the southern hemisphere. Fig. 5-5(c) shows the parameterized eddy-induced transport due to Gent and McWilliams parameterization. In the northern hemisphere, the eddy-driven overturning circulation and the Eulerian mean circulation have the same sign, enhancing the deep water ventilation in the northern hemisphere. In the southern hemisphere, the eddy-driven overturning circulation nearly cancels out the Eulerian mean circulation. Fig. 5-5(c) shows the residual mean overturning circulation which is the net effect of the Eulerian mean and the eddy-induced transport, and drives the advective transport of tracers in the model. The meridional overturning circulation is reduced to approximately 6 Sv in the circumpolar current, and a weak bottom cell emerges.

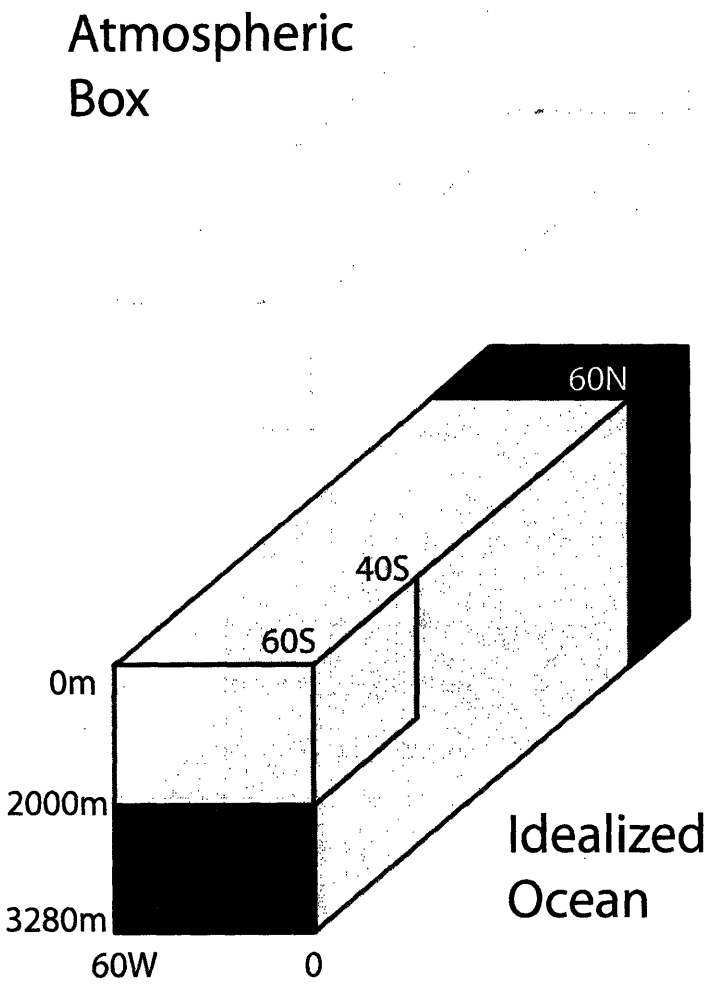

Figure 5-4: A schematic diagram of the idealized atmosphere-ocean carbon cycle model. The model is configured for a rectangular basin with an open channel in the southern hemisphere. Periodic boundary conditions are used for the latitudes between 40S and 60S from surface to 2000m depth.

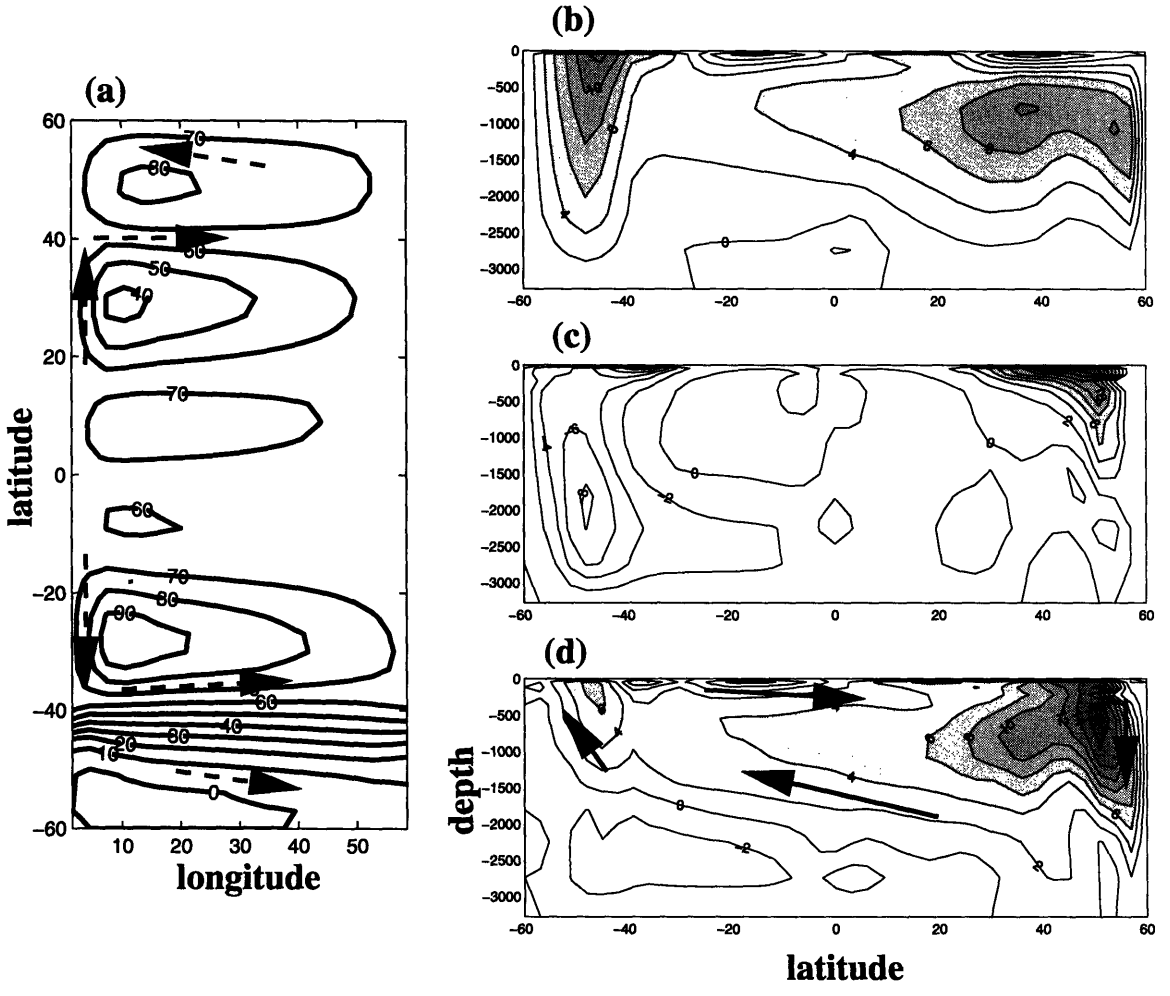

Figure 5-5: Steady state physical circulation. (a) Barotropic stream function is the depth integrated flow. Contour spacing is 10 Sv (b) Meridional overturning circulation is the zonally averaged overturning circulations. Contour spacing is 2 Sv. Top, middle and bottom panel represent Eulerian mean flow, eddy-induced flow and the "residual" (or "effective") flow. The residual circulation is the sum of the Eulerian mean and the eddy-induced circulation.

5.3.2 Biogeochemical model

The biogeochemical model includes oxygen, phosphate and DIC as passive tracers which include physical transports, biological uptake and remineralization and air-sea gas transfer.

$$\frac{\partial P}{\partial t} + \mathbf{u} \cdot \nabla P = \nabla \cdot \mathbf{K} \nabla P + \frac{\partial F_P}{\partial z} \tag{5.22}$$

$$\frac{\partial O_2}{\partial t} + \mathbf{u} \cdot \nabla O_2 = \nabla \cdot \mathbf{K} \nabla O_2 - R_{O2:P} \frac{\partial F_P}{\partial z} - \frac{K_W}{\Delta z_1}(O_2 - O_2^{sat}) \tag{5.23}$$

$$\frac{\partial C}{\partial t} + \mathbf{u} \cdot \nabla C = \nabla \cdot \mathbf{K} \nabla C + R_{C:P} \frac{\partial F_P}{\partial z} - \frac{K_W}{\Delta z_1}([CO_2] - [CO_2]^{sat}) \tag{5.24}$$

Here K_W is the gas transfer velocity and Δz_1 is the thickness of the first vertical layer which is set to 50m in this model. The surface water exchanges oxygen and CO_2 with the atmosphere using a constant K_W of $5 \cdot 10^{-5}$ ms^{-1}.

Biological uptake is parameterized as a linear damping of phosphate at the surface layer of the model. F_P represents the downward flux of sinking organic material measured in units of phosphate.

$$F_P(z = z_1) = -\tau_{bio}^{-1} \Delta z_1 \, P \tag{5.25}$$

$$F_P(z < z_1) = F_P(z = z_1) \left(\frac{z}{z_1}\right)^{-0.85} \tag{5.26}$$

where z_1 is the depth of the bottom of the surface layer. The timescale for uptake, τ_{bio}, a global constant which controls the sinking organic flux, is varied from 1.5 months to 10 years in the sensitivity studies. The vertical profile of F_P is parameterized using the Martin function (Martin et al., 1987) and we neglect burial at the seafloor. The production and transport of calcium carbonate is not parameterized in this model.

A well-mixed, atmospheric box is coupled to the ocean carbon cycle such that the partitioning of carbon between the atmosphere and the ocean is explicitly calculated in the model. The model conserves total amount of carbon in the atmosphere and the ocean. Atmospheric mixing ratio of CO_2 can adjust with the net air-sea CO_2 flux at each time step. Carbonate chemistry is solved assuming using a uniform alkalinity

of 2300 μ eq kg^{-1} (including Boric acid, Silicic acid and Phosphoric acid (Millero, 1995)).

The model is initialized with uniform DIC, oxygen and phosphate concentrations, and atmospheric CO_2 of 278 ppmv. The control run is spun up for 5000 years with the fixed atmospheric pCO_2, and biological export timescale is set to 360 days. After 5000 years of integration, the model fields are very close to the steady state. Then, we further spin up the model allowing atmospheric pCO_2 to adjust with the net air-sea CO_2 exchange. After additional 1000 year of integration, modeled atmospheric pCO_2 is found at 270 ppmv.

5.3.3 Control run

Fig. 5-6 shows the steady state distribution of (a) phosphate, (b) oxygen and (c) DIC for the control run. The large scale distribution of these tracers broadly resembles those observed in the modern North Atlantic. The newly formed deep water in the northern hemisphere is relatively depleted in phosphate and rich in oxygen. As the deep water travels southward, it accumulates regenerated phosphate and carbon. The subtropical thermocline is generally depleted in phosphate. In the southern hemisphere, phosphate concentration is notably high, particularly at depth due to the old "age" of the deep waters there, and the slow ventilation (upwelling) in the southern hemisphere. As Fig.5-5 shows, the compensation between the Eulerian mean flow and the eddy induced flow results in reduction of upwelling rate, allowing the regenerated phosphate and carbon to accumulate in the region.

Fig. 5-7 shows the steady state distribution of (a) preformed phosphate, (b) regenerated phosphate, (c) saturated component (C_{sat}) and (d) the degree of saturation (ΔC) for the control run. (We separate carbon pump components of the model using (5.3) through (5.8)). The model includes soft tissue pump only, and the regenerated phosphate and carbon are diagnosed using modeled oxygen distribution following (5.3) and (5.7). Oxygen disequilibrium is small in this model due to the lack of sea ice cover at high latitudes. Undersaturation of oxygen at high latitude southern hemisphere is on the order of -10 μM and associated error in C_{org} is on the order of 7 μM

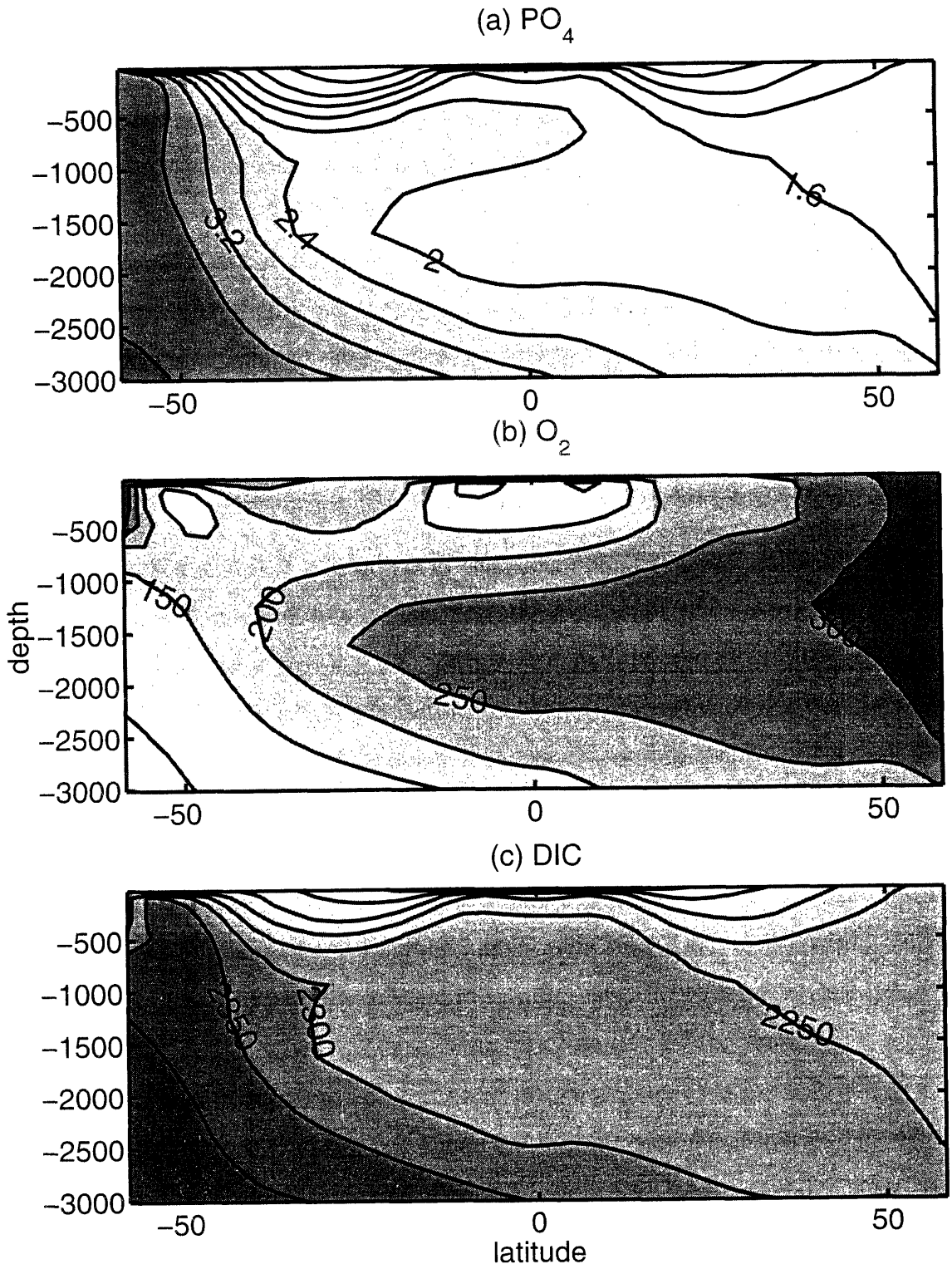

Figure 5-6: Modeled phosphate, oxygen and DIC in the control run. (a) Zonally averaged phosphate at steady state. Contour interval is 0.4 μ M. (b) Zonally averaged oxygen at steady state. Contour interval is 50 μ M. (c) Zonally averaged DIC distribution at steady state. Contour interval is 50 μ M.

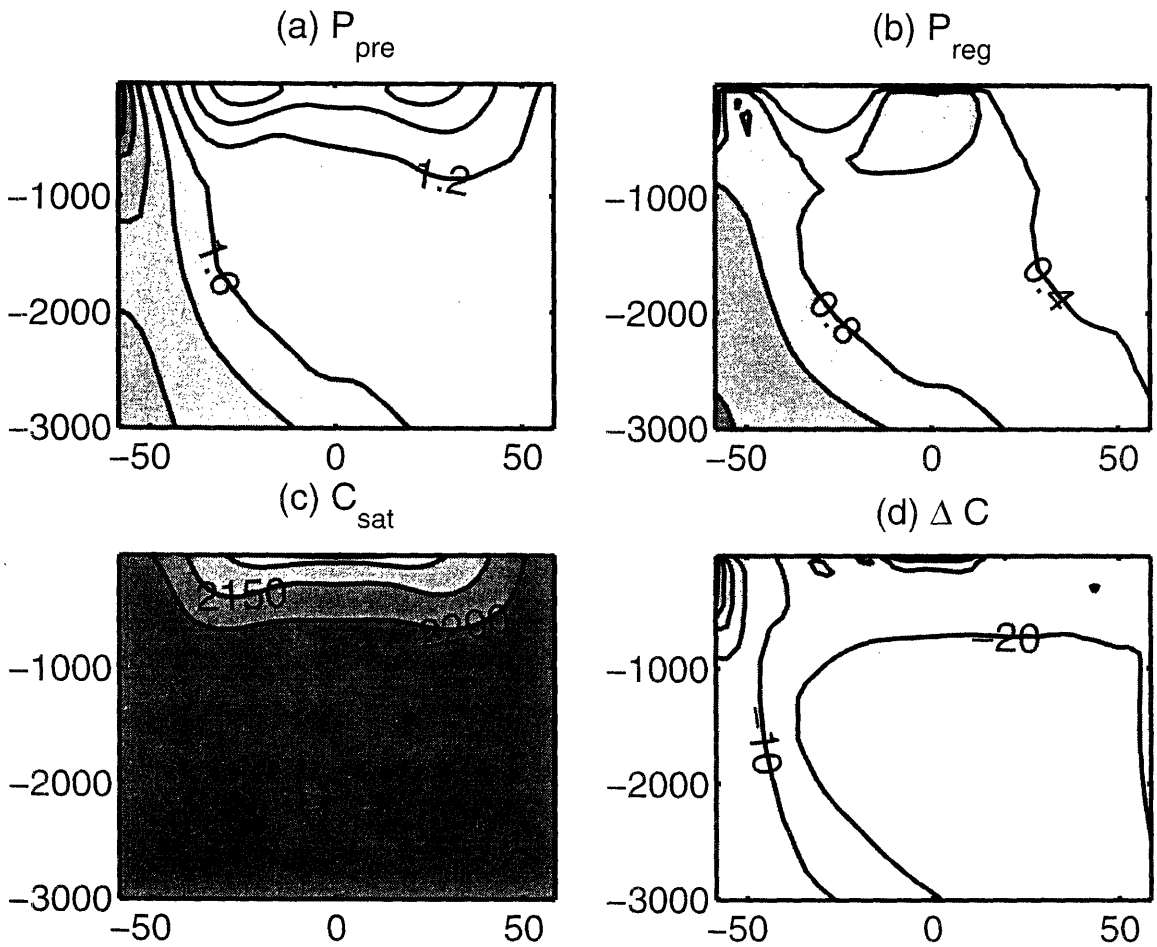

Figure 5-7: Zonally averaged carbon pump components at steady state in the control run. (a) Preformed phosphate, P_{pre}, in units of μM. Contour interval of 0.4 μM. (b) Regenerated phosphate, P_{reg}, with the same units and contour interval as (a). (c) Saturated carbon component, C_{sat}, in units of μM. Contour interval is 50 μM. (d) Disequilibrium component, ΔC, in units of μM. Contour interval is 10 μM.

causing a slight overestimation of respiration.

In the deep ocean, the lowest P_{reg} is found in the newly formed deep waters in the northern hemisphere. As the deep water moves southwards, regenerated phosphate increases due to remineralization. P_{reg} has its maximum concentration in the southern hemisphere. Fig.5-7(c) shows the saturated carbon distribution with respect to atmospheric pCO_2 of 270 ppmv. It largely reflects the variation of solubility of CO_2 with the thermal structure of the ocean. Fig.5-7(d) shows the distribution of disequilibrium carbon component. The deep ocean is mostly undersaturated with respect to the atmospheric CO_2 in this particular model due to the effect of heat loss at the region of deep water formation.

The surface phosphate concentration is carried into the ocean interior as preformed phosphate, thus, the water masses show distinct P_{pre} concentration. In this model, the subtropical thermocline is depleted in P_{pre}, reflecting the high degree of surface nutrient utilization in this region. In the deep ocean, the newly formed deep waters in the northern hemisphere carry approximately 0.9 μ M of P_{pre}, somewhat similar to the observed P_{pre} in North Atlantic Deep Water (NADW) shown in Fig. 5-2. In the southern hemisphere, the preformed phosphate concentration is very high, above 2.0 μM, reflecting high surface phosphate concentration.

Fig.5-5 reveals that a weak bottom overturning cell ventilates the deepest part of the ocean in the southern hemisphere. The formation of deep waters occurs at the southernmost grid near the western boundary of the model domain in this particular configuration. Polewards of the circumpolar current, the region of upwelling and the region of sinking are at similar latitudes. The upwelling deep waters are enriched in phosphate and carbon because of the integrated effect of remineralization. The biological uptake and export consume phosphate and carbon at the surface, however, the surface residence time of water is relatively short due to the convective mixing and the formation of deep waters. The upwelled water parcel leaves the surface layer before phosphate is completely utilized, and it maintains the large preformed nutrient concentration.

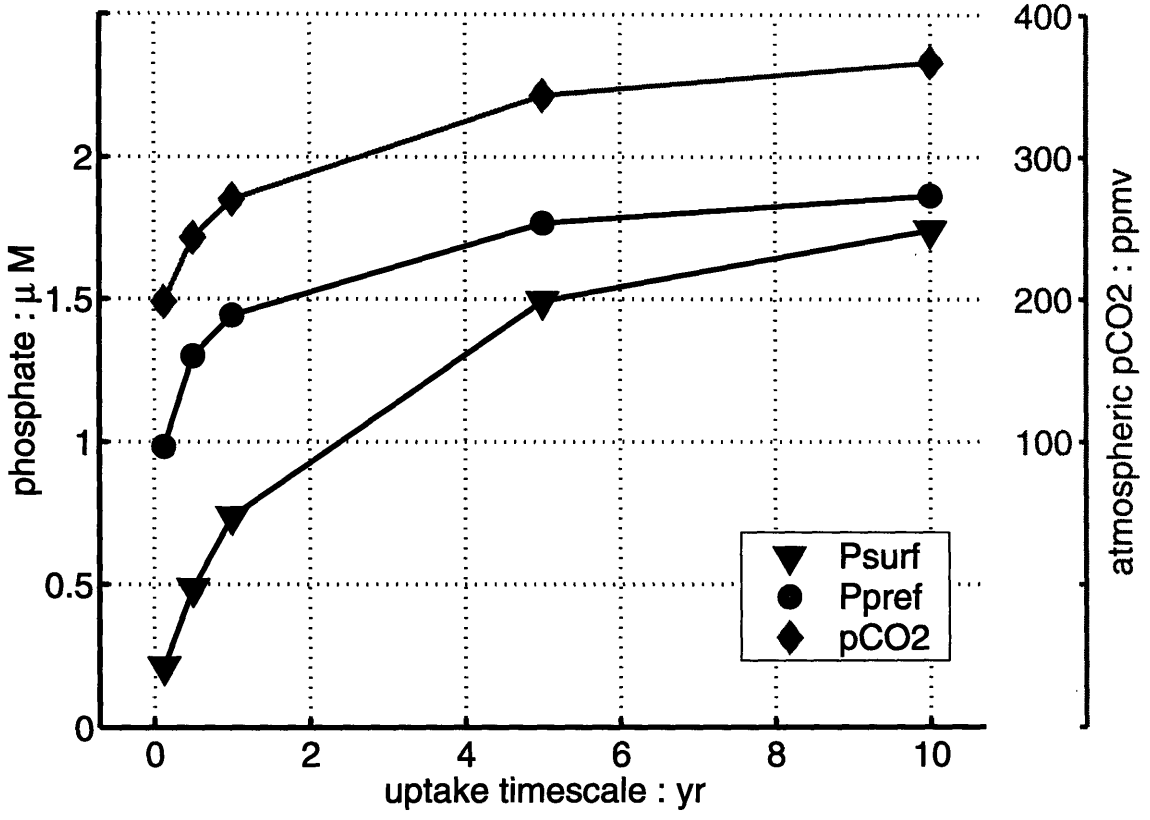

Figure 5-8: Simulated response of atmospheric CO_2, global mean P_{pre} and mean surface P to the variation of the biological uptake timescale.

5.3.4 Sensitivity run

We examine the sensitivity of atmospheric pCO_2 to a wide range of biological uptake parameter, τ_{bio}; from 1.5 months to 10 years. The total amount of carbon in the atmosphere and the ocean is conserved. Each experiment starts with the tracer distribution of the control run, and the model is spun up using different τ_{bio} for 1000 years. The response in atmospheric pCO_2 is evaluated.

Fig. 5-8 shows the variation of atmospheric CO_2, globally averaged preformed phosphate and the surface average phosphate concentration. As the biological uptake timescale becomes shorter, rapid removal depletes surface phosphate and draws down atmospheric CO_2. The relationship between biological export rate and atmospheric pCO_2 is not linear.

Fig.5-9 shows the relationship between pCO_2^{atm} and $\overline{P*}$ (and $\overline{P_{pre}}$), which is in a

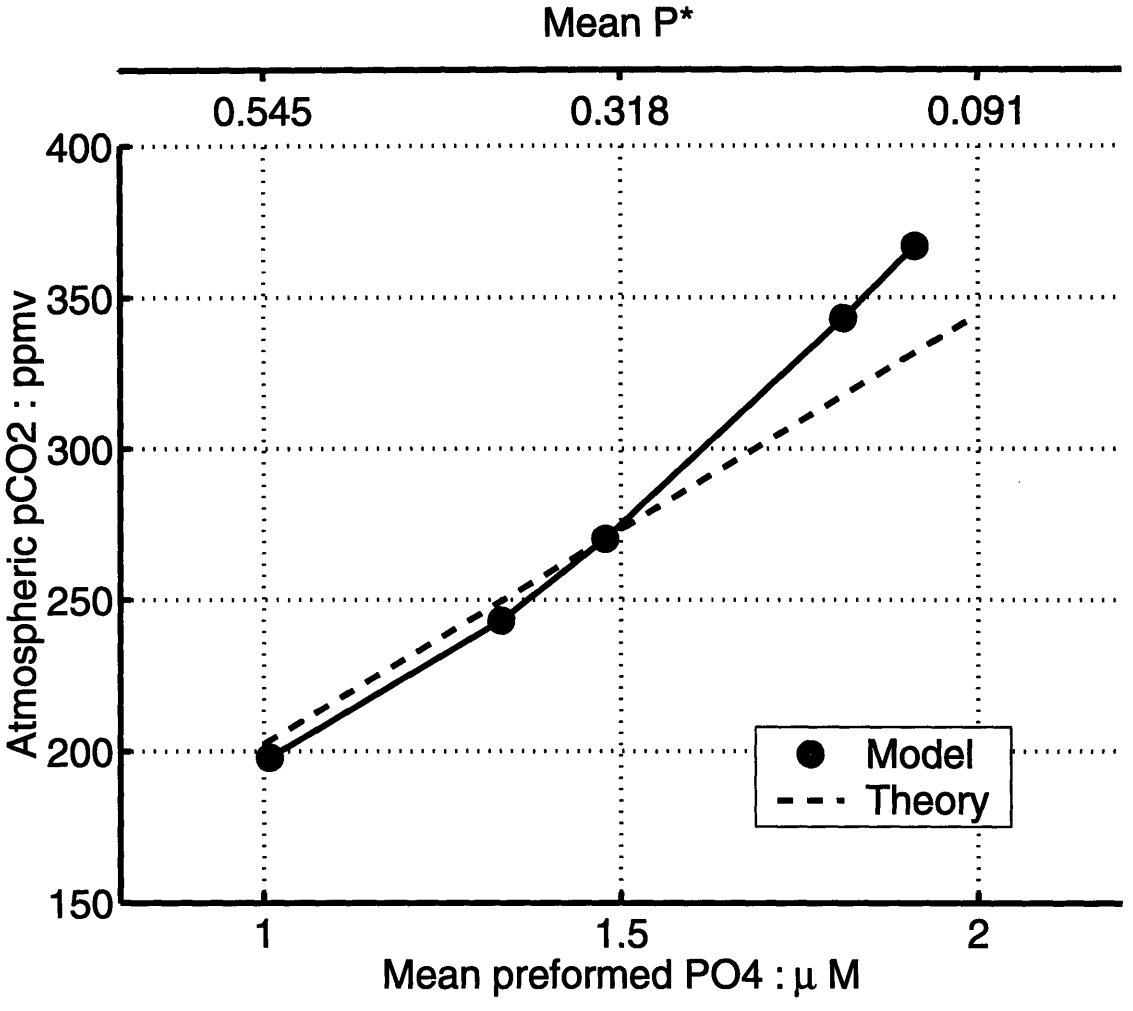

Figure 5-9: Simulated co-variation of atmospehric CO_2 to the global mean P_{pre}

reasonable agreement with the theoretical prediction (5.20). The dashed line represents the sensitivity of atmospheric CO_2 predicted by the simple theory. The theoretical slope, $\partial pCO_2^{atm}/\partial \overline{P*} = 312$ ppmv, and the intercept are chosen such that the theoretical sensitivity is referenced to the control run. The soft tissue pump is more efficient when preformed phosphate is drawn down by biological uptake. Atmospheric CO_2 varies from 200 ppmv to 360 ppmv corresponding to the variation of globally averaged P* of 0.45. When the mean preformed phosphate is high (above 1.7 μM), the theory somewhat underestimates the sensitivity. As we illustrate later, the difference between the theoretical prediction and the results from sensitivity experiments is partly due to the response of ΔC, and the finite amplitude of the perturbation.

Fig.5-10 shows the relationship between global mean preformed phosphate and mean surface phosphate. We have used wide range of the biological uptake timescales from 1.5 months to 10 years. Even with the uptake timescale of 1.5 months, we still find $\overline{P*}$=0.55 suggesting that only 55% of dissolved phosphate is formed by respiration on the global average. In contrast, the corresponding mean surface phosphate is very low on the order of 0.22 μM. There is a strong decoupling of surface phosphate and preformed phosphate when biological uptake is very rapid. In a limit case where surface phosphate is completely depleted, we would expect $\overline{P*}$ to be very close to 1 indicated by dash line in Fig. 5-10. However, the export timescale of 1.5 months close to the reasonable biological limit for marine biological organisms. Physical transport plays a critical role in relating the surface phosphate distribution and the preformed phosphate in the interior ocean. Deep waters are formed in highly localized regions in the high latitude oceans. The properties of surface waters at these localized regions control the preformed properties of the global deep waters. Formation of deep waters may be associated with intense convective mixing which supports a locally elevated phosphate concentration in the region of deep convection. Fig 5-11 illustrates the convective supply of phosphate in the region of deep convection, which plays a critical role in setting the upper bound of P* in the model. The preformed phosphate (and P*) of deep waters is set at the outcrop of deep isopycnals which is largely decoupled from the rest of the surface oceans. Vertical supply of phosphate due to convective mixing is sufficient to support elevated preformed phosphate even when the biological export is very efficient ($\tau_{bio} \sim$ 1.5 month). We suggest that the dynamics of the deep water formation limits the possible range of P* and the efficiency of the soft tissue pump.

Table 5.3.4 shows detailed results of the sensitivity experiments, showing the variation of the global average of each carbon pump component and atmospheric pCO_2 with corresponding values of τ_{bio}. We examine the carbon mass balance and diagnose the partitioning of carbon between the atmosphere and the ocean in order to better understand the carbon and nutrient balances in the model and evaluate the theory presented in section 5.2.3.

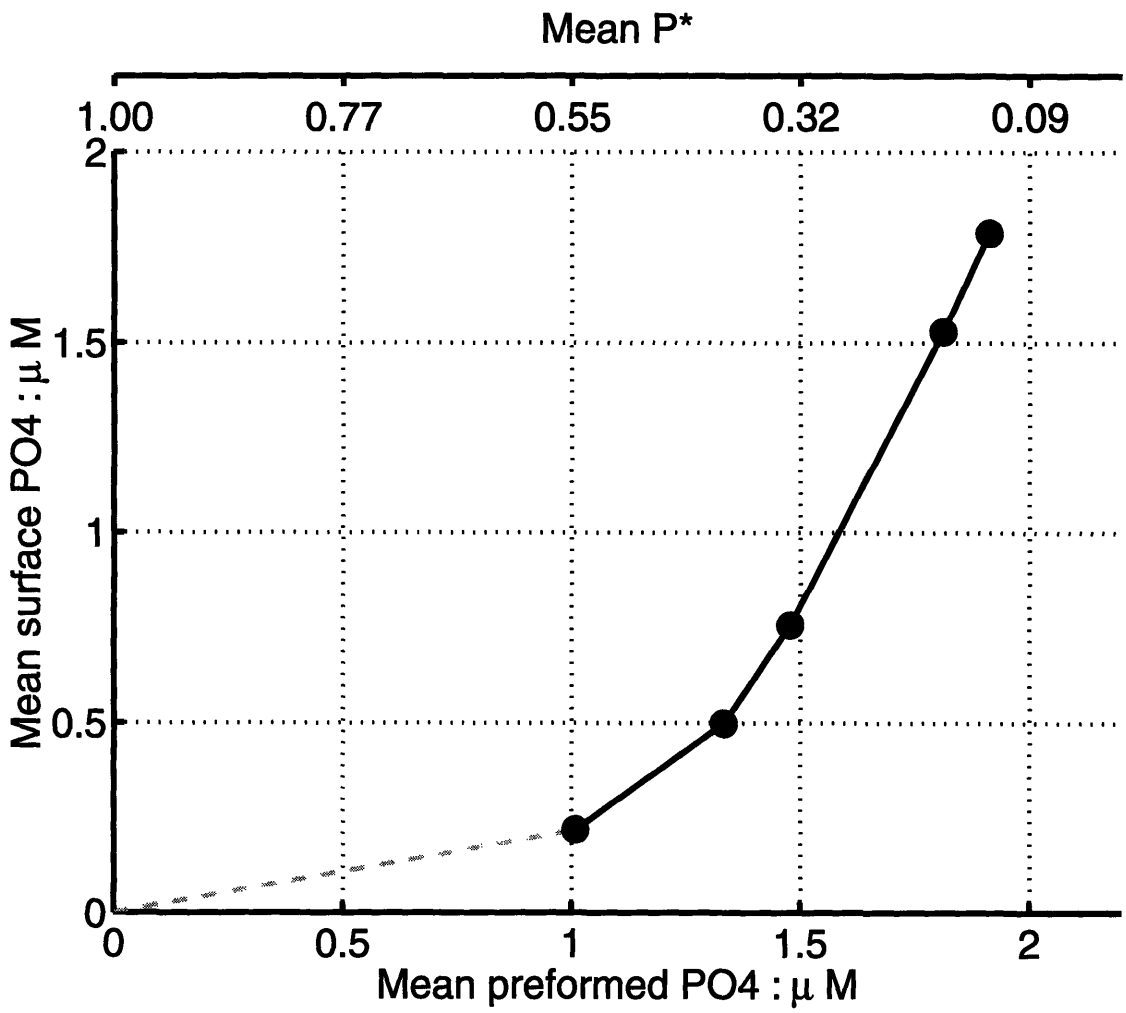

Figure 5-10: Relationship between the global mean P_{pre} and the mean surface P

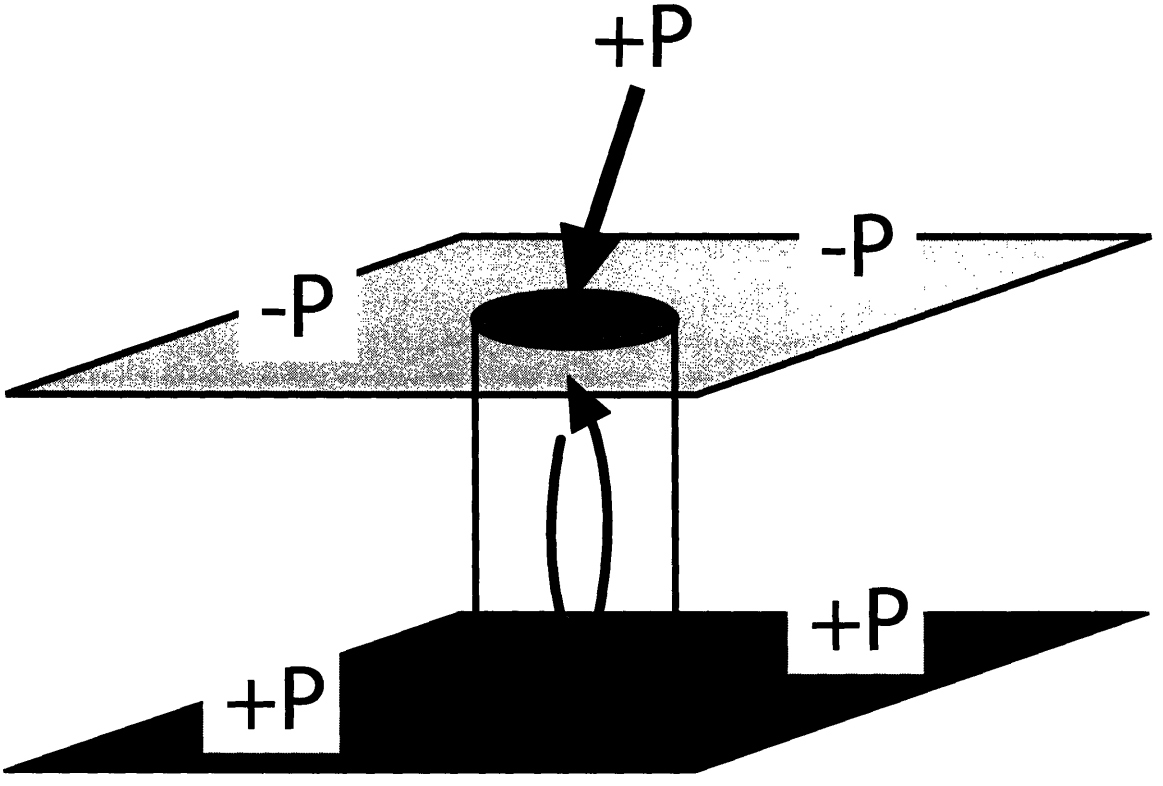

Figure 5-11: Preformed phosphate at a high latitude surface outcrop is elevated due to the vertical supply of phosphate through convective mixing

.

Table 5.2: Results from sensitivity experiments

Model Variable	Units	Exp1	Exp2	Control	Exp3	Exp4
τ_{bio}	days	45	180	360	1800	3600
pCO_2^{atm}	ppmv	198	243	270	343	367
$\overline{AOU}$	μM	196	141	117	60.3	43.4
$\overline{P_{surf}}$	μM	0.22	0.50	0.76	1.53	1.79
$\overline{P_{pre}}$	μM	0.98	1.30	1.44	1.77	1.87
$\overline{C_{reg}}$	μM	131	94.7	78.3	40.5	29.2
$\overline{\Delta C}$	μM	-5.65	-9.67	-13.6	-23.4	-25.6
$\overline{C_{sat}}$	μM	2057	2094	2112	2151	2161
$\overline{C}$	μM	2182	2179	2177	2168	2165

Fig. 5-12 is a graphical summary of the data presented in Table 5.3.4, showing the variation of the global inventory of each carbon pump components. Each of the runs has different partitioning of carbon between the atmosphere and the ocean, and between different carbon pump components within the ocean. We examine the partitioning of carbon among four reservoirs; (1) atmosphere, $M\,pCO_2^{atm}$, (2) saturated component, $V\,\overline{C_{sat}}$, (3) regenerated component, $V\,\overline{C_{reg}}$ and (4) disequilibrium component, $V\,\overline{\Delta C}$. In Fig. 5-12, the sum of variations in the four reservoirs (1) through (4) is always zero due to the global conservation of carbon. Partitioning of carbon changes significantly with the biological pump. The dominant balance is between the saturated component (2) and the regenerated component (4). As τ_{bio} increases (decreasing the biological uptake rate), the regenerated component decreases as a result of weaker biological pump. The decrease in $\overline{C_{reg}}$ is mainly balanced by the increase in $\overline{C_{sat}}$ consistent with the increase in atmospheric pCO_2.

There is a relatively small change in the disequilibrium component in response to the variations in the soft tissue pump. Toggweiler et al.(2003b) pointed out that air-sea disequilibrium enhances the effect of the biological pump, which is true in our model. Fig. 5-12 shows that $\delta\overline{\Delta C}$ and $\delta\overline{C_{org}}$ covary in the same sign. $\delta\overline{\Delta C} \sim 0.2\delta\overline{C_{org}}$. As the preformed nutrient is drawn down (i.e. stronger soft tissue pump and an increase in C_{org}), the degree of saturation also increases. When deep waters upwell and entrained into the mixed layer in the southern hemisphere, the surface water tends to be supersaturated because deep waters are enriched in phosphate and carbon through the integrated effect of remineralization, causing the outgassing of CO_2. In the regions of deep water formation, particularly, to the south of the circumpolar current, surface residence time of water parcel is relatively short, and the newly formed deep waters maintain some degree of supersaturation as they are subducted again.

Can we quantify the effect of supersaturation on the efficiency of the soft tissue pump ? Using (5.12) and (5.14), we can show that the sensitivity of atmospheric CO_2

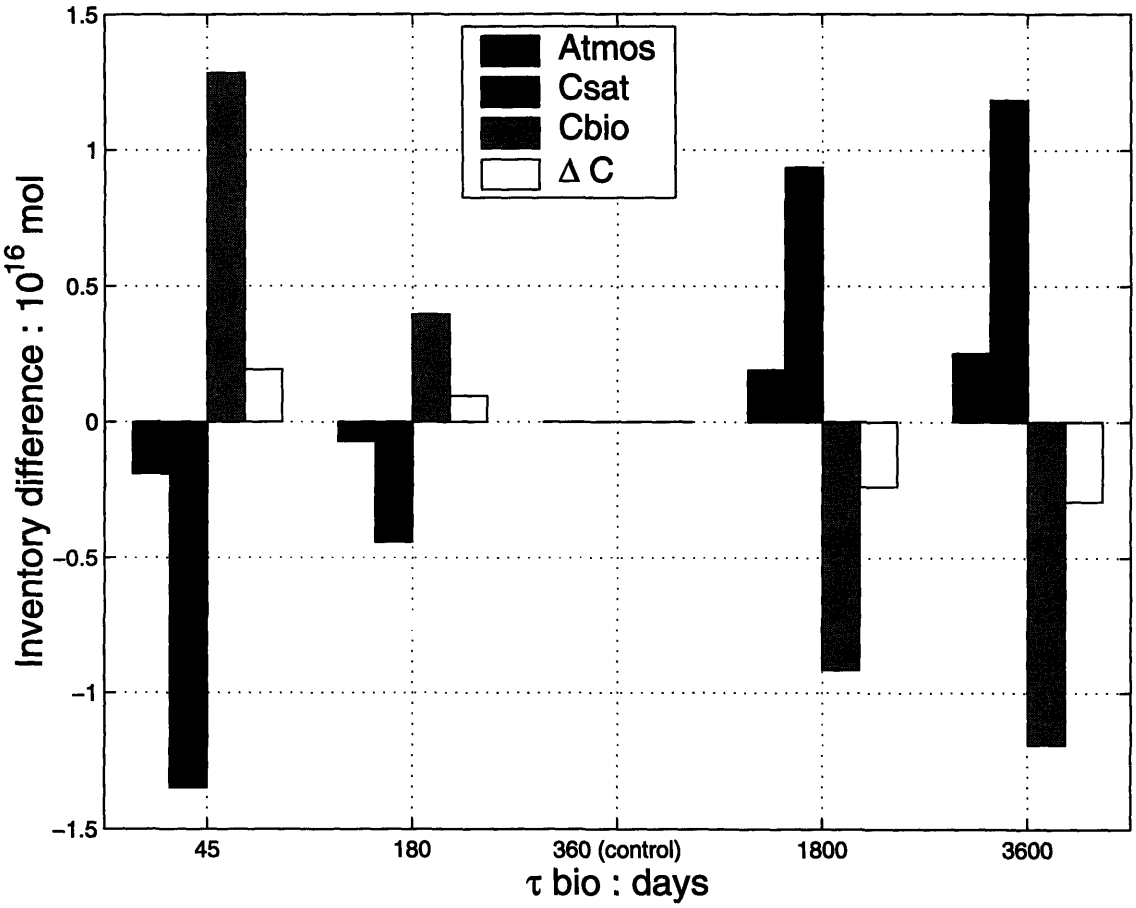

Figure 5-12: Carbon inventory difference relative to the control run. We consider the partition of carbon among four reservoir; (1) atmosphere, $M\,pCO_2^{atm}$, (2) saturated component, $V\,\overline{C_{sat}}$, (3) regenerated component, $V\,\overline{C_{reg}}$ and (4) disequilibrium component, $V\,\overline{\Delta C}$.

to globally averaged ΔC is identical to (5.15):

$$\frac{\delta pCO_2^{atm}}{\delta \overline{\Delta C}} = -\frac{V}{M\gamma} \tag{5.27}$$

The net response of atmospheric CO_2 to changes in both C_{org} and ΔC can be calculated by

$$\begin{aligned} \delta pCO_2^{atm} &= \frac{\delta pCO_2^{atm}}{\delta \overline{C_{org}}} \delta \overline{C_{org}} + \frac{\delta pCO_2^{atm}}{\delta \overline{\Delta C}} \delta \overline{\Delta C} \\ &= -\frac{V}{M\gamma} \{\delta \overline{C_{org}} + \delta \overline{\Delta C}\} \end{aligned} \tag{5.28}$$

While the theory does not predict the response of ΔC, in the sensitivity experiments studied here, we find $\delta \overline{\Delta C} \sim 0.2 \delta \overline{C_{org}}$. Thus, the air-sea disequilibrium enhances the effect of the biological pump by approximately 20%, a minor adjustment to the simple relationship (5.15).

The leading order balance in (5-12) is between $\overline{C_{sat}}$ and $\overline{C_{org}}$. Since the oceanic reservoir of carbon is much larger than the atmosphere, the variations in the carbon pump components tend to cancel out within the ocean. The atmospheric reservoir does not play a leading role in the carbon mass balance, and pCO_2^{atm} simply covaries with the saturated component, $\overline{C_{sat}}$.

5.4 Discussion

We have examined the relationship between atmospheric pCO_2 and the partitioning of phosphate between the preformed and regenerated pools using simple theory, observations and numerical experiments. Preformed phosphate is a clear signature of the major water masses in the oceans (Broecker et al., 1985; Broecker et al., 1998) and the associated P*, which is defined in Eq.(5.21), can be used as an indicator of the efficiency of the organic pump. Analysis of observed phosphate and oxygen data suggests that P* of newly formed NADW is on the order of 0.55 and that of AABW is on the order of 0.15. In the modern ocean, the value of the globally averaged P* is

approximately 0.36, indicating that 36% of phosphate returns to the interior ocean through biological export and remineralization. The soft tissue pump of the modern ocean is operating well below the theoretical maximum efficiency.

We develop a simple theory, combining the analysis of the carbon pumps with global conservation constraints, which predicts the relationships between the global mean P* and atmospheric pCO_2. The theory predicts that atmospheric pCO_2 decreases by ~30 ppmv for an increase in globally averaged P* by 0.1. The predicted sensitivity of atmospheric CO_2 is clearly supported by a suite of experiments with a numerical ocean-atmosphere carbon cycle model, over a wide range of biological uptake rates. The numerical experiments also reveal that the disequilibrium of CO_2 at the sea surface responds to changes in the variations in the soft tissue pump, increasing the sensitivity of atmospheric pCO_2 approximately by 20%.

Since the modern diagnostics suggest that global deep ocean preformed phosphate is currently on the order of 1.4 μM (Broecker et al., 1998; Conkright et al., 2002) and the corresponding $\overline{P^*}$ is 0.36, it seems to suggest that there is sufficient potential for change in the soft tissue pump to cause a glacial scale draw down of pCO_2 (~100ppmv). If surface macro-nutrients in the polar oceans are utilized and $\overline{P^*}$ increases to 0.7, the theory predict a glacial scale draw down of pCO_2 by 100 ppmv as a direct response to the changes in the biological pump. However, nutrient depletion experiments with numerical models have not borne this out (Archer et al., 2000). Such experiments have typically manipulated the surface PO_4 distribution through strong damping. It is implicitly assumed that very low surface nutrient concentrations must be equivalent to low preformed nutrient concentrations. However, the relationship between the surface nutrient distribution and global mean preformed nutrients (and P*) is not clear, as we have emphasized earlier.

In our numerical experiments, the case with very rapid export of surface PO_4 ($\tau = 1.5$ months) exhibited low surface nutrient concentrations (See, Fig.5-10) almost everywhere but the global mean preformed PO_4, the property significant for the carbon pumps, is still close to $1\mu M$. Deep waters are formed and ventilated at a few limited locations in the high latitude surface oceans, and the formation of deep

waters is often associated with intense convective mixing which supports a locally elevated phosphate concentration. The dynamics of deep water formation limits the potential range of P* at relatively low values (~ 0.55). Preformed phosphate and P* of deep waters are set at the outcrops of deep isopycnals which are largely decoupled from the rest of the surface oceans. We suggest that box models, which show a much stronger response of pCO_2 to draw down of surface nutrients, typically have wider range in preformed phosphate and P* due to the lack of representation of deep convection. Our theoretical predictions and numerical simulation indicate that the upper bound of $\overline{P*}$ is ultimately set by the localized dynamics of deep water formation. Furthermore, seasonal cycle of the biological productivity and deep mixing can further limit the efficiency of the biological pump. Biological uptake and export typically occur during spring and summer seasons when surface ocean is stratified and enough light is available for photosynthesis. Since the deep convection and the ventilation of deep oceans mainly occur during winter seasons, preformed nutrient is set to the surface nutrient concentration during the winter seasons when biological uptake is not active. These mechanism could ultimately control the efficiency of biological pumps even in a climate with higher rates of atmospheric dust deposition to the Southern Ocean.

We stress that the carbon pump analysis based on the concept of preformed and regenerated nutrients is the appropriate diagnostic framework for understanding and quantifying the relationships of biological activity and atmospheric CO_2. In order to better understand the existing body of numerical model experiments we suggest a reanalysis of the results and some effort to understand the relationships between mean surface ocean nutrient budgets and global mean preformed nutrients. With sufficient global data coverage it may be possible to quantify the current carbon pumps. The distributions of the preformed, regenerated and disequilibrium carbon pools provide a meaningful quantitative benchmark for comparison with modeled carbon pumps. We note that it is important that the regenerated components are evaluated with respect to the isopycnal outcrops using the concept of preformed properties of the waters (Broecker and Peng, 1982; Broecker et al., 1985; Broecker et al., 1998). Referencing

changes to global surface mean properties (e.g. Gruber and Sarmiento, 2002), focusing on the mean vertical gradients (e.g. Volk and Hoffert, 1985), or relating the carbon pumps to the global surface ocean nutrient inventory (Archer et al., 2000) leads to complications because the significant horizontal variations of properties are not accounted for.

Finally, our numerical model illustrates the compensation between C_{org} and C_{sat}: Increasing the soft tissue carbon component is largely compensated by the reduction in atmospheric CO_2 and the resulting reduction in C_{sat}, such that global carbon inventory is conserved. In addition, the disequilibrium carbon pool, ΔC, responds to the changes the biological pump, and the variation in the ΔC inventory has similar magnitude to that of the atmospheric CO_2 inventory, which makes some contribution to the amplification of the sensitivity of atmospheric pCO_2. The disequilibrium in regions of deep water formation reflects a complex interplay of the prior history of a water parcel, its residence time in the surface waters and the air-sea equilibration timescale for CO_2 (Toggweiler et al., 2003b). We believe that it is important to better understand what sets ΔC in the deep water formation regions in order to understand our models and the diagnostics from the modern ocean carbon cycle.

Chapter 6

Concluding remarks

6.1 Summary

This study examined the role of the ocean circulation in the biogeochemical cycles in the Southern Ocean using idealized, conceptual models of tracer transport and biogeochemistry. Mesoscale eddy transfers play dominant role in the dynamical and tracer balances in the ACC, and the transport of tracers is driven by the residual mean circulation which is the net effect of the Eulerian mean circulation and the eddy-induced circulation.

Using a simple analytical framework I have illustrated the sensitivity of the uptake of transient tracers to surface wind stress and buoyancy fluxes over the Southern Ocean. The uptake of CFC11, bomb-Δ^{14}C and anthropogenic CO_2 is simulated using a zonally averaged tracer transport model in which tracers are advected by the residual mean flow diagnosed from surface wind stress and buoyancy fluxes from the long-time mean NCEP-NCAR reanalysis. The model qualitatively reproduces observed distribution of CFC11 and bomb-Δ^{14}C, and a suite of sensitivity experiments illustrate the physical processes controlling the rates of the oceanic uptake of these tracers. The simulated relationship between CFC11 and bomb-Δ^{14}C is sensitive to the rates of the residual mean transport near the surface in the ACC, and observed distributions of these tracers provides a constraint on the rates of the residual mean transport in the ACC. The sensitivities of the uptake of CFC11 and bomb-Δ^{14}C are

largely different because of the differences in their air-sea equilibration timescales. The uptake of CFC11 is mainly determined by the rates of physical transport in the ocean, and that of bomb-$\Delta^{14}C$ is mainly controlled by the air-sea gas transfer velocity (piston velocity). Anthropogenic CO_2 falls in between these two cases, and the rate of anthropogenic CO_2 uptake is affected by both processes.

Biological productivity in the Southern Ocean is characterized as an "Antarctic Circumpolar Productivity Belt". I estimated the annually and zonally averaged export of biogenic silica through fitting the zonally averaged tracer transport model to the climatology of silicic acid using the method of least squares. The pattern of export production inferred from the inverse calculation is qualitatively consistent with recent observations. The pattern of inferred export production shows a maximum in the southern flank of the ACC. The advective transport by the residual mean circulation is the key process in bringing the estimated profile of the export production close to the observed pattern. The optimal solution can reproduce the Antarctic Circumpolar Productivity Belt reasonably well when the vigorous residual mean flow is included in the transport model.

Furthermore I examined simulated biological production in a physical-biogeochemical model which includes an explicit ecosystem model coupled to the phosphate, silica and iron cycle, in order to illustrate the mechanisms controlling the biological productivity in the Southern Ocean. Diagnosis of the simulated biological production and nutrient fields provide insights into the processes controlling the magnitude and the spatial pattern of the biological productivity. Simulated biological productivity shows the circumpolar belt of elevated biological productivity and indicates that it should coincide with the regime transition between the iron-limited Antarctic zone and the macro-nutrients limited Subantarctic zone. At the transition, organisms have relatively good access to both micro and macro-nutrients. The residual mean circulation upwells on the southern flank of the ACC, and downwells on the northern flank. This pattern of the overturning circulation, combined with the atmospheric dust deposition, controls the position of the regime transition and the productivity belt in the model.

Kohfeld (in Bopp et al.; 2003) suggested that there is a distinct, dipole pattern in the paleo-proxy of biological export in the Southern Ocean at the LGM. The reconstructed export production is higher to the north of the Polar Front during the LGM relative to modern conditions. Also, reconstructed export production was lower south of the Polar Front during the LGM. The observed paleo-productivity proxies may reflect the changes in the position of the Antarctic Circumpolar Productivity Belt over glacial-interglacial timescales. If the productivity belt is at lower latitudes during the LGM relative to modern conditions, the changes in the export production would be consistent with the pattern inferred from the paleo-productivity proxies. I examined possible changes in the position of the productivity belt to the changes in physical environment in the Southern Ocean.

Increased dust deposition during ice ages is unlikely to explain the equatorward shift in the position of the productivity belt. Since it will increase the area of the macro-nutrient limited regime, and the transition between the iron-limited regime and the macro-nutrient limited regime will migrate poleward. Then, the position of the productivity belt also migrates poleward, and the inferred changes in the biological production would be opposite from the pattern suggested by the paleo-productivity proxies.

The productivity belt is found at the transition between the iron-limited regime and the macro-nutrient regime where Fe* changes its sign. These regimes are strongly influenced by the pattern and strength of the overturing circulation in the Southern Ocean. Thus I examined the sensitivity of the meridional overturning circulation using a simple dynamical model. The overturning circulation of the Southern Ocean consists of the upper cell and the lower cell. The division between the upper cell and the lower cell is near the core of the upwelling region, and is characterized with $\Psi_{res} = 0$. A simple theoretical framework has been developed to illustrate the possible changes in the position of the cell partition in response to the variations in the wind stress in the Southern Ocean.

If surface wind stress was generally stronger in the LGM relative to the modern climate, the depth of the thermocline could have been greater. The theory suggests

that the net effect of the stronger wind stress and the deeper thermocline leads to an intensification of the surface residual mean flow. The stronger surface residual flow could shift the position of the productivity belt northward during the LGM consistent with the observed paleo-productivity proxies. This simple theory does not include many other potential changes during the LGM including the $Si:NO_3$ uptake ratio of diatoms and sea-ice distribution, which are the subject of future study.

This thesis is motivated by the outstanding record of the coupling between the atmospheric pCO_2 and the global climate over the glacial-interglacial timescales, and its potential link to the Southern Ocean. I have considered the role of the Southern Ocean biogeochemistry in the global carbon cycle and the glacial-interglacial variations in the atmospheric pCO_2. Simple box models developed in 1980s showed that atmospheric pCO_2 is sensitive to the "preformed" nutrient concentration which is connected to the high latitude surface oceans. Depleting surface macro-nutrients in high latitudes can explain the glacial pCO_2 drawdown in these simple box models. A possible mechanism for depleting the preformed nutrient in the LGM is to utilize the surface nutrients with an enhanced atmospheric dust deposition. A suite of sensitivity experiments are carried out with an ocean-atmosphere carbon cycle model with a wide range of the rate of nutrient uptake in the surface ocean. These experiments suggest that the ocean carbon cycle is unlikely to approach the theoretical limit where preformed nutrient is completely depleted due to the dynamics of deep water formation. The rapid vertical mixing timescales of convection precludes the ventilation of strongly nutrient depleted waters. Thus the utilization of macro-nutrients in the Southern Ocean is unlikely to be the direct cause for the glacial pCO_2.

6.2 Future outlook

Our ability to reconstruct past climate ultimately depends on the climate records and their interpretations. Paleoclimate records include geochemical measurements from the sea floor sediments, polar ice cores and terrestrial sediments. Development of physical-biogeochemical models helps improve our understanding of the paleocli-

matic proxies as well as the biogeochemical cycles of the modern climate. However, paleoclimatic proxies are sparse in space and time, and multiple interpretations are typically possible. The drawdown of surface macro-nutrients in the surface Southern Ocean has been proposed as a mechanism to lower atmospheric pCO_2 during ice ages (Francois et al., 1997; Sigman and Boyle, 2000; Toggweiler, 1999). The "preformed" nutrient concentration dictates the efficiency of the soft tissue pump of CO_2, and in simple box models, the high latitude surface ocean determines the "preformed" concentrations of deep waters. In chapter 5 of this thesis, I showed that "preformed" nutrients has a relatively high lower bound due to the rapid timescales of deep convection in the polar oceans. Therefore, I argue that the depletion of "preformed" nutrient cannot explain $\sim$ 100 ppmv drawdown of atmospheric pCO_2 even if global biological uptake timescale becomes on the order of a month.

What could be the alternative mechanism? One possibility is the changes in the saturation state of surface waters in the region of deep water formation. When the CO_2-enriched deep waters upwells in the high latitude Southern Ocean, outgassing of CO_2 occurs to release excess CO_2 into the atmosphere. Since the surface residence time is short in the convective regions, relative to the timescale of air-sea gas transfer, the surface CO_2 concentration may be far from equilibrium. The supersaturation of CO_2 due to the convective mixing and the entrainment of intermediate and deep waters is somewhat canceled out by the heat loss and associating solubility increase (Murnane et al., 1999). The saturation state of the "preformed" DIC concentration can make a significant impact on the global carbon cycle. The simple scaling of eq.(5.27) suggests that an increase in the global averaged ΔC by 10 μM leads to a drawdown of atmospheric pCO_2 by 12 ppmv. Thus, increasing ΔC together with the depletion of preformed nutrient could drive larger drawdown of atmospheric pCO_2. It is not yet clear what might be the possible range of variation in the saturation state of surface water, ΔC. The distribution of ΔC in the surface ocean dictates air-sea flux of CO_2, it has important implications for the uptake of CO_2 into the ocean. Air-sea heat flux, physical transport and biological sources drive surface concentrations away from equilibrium, and the degree of saturation depends on the relative timescale of

these processes with respect to the timescale of air-sea gas exchange. It is a subject of future study to separate and quantify the relative importance of these processes using models and observations of trace gases in the oceans.

So far, I have taken a "closed system" view of carbon cycle in the atmosphere-ocean system. On longer timescales ($\sim$ 10,000 years) the oceanic budget of carbon and alkalinity is controlled by the input of calcium carbonate from rivers and the burial at the sea floor sediments. Including these processes into existing physical-biogeochemical models brings a "open system" effects into the carbon cycle. Understanding interactions between the biogeochemistry and physical circulation of the oceans including dynamic adjustment of the oceanic calcium carbonate budget is a significant step towards understanding long term climate variability, and is certainly worthy of closer study.

Appendix A

Aquatic chemistry of CFC11

We briefly describe chemical component of the numerical model. We calculate the solubility of CFC11 following Warner and Weiss (1985). The equilibrium concentration of CFC11 is given as

$$C_{at} = k_{CFC11} pCFC \tag{A.1}$$

The air-sea flux of CFC11 is parameterized such that the air-sea flux (positive into the ocean) is

$$F = K_W (C_{at} - C) \tag{A.2}$$

The gas transfer coefficient, K_W is parameterized following Wanninkhof (1992).

Appendix B

Aquatic chemistry of CO_2

Chemical equilibrium is assumed for carbonate chemistry in the model, and the equilibrium constants are calculated following Millero (1995). In order to calculate the effective solubility for anthropogenic CO_2, we used the fact that variations in saturated DIC concentration are related to variations in partial pressure of CO_2 through the Buffer factor.

$$\delta DIC = \frac{DIC}{B_u \, pCO_2} \delta pCO_2 \tag{B.1}$$

where DIC and pCO_2 are the concentration and the partial pressure in the preindustrial sea water. We prescribe the anthropogenic perturbation in the partial pressure of CO_2, δpCO_2, to the values shown in Fig. 2-1. δDIC represents the anthropogenic perturbation in the equilibrium DIC, which would be the anthropogenic component of the DIC concentration if the surface water is saturated with the atmospheric pCO_2. Thus, the effective solubility of anthropogenic CO_2 can be calculated with preindustrial values of DIC, pCO_2, and B_u, assuming that the Buffer factor remains constant for the range of perturbation in pCO_2.

The saturated DIC concentration is determined as follows:

$$DIC_{at} = k_{CO_2} \left[1 + \frac{K_1}{[H^+]} + \frac{K_1 \, K_2}{[H^+]^2} \right] pCO_2^{at} \tag{B.2}$$

where k_{CO_2} is the solubility of CO_2 in sea waters (Weiss, 1974). Here, K_1 and K_2 are equilibrium constants for bicarbonate ions and carbonate ions (Mehrbach et al., 1973). In order to determine the relationship between the DIC concentration and the partial pressure of CO_2, the pH of the sea water must be determined. We calculate the pH of the surface water by an iterative method assuming that (1) the preindustrial atmospheric partial pressure, pCO_{20} is equal to 278 ppmv, and (2) temperature, salinity, and alkalinity of the surface water are prescribed. For temperature and salinity, we use streamline-averaged Levitus climatology. For alkalinity, we assume a spatially uniform concentration of 2300 μeq kg^{-1}. $[H^+]$ is solved using Newton's method, and the resulting equilibrium DIC concentration, DIC_0, is used to parameterize the effective solubility of anthropogenic CO_2. The Buffer factor, B_u, is also calculated by perturbing pCO_2 and recalculating DIC from with (B.2). DIC_0 and B_u are used to define C_{at} for anthropogenic CO_2.

$$C_{at} = \frac{DIC_0}{B_u\, pCO_2}(pCO_{20} - 278ppmv) \tag{B.3}$$

The gas exchange timescale for CO_2 is different from that of CFC11 because of the carbonate chemistry (Broecker and Peng, 1974) - see Table 2.2. The air-sea flux of anthropogenic CO_2 is parameterized as

$$F = \frac{K_W\, pCO_{20}}{DIC_0\, B_u}(C_{at} - C) \tag{B.4}$$

Bibliography

Anderson, L, A. (1995). On the hydrogen and oxygen content of marine phytoplankton. *Deep Sea Research, Part I*, 42(9):1675–1680.

Anderson, R., Kumar, N., Mortlock, R., Froelich, P., Kubik, P., Dittrich-Hannen, B., and Suter, M. (1998). Late-quaternary changes in productivity of the southern ocean. *Journal of Marine systems*, 17:497–514.

Andrews, D. and McIntyre, M. (1976). Planetary waves in horizontal and vertical shear : The generalized eliassen-palm relation and the zonal mean acceleration. *J. Atmos. Sci.*, 33:2031–2048.

Archer, D., Eshel, G., Winguth, A., W., B., and *et al.* (2000). Atmospheric co2 sensitivity to the biological pump in the ocean. *Global Biogeochemical Cycles*, 14:1219–1230.

Archer, D. and Johnson, K. (2000). A model of the iron cycle in the ocean. *Global Biogeochem. Cycles*, 14:269–279.

Archer, D., Martin, P., Milovich, J., Brovkin, V., Plattner, G., and Ashendel, C. (2003). Model sensitivity in the effect of antarctic sea ice and stratification on atmospheric pco2. *Paleoceanography*, 18(1). doi:10.1029/2002PA000760.

Bolin, B. and Eriksson, E. (1959). Changes in the carbon dioxide content of the atmosphere and sea due to fossil fuel combustion. In Bolin, B., editor, *The atmosphere and the sea in motion*, pages 130–142. Rockefeller institute press.

Bopp, L., Kohfeld, K., and Quéré, C. L. (2003). Dust impact on marine biota and atmospheric co_2. *Paleo.*, 18:doi:10.1029/20002PA0000810.

Boyd, P., Watson, A., Law, C., and *et al.* (2000). A mesoscale phytoplankton bloom in the polar southern ocean stimulated by iron fertilization. *Nature*, 407:695–702.

Boyle, E. (1998). Pumping iron makes thinner diatoms. *Nature*, 393((25 June)):733–734.

Brewer, P. G. (1978). Direct observation of oceanic co2 increase. *Geophysical research letters*, 5(12):997–1000.

Broecker, W. S. (1974). No a conservative water-mass tracer. *Earth and Planetary Science Letters*, 23(1):100–107.

Broecker, W. S., Peacock, S. L., Walker, S., Weiss, R., Fahrbach, E., Schroeder, M., Mikolajewicz, U., Heinze, C., Key, R., Peng, T.-H., and Rubin, S. (1998). How much deep water is formed in the southern ocean? *J. Geophys. Res.*, 103:15833–15843.

Broecker, W. S. and Peng, T. H. (1982). *Tracers in the sea.* Eldigio Press, Palisades, NY.

Broecker, W. S., Takahashi, T., and Takahashi, T. (1985). Sources and flow patterns of deep ocean waters as deduced from potential temperature, salinity, and initial phosphate concentration. *J. Geophys. Res.*, 90:6925–6939.

Bryan, F. (1986). High-latitude salinity effects and interhemispheric thermohaline circulations. *Nature*, 323:301–304.

Brzezinski, M., Pride, C., Franck, V., Sigman, D., Sarmiento, J., Matsumoto, K., Gruber, N., Rau, G., and Coale, K. (2002). A switch from si(oh)4 to no3- depletion in the glacial southern ocean. *Geophys. Res. Letters*, 29(12). doi:10.1029/2001GL014349.

Buesseler, K. O., Ball, L., Andrews, J., Cochran, J. K., Hirschberg, D. J., Bacon, M. P., Fleer, A., and Brzezinski, M. (2002). Upper ocean export of particulate organic carbon and biogenic silica in the southern ocean along 170°w. *Deep Sea Res. Part II*, 48:4275–4297.

Chen, G. T. and Millero, F. J. (1979). Gradual increase of oceanic co_2. *Nature*, 277:205–206.

Coale, K., Fitzwater, S., Gordon, R., Johnson, K., and Barber, R. (1996). Control of community growth and export production by upwelled iron in the equatorial pacific ocean. *Nature*, 379:621–624.

Conkright, M. E., Locarnini, R. A., Garcia, H. E., O'Brien, T. D., Stephens, C., and Antonov, J. I. (2002). *World Ocean Atlas 2001: Objective Analyses, Data Statistics, and Figures. CD-ROM Documentation.* National Oceanographic Data Center, Silver Spring, MD.

Dutay, J., Bullister, J., Doney, S., Orr, J., Najjar, R., Caldeira, K., Campin, J., Drange, H., Follows, M., Gao, Y., Gruber, N., Hecht, M., Ishida, A., Joos, F., Lindsay, K., Madec, G., Maier-Reimer, E., Marshall, J., Matear, R., Monfray, P., Plattner, G.-K., Sarmiento, J., Schlitzer, R., Slater, R., Totterdell, I., Weirig, M.-F., Yamanaka, Y., and Yool, A. (2002). Evaluation of ocean model ventilation with cfc-11: comparison of 13 global ocean models. *Ocean Modeling*, 4:89–120.

Dutkiewicz, S., Follows, M., Marshall, J., and Gregg, W. (2001). Interannual variability of phytoplankton abundances in the north atlantic. *Deep-Sea Res. II*, 48:2,323–2,344.

Dutkiewicz, S., Follows, M., and Parekh, P. (2004). Interactions of the iron and phosphorus cycles: a three-dimensional model study. *Global Biogeochem. Cycles.* submitted.

Follows, M., Ito, T., and Marotzke, J. (2002). The wind-driven, subtropical

gyres and the solubility pump of co_2. *Global Biogeochemical Cycles*, 16. doi:10.1029/2001GB001786.

Francois, R., Altabet, M. A., Yu, E.-F., Sigman, D. M., Bacon, M. P., Frank, M., Bohrmann, G., Barielle, G., and Labeyrie, L. D. (1997). Contribution of southern ocean surface-water stratification to low atmospheric co_2 concentrations during last glacial period. *Nature*, 389:929–935.

Gates, W. L., Boyle, J., Covey, C., Dease, C., Doutriaux, C., Drach, R., Fiorino, M., Gleckler, P., Hnilo, J., Marlais, S., Phillips, T., Potter, G., Santer, B., Sperber, K., Taylor, K., and Williams, D. (1998). *An Overview of the Results of the Atmospheric Model Intercomparison Project (AMIP).* PCMDI Report 45, Program for Climate Model Diagnosis and Intercomparison, Lawrence Livermore National Laboratory.

Gent, P. R. and McWilliams, J. C. (1990). Isopycnal mixing in ocean circulation model. *J. Phys. Oceanogr.*, 20:150–155.

Gildor, H. and Tziperman, E. (2001). Physical mechanisms behind biogeochemical glacial-interglacial co_2 variations. *Geophys. Res. Letters*, 28(12):2421–2424.

Gill, A. (1982). *Atmosphere-Ocean Dynamics.* Academic Press, London.

Gille, S. (1994). Mean sea-surface height of the antarctic circumpolar current from geosat data-method and application. *J. Geophys. Res.*, 99(C9):18255–18273.

Gille, S. (1995). *Dynamics of the Antarctic Circumpolar Current: Evidence for topographic effects from altimeter data and numerical model output.* PhD thesis, MIT/WHOI. Available from Woods Hole Oceanographic Institution, Woods Hole, MA 02543.

Gnanadesikan, A. (1999). A global model of silicon cycling: Sensitivity to eddy parameterization and dissolution. *Global Biogeochem. Cycles*, 13(1):199–220.

Gruber, N. (1998). Anthropogenic co_2 in the atlantic ocean. *Global Biogeochem. Cycles*, 12:165–191.

Gruber, N., Sarmiento, J. L., and Stocker, T. F. (1996). An improved method for detecting anthropogenic co_2 in the oceans. *Global Biogeochem. Cycles*, 10:809–837.

Honjo, S., Francois, R., Manganinia, S., Dymond, J., and Collier, R. (2000). Particle fluxes to the interior of the southern ocean in the western pacific sector along 170°w. *Deep Sea Res. Part II*, 47(15):3521–3548.

Hutchins, D. and Bruland, K. (1998). Iron-limited diatom growth and si:n uptake ratios in a coastal upwelling regime. *Nature*, 393:561–564.

Ito, T., Marshall, J., and Follows, M. (2004). What controls the uptake of transient tracers in the southern ocean? *Global Biogeochem. Cycles*, 18. GB2021, doi:10.1029/2003GB002103.

Johnson, G. and Bryden, H. L. (1989). On the size of the antarctic circumpolar current. *Deep Sea Res.*, 36:39–53.

Joussaume, S. and Taylor, K. (2000). The paleoclimate modeling intercomparison project. In Braconnot, P., editor, *Paleoclimate Modeling Intercomparison Project (PMIP) : proceedings of the third PMIP workshop*, WCRP-111, WMO/TD-1007. World Climate Research Programme.

Kalnay, E., Kanamitsu, M., Kistler, R., Collins, W., Deaven, D., Gandin, L., Iredell, M., Saha, S., White, G., Woollen, J., Zhu, Y., Leetmaa, A., Reynolds, B., Chelliah, M., Ebisuzaki, W., Higgins, W., Janowiak, J., Mo, K., Ropelewski, C., Wang, J., Jenne, R., and Joseph, D. (1996). The ncep/ncar 40-yr reanalysis project. *Bull. Amer. Meteor. Soc.*, 77:437–471.

Karsten, R., Jones, H., and Marshall, J. (2002). The role of eddy transfer in setting the stratification and transport of a circumpolar current. *J. Phys. Oceanogr.*, 32(1):39–54.

Karsten, R. and Marshall, J. (2002). Constructing the residual circulation of the antarctic circumpolar current from observations. *J. Phys. Oceanogr.*, 32(12):3315–3327.

Keeling, R. and Visbeck, M. (2001). Antarctic stratification and glacial co_2. *Nature*, 412:605–606.

Khatiwala, S., Visbeck, M., and Cane, M. (2004). Accelerated simulation of passive tracers in ocean circulation models. *Ocean Modelling.* submitted.

Knox, F. and McElroy, M. B. (1984). Changes in atmospheric co_2 — influence of the marine biota at high-latitude. *J. Geophys. Res. Atmos.*, 89:4629–4637.

Kumar, N., Anderson, R. F., Mortlock, R. A., Froelich, P. N., Kubik, P. W., Dittrich-Hannen, B., and Suter, M. (1995). Increases biological productivity and export production. *Nature*, 378:675–680.

Kumar, N., Gwiazda, R., Anderson, R., and Froelich, P. (1993). $^{231}pa/^{230}th$ ratios in sediments as a proxy for past changes in southern ocean productivity. *Nature*, 362:45–48.

Lefevre, N. and Watson, A. J. (1999). Modeling the geochemical cycle of iron in the oceans and its impact on atmospheric co_2 concentrations. *Global Biogeochem. Cycles*, 13:727–736.

Luyten, J., Pedloski, J., and Stommel, H. (1983). The ventilated thermocline. *J. Phys. Oceanogr.*, 13:292–309.

Mahowald, N., Luo, C., del Corral, J., and Zender, C. S. (2003). Interannual variability in atmospheric mineral aerosols from a 22-year model simulation and observational data. *J. Geophys. Res.*, 108(D12)(4352). doi:10.1029/2002JD002821.

Marotzke, J. and Willebrand, J. (1991). Multiple equilibria of the global thermohaline circulation. *J. Phys. Oceanogr.*, 21:1372–1385.

Marshall, D. (1995). Topographic steering of the antarctic circumpolar current. *J. Phys. Oceanogr.*, 25:1636–1650.

Marshall, D. (1997). Subduction of water masses in an eddying ocean. *J. Marine Res.*, 55:201–222.

Marshall, J., Adcroft, A., Hill, C., Perelman, L., and Heisey, C. (1997a). A finite-volume, incompressible navier stokes model for studies of the ocean on parallel computers. *J. Geophys. Res.*, 102(C3):5753–5766.

Marshall, J., Hill, C., Perelman, L., and Adcroft, A. (1997b). Hydrostatic, quasi-hydrostatic, and nonhydrostatic ocean modeling. *J. Geophys. Res.*, 102(C3):5733–5752.

Marshall, J. and Radko, T. (2003). Residual mean solutions for the antarctic circumpolar current and its associated overturning circulation. *J. Phys. Oceanogr.*, 33(11):2341–2354.

Martin, J. (1990). Glacial-interglacial co_2 change: The iron hypothesis. *Paleoceanography*, 5:1–13.

Martin, J., Coale, K., Johnson, K., Fitzwater, S., Gordon, R., Tanner, S., Hunter, C., Elrod, V., Nowicki, J., Coley, T., Barber, R., Lindley, S., Watson, A., Scoy, K. V., Law, C., Liddicoat, M., Ling, R., Stanton, T., Stockel, J., Collins, C., Anderson, A., Bidigare, R., Ondrusek, M., Latasa, M., Millero, F., Lee, K., Yao, W., Zhang, J., Fredrich, G., Sakamoto, C., Chavez, F., Buck, K., Kolber, Z., Green, R., Falkowski, P., Chisholm, S., Hoge, F., Swift, R., Yungle, J., Turner, S., Nightingale, P., Hatton, A., Liss, P., and Tindale, N. (1994). Testing the iron hypothesis in ecosystems of the equatorial pacific ocean. *Nature*, 371:123–129.

Martin, J. and Fitzwater, S. (1988). Iron deficiency limits phytoplankton growth in the north-east pacific subarctic. *Nature*, 331:341–343.

Martin, J., Knauer, G., Karl, D., and Broenkow, W. (1987). Vertex: carbon cycling in the northeast pacific. *Deep Sea Research*, 34:267–285.

Matsumoto, K., Lynch-Stieglitz, J., and Anderson, R. (2001). Similar glacial and holocene southern ocean. *Paleoceanography*, 16(5):445–454. 10.1029/2000PA000549.

Millero, F. (1995). Thermodynamics of the carbon dioxide system in the oceans. *Geochimica et Cosmochimica Acta*, 59:661–667.

Moore, J. K. and Abbott, M. R. (2000). Phytoplankton chlorophyll distributions and primary production in the southern ocean. *J. Geophys. Res.*, 105(C12):28709–28722.

Moore, J. K. and Abbott, M. R. (2002). Surface chlorophyll concentrations in relation to the antarctic polar front: seasonal and spatial patterns from satellite observations. *J. Mar. Systems*, 37:69–86.

Murnane, R. J., Sarmiento, J. L., and C, L. (1999). Spatial distribution of air-sea co2 fluxes and the interhemispheric transport of carbon by the oceans. *Global Biogeochemical Cycles*, 13(2):287–305.

Najjar, R. (1990). *Simulations of the phosphorus and oxygen cycles in the world ocean using a general circulation model.* PhD thesis, Princeton University.

Orr, J., Maier-Reimer, E., Mikolajewicz, U., Monfray, P., Sarmiento, J., Toggweiler, J., Taylor, N., Palmer, J., Gruber, N., Sabine, C., Qur, C. L., Key, R., , and Boutin, J. (2001). Estimates of anthropogenic carbon uptake from four three-dimensional global ocean models. *Global Biogeochem. Cycles*, 15(1):43–60.

Parekh, P., Follows, M., and Boyle, E. (2004a). Decoupling of phosphorus and iron in the global ocean. *Global Biogeochem. Cycles.* submitted.

Parekh, P., Follows, M., and Boyle, E. (2004b). Modeling the global ocean iron cycle. *Global Biogeochem. Cycles*, 18(GB1002). doi:10.1029/2003GB002061.

Pedlosky, J. (1986). *Geophysical Fluid Dynamics.* Springer-Verlag, Berlin Heidelberg.

Petit, J. R., Jouzel, J., Raynaud, D., Barkov, N. I., Barnola, J.-M., Basile, I., Bender, M., Chappellaz, J., Davis, M., Delaygue, G., Delmotte, M., Kotlyakov, V. M., Legrand, M., Lipenkov, V. Y., Lorius, C., Pepin, L., Ritz, C., Saltzman, E., and Stievenard, M. (1999). Climate and atmospheric history of the past 420,000 years from the vostok ice core, antarctica. *Nature*, 399:429–436.

Press, W. H., Flannery, B. P., Teukolsky, S. A., and Vetterling, W. T. (1992). *Numerical recipes in Fortran.* Cambridge University Press, Cambridge, UK.

Rintoul, S., Hughs, C., and Olbers, D. (2001). *Ocean circulation and climate: observing and modelling the global ocean*, chapter The Antarctic Circumpolar Current System, pages 271–302. Academic Press.

Robitaille, D. and Weaver, A. (1995). Validation of subgrid-scale mixing schemes using cfcs in a global ocean model. *Geophys. Res. Letters*, 22(21):2917–2920.

Rubin, S. and Key, R. (2002). Separating natural and bomb-produced radiocarbon in the ocean: The potential alkalinity method. *Global Biogeochem. Cycles*, 16(4). doi:10.1029/2001GB001432.

Sabine, C., Key, R. M., Millero, F. J., Poisson, A., Sarmiento, J. L., Wallace, D. W. R., and Winn, C. D. (1999). Anthropogenic co_2 inventory of the indian ocean. *Global Biogeochem. Cycles*, 13(1):179–198.

Sarmiento, J. L. and Orr, J. C. (1991). Three-dimensional simulations of the impact of southern ocean nutrient depletion on atmospheric co_2 and ocean chsmistry. *Limnol. Oceanogr.*, 36(8):1928–1950.

Sarmiento, J. L. and Toggweiler, J. R. (1984). A new model for the role of the oceans in determining atmospheric pco_2. *Nature*, 308(5960):621–624.

Schlitzer, R. (2002). Carbon export fluxes in the southern ocean: results from inverse modeling and comparison with satellite based estimates. *Deep Sea Res. Part II*, 49:1623–1644.

Schlosser, P., Bullister, J. L., and Bayer, R. (1991). Studies of deep water formation and circulation in the weddel sea using natural and anthropogenic tracers. *Mar. Chem.*, 35:97–122.

Siegenthaler, U. and Sarmiento, J. (1993). Atmospheric carbon dioxide and the ocean. *Nature*, 365:119–125.

Siegenthaler, U. and Wenk, T. (1984). Rapid atmospheric co_2 variations and ocean circulation. *Nature*, 308(5960):624–626.

Sigman, D. and Boyle, E. (2000). Glacial/interglacial variations in atmospheric carbon dioxide. *Nature*, 407:859–869.

Sigman, D. M. and Haug, G. H. (2003). The biological pump in the past. *Treatise on Geochemistry*, 6:491–528.

Smith, W. O. J., Anderson, R. F., Moore, K., Codispotid, L. A., and Morrisone, J. M. (2000). The us southern ocean joint global ocean flux study: an introduction to aesops. *Deep Sea Res. Part II*, 47(15):3073–3093.

Speer, K., Rintoul, S. R., and Sloyan, B. (2000). The diabatic deacon cell. *J. Phys. Oceanogr.*, 30:3212–3222.

Stephens, B. B. and Keeling, R. F. (2000). The influence of antarctic sea ice on glacial-interglacial co_2 variations. *Nature*, 404:171–174.

Sverdrup, H., Johnson, M., and Fleming, R. (1942). *The oceans: their physics, chemistry and general biology*, chapter 15. Prentice Hall, Englewood Cliffs, NJ.

Takahashi, T., Sutherland, S. C., Sweeney, C., Poisson, A., Metzl, N., Tilbrook, B., Bates, N., Wanninkhof, R., Feely, R. A., Sabine, C., Olafsson, J., and Nojirih, Y. (2002). Global sea-air co_2 flux based on climatological surface ocean pco_2, and seasonal biological and temperature effects. *Deep Sea Res.*, 49:1601–1622.

Thacker, W. (1989). The role of the hessian matrix in fitting the models to measurements. *J. Geophys. Res.*, 94(C5):6177–6196.

Toggweiler, J., Carson, S., and Murnane, R. (2003a). Representation of the carbon cycle in box models and gcms: 2.organic pump. *Global Biogeochemical Cycles*, 17(1). doi:10.1029/2001GB001841.

Toggweiler, J., Gnanadesikan, A., Carson, S., Murnane, R., and Sarmiento, J. (2003b). Representation of the carbon cycle in box models and gcms: 1.solubility pump. *Global Biogeochemical Cycles*, 17(1):1026. doi:10.1029/2001GB001401.

Toggweiler, J. R. (1999). Variation of atmospheric co_2 by ventilation of the ocean's deepest water. *Paleoceanography*, 14(5):571–588.

Trenberth, K. E., Olson, J. G., and Large, W. G. (1989). *A global ocean wind stress climatology based on ECMWF analyses.* Tech. Rep. NCAR/TN-338+STR, NCAR, Boulder, CO.

Visbeck, M., Marshall, J., Haine, T., and Spall, M. (1997). Specification of eddy transfer coefficients in coarse-resolution ocean circulation models. *J. Phys. Oceanogr.*, 27(3):381–402.

Volk, T. and Hoffert, Martin, I. (1985). Ocean carbon pumps: Analysis of relative strengths and efficiencies in ocean-driven atmospheric co_2 changes. In Sundquist, E, T. and Broecker, W, S., editors, *The carbon cycle and atmospheric CO_2: Natural variations Archean to present*, volume 32 of *Geophysical Monograph.* American Geophysical Union.

Weiss, R. R., Ostlund, H. G., and Craig, H. (1979). Geochemical studies of the weddel sea. *Deep Sea Res.*, 26:1093–1120.

Williams, R. and Follows, M. (2003). Physical transport of nutrients and the maintenance of biological production. In Fasham, M., editor, *Ocean Biogeochemistry.* Springer-Verlag.

Wunsch, C. (1996). *The ocean circulation inverse problem.* Cambridge University Press, Cambridge, UK.

Wyputta, U., Grieger, B., Paul, A., and Herterich, K. (2000). Investigating the boundary conditions for ocean models from PMIP simulations. In Braconnot, P., editor, *PMIP 2000: Paleoclimate Modelling Intercomparison Project (PMIP). Proceedings of the Third PMIP Workshop*, number WMO/TD-No. 1007 in WCRP-111, pages 135–140, Canada.

Yu, E.-F., Francois, R., and Bacon, M. P. (1996). Similar rates of modern and last-glacial ocean thermohaline circulation inferred from radiochemical data. *Nature*, 379:689–694.